Spectroscopic Characterization of the Surface Hydroxyls of Zeolitic Catalysts

Thesis for the Master's degree in Chemistry

So Hyun Kwak

Faculty of Mathematics and Natural Sciences

UNIVERSITY OF OSLO

December 2014

Spectroscopic Characterization of the Surface Hydroxyls of Zeolitic Catalysts

Thesis for the Master's degree in Chemistry

So Hyun Kwak

Faculty of Mathematics and Natural Sciences

UNIVERSITY OF OSLO

December 2014

2014

Spectroscopic Characterization of the Surface Hydroxyls of Zeolitic Catalysts

So Hyun Kwak

http://www.duo.uio.no/

Trykk: Reprosentralen, Universitetet i Oslo

Abstract

Methanol-to-hydrocarbons (MTH) process is a very important step in fuel and olefin production from alternative carbon sources. Products from the process can vary and be controlled by proper choice of catalyst and reaction conditions. Starting from ZSM-5 zeolite, many efforts have been put in to study various materials with different topologies over the last four decades [1].

Main goal for the study is to investigate factors that affect catalytic behavior of zeolites during MTH reaction using spectroscopic techniques. Among possible factors, special focus was directed to acid strength and concentration of zeolites as both are known to be one of the features responsible of catalysts performances regarding activity and lifetime. 12 different zeolites with 9 different topologies and various acid properties were selected for this purpose and characterized for acid density and strength by FTIR spectroscopy with probe molecules such as CO and pyridine. In-situ FTIR spectroscopy on the zeolites during the MTH reaction was performed as well in order to observe catalytic behavior of the 12 zeolites during the reaction. For more comprehensive understanding of these zeolites, part of these samples were tested on fixed bed reactor, and lifetime of the catalysts and product distributions were studied by Samaneh Etemadi [2].

It was observed that the intensity of so-called “coke bands” which were observed during in-situ FTIR spectroscopy in the MTH reaction has close relation with the acid concentration measured by pyridine adsorption experiment for the most of the zeolites investigated except ones with one-dimensional 10-ring channels (H-ZSM-23, H-ZSM-22). The reason for exceptional behavior of 1D 10-ring zeolites is thought to be deactivation of the samples occurred by blockage of pore mouth.

Meaningful relation between catalytic behavior and acid strength could not be found in this work. However, this does not mean that acid strength can be completely ruled out from the list of parameters affecting the MTH reaction. It could be the case that the acid strength between chosen twelve samples were not widely distributed enough to see the clear effect of the acid strength in the MTH reaction.

Acknowledgements

I would like to express my sincere gratitude to Prof. Stian Svelle, Dr. Sachin M. Chavan, and Prof. Unni Olsbye for being my supervisor and allowing me to perform this work. Stian, thank you for being my main supervisor, guiding me to the right direction during my study and believing in me. Your support meant a lot to me. Sachin, I sincerely appreciate that you spent so much time with me in the IR laboratories helping me out. You are always so passionate about the new findings we encounter, and it has been a great encouragement for me. I have learned incredibly a lot from you for the last two years. Thanks to Selene H. Morejudo for all the help in the synthesis and BET laboratory, and the MCM-22 sample. Nataliia Kasian, thank you for synthesizing IM-5, ITQ-13 and TNU-9 samples. I would like to express my gratitude to Rasmus Y. Brogaard for helping me through the calculation. Thank you so much David Wragg for kind explanation regarding XRD-related issues. Thanks to Marius W. Erichsen for interpretation of effluent analysis.

I appreciate that I could study in really nice environment with all the people at the inGAP. Thank you everyone in the group for providing friendly atmosphere and being open to interesting discussions. I really like the lunch at the inGAP, it has been always so cozy and fun.

Karina Mathisen and Stian Forselv at NTNU are greatly acknowledged for allowing me and helping me to perform the in-situ FTIR investigation in Trondheim.

I would like to express my sincere appreciation to my family for their support. Last but not least, Mats, thank you so much for supporting me during my master's study.

학위 과정 동안 항상 저를 믿어주시고 응원해주신 조부모님, 부모님, 민우, 그리고 다른 가족들께 너무나 감사드립니다. 제가 하는 선택을 언제나 지지해 주시는 가족들 덕에 정말 즐겁게 공부할 수 있었던 2 년이었습니다. 특히 할아버지, 할머니, 두 분이 집안에 조성해주신 면학 환경과 격려 덕에 항상 도전하고 노력하는 자세를 가질 수 있게 되었다고 생각합니다. 감사드립니다. 아버지, 어머니, 항상 열린 마음으로 저희를 대해주시고, 이끌어 주셔서 정말 감사드립니다.

Table of Contents

List of Abbreviations

A.U.	Arbitrary units
BET	Brunnauer, Emmet and Teller
CASTEP	Cambridge Serial Total Energy Package
CO	Carbon Monoxide
DFT-D Correction	Density Functional Dispersion Correction
DLATGS	Deuterated L-Alanine doped Triglycene Sulphate
DME	Dimethylether
DRFIT Spectroscopy	Diffuse Reflectance Infrared Fourier Transform Spectroscopy
EDS	Energy-Dispersive X-ray Spectroscopy
EFAl	Extraframework Alumium
FID	Flame Ionization Detector
FTIR Spectroscopy	Fourier Transform Infrared Spectroscopy
GC	Gas Chromatograph
HeptaMB	Heptamethylbenzene
HMMC	Hexamethylmethylenecyclohexadiene
HOMO	Highest Occupied Molecular Orbital
HTHP	High Temperature High Pressure
i.d.	Inner Diameter

IMEC	Integrated Molar Extinction Coefficients
inGAP	Innovative Natural Gas Processes and Products
IR	Infrared
IZA	International Zeolites Association
MCT	Mercury Cadmium Telluride
MeOH	Methanol
MO	Molecular orbital
MS	Mass Spectrometer
MTG	Methanol to Gasoline
MTH	Methanol to Hydrocarbon
MTO	Methanol to Olefin
MTP	Methanol to Propylene
NTNU	Norwegian University of Science and Technology
SEM	Scanning Electron Microscopy
TOS	Time on Stream
UiO	University of Oslo
WHSV	Weight hourly space velocity
XRD	X-ray Diffraction
Å	Ångstrøm

1 Introduction

1.1 Catalysis

Catalysis is very important in chemical industry as well as in our body since it allows reactions to happen under much milder conditions compared to the situation where a catalyst is not involved. Milder conditions in chemical industry lead to huge cost saving, and easier control of the condition.

A catalyst is a substance which accelerates a chemical reaction without itself being consumed. It does so by lowering the activation energy which reactants A and B have to overcome in order to form products. Catalysts might react to form an intermediate, but it is regenerated in subsequent steps.

In the Arrhenius equation,

$$k=Ae^{-Ea/RT}$$

where
k= rate constant
A=pre-exponential factor,
E_a=activation energy of a reaction
R=gas constant
T=absolute temperature

, the rate constant increases as activation energy decreases, and that's how catalysts increase the rate of a reaction. As seen from Figure 1. 1, the activation energy of uncatalyzed reaction (E_a) is bigger than that of catalyzed reaction (E_a'), Ea > Ea', and from the Arrhenius equation, it can be said that $Rate_{catalyzed} > Rate_{uncatalyzed}$ [3].

Depending on the nature of catalyst, catalysis can be categorized into three different groups: Homogeneous, heterogeneous, and biocatalysis.

In homogeneous catalysis, the reactants and catalysts are in the same phase, usually liquid. This type of catalysis is normally used in production of fine chemicals. Advantage of homogeneous catalyst are 1) easy mixing of reactants and catalysts which leads to a good heat transfer during the reaction, and 2) high selectivity of products. Disadvantages of homogeneous catalyst, however, are 1) difficult separation of catalysts and products, and 2) the high price of catalysts [4].

In heterogeneous catalysis, the reactants and catalysts are in different phase. In most of the cases, the reactants are either gas or solution while the catalyst is a solid. This type of catalysis is usually applied to larger processes (industrial chemistry). Advantages of heterogeneous catalysis are 1) easy separation of catalysts from the products, 2) more flexible regeneration of catalysts and 3) less expensive catalyst. However, a reaction is often less selective than homogeneous catalysis, since the reaction happens over a heterogeneous catalyst with a distribution of active sites [5].

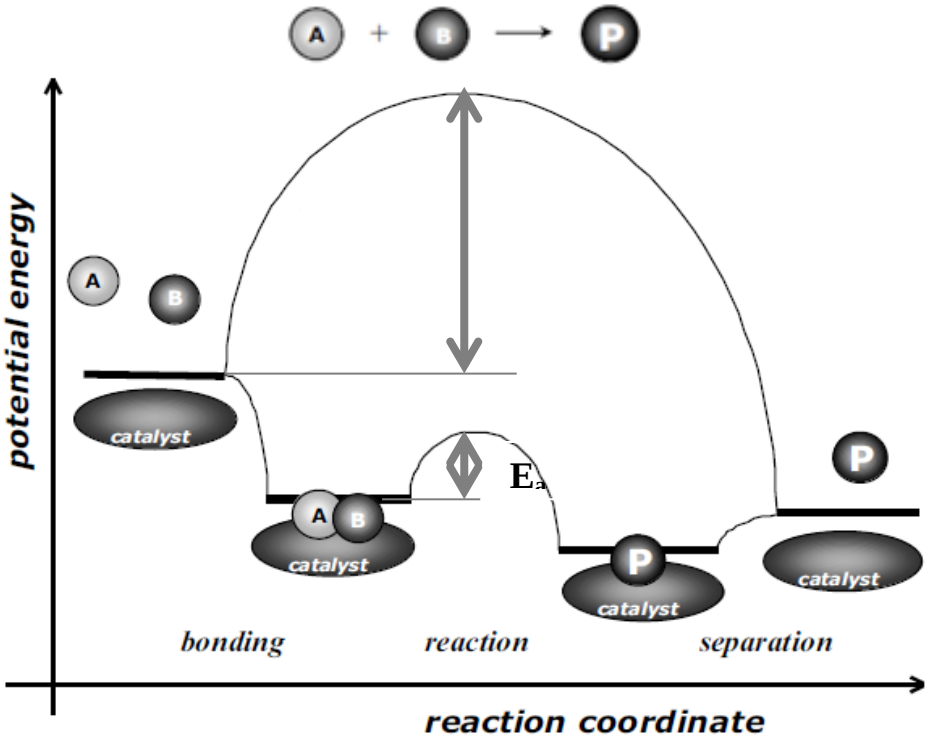

Figure 1. 1: Potential energy diagram of uncatalyzed reaction and heterogeneous catalytic reaction. From reference [6]

Enzymes are the catalysts of biocatalysis. They are originally from the nature, and highly effective and specific as an enzyme only acts on certain reactants (usually called substrates). They can increase the rate of biochemical reaction by factors of 10^6 to 10^{18}. Biocatalysis is usually homogeneous, as the enzyme and reactants are in aqueous solution. [3]

In this work, heterogeneous catalysis is the main target of interest since catalysts used in this work are solid zeolites. They are mainly involved in the reaction, methanol to hydrocarbon, with gas phase reactants and products.

1.2 Zeolites

Zeolites are aluminosilicate crystalline solids existing both naturally and synthetically. The word zeolite came from the Greek word "zeo (to boil)" and "lithos (stones)" [7] meaning boiling stones as zeolites release lots of water upon heating.

One of the features which make zeolites special is porosity. Thanks to its porosity, zeolites have very high surface area, and this is important since catalytic reactions involving zeolite happen on the surface of catalyst. Typically surface areas of zeolite are of the order of 300-700 m^2/g. For example, for a zeolite sample with 500 m^2/g surface area, 10g of this catalyst has a surface area close to the size of a U.S. football field (5350 m^2) [8, 9] . Porous materials can be categorized according to pore width: microporous material (pore diameter $\leq$ 2.0 nm), mesoporous material (2.0 nm < pore diameter $\leq$ 50 nm), and macroporous material (pore diameter > 50 nm). Zeolites and zeotypes are microporous materials. [10]

In zeolite structures, TO_4 units (T=Si or Al) are connected to each other by sharing oxygens at each tetrahedral corner (Figure 1. 2). This connection creates an infinite lattice, and makes it possible to build various pore geometries. It is possible that the T atom is something else than Si or Al such as in zeolite-like materials called SAPO. SAPOs consist of TO_4 units as in zeolites, but T atoms can be silicon, aluminium or phosphorous. However, in this case, it is more common to categorize as zeotypes rather than zeolites [11].

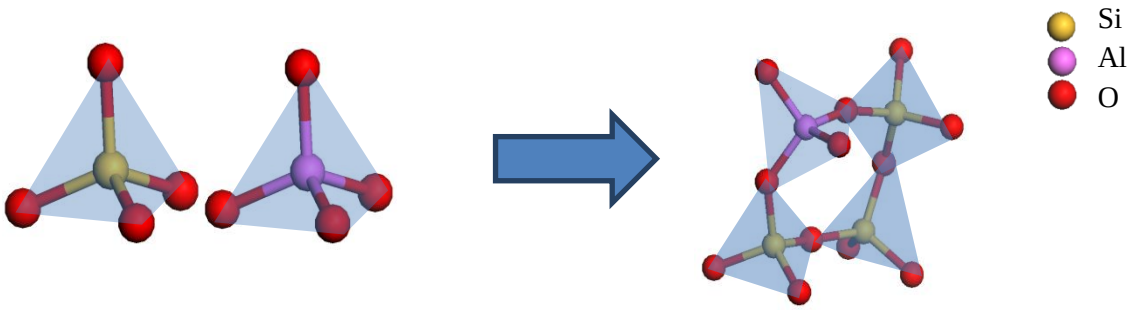

Figure 1. 2: Tetrahedra of $(SiO_4)^{4-}$, $(AlO_4)^{5-}$, and corner sharing of TO_4 tetrahedra. Adapted from [12].

1.2.1 Acidity

Assuming zeolites consist of only $[SiO_4]^{4-}$ tetrahedral unit, it would have electrically neutral framework with chemical formula of SiO_2. However, if one substitute $[SiO_4]^{4-}$ tetrahedron with an $[AlO_4]^{5-}$ tetrahedron, charge balance gets broken and zeolite will acquire a negative charge in the framework. This has to be balanced by non-framework cations. In this work, we are most interested in the case where the proton functions as a charge-balancing cation, and forms a bridging Brønsted acid site (-Si(OH)Al-). By definition, a Brønsted acid site is a proton donor. Figure 1. 3 illustrates how a Brønsted acid site is formed, replacing of a $[SiO_4]^{4-}$ with $[AlO_4]^{5-}$ followed by adding of hydrogen for charge balancing. This acid site has a key role as active site in MTH reaction.

For some of zeolite samples, Lewis acid site, which works as electron acceptor, is observed. This Lewis site is usually generated because of lattice defect or extraframework aluminium (EFAl) in the system.

In the topic of acidity in zeolites, usually two things are considered to be important, acid strength and acid density. Method implemented in this work to measure the acid strength is to observe FTIR spectra of zeolite under carbon monoxide (CO) adsorption experiment. Carbon monoxide, as weak basic probe molecule, adsorbs on acid site of zeolite forming hydrogen bond with hydroxyl group in zeolite, and pertubates the hydroxyl stretching band. That is, one can observe red shift of hydroxyl stretching band as it interacts with carbon monoxide. Acid strength can be compared by using the degree of the perturbation. The bigger the red shift is,

the stronger the acid strength is. It will be explained more deeply in section 2.2.2. Acid density refers to concentration of acid sites per gram area catalyst. FTIR experiment on zeolites using pyridine as probe molecule was performed in this work to investigate the acid density of different zeolites. Pyridine, as a strong base, interacts with acid sites of zeolites. From the absorb peak of pyridinium ion adsorbed on Brønsted acid site and pyridine adsorbed on Lewis acid site, one can calculate the concentration of the acid sites per gram area catalyst. More of the theory will be dealt in section 2.2.2.

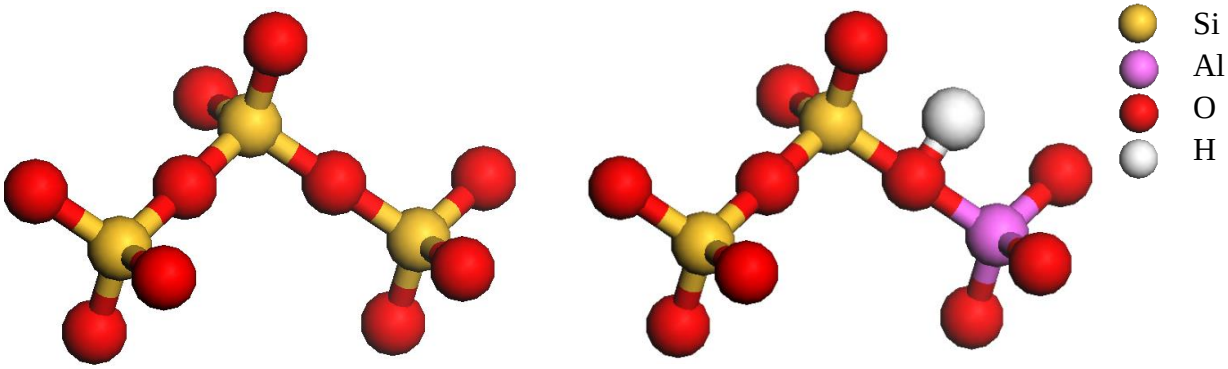

Figure 1. 3: Three $[SiO_4]^{4-}$ tetrahedral connected via oxygen bridge (left), and formation of Brønsted acid site by replacing a $[SiO_4]^{4-}$ tetrahedron with a $[AlO_4]^{5-}$ tetrahedron. Adapted from [12]

1.2.2 Shape Selectivity

As mentioned earlier, zeolite is a porous material. However, pore size is different from framework to framework of zeolite. Thanks to this difference, zeolite can let certain reactants selectively into the pore, let certain products selectively get out of the pore, or let certain transition states selectively form inside of the pore.

Reactant selectivity (Figure 1. 4 (a)) occurs when bulky reactants are excluded from entering into the pore system, thus interaction with internal active sites (mostly acid sites in zeolites) is prohibited. Product selectivity (Figure 1. 4 (c)) takes place when several different products are formed inside of the pore of zeolites, but some of them are too big to diffuse out of the system unless there is further reaction to form smaller molecules from them. This often happens in zeolites with large internal cavities connected with narrow channels. Large molecules are

formed inside of internal cavities, but cannot diffuse out through narrow channels, and trapped inside of cavities. This can lead to coking of the catalyst as bulky products block the pore inside of zeolites which makes active sites inside of the pore inaccessible to other molecules. Transition sate shape selectivity (Figure 1. 4 (c)) refers to the case when certain transition states and reaction intermediates are not allowed inside of pores because of steric restriction which prevents the progress of certain reactions.

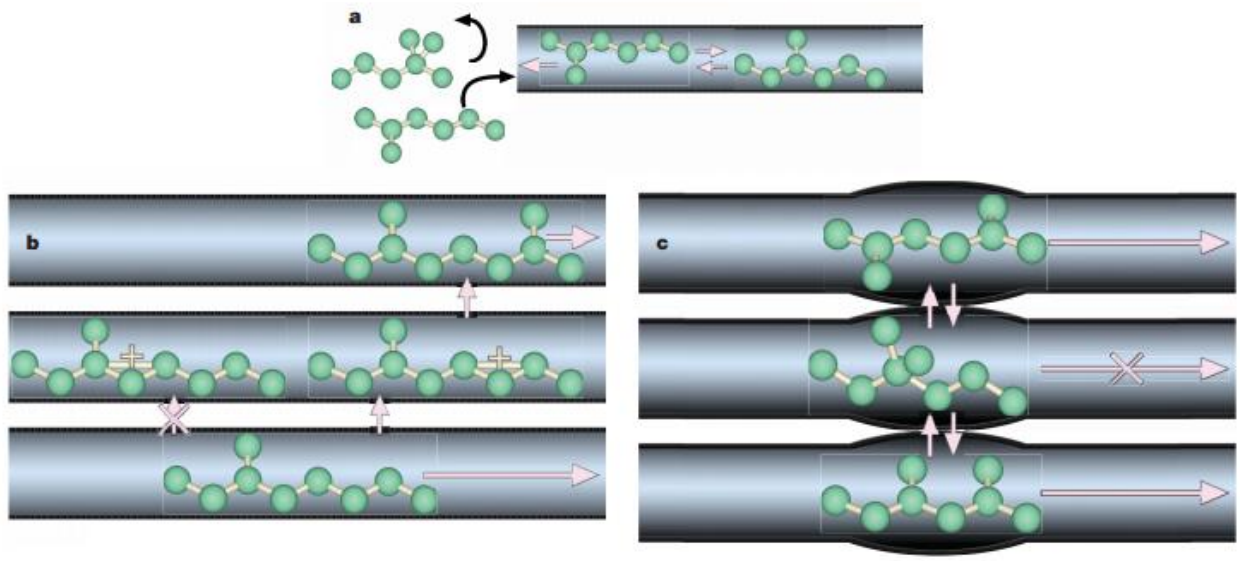

Figure 1. 4: Representation of (a) reactant shape selectivity in zeolite channels, (b) transition state shape selectivity in zeolite channels, and (c) product shape selectivity in zeolite channels. From reference [13]

1.2.3 Zeolite Structures relevant to this work

There are 9 zeolitic frameworks which are relevant to this work: MTT, TON, MOR, MWW, IMF, ITH, MFI, SZR, TUN, and *BEA. Choice of frameworks was based on the materials extensively used in the group, inGAP (Innovative Natural Gas Processes and Products), with diversity in framework types, channel types and active sites properties. One can find framework types, materials, Si/Al, channel types & size, and maximum diameter of a sphere which can be included in the channels from Table 1. 1.

Table 1. 1: List of framework types relevant to this work with details. (Sample names, Si/Al, channel type, channel size, and maximum diameter of sphere that can be included in the channels.) Bold number on 'size of channel' column refers to ring size (e.g. **10** 4.5x5.2 Å [001] means that there are 10-ring channels with diameter of 4.5 Å and 5.2 Å, along [001] direction.)

Framework Type	Material	Si/Al	Channels	Size of channels [14]	Max. Diameter of a sphere [14]
MTT	ZSM-23	23	1D, 10-ring	**10** 4.5x5.2 Å [001]	6.19 Å
TON	ZSM-22	45	1D, 10-ring	**10** 4.6x5.7Å [001]	5.71 Å
MOR	Mordenite	22	1D, 12-ring 8-ring	**12** 6.5x7.0Å[001] **8** 2.6x5.7Å[001]	6.70 Å
MWW	MCM-22	15	2D, 10-ring	**10** 4.0x5.5Å[001] **10** 4.1x5.1Å[001]	9.69 Å
IMF	IM-5	15	3D, 10-ring	**10** 5.5x5.6Å[001] **10** 4.8x5.4Å[001] **10** 5.3x5.4Å[100] **10** 5.1x5.3Å[100] **10** 5.3x5.9Å[010]	7.34 Å
ITH	ITQ-13	50	3D, 10-ring 9-ring	**10** 4.8x5.3Å[001] **10** 4.8x5.1Å[010] **9** 4.0x4.8Å[100]	6.72 Å
MFI	MFI-27 Pentasil ZSM-5	13.5 45 50	3D, 10-ring	**10** 5.1x5.5 Å [100] **10** 5.3x5.6 Å [010]	6.36 Å
SZR	SUZ-4	8	3D, 10-ring 8-ring	**10** 4.1x5.2Å[001] **8** 3.2x4.8Å[010] **8** 3.0x4.8Å[110]	6.27 Å
TUN	TNU-9	15	3D, 10-ring	**10** 5.6x5.5Å [010] **10** 5.1x5.5Å [010] **10** 5.4x5.5Å [10$\bar{1}$]	8.46 Å
*BEA	Beta	12.5	3D, 12-ring	**12** 6.6x6.7Å[100] **12** 5.6x5.6[001]	6.68 Å

One-dimensional 10-ring zeolites

MTT and TON are two framework types with one-dimensional 10-ring channel system. MTT has a tear-drop shape channels with side pockets while TON has an elliptical channels and the channels aligned in zigzag shape [15]. Maximum diameter of a sphere that can be included in the channel is larger in MTT (6.19 Å) compare to TON (5.71 Å).

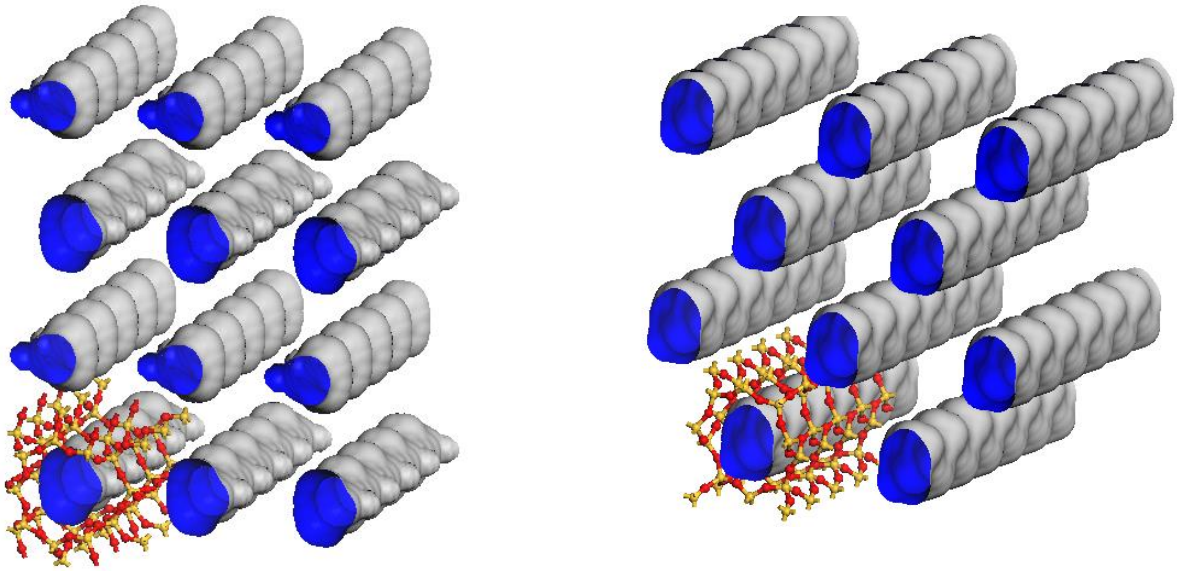

Figure 1. 5: Illustration of MTT topology (left) and TON topology (right)

One-dimensional 12-ring zeolite

Mordenite is the only one-dimensional 12-ring zeolite studied in this work. It is one of the materials with MOR framework type. Mordenite has one-dimensional 12-rings along [001] with size of 6.5x7.0 Å, and one-dimensional 8-rings along [001] with size of 2.6x5.7Å. 8-ring channels are located between 12-ring channels [14]. The maximum diameter of sphere that can be included in the channels is 6.70 Å.

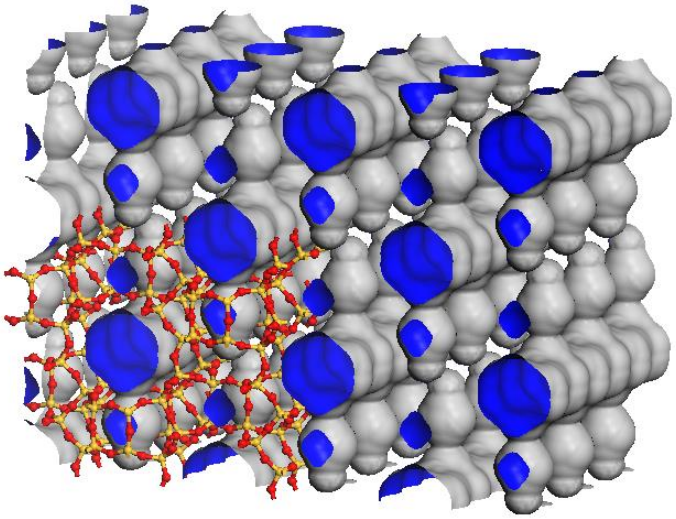

Figure 1. 6: Illustration of the MOR topology.

Two-dimensional 10-ring zeolite

MCM-22 is one of materials with MWW framework type. MCM-22 has two non-intersecting two-dimensional 10-rings normal to [001], one with size of 4.0x5.5 Å, located between layers, and another with size of 4.1x5.1 Å, located within the layers [14]. Maximum diameter of sphere that can be included in the channels is 9.69 Å, and this value is the largest among all 12 samples.

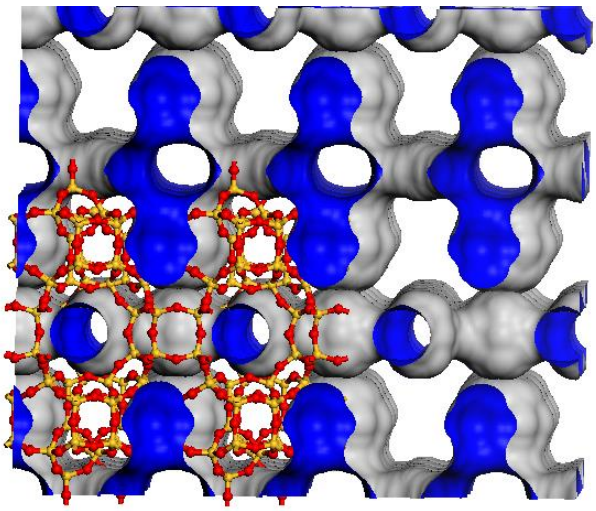

Figure 1. 7: Illustration of the MWW topology.

Three-dimensional 10-ring zeolites

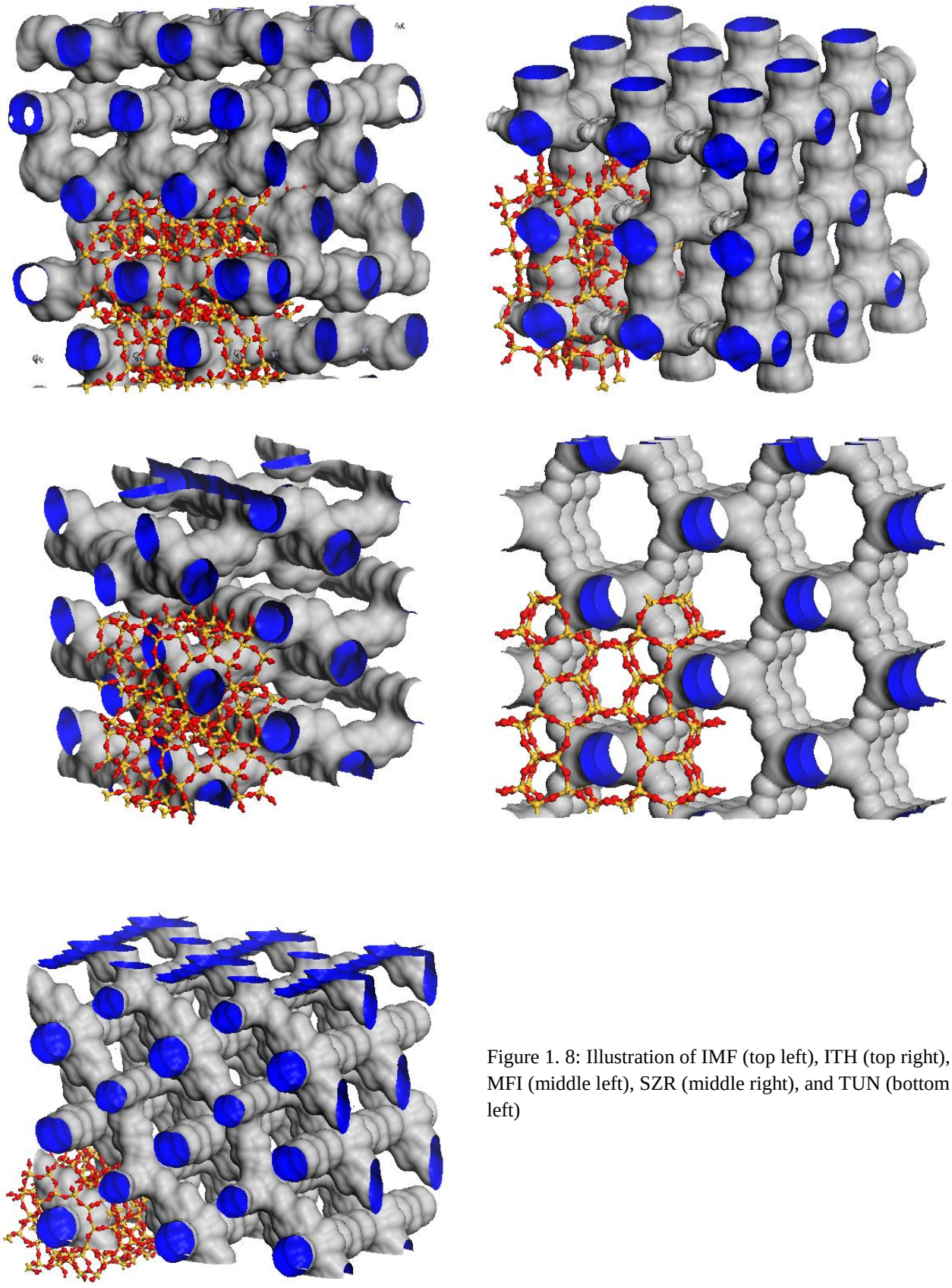

Figure 1. 8: Illustration of IMF (top left), ITH (top right), MFI (middle left), SZR (middle right), and TUN (bottom left)

IM-5 (IMF), ITQ-13 (ITH), ZSM-5/MFI-27/Pentasil (MFI), SUZ-4 (SZR), and TNU-9 (TUN) zeolites are the samples with three-dimensional 10-ring channels.

It should be noted that three ZSM-5 samples (MFI) with different Si/Al ratio were studied in this work, and they were named as MFI-27 (Si/Al=13.5), Pentasil (Si/Al=45), and ZSM-5 (Si/Al=50) for convenience.

For ITQ-13 and SUZ-4, there are smaller channels in the system as well. ITQ-13 has 9-ring channels, and SUZ-4 has 8-ring channels as well as 10-ring channels. TNU-9 has the maximum diameter of sphere that can be included in the channels (8.46 Å) followed by IM-5 (7.34 Å), ITQ-13 (6.72 Å), ZSM-5 (6.36 Å) and SUZ-4 (6.27 Å).

More detailed information regarding the channel size and others can be found in Table 1. 1.

Three-dimensional 12-ring zeolite

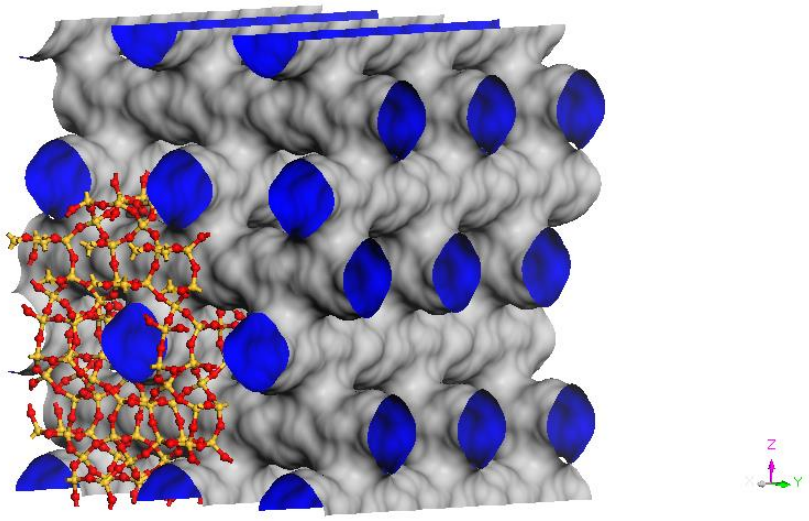

Figure 1. 9: Illustration of the BEA topology.

Beta is the only zeolites studied in this work with three-dimensional 12-ring channel system. It is one of the materials with *BEA framework type. Asterisk in front of framework type code means that Beta is disordered in the c-direction. That is, well-defined layers are stacked in the c-direction in a more or less random fashion [16]. Beta has 3-dimensional channel

system. There are 12-ring channels along [100] direction (6.6x6.7 Å in size) and [001] direction (5.6x5.6 Å in size).

1.3 Methanol to Hydrocarbons (MTH) process

MTH reaction literally refers to the conversion of methanol to hydrocarbons. As hydrocarbon contains broad spectrum of different species, one can guide a reaction to get gasoline-rich products (Methanol to Gasoline, MTG), olefin-rich products (Methanol to Olefin, MTO) or propylene-rich products (Methanol to Propylene, MTP) by adapting proper shape-selective zeolite and reaction conditions.

Studies to explain the mechanism of MTH reaction has been performed for more than 30 years, but the mechanism has not yet been fully understood. Earlier research of MTH mechanism focused on direct formation of carbon-carbon bonds from methanol (MeOH) or dimethyl ether (DME). However, as Song et al. addressed, a dramatic decrease in the initial rate of methanol conversion under extremely purified reagent regarding C-C bond containing impurities [17], C-C bond formation mechanism started to be considered as a subject of little practical importance.

In the mid-1990s, Hydrocarbon-pool mechanism was proposed by Dahl and Kolboe. They performed isotopic labeling experiment co-feeding ^{13}C-methanol with ethene and propene. What they observed was that most of the products were formed from methanol, directly, and ethene and propene showed very little reactivity during the reaction. This observation led them to the hydrocarbon-pool mechanism, and Figure 1. 10 shows schematic description of the mechanism.

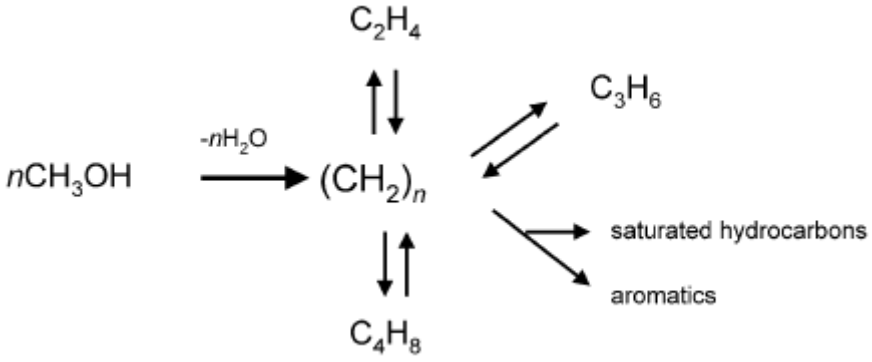

Figure 1. 10: The hydrocarbon pool mechanism proposed by Dahl and Kolboe. Fromreference [18]

Intermediate $(CH_2)_n$ was originally not specified, but the following studies focused mainly on aromatic or cyclic intermediates [19]. This led to two mechanisms, paring and side-chain mechanism (Figure 1. 11). These mechanisms are to explain how alkene in MTH reaction can be formed via aromatic and cyclic intermediates, and they are adapted or refined version of mechanisms proposed earlier than hydrocarbon pool mechanism. Both mechanisms start with successive methylation of benzene ring and get to the point where gem-methylated specie is formed. From there, they show different explanation. In paring mechanism, gem-methylated specie undergoes ring contraction and becomes five-ring specie. Alkene specie can be eliminated from the five-ring specie, and this ring will undergoes further reactions and become six-ring specie again, and stay inside of reaction cycle. In side-chain reaction, there is no ring contraction step but formation of exocyclic double bond. Then the side-chain is methylated which either leads to ethene elimination or further reaction for propene elimination.

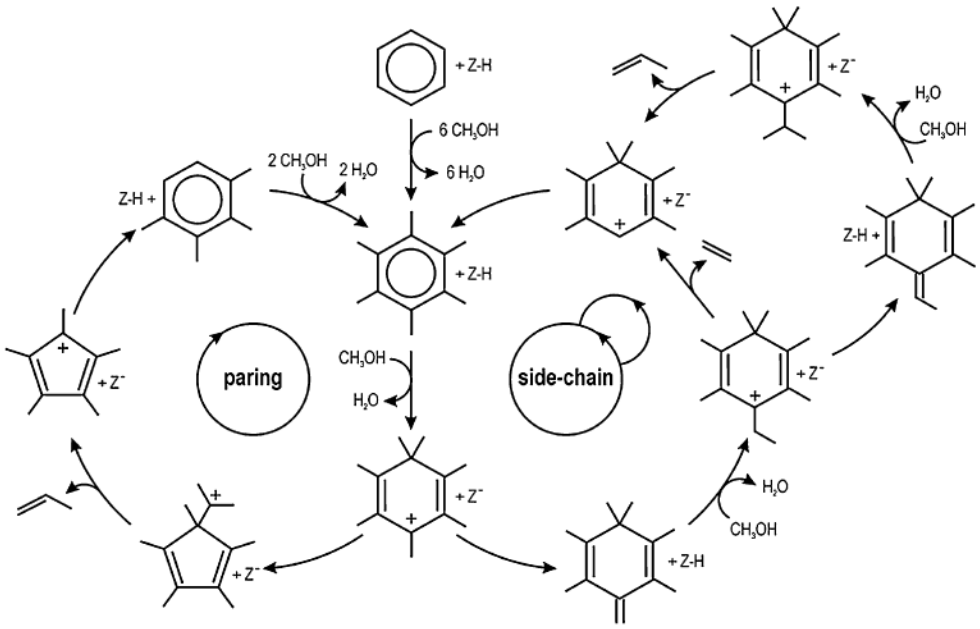

Figure 1. 11: Illustration of paring and side-chain reaction mechanisms. Detailed reaction steps are not included for clarity. Z represents the zeolite while Z-H is its protonated form and Z^- is deprotonated form. From reference [20]

In 2006, Svelle et al. found out that ethene formation during the MTH reaction over H-ZSM-5 went through different mechanism from other higher alkenes [21], and aromatics are not intermediates for all alkene formation. These findings led to proposal of dual-cycle concept

[22] (Figure 1. 12). The figure illustrates two partly separated cycles. The right cycle represents arene cycle where ethene formation from lower methylbenzene followed by re-methylation happens, while the left cycle represents alkene cycle where C_{3+} alkene formation from methylation and cracking happens [22].

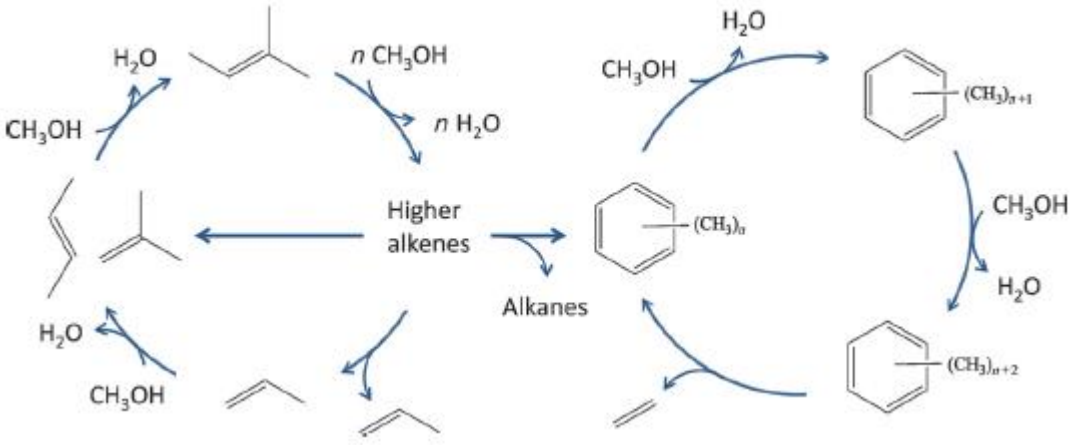

Figure 1. 12: Suggested Dual-cycle concept for the conversion of methanol over H-ZSM-5. From reference [1]

Detail of reaction mechanism can be different from zeolite to zeolite, for example, depending on topology and possibly acid strength [21]. For example, MTH reaction over Beta zeolite involves hydrocarbon pool aromatic reaction intermediates such as penta- and hexamethylbenzene [23] while alkene cycle is favored during the reaction over ZSH-22 [24].

2 Background for Experimental Techniques

2.1 Basic characterizations

2.1.1 X-ray Diffraction (XRD)

X-ray diffraction is a technique used to investigate crystal structure of materials. From the diffraction pattern, one can deduce how particles are arranged in the crystalline solid [3]. When the beam hits atomic layers in a material, scattering occurs as in Figure 2. 1 (a). To make a matter simple let us only consider two lattice planes (Figure 2. 1 (b)). Wave scattered from top- and bottom-plane travel different distance. Depending on the difference in travel distance, either constructive or destructive interference can occur. Constructive interference happens when two waves are in phase, and this can be expressed by using Bragg relation. The relation is written as :

$$2d\sin\theta = n\lambda$$

where:

λ = wavelength of the X-rays;
d = distance between two lattice planes;
θ = angle between incoming X-rays and the normal to the reflecting lattice plane;
n = integer called the order of the reflection.

From Figure 2. 1 (b), red line represents the path difference between scattered waves ($d\sin\theta$), and the total path difference becomes twice of it, $2d\sin\theta$. Two waves are in phase when the path length difference is equal to integer multiply of wavelength ($2d\sin\theta = n\lambda$).

Diffraction patterns are measured as function of the angle 2θ (Figure 2. 1 (c)), and the diffractograms become plot of 2θ against intensity. There is a stationary X-ray source and a movable detector, which scans the diffracted radiation as a function of 2θ [25]. When powder samples are scanned, a small fraction of particles which are oriented in “right” direction scattered the incident beam with the angle of θ which corresponds to the constructive

interference, and this gives rise to the diffraction lines [25]. For the case of known materials, there are available reference diffraction patterns which can be compared with experimental results. By comparing these two patterns, one can identify the crystallographic phase of the materials of interest. [25].

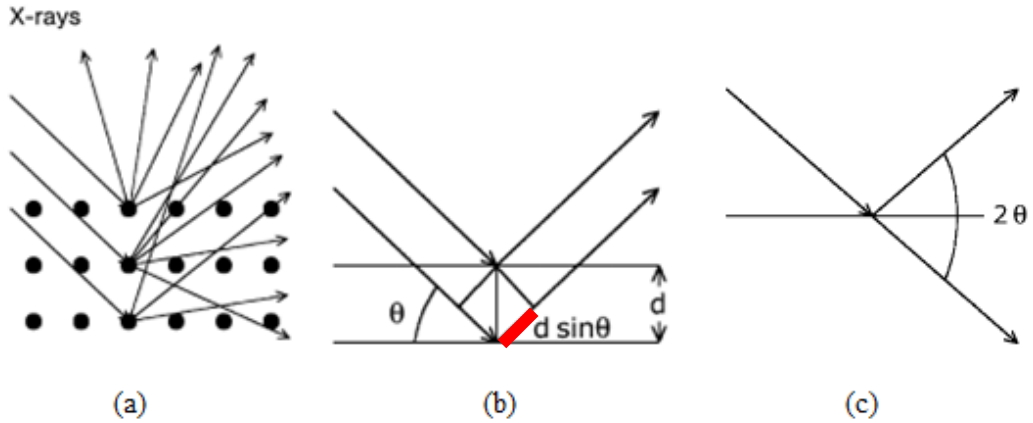

Figure 2. 1: (a) Scattering of x-rays in atomic layers of a material. (b) Schematic description of Bragg relation. (c) Diffraction patters are measured as function of the angle 2θ. From reference [25]

2.1.2 Scanning Electron Microscopy (SEM)

Scanning Electron Microscopy (SEM) is used for study of size and shape of sample. The schematic set up of SEM is shown in Figure 2. 2. First, electron beam is emitted from electron gun. As it passes through the condenser lenses, the beam gets more focused. Scan coils make beams raster pattern, and the beam gets focused again at the objective lens. This rastering narrow beam gets to the surface of sample, and detector reads the yield of secondary or backscattered electrons. Parts of the surface towards the detectors look brighter while parts of the surface pointing away from the detector look darker [6], and this consists the image that we see from SEM experiment. The difference between secondary and backscattered electrons is that secondary electrons are originated from the surface region of the sample with mostly low in energies while backscattered electrons are from deeper region of the sample carrying information about elements in sample as heavier elements show more scattering which leads to brighter image [6].

Also, the collision of a beam with a sample leads to emission of x-ray, and this x-ray can be used in the technique called Energy Dispersive X-ray Spectroscopy (EDS). When incident electron beam hits a sample, the electron at the inner shell gets ejected and there will be a hole instead. The electron beam which hit the electron in the inner shell would lose its energy under collision as it is transferred to the ejected electron. To achieve lower energy state in the system, the hole in the inner shall is then filled up by valence electron. In this process, emission of x-ray happens because of surplus energy. The energy of emitted x-ray is element specific as the energy level is different from element to element.

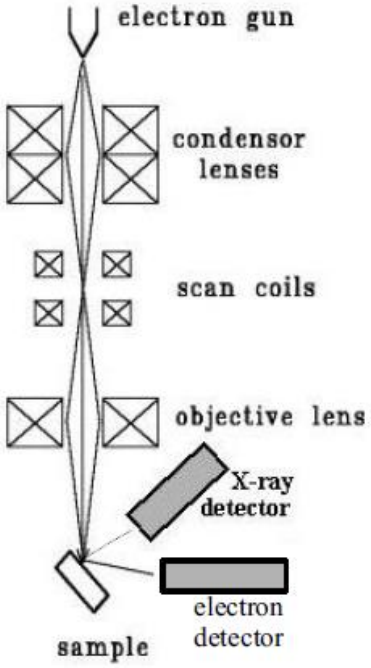

Figure 2. 2: Schematic set up of Scanning Electron Microscopy (SEM) [6].

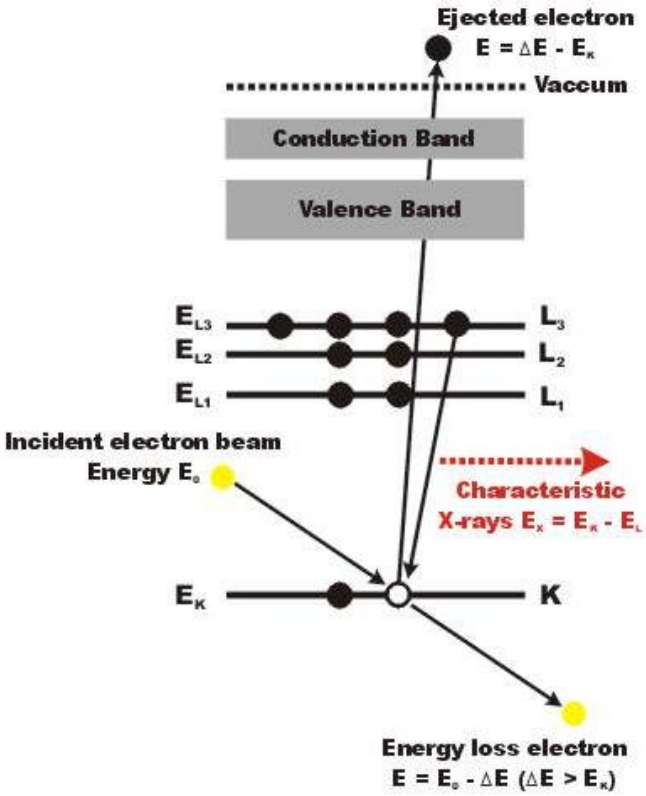

Figure 2. 3: Generation of X-ray [26]

2.1.3 N_2 adsorption

Surface area of zeolites can be measured by adsorption of small inert gas molecules such as nitrogen [6]. From the volume of nitrogen molecules which adsorb on the surface of a zeolite at liquid nitrogen temperature (77 K), one can calculate the surface area of the adsorbent by using Brunauer–Emmett–Teller (BET) method.

BET isotherm assumes that 1) Surface is energetically homogeneous, 2) There is no lateral interaction between adsorbed molecules, and 3) The adsorption energies, in the second and all higher layers (E_2, E_3, ⋯) are equal to the condensation energy of the adsorptive; i.e., $E_2=E_3=\cdots=E_i=E_L$ [27]. In mathematical way, the isotherm can be expressed by following equation:

$$\nu_{ads} = \frac{\nu_{mono} \cdot C \cdot p_{rel}}{(1-p_{rel}) \cdot (1+(C-1) \cdot p_{rel})})$$

where

ν_{ads} = the amount of the adsorbed gas (nitrogen gas);

ν_{mono} = the amount of the adsorbed gas (N_2) corresponding to a monolayer;

C = constant;

p_{rel} = relative pressure ($=\frac{\text{partial pressure } p}{\text{standard pressure } p_0}$) [28].

Plot of ν_{ads} (y-axis) against p_{rel} (x-axis) shows S-shape isotherm, and it is shown in series of figures (e.g. From Figure 4. 25 to Figure 4. 36, it should be noted that p/p_0 notation is used in the figures instead of p_{rel}). By rearranging the equation, we can get closely straight line from the plot of $p_{rel}/\nu_{ads}(1-p_{rel})$ against p_{rel} between relative pressure of 0.05 and 0.35 [28].

$$\frac{p_{rel}}{\nu_{ads} \cdot (1 - p_{rel})} = \frac{1}{\nu_{mono} \cdot C} + \frac{C - 1}{\nu_{mono} \cdot C} \cdot p_{rel}$$

Therefore, in the range of $0.05 \leq p_{rel} \leq 0.35$, one can treat the plot as a linear one whose slope is $\frac{C-1}{\nu_{mono} \cdot C}$ and y-intercept is $\frac{1}{\nu_{mono} \cdot C}$. From the nitrogen adsorption experiment, the slope and y-intercept values can be gotten, and then ν_{mono} and C values can be calculated. Once ν_{mono} value is revealed, it's not very difficult to get the total BET surface area of the sample. First, from the amount of the adsorbed nitrogen gas, number of adsorbed nitrogen gas molecules can be calculated using ideal gas law ($N = N_A pV/RT$) at standard temperature and pressure (STP, 0°C and 1 bar). Ismail reported in 1990 that the area each nitrogen molecule covers upon adsorption, cross-sectional area (A_m) is 0.162 nm^2 [29] when p_{rel} is in between 0.05 and 0.21. The total BET surface area (S_{Tot}) of the sample now becomes:

$$S_{Tot} = \frac{N_A \cdot p \cdot \nu_{mono}}{RT} \cdot A_m$$

And specific surface area (S) can be expressed as:

$$S = \frac{S_{Tot}}{w}$$

where w is weight of the sample. The unit of S is m^2g^{-1}.

2.2 Spectroscopic Investigation

2.2.1 Fourier Transform Infrared Spectroscopy (FTIR)

Infrared (IR) spectroscopy measures transition between molecular vibrational energy level as a result of the absorption of mid-IR radiation [30]. Mid-IR refers to the infrared radiation with wavenumber of 200-4000 cm^{-1} where molecular vibrations are detected [25]. Absorption bands from molecular vibrations can be a fingerprint for a particular molecule. Moreover, structural information of the material of interest can be deducted from IR spectroscopy by identifying adsorption bands of a specific functional group or specific type of bond in the system investigated.

Molecular Vibrations

For simplicity, let's consider a diatomic molecule with spring-like chemical bond between two atoms (Ball-and-spring model of a diatomic molecule [31, 32]. Figure 2. 4).

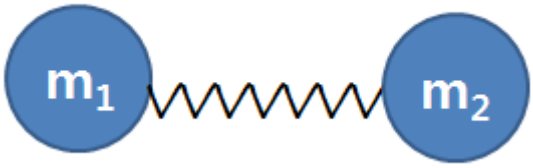

Figure 2. 4: Ball-and-spring model of a diatomic molecule. Two different atoms have mass of m_1 and m_2, respectively. Adapted from reference[32]

Since the chemical bond between two atoms is spring-like, it can be assumed that a system experiences a restoring force proportional to the displacement from equilibrium, which is observed in harmonic oscillator [33]. From the Hooke's law, the restoring force (F) in one-dimensional harmonic oscillator is proportional to force constant (k_f) and degree of displacement from the equilibrium position (x).

$F = -k_f x$ [33]

The relation between the force and the potential energy is $F = -dV/dx$ [33], and this leads us to acquire potential energy of harmonic oscillator.

$V(x) = -\int F\,dx = -\int k_f x\,dx = \frac{1}{2}k_f x^2$ [33]

The graph of the relative energy against the displacement is as in Figure 2. 5 (a).

From Schrödinger equation,

$H\psi = E\psi$

where E is Energy and Hamiltonian operator (H) is

$H = T + V$

with kinetic energy operator (*T*) and potential energy operator (*V*). In more detailed way, kinetic energy operator in one-dimension, single-atom system can be written as

$$T = \frac{p_x^2}{2m} = \frac{1}{2m}\left(\frac{\hbar}{i}\frac{d}{dx}\right)^2 = -\frac{\hbar^2}{2m}\frac{d^2}{dx^2}$$

[33]

where m is mass of the atom, p_x is momentum operator which can be expressed in position representation, $\frac{\hbar}{i}\frac{d}{dx}$. ħ equals to $\frac{h}{2\pi}$ with *h* being the Planck constant.

Whole Hamiltonian operator then becomes

$$H = -\frac{\hbar^2}{2m}\frac{d^2}{dx^2} + V(x)$$

Considering diatomic molecules have two atoms with different mass, m_1 and m_2, Hamiltonian operator can be specified even further as

$$H = -\frac{\hbar^2}{2\mu}\frac{d^2}{dx^2} + \frac{1}{2}k_f x^2$$

where $\frac{1}{\mu} = \frac{1}{m_1} + \frac{1}{m_2}$ with μ being effective mass [33].

Therefore, the Schrödinger equation for the harmonic oscillator is

$$-\frac{\hbar^2}{2\mu}\frac{d^2\psi}{dx^2} + \frac{1}{2}k_f x^2\psi = E\psi$$

It is possible to solve the equation regarding to ψ, and then find the allowed values of the energy with a certain mathematical method [33], but it will not be discussed in this work as it has little relevance. Allowed values of the energy in harmonic oscillator is given by

$$E = \left(\mathrm{v} + \frac{1}{2}\right) h\nu \qquad where \quad \nu = \frac{1}{2\pi}\sqrt{\frac{k_f}{\mu}} \qquad \mathrm{v} = 0,1,2,\cdots$$

where v is the vibrational quantum number and ν is the classical vibrational frequency of the oscillator [31, 33]. The expression for the energy shows that the harmonic oscillator has discrete energy levels, not continuous, as in Figure 2. 5 (a), and the energy difference between neighbors is equidistant with value of $\Delta E = h\nu$. In this model, only transitions to adjacent levels, which is referred to as fundamental transition, are allowed (Δv = ±1) [30] even though allowed energy levels are continues up to infinity [33]. Moreover, there is meaningful information which can be deducted from the expression of the vibrational frequency. First it should be noted that wavenumber ($\bar{\nu}$, in cm^{-1}) is more commonly used in IR spectroscopy. Therefore,

$$\bar{\nu} = \frac{1}{2\pi c}\sqrt{\frac{k_f}{\mu}}$$

where c is the velocity of the light.

The expression implies that absorption band in IR spectroscopy will appear at higher wavenumber with the condition of larger force constant (k_f) and smaller effective mass (μ). The larger value of k_f is for the stronger bond between atoms. For example, k_f of triple bond is bigger than k_f of single bond. Regarding effective mass, the bond between atom A and B vibrates at higher wavenumber compare to the bond between atom A and C if C is heavier than B.

Despite the fact that harmonic oscillation has been intensively discussed so far and it is the model widely used to describe the vibration motion of diatomic molecules [34], real molecules do not behave exactly as described in the model. According to the Figure 2. 5 (a), a diatomic molecule will never dissociate no matter how far they are displaced from the equilibrium position. This is not true for real molecules, and anharmonic oscillation model (Figure 2. 5) (b) can describe this matter in more realistic way. The potential energy of

diatomic molecules against internuclear distance is not symmetric. As distance between two atoms in the diatomic molecule increases from equilibrium position (where potential energy is minimum), first the potential energy increases. However, it stops increasing and levels off as it reaches dissociation limit. The potential energy difference between the zero point energy (energy when v=0) and the dissociation limit is a dissociation energy, D_0.

The energy term corrected for anharmonicity is given by

$$E = \left(\mathrm{v} + \frac{1}{2}\right) h\nu - \left(\mathrm{v} + \frac{1}{2}\right)^2 h\nu x_e \qquad where \quad \nu = \frac{1}{2\pi}\sqrt{\frac{k_f}{\mu}} \qquad \mathrm{v} = 0,1,2,\cdots \quad [30]$$

It should be noted that it still shows discrete energy levels, but gap between two adjacent energies are not equidistant in anharmonic oscillator. Also, overtones become allowed in this model. Overtones are the vibrational transition with $\Delta v>1$ and they appear as absorption band at a whole number times the fundamental wavenumber [30]. Separation between the vibrational levels decreases with increasing quantum number, and this explains why the second overtone appears at wavenumber slightly less than twice that of the fundamental vibration [25].

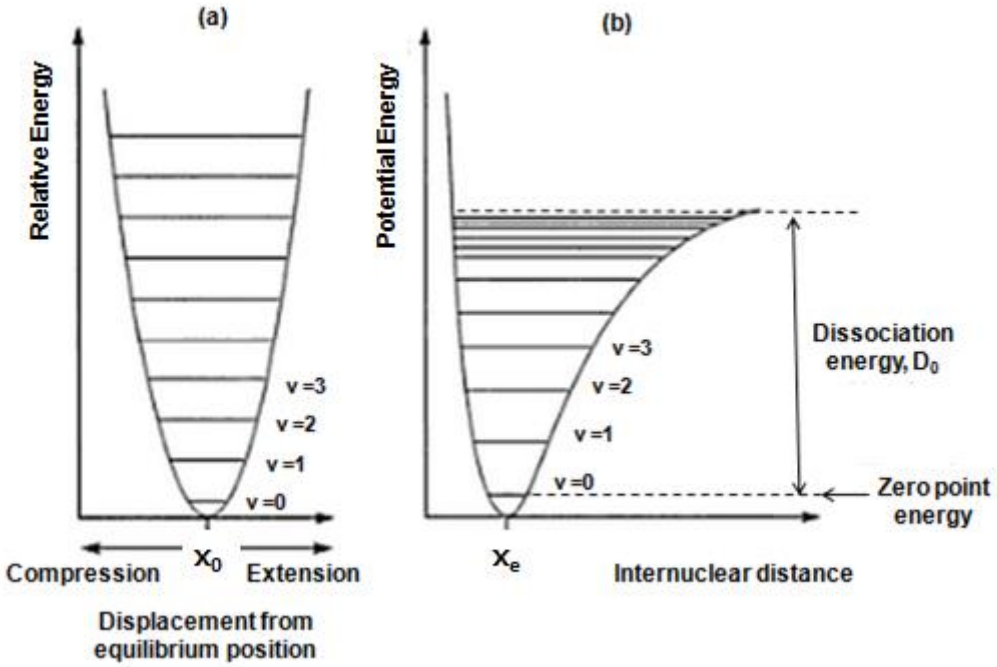

Figure 2. 5: (a) The quantized energy levels for a diatomic molecule undergoing simple harmonic motion. (b) The quantized energy levels for a diatomic molecule undergoing anharmonic motion. From reference [34]

In absorption process of IR spectroscopy, it is necessary that the frequency of infrared radiation is in match with vibrational frequencies of the molecule [35]. However, there are cases where absorption of IR radiation does not happen even though the frequency of the radiation matches the vibrational frequencies of molecule. An additional condition for IR radiation absorption is the change of molecular dipole moment during vibration [35]. For example, symmetric diatomic molecules such as N_2 and O_2 do not absorb IR radiation even it matches the frequency of molecular vibration (IR inactive). In the case of carbon dioxide, symmetric stretch is IR inactive as there is no change of molecular dipole moment during vibration while asymmetric stretch absorbs IR radiation (IR active). Symmetric stretch and asymmetric stretch fall into types of vibration. There are four types of vibration:

-Stretching vibrations (ν) : Changing in the bond length. There is symmetric and asymmetric stretching.
-In plane bending vibrations (δ) : Changing in the bond angle, but not the bond length. In large molecules there is rocking, twisting and wagging vibrations.
-Out of plane bending vibrations (γ) : Changing in the bond angle by oscillation of an atom through a plane defined by at least three neighboring atoms.
-Torsion vibrations (τ) : Changing in angle between two planes through atoms. [25]

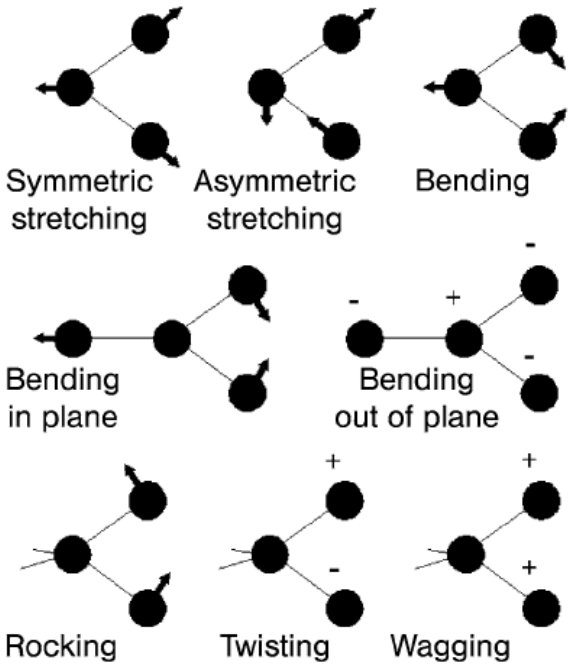

Figure 2. 6 : Types of vibrations in non-linear molecules. From reference [25].

Fourier Transform Infrared Spectrometer

A schematic diagram of FTIR spectrometer can be found in Figure 2. 7. The square box in the figure is an interferometer. Inside of the interferometer, the change of energy from the light source is detected as it passes through the sample. The IR radiation from the IR source first goes to the beam splitter. The beam splitter is placed at 45° angle to the incoming beam [35]. As the original beam passing through the beam splitter, it is split into two beams, one deflected 90° towards the fixed mirror, and another undeflected moving towards to the moving mirror. Both beams are reflected by the each mirror and come back to the beam splitter. Since fixed mirror keeps fixed distance between the beam splitter and the mirror, the path length of the beam is always constant. However, for the beam reflected from the moving mirror, the path length keeps changing. So, when the two beams meet again at the splitter, there will be a path length difference, and it varies depending on the position of the moving mirror at the time of reflection of the beam. This causes both constructive and destructive interference, and the combined beam containing these interference pattern is referred to as interferogram [35]. This interferogram travels further to the sample cell, oriented by the beam splitter, and passes through the sample of interest. During this process the frequencies of the interferogram which matches the molecular vibrational frequencies in the sample are absorbed, and the detector receives the transmitted interferogram. This transmitted interferogram contains the concentration information of substance of interest.

By the Beer-Lambert's law,

$$\frac{I}{I_0} = e^{-abc}$$

$$\log\frac{I}{I_0} = -abc$$

$$\log\frac{I_0}{I} = abc = A$$

where I_0 is the intensity of radiation entering the substance, I is the intensity of radiation leaving the substance (transmitted radiation), a is the molar extinction coefficient in $dm^3/(mol \cdot cm)$, b is the path length inside of the cell in cm, c is the concentration of substance in mol/dm^3, and A is the absorbance [36].

At the detector, the interferogram containing the absorbance information is in a format of intensity versus time (a time-domain spectrum) [35]. To exclude the contributions coming from other than the sample, subtraction of background is needed. Background spectrum acquisition can be done by collecting spectrum at the detector without sample mounted.

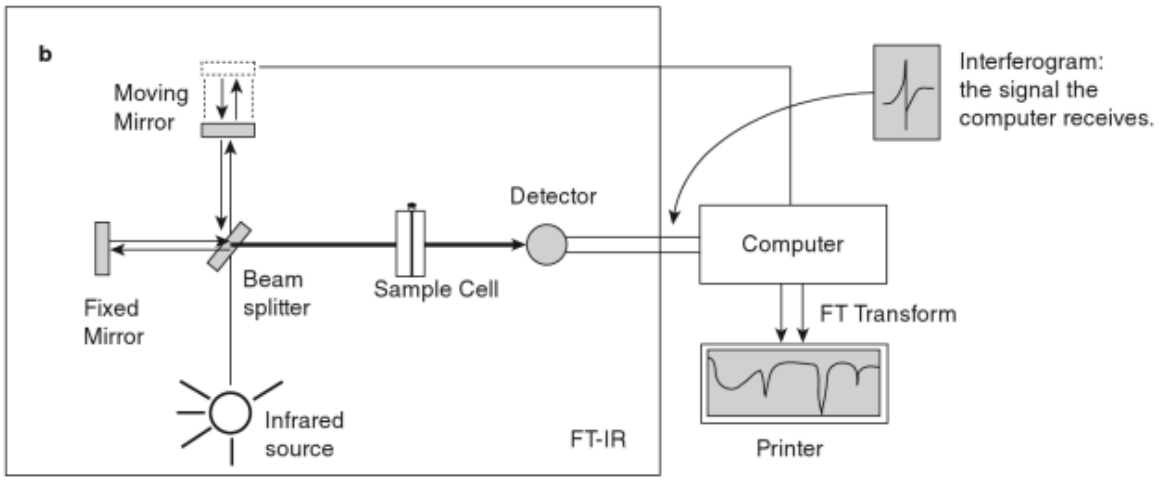

Figure 2. 7 : Schematic diagram of Fourier Transform Infrared spectrophotometer. From reference [35]

Background subtracted interferogram is still a time-domain spectrum. A mathematical operation Fourier Transform can change this pattern to a plot of intensity versus frequency (a frequency-domain spectrum) [35] which is more familiar to us. Mathematical detail in Fourier Transform, however, will not be discussed here.

2.2.2 FTIR on zeolites using probe molecule

The IR Spectra of zeolite itself reveals fundamental information regarding acid sites in zeolites. For example, the absorption band of bridging Brønsted acid and silanol groups appear in the spectrum and this helps us to confirm the existence of these acid sites. However, acidity cannot be assessed by investigating the acid alone, but need to be probed by interaction of a base molecule [37]. Probe molecules can help us to get more information regarding acid strength and concentration of acid sites. There are quite a few frequently used probe molecules for characterization of acid sites in zeolite [37], but carbon monoxide and pyridine are chosen as probe molecule for investigation of acid strength and concentration respectively in this work. Both are most commonly used method for each purpose [37], so

many of literatures and former experimental data are available. For pyridine, especially, the integrated molar extinction coefficient (IMEC) values are essential for investigation of acid sites concentration, and they are available from many different literatures [38-49] even though difference between values is rather large.

In activated zeolite samples, peaks we are most interested in commonly appear at the wavenumber between 3750 cm^{-1} and 3610 cm^{-1} [50]. Figure 2. 8 is an activated spectrum of H-IM-5 zeolite which is shown as an example. Usually the band observed at 3750-3745 cm^{-1} is assigned to the isolated silanol groups on external surfaces [37, 50]. Even though this peak is originally narrow and symmetric [50], we often observe asymmetric peak in this wavenumber with tail towards the lower region. This is because of the terminal silanol groups of a hydrogen-bonded chain appear at slightly lower wavenumber than isolated ones [50]. Description of isolated and terminal silanol groups can be found in Figure 2. 9. Another important absorption band is observed at 3625-3610 cm^{-1} which is stretching mode of bridging hydroxyl groups (-Al(OH)Si-) [50].

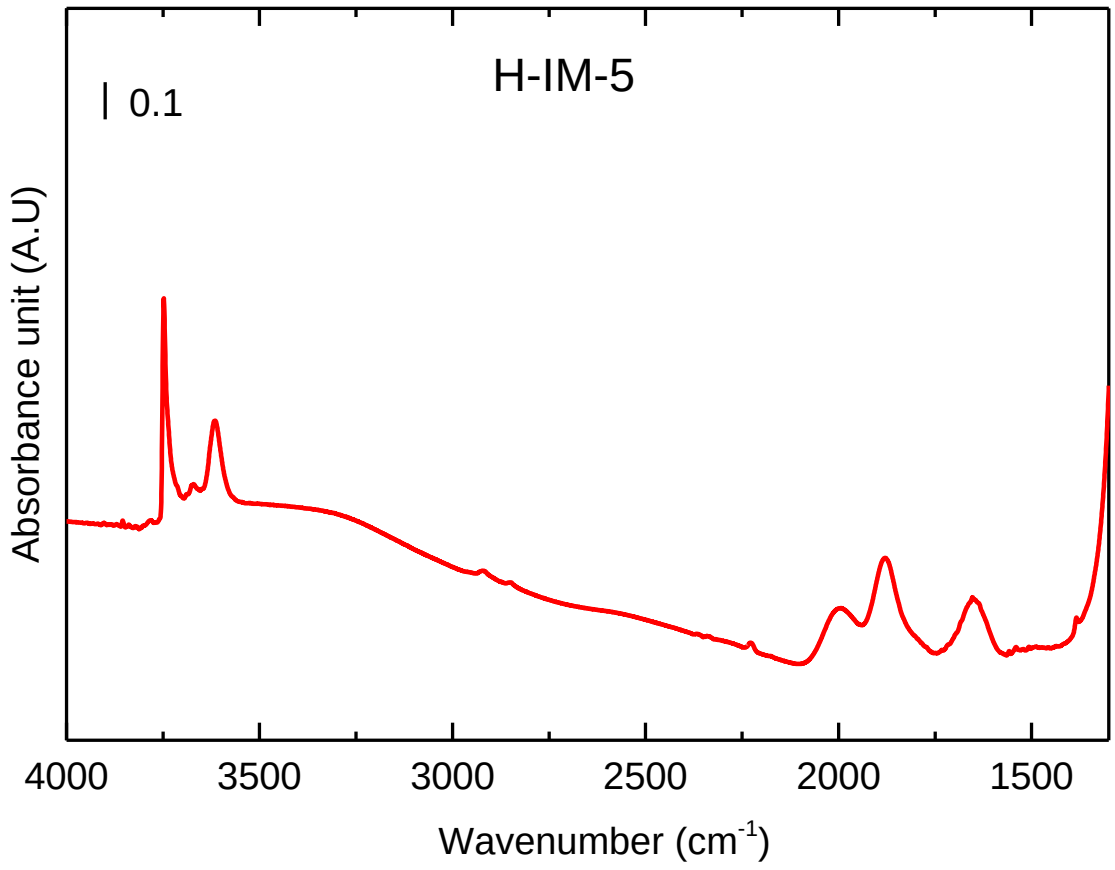

Figure 2. 8: Activated spectrum of H-IM-5 zeolite

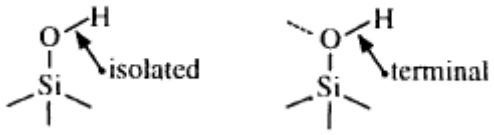

Figure 2. 9 : Description of isolated and terminal silanol groups [50]

In the range between 2100 cm^{-1} and 1500 cm^{-1}, overtones of zeolite lattice vibrations (stretching and bending modes of T-O units (T = Si or Al)) appear [37]. More detail of spectra will be discussed in section 4.2 with plots of experimental results.

CO as a probe molecule

Carbon monoxide acts as a weak base when reacts with acid sites in zeolite. Hydrogen bonds are formed between carbon monoxide and hydroxyl groups in zeolites, and these H-bonding interactions can be observed by IR spectroscopy in O-H and C≡O stretching regions [51]. For example, the hydroxyl band in the bridging Brønsted acid sites gets pertubated, and shows red-shift in the spectrum. Red-shift is the change of absorption band to shorter wavenumber. The degree of red-shift depends on the strength of acid sites, and zeolites implemented in this work show wavenumber shift of 296-324 cm^{-1}. The stronger perturbation is, the stronger acid strength is. Simultaneously, C≡O shows blue shift, change in wavenumber to longer wavenumber, relative to the wavenumber of gas phase CO (2143 cm^{-1}) [37, 51, 52] upon hydrogen bonding with bridging Brønsted acid sites. Similar trends are observed, only with weaker perturbation, when CO forms hydrogen bond with hydroxyl group of silanols.

The example of CO adsorption experiment on H-IM-5 zeolite is shown in Figure 2. 10. O-H stretching of silanol groups appears at ~3748 cm^{-1}, and that of bridging Brønsted acid sites appears at ~3615 cm^{-1}. When CO molecules are adsorbed on the acid sites (black curve), hydroxyl group of silanols and Brønsted acid sites is pertubated to ~3652 cm^{-1} and ~3302 cm^{-1}, respectively. Physically adsorbed CO shows band at ~2140 cm^{-1}. This species is referred to as liquid-like CO as well as physically adsorbed CO. CO hydrogen-bonded to the zeolite shows the stretching at ~2175 cm^{-1}, which is shifted by -32 cm^{-1} compare to gas phase CO. This is only a brief analysis of the spectra, and more will be discussed in section 4.2.1.

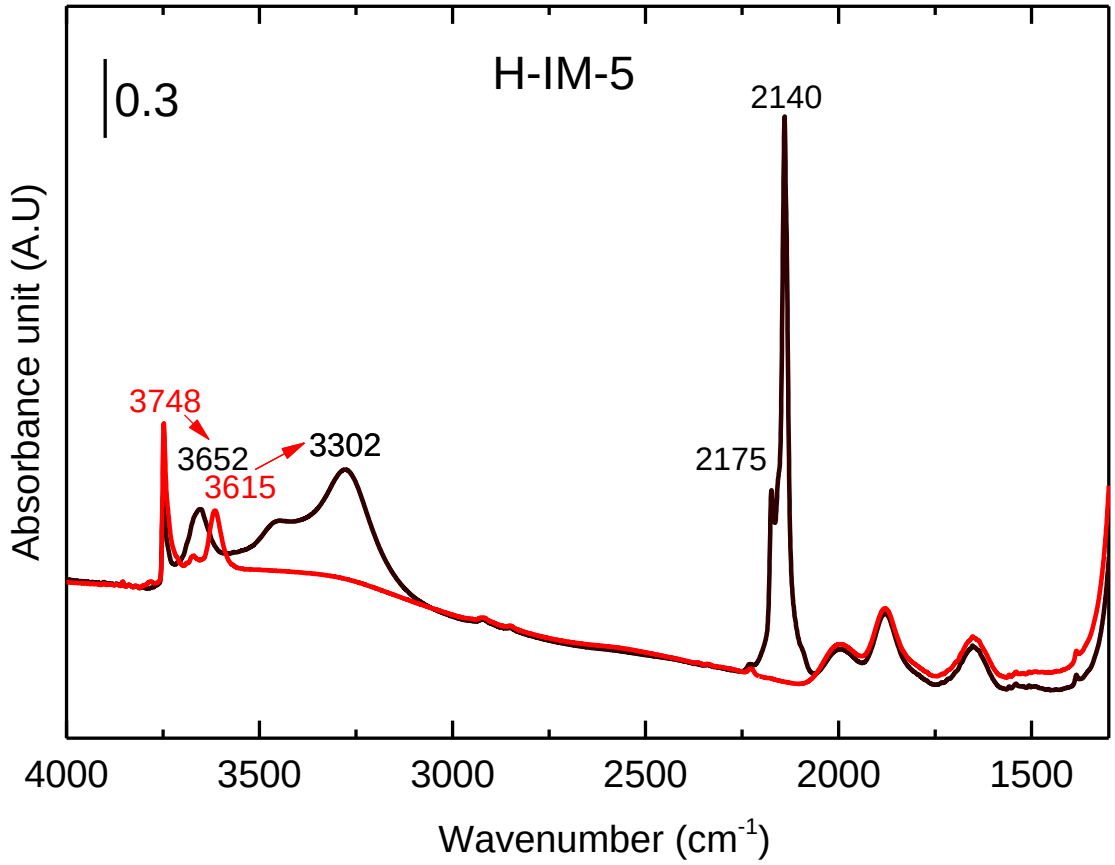

Figure 2. 10: Spectrum of activated H-IM-5 zeolite (red) and spectrum after CO adsorption on the zeolite (black).

We have discussed about what we observe from CO adsorption experiment on zeolite samples. To explain why it happens, it should be first noted that it is carbon atom which forms hydrogen bond with hydroxyl groups, not oxygen atom when CO interacts with acid sites in zeolites. Neyman et al.[53] performed calculation regarding this matter. They reported that computed value of binding energy of carbon monoxide (oxygen-down, Figure 2. 11 (c)) adsorption on bridging OH was 0.06 eV with O-H···O≡C bond length of 2.182 Å, while carbon-down case (Figure 2. 11 (b)) gave the binding energy of 0.19 eV with OH···CO bond length of 2.057 Å. This can be explained using molecular orbital (MO) theory. MO of carbon monoxide looks like Figure 2. 12. One can see that, in 2p level, oxygen contributes 4 electrons for bonding while carbon only contributes 2 electrons. One of the bonding orbitals in this level then consists of electrons from oxygen only, which makes dative covalent bond between oxygen and carbon giving δ^- charge to carbon. That bonding orbital is σ_{2p} orbital, Highest Occupied Molecular Orbital (HOMO). Figure 2. 13 shows the HOMO orbital, and

one can see that the highest energy pair of electrons, in the σ_{2p} orbital, is concentrated on the carbon [54]. With δ- charge, it is more probable that carbon interacts with acidic bridging OH group.

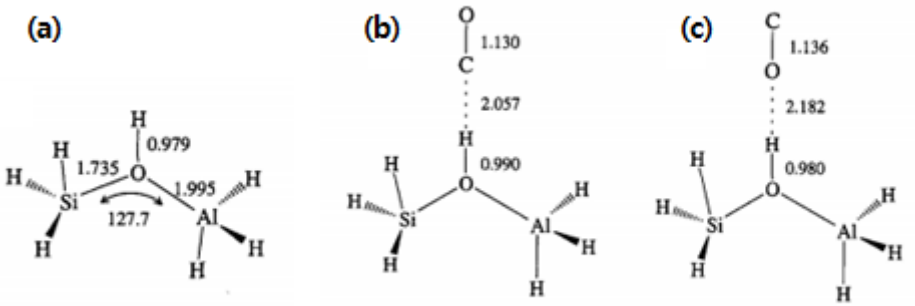

Figure 2. 11: Calculated structural parameters (bond lengths in angstrom, angles in degrees) of Brønsted acid site in bridging OH group and OH group interacting with carbon monoxide by Neyman et al. From reference[53]

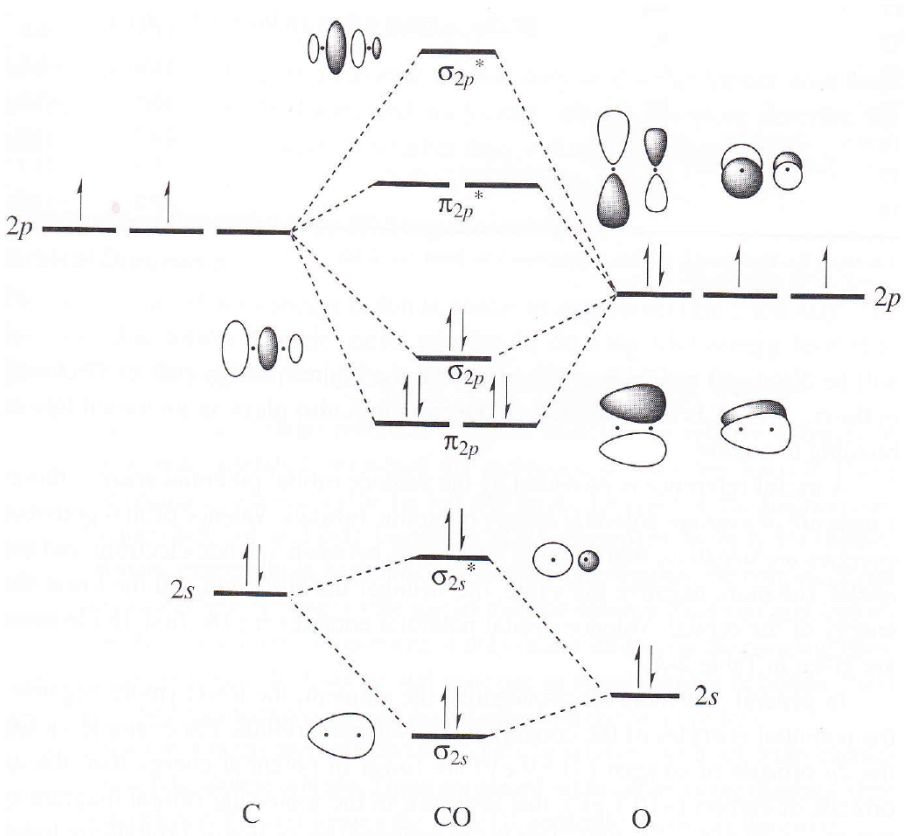

Figure 2. 12: Molecular orbital of carbon monoxide. From reference [54]

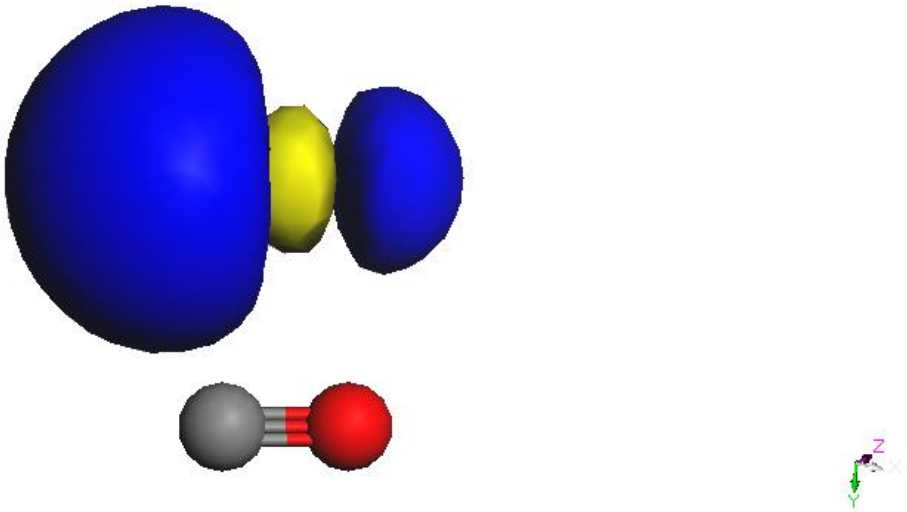

Figure 2. 13: HOMO of molecular orbital of carbon monoxide. (Upper) Calculated using DMol3 module, GGA PBE function with Grimme DFT-D correction. Material Studio 7.0 Software was used. Blue and yellow lobe represent different signs of wave function. (Down) Grey ball and red ball represent the carbon atom and the oxygen atom, respectively.

The reason for red- and blue-shift can be explained by expression of classical vibrational frequency of the oscillator. For simpler explanation we use the expression with wavenumber instead:

$$\bar{\nu} = \frac{1}{2\pi c}\sqrt{\frac{k_f}{\mu}}$$

From hydroxyl point of view, interaction with probe molecule is acid-base reaction. If the probe molecule was strong base such as pyridine, proton would be transferred to pyridine and form pyridinium ion. However, carbon monoxide is a weak, so only hydrogen bonding is formed. Upon hydrogen bonding, bond length between oxygen and hydrogen in hydroxyl group gets longer as the bond strength gets weaker. This implies the decrease of force constant (k_f) leads to appearance of absorption band at lower wavenumber (red-shift). From Figure 2. 11 (a) and (b), it can be also confirmed that the bond length of O-H gets longer upon adsorption of CO.

However, the case for carbon monoxide is different. It shows blue-shift upon forming of hydrogen bond with hydroxyl group. To explain this, the total dipole moment of carbon

monoxide should be evaluated. It should be noted that there are cases where the shape of frontier orbitals do not agree with the topography of the charge distribution [55]. As it is discussed earlier in this section, the HOMO shows heavy charge concentration in the carbon atom. However, the total electron density distribution of the molecule is as in Figure 2. 14.

Figure 2. 14: Total electronic density distribution in carbon monoxide. The contours correspond to the values 10.0, 1.0, 0.7, and 0.4, moving out from each nucleus [56].

One can see a strongly polarized oxygen atom from the figure, and this has a key to the explanation why carbon monoxide experiences blue shift upon hydrogen bonding with hydroxyl group. Positively charged hydrogen in the hydroxyl group attracts the electron from CO upon hydrogen bonding, O-H···C≡O, which leads to less polarization in CO [56], thereby increasing covalency of the molecule and the value of force constant (k_f) [57]. Since it is electric field created by a positive charge causing a polarization of CO molecule which depends on the local electric field of the site [52], it is called electrostatic effect [52, 55-58]. Increasing in force constant in C≡O bonding results in shifting of absorption band to higher wavenumber, blue-shift.

Pyridine as a probe molecule

While the main information we get from IR experiment with CO as a probe molecule is qualitative acid strength, the main purpose of IR experiment with pyridine as a probe molecule is to get quantitative information about concentration of acid sites.

In pyridine adsorption on zeolites, pyridine interacts, as strong base, with acid sties in zeolite, which are Silanol, -AlOHSi- Brønsted acid site, and Lewis acid site. For example, Figure 2. 16 shows how spectrum changes with adsorption of pyridine on the H-Beta zeolite. One can see that little amount of silanol (~3736 cm^{-1}) and all bridging Brønsted acid site (~3588 cm^{-1}) was consumed, and new peaks at 3300-2400 cm^{-1} and 1700-1400 cm^{-1} appeared. In the 3300-2400 cm^{-1} region, bands with ν(CH) and δ(NH) characters, and overtones of 8a, 8b, 19a and

19b modes of species originated from pyridine appear [59]. 8a, 8b, 19a and 19b are for vibrational modes of pyridine which are adapted from Wilson's notation [60] for benzene. These modes for pyridine are described in Figure 2. 15.

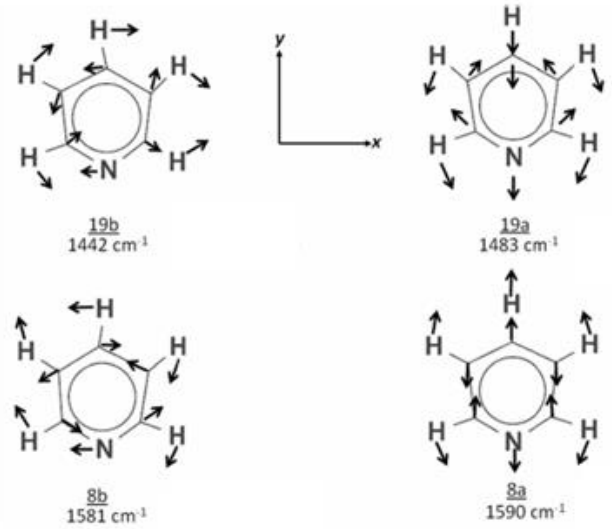

Figure 2. 15: Vibrational modes of pyridine. From reference [61]

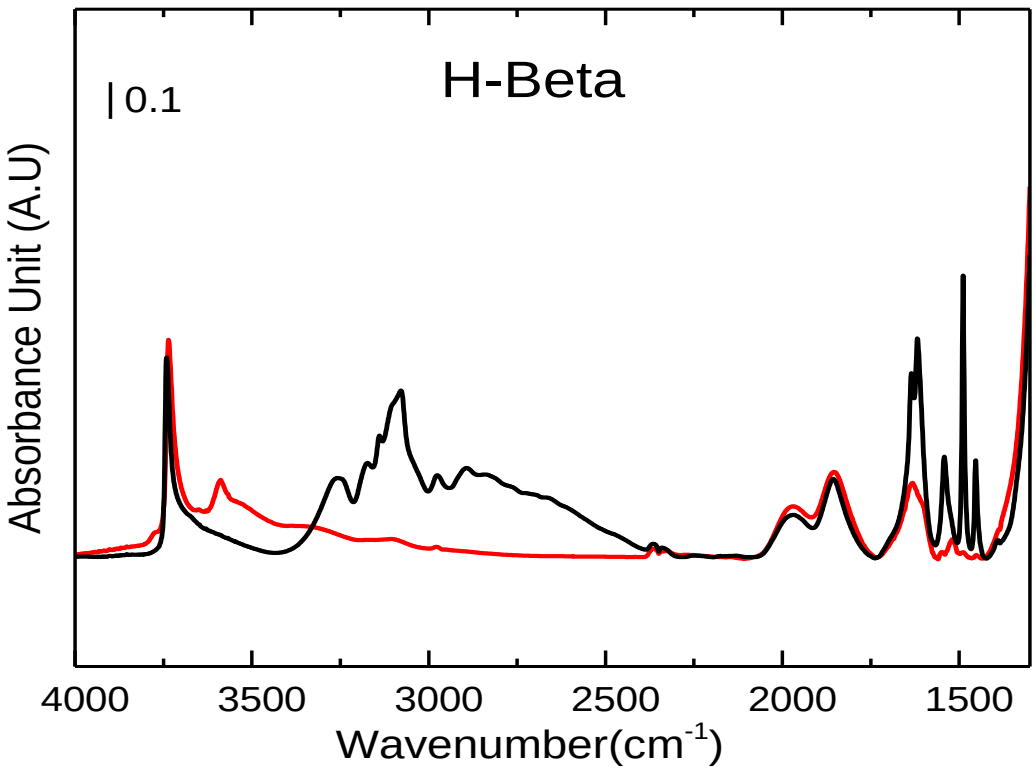

Figure 2. 16: Spectrum of activated H-Beta (red), and that of after dosing of pyridine and evacuation at 200°C until there was no change of the spectra.

When pyridine interacts with silanol, hydrogen bonds are formed. Hydrogen bonded pyridine gives rise to bands at wavenumber ~1597, 1581, 1481, and 1444 cm^{-1} (8a, 8b, 19a and 19b modes) [59]. These new bands accompany the decrease of silanol band. [59] When pyridine is adsorbed on –AlOHSi– Brønsted acid site, pyridine is protonated by the site and becomes pyridinium ion. This species is observed by the IR spectroscopy band at ~1634, 1623, 1491 and 1544 cm^{-1} (8a, 8b, 19a and 19b modes) [38, 59]. Simultaneously the band for –AlOHSi– Brønsted acid sites decreases. For the case of pyridine adsorption on Lewis acid sites, ~1622, 1578, 1492 and 1455 cm^{-1} (8a, 8b, 19a and 19b modes) bands appear [38, 62, 63].

Among all these bands in IR spectra, conventionally quantification of acid sites has been done using two bands, ~1544 cm^{-1}(pyridinium ion adsorbed on bridging Brønsted acid sites, 19b mode) and ~1455 cm^{-1} (pyridine adsorbed on Lewis acid sites, 19b mode). Plenty of molar extinction coefficients are available from the literatures for the bands [38-49]. One can wonder why the most prominent band at ~1490 cm^{-1} is not used for the quantification. It is because the band is assigned for the combination of species giving rise to the bands at ~1544 and ~1455 cm^{-1}, not for the single species. From here, the focus will be on ~1544 and ~1455 cm^{-1} peak which are directly related to quantification of acid site density in this work, and the rest of the bands will not be discussed in detail.

From the Beer-Lambert law mentioned earlier, we know that the absorbance is proportional to molar extinction coefficient, concentration of the sample which the light is traveling through, and the path length which the distance the light goes through the material. This relationship can be expressed by equation

$$A = abc$$

where A=absorbance, $\log_{10}(I_0/I)$, where I_0 and I are the intensities of incident and transmitted radiation, a= molar extinction coefficient ($dm^3/(mol \cdot cm)$), b=path length (cm), and c= concentration of species (mol/dm^3) [38].

If one integrates both sides of the equation, and rearranges it regarding concentration of sample, it becomes:

$$c(Y) = \frac{\int A\, dx}{b \cdot IMEC} = \frac{IA(X)}{b \cdot IMEC(X)}$$

for absorption band X of species Y, where

$$IMEC(Integrated\ Molar\ Extinction\ Coefficients) = \int a\, dx\,, \quad cm \cdot \mu mol^{-1} \quad .$$

The path length which the distance the light goes through the material can be considered as a thickness of a disk in this kind of experiment as the self-support catalyst disks are commonly used.

Specie we are interested in this experiment is pyridine interacting with active sites of zeolites, and to serve the purpose, the term Φ, the amount of Y per cm^2 catalyst disk, should be introduced.

$$\Phi\,(Y) = c(Y) \cdot b = \frac{IA(X)}{IMEC(X)}\,, \quad mmol/cm^2$$

The amount of pyridine per gram catalyst (C) is obtained by dividing Φ by the weight of the disk and then by multiplying the total area of disk.

$$C(Y) = \frac{IA(X)}{IMEC(X)} \frac{A}{W} \quad , \qquad mmol/g\ catalyst$$

A = Area of catalyst disk (cm^2)
W = Weight of catalyst disk (mg) [38]

IA(X) can be easily acquired from the FT-IR spectra by integrated the right bands, i.e. ~1544 cm^{-1} band for pyridinium ion adsorbed on bridging Brønsted acid site, and ~1455 cm^{-1} band for pyridine adsorbed on Lewis acid site [64]. IMEC(X) values are available from literatures. However, the values from different literatures vary in quite large extent [38-49], and different experimental condition is considered for the reason [40].

With concentration of Brønsted and Lewis acid sites calculated from pyridine adsorption experiment, Si/Al ratio of the sample can be calculated further. Assuming that every single –

AlOHSi– Brønsted acid site is generated by replacing one Si with an Al and species responsible for Lewis acid sites are originated from EFAl species, sum of concentration of Brønsted and Lewis acid sites per g catalyst, C(Brønsted Acid Site)+C(Lewis Acid Site), equals the concentration of Al per g catalyst. Since there is 16.6 mmol of SiO_2 per g zeolite, concentration of Si per g zeolites becomes

$$C(Si) = 16.6 - C(Al) = 16.6 - [C(Brønsted\ Acid\ Site) + C(Lewis\ Acid\ Site)],\quad mmol/g\ catalyst$$

Then, Si/Al now can be easily calculated by C(Si)/C(Al).

It is assumed that Lewis acid sites interacting with pyridine in this experiment are originated from EFAl species even though exact species of EFAl has not been fully revealed yet.

2.2.3 In-situ FTIR on zeolites during MTH

In-situ FTIR can provide information regarding species formed during the MTH reaction and the development of coke species. There are relatively much less literature data available in this topic compare to CO adsorption and pyridine adsorption on zeolites. Thus, this topic in this project is considered as rather exploratory work.

The spectrum of activated H-IM-5 (orange) and that of the sample after 4 hours of methanol injection (black) are shown in Figure 2. 17. The spectra can be divided into three different regions for purpose of analysis: 1) ν(OH) (3800-3400 cm^{-1}), 2) ν(CH) (3200-2800 cm^{-1}) and 3) ν(CC) of unsaturated hydrocarbons and δ(CH) of paraffinic species (1700-1300 cm^{-1}) [35, 65-67]. Region 2) can be further divided into two sub-regions, ν(CH) of aromatics (3000-3200 cm^{-1}) and ν(CH) of paraffinic species (3000-2800 cm^{-1}) [67]. Mostly CH stretching modes of methylation products and those of methoxy adsorbed on silanols, Brønsted acid sites and EFAl give rise to the bands in the wavenumber between 3000-2800 cm^{-1}. More specific assignment of the bands in this region can be found in 4.2.4. Symmetric stretching band of CH in methoxy adsorbed on silanol, Brønsted acid sites and EFAl are located quite close to each other making interpretation of the bands difficult.

It is considered that information regarding coke formation can be found in region 3) [67-71], and it will be the main focus in this work. The coke development shows different trends

depending on temperature implemented in the experiment, and the condition in this work (400°C) can be defined as high temperature [67, 69, 72, 73]. At the high temperature condition, often two prominent bands are observed, 1580-1570 cm^{-1} and 1370-1300 cm^{-1}. Both are known to be related to coke species [65, 68]. 1580-1570 cm^{-1} band is referred to as "coke" band with assignment to aromatic species [67, 68, 74]. In this work, the coke is defined as hydrocarbon residues which are responsible for catalyst deactivation [1, 67]. Similar band is observed at low temperature condition, but at slightly higher different wavenumber [67, 69, 70]. Among the peaks appear at 1370-1300 cm^{-1}, ones at 1390-1360 cm^{-1} are relatively well defined. They are attributed to bending modes of CH_3 of isopropyl or tertiary butyl groups which may be attached to aromatic coke species [67].

A number of absorption bands and their assignments are listed in Table 4. 11 and Table 4. 12. These will be applied to analysis of in-situ spectra in section 4.2.4.

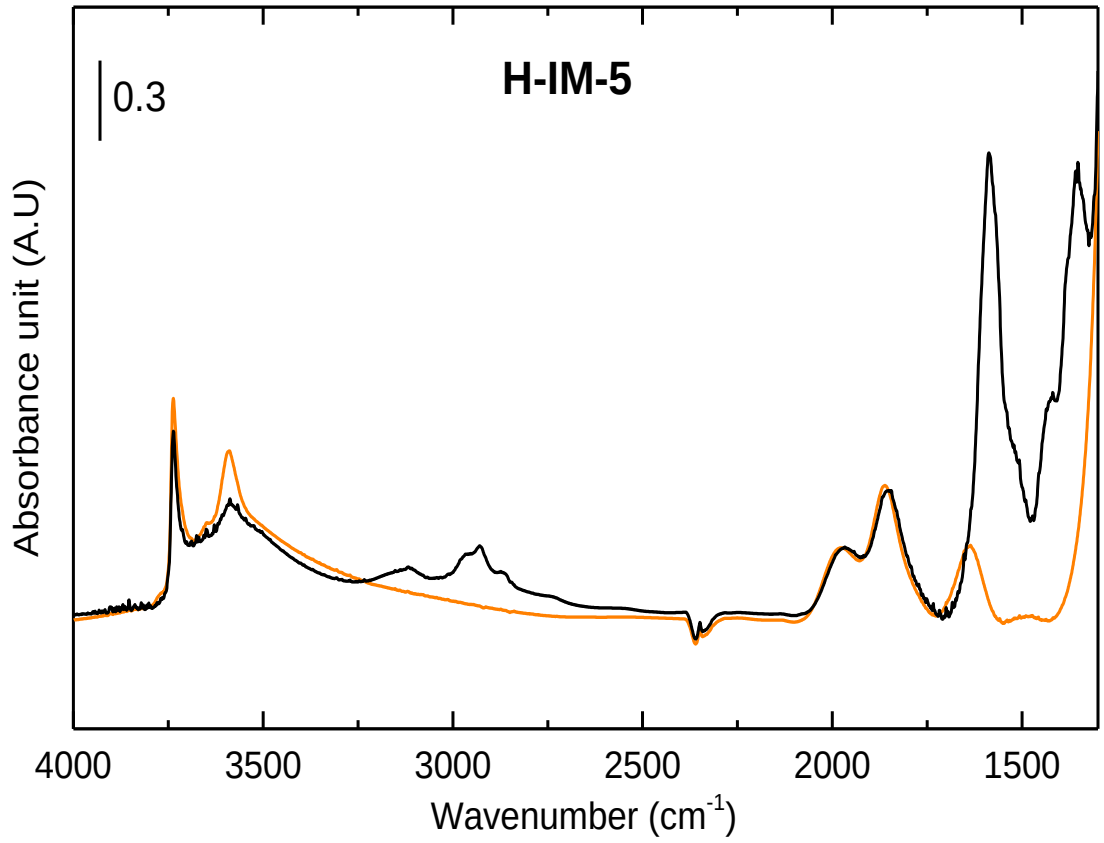

Figure 2. 17: spectrum of activated H-IM-5 (black) and the spectrum collected after 4 hours of MeOH injection to the sample (orange).

3 Experimental

3.1 Samples

Zeolites samples provided from different manufacturers are listed in Table 3. 1.

Table 3. 1: Manufacturers of samples. inGAP* implies that the samples were synthesized at Innovative Natural Gas Processes and Products (inGAP), National Center of Research-based Innovation.

		Manufacturer
MTT	ZSM-23	ZEOLYST
TON	ZSM-22	ZEOLYST
MOR	Mordenite	VENTRON
MWW	MCM-22	inGAP*
IMF	IM-5	inGAP*
ITH	ITQ-13	inGAP*
MFI	MFI-27	SÜD CHEMIE
	Pentasil	SÜD CHEMIE
	ZSM-5	ZEOCAT
SZR	SUZ-4	inGAP*
TUN	TNU-9	inGAP*
*BEA	Beta	SÜD CHEMIE

3.2 Basic characterizations

3.2.1 XRD

Powder X-ray Diffraction pattern of samples was performed by using Bruker D8 Advance diffractometer with CuKα1 (λ = 1.5406 Å) radiation selected by Germanium (111) Johansson monochromator. The detector is a LynxEye position sensitive strip detector [75]. Pawley refinement was performed using TOPAS 4.2 software from Bruker AXS. hkl phase

information of each zeolite used for the refinement was acquired in the software from .cif file provided by International Zeolite Association (IZA) database [76].

3.2.2 SEM

The morphology and particle size of zeolite samples were studied by using Scanning Electron Microscopy (SEM). This was performed on a FEI Quanta 200 except for TNU-9 sample. For the TNU-9, HITACHI SU8230 instrument was used. Zeolite samples were dispersed over carbon tape attached to a copper grid, and the grid was mounted inside of the instrument. The image of zeolite samples were taken at working distance of about 10 mm with acceleration voltages of 5-10 kV with low vacuum condition.

Energy-Dispersive X-ray Spectroscopy (EDS) analysis was performed in addition in order to investigate the elemental composition, mainly ratio of Si to Al.

3.2.3 N_2 Adsorption

N_2 adsorption isotherms were measured using a BELSORP-mini II instrument from BEL JAPAN at liquid nitrogen temperature, -196°C. The sample pre-treatment was done for 1 hour at 80°C and 4 hours at 300°C . Total BET surface areas of the samples were calculated using BET equation on BEL Analysis Software in the range of $0.01 \leq p/p_0 \leq 0.16$. More explanation regarding calculation of surface area using BET equation can be found in section 2.1.3.

3.3 Spectroscopic Investigations

3.3.1 Transmission FTIR using CO as a probe molecule

FTIR measurement using CO as a probe molecule was done at University of Oslo (UiO), in Oslo, Norway, using Bruker Vertex 80 instrument with MCT (Mercury Cadmium Telluride) detector and KBr Beam Splitter. Thin wafer supported by gold envelope was put into quartz transmission cell with KBr window.

Sample activation was done by heating the sample at 150°C for 1h, 300°C for 1h and 450°C for 1h under vacuum. After the activation, the cell and the sample were cooled back to room temperature. About 50mbar of carbon monoxide was filled in the line, and the cell was open to the line afterwards. When the equilibrium between the line and the cell was reached, the cell is closed again and temperature of the cell was adjusted to -196°C using liquid nitrogen for adsorption of carbon monoxide on zeolite. After reaching the point where no spectra change was observed, desorption process was preceded.

3.3.2 Transmission FTIR using Pyridine as a probe molecule

FTIR measurement using pyridine as a probe molecule was carried out at UiO in Oslo, Norway. The instrument used was Vertex 70 with DLATGS (Deuterated L-Alanine doped Triglycene Sulphate) detector and KBr Beam Splitter. Self-supported thin wafer was mounted in high temperature cell with KBr Windows.

Sample was activated by being heated to 450°C with synthetic air and the temperature was held for 30 minutes. It was made sure that all the samples were activated by observing the IR spectra. After the activation, the sample was cooled down to 150°C. Pyridine was introduced by using Nitrogen as carriage gas until there was no recognizable change in spectra. The time pyridine introduced was different from sample to sample. Once the introduction of pyridine to zeolites was done, system was flushed with continuous Nitrogen flow until there was no significant change of spectra. Then the temperature was increased to 200°C and stabilized. Two spectra were recorded with 10 minutes interval. If the spectra recorded were identical, temperature was increased by 50°C. Same procedure was repeated up to 400°C. Integration of absorption bands was done by using OPUS 7.0 software.

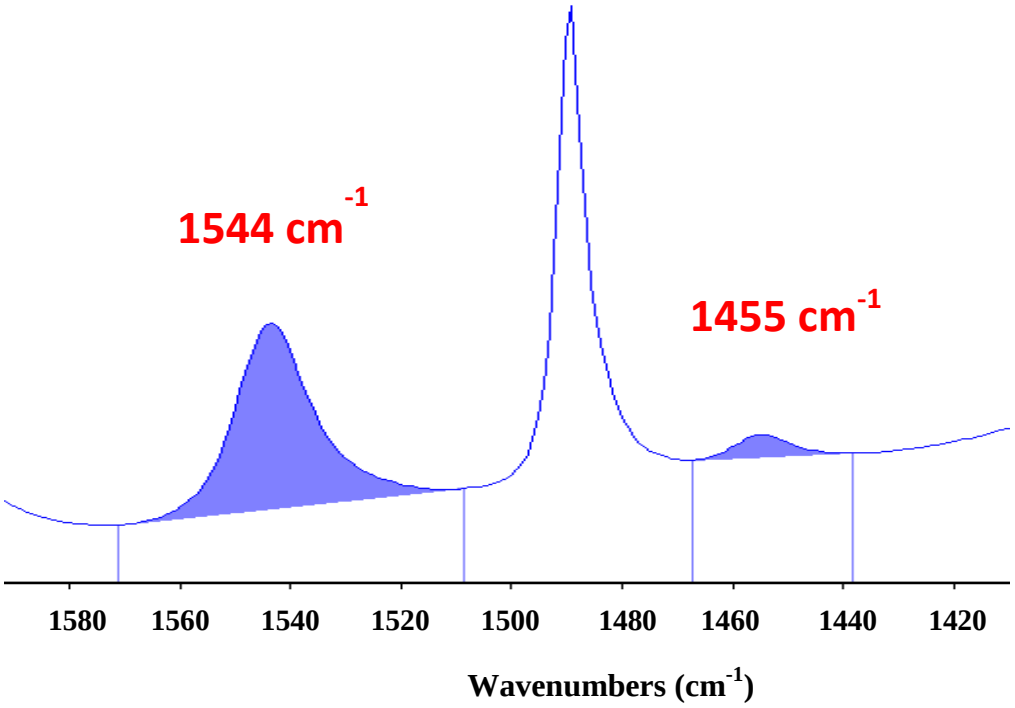

Figure 3. 1: Integration of bands at 1544cm-1 and 1455 cm-1 using OPUS software.

Calculation regarding pyridine adsorption on zeolite

The calculation was performed to find explanation for the results from pyridine adsorption experiments on H-ZSM-23 and H-SUZ-4. Calculation was done by using Accelrys Material Studio 7.0 Software. This can rather be considered as side-project of this work in order to find an explanation why not all acid sites was consumed during pyridine adsorption experiment on H-ZSM-23 and H-SUZ-4 zeolites. Calculations were performed under supervision of the postdoc, Rasmus Y. Brogaard, in the group.

Zeolite framework structures used in the calculation were from the software itself. Cambridge Serial Total Energy Package (CASTEP) module with GGA PBE function and Grimme method for Density Functional Dispersion Correction (DFT-D correction) was used for the calculation. Energy cutoff was set to 350eV after comparing adsorption energy of pyridine on zeolite H-ZSM-22 with different energy cutoff. Values of adsorption energy calculated didn't show much difference from 300eV as it is shown in Figure 3. 2. To make sure that the energy cutoff doesn't affect the quality of the calculation, 350eV was chosen for the further calculation.

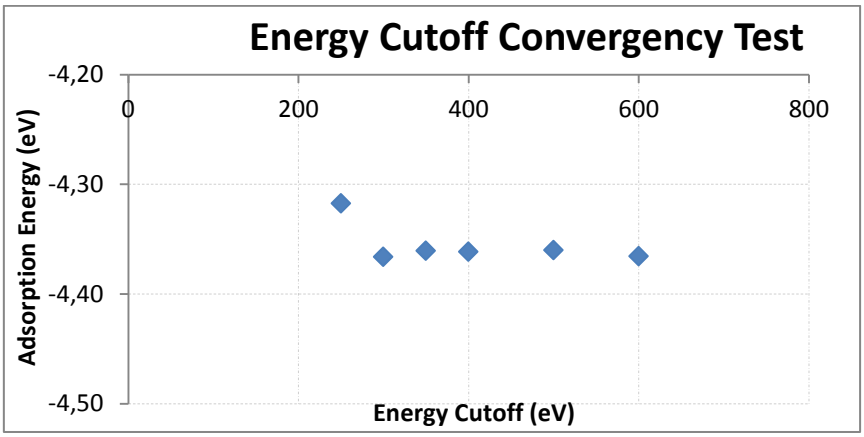

Figure 3. 2: Energy cutoff comparison using Adsorption Energy of pyridine on zeolite ZSM-22.

It should be noted that the geometry optimization was not performed for this, so the adsorption energy calculated is not accurate. This calculation only had a purpose to find out which energy cutoff could be used for further calculation, not to find out exact adsorption energy.

Since zeolite is crystalline but pyridine is not, it was needed to treat pyridine as crystalline to have consistency in calculation with same module and condition. So, unit cell including a pyridine molecule was created, and the energy of pyridine was calculated in different unit cell size. One can see from Figure 3. 3 that the energy starts to converge from lattice length of 10 Å. To make sure that the lattice length doesn't play severe role in calculation, 14 Å was chosen. That is, the unit cell size of pyridine applied to this work is 14 x 14 x 14 $Å^3$.

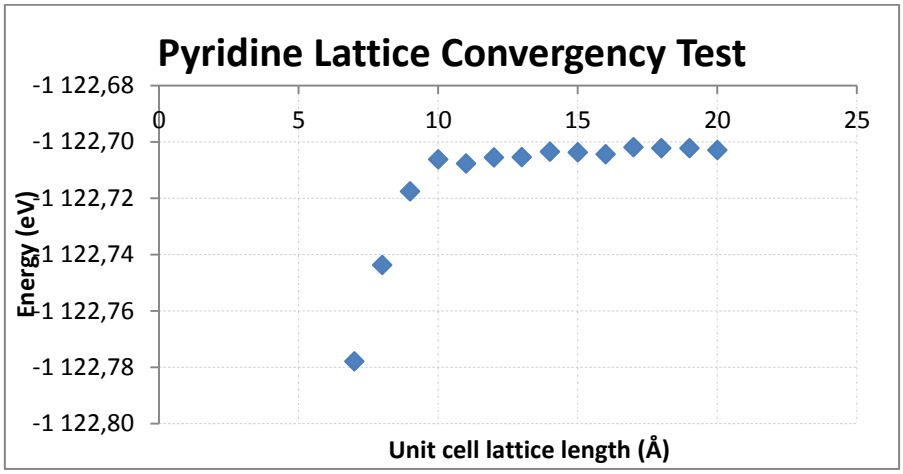

Figure 3. 3: Energy of pyridine calculated from different lattice length of unit cell

With these parameters, the calculations of adsorption energy of pyridine on two zeolite samples (H-ZSM-23, H-SUZ-4) were performed. First, the unit cell of the zeolite structure was geometrically optimized. Then single or plural acid sites were created by replacing single or plural silicon atom(s) with aluminium atom(s) and by adding extra hydrogen atom(s) to neighboring oxygen(s). The H-form zeolite structure went through the geometry optimization again. Afterwards, pyridine was added to the system, and one more geometry optimization was performed. The energies calculated from the geometry optimizations were used in the calculation of adsorption energy.

3.3.3 In-Situ FTIR on zeolites during the MTH reaction

The in-situ FTIR on MTH reaction was performed at Norwegian University of Science and Technology (NTNU) in Trondheim, Norway. Bruker Vertex 80 instrument with MCT (Mercury Cadminium Telluride) detector and KBr beam splitter was used. Self-supported thin wafer was mounted in Specac High Temperature High Pressure (HTHP) cell with ZnSe windows.

Before the Methanol was introduced to the system, sample was heated to 350°C with rate of 300°C per hour, and stayed at the temperature for an hour with synthetic air for activation. After an hour, sample was heated up to 400°C, experiment temperature for MTH reaction. Nitrogen was used as a carriage gas. There were two separate lines for Nitrogen flow, and one flow was passing through methanol saturator, while the other one was not. Amount of methanol fed was set to satisfy the condition WHSV=2 ($gg^{-1}h^{-1}$) by adjusting flow of the line passing through the methanol saturator. The other line was used to set the total flow of nitrogen to 20ml/min. This was done because the total volume of the transmission cell was 60 ml/min, and it was not efficient enough with only methanol-saturated-nitrogen gas, which usually gave flow under 10 ml/min. Because of difference in weight between wafers for different samples, the partial pressure of MeOH is different in each experiment. Partial pressure condition of MeOH in the experiment for each sample is shown in Table 3. 2.

Methanol was introduced to the system for 4 hours, and spectra were recorded every 2 minutes. Outlet from the high temperature high pressure cell was connected to Agilent 7890A Gas Chromatography (GC)/5975C Mass Selective Detector (MSD) equipped with Flame

Ionization Detector (FID). Agilent J&W HP-PONA column (50m, 0.200 mm i.d.) was used in GC. Injections to the GC-MS-FID instrument were done every 28-30 minutes while the methanol was introduced.

Table 3. 2: Implemented MeOH partial pressure conditions in in-situ FTIR on zeolites during the MTH reaction

Sample	MeOH Partial Pressure (mbar)
H-ZSM-23	10
H-ZSM-22	9
H-Mordenite	12
H-MCM-22	8
H-IM-5	25
H-ITQ-13	7
H-MFI-27	10
H-Pentasil	10
H-ZSM-5	19
H-SUZ-4	7
H-TNU-9	15
H-Beta	11

4 Result and Discussion

4.1 Basic Characterization

4.1.1 XRD

X-ray diffraction patterns from all 12-samples are shown in Figure 4. 1 ~ Figure 4. 12. Black curves are diffractogram of each sample measured at the lab, red ones are Pawley-refined XRD curves, and blue curves are difference between experimental and Pawley-refined diffraction pattern.

In case of H-ZSM-22, measured diffractogram of H-ZSM-22 shows quite large difference compare to reference pattern. It is because of sample preparation for H-ZSM-22 was different from other samples. All the other samples were measured using disk type holder. However, there was difficulty mounting H-ZSM-22 in disk type sample holder as a powder since the sample did not hold itself inside of the holder. So, distilled water was added to the H-ZSM-22, sample was dispersed on flat disk glass plate, dried, and measured. As water was added, the height of sample at the surface level was not as even as when sample was mounted in disk type holder. Also, additional water in the zeolite, even though it was dried out, could affect the intensity of diffractogram. This can be applied to other samples as well. Since the measurement was carried out at room temperature, adsorbed water in zeolites cannot be totally ignored. So, for the intensity difference between black and red curves, water can be the simplest explanation for all 12 samples.

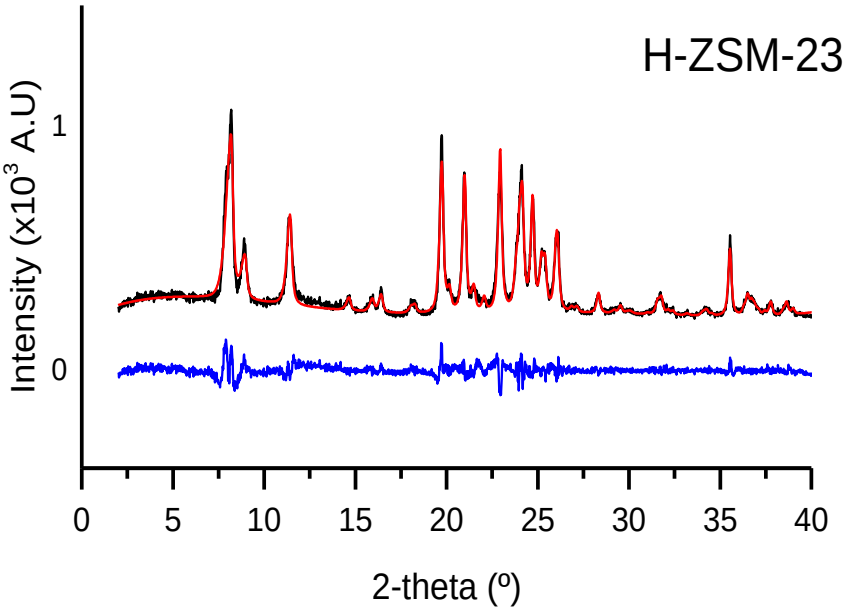

Figure 4. 1: Measured X-ray diffraction pattern of H-ZSM-23 sample (black), Pawley-refined XRD curve of MTT framework (red, R_{wp} = 14.89%), and their difference (blue).

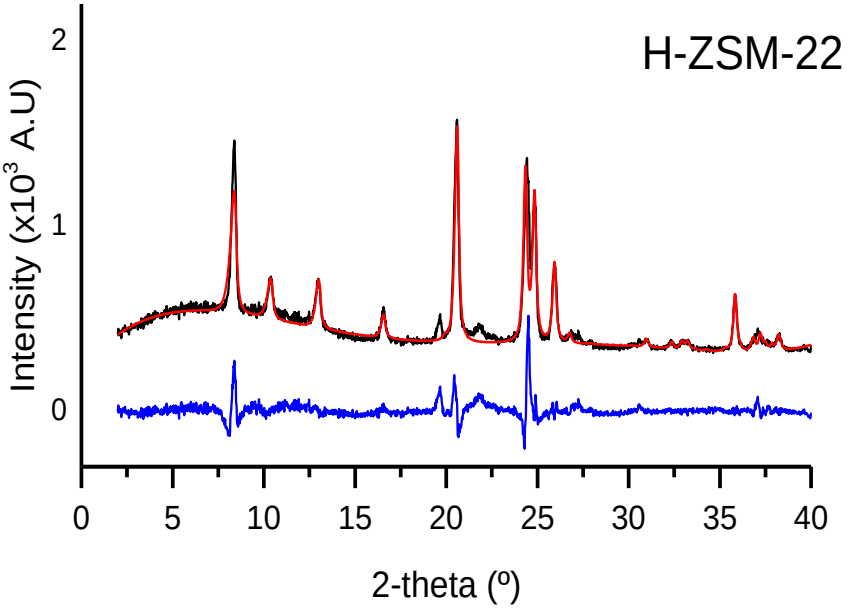

Figure 4. 2: Measured X-ray diffraction pattern of H-ZSM-22 sample (black), Pawley-refined XRD curve of TON framework (red, R_{wp} = 18.21%), and their difference (blue).

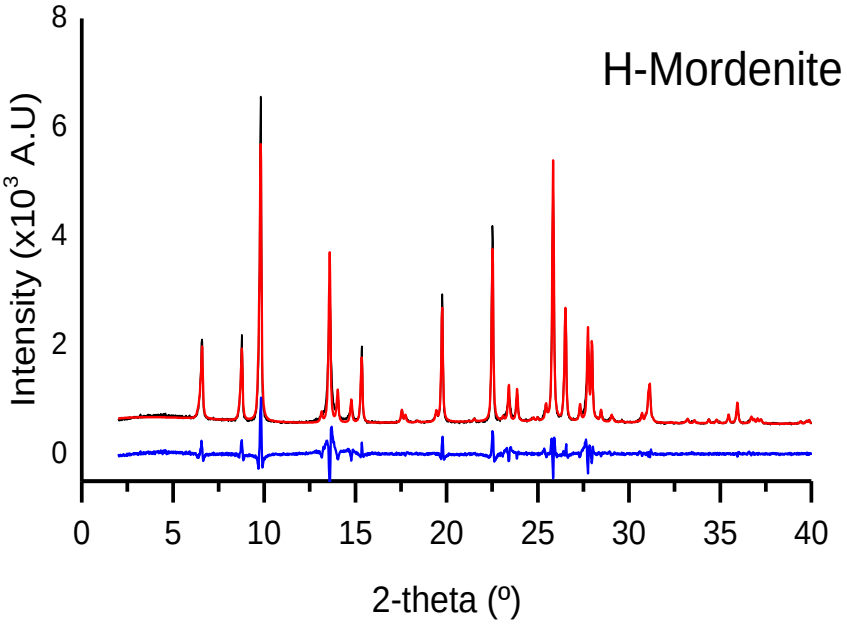

Figure 4. 3: Measured X-ray diffraction pattern of H-Mordenite sample (black), Pawley-refined XRD curve of MOR framework (red, R_{wp} = 16.50 %), and their difference (blue). The diffractogram was measured by S. Etemadi [2].

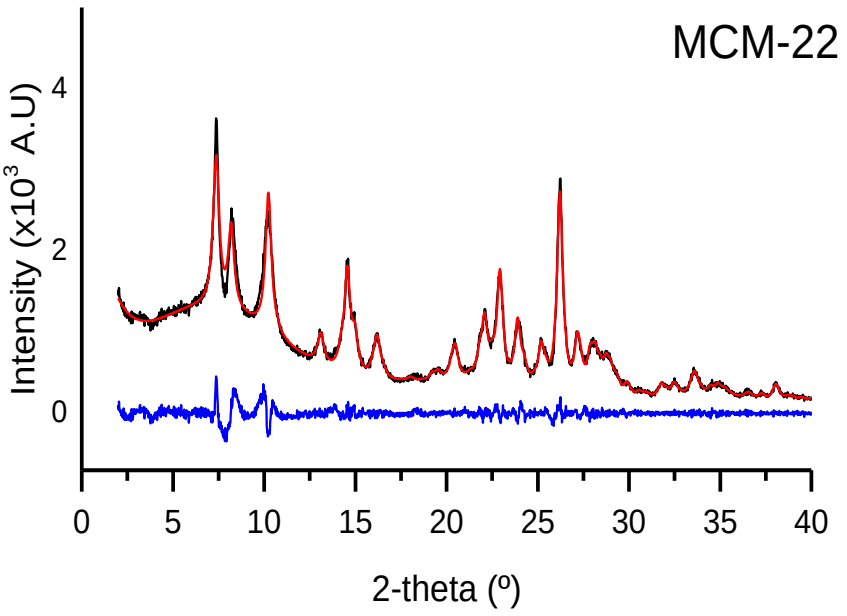

Figure 4. 4: Measured X-ray diffraction pattern of MCM-22 sample (black), Pawley-refined XRD curve of MWW framework (red, R_{wp} = 6.41 %), and their difference (blue). The diffractogram was measured by S.H. Morejudo [77].

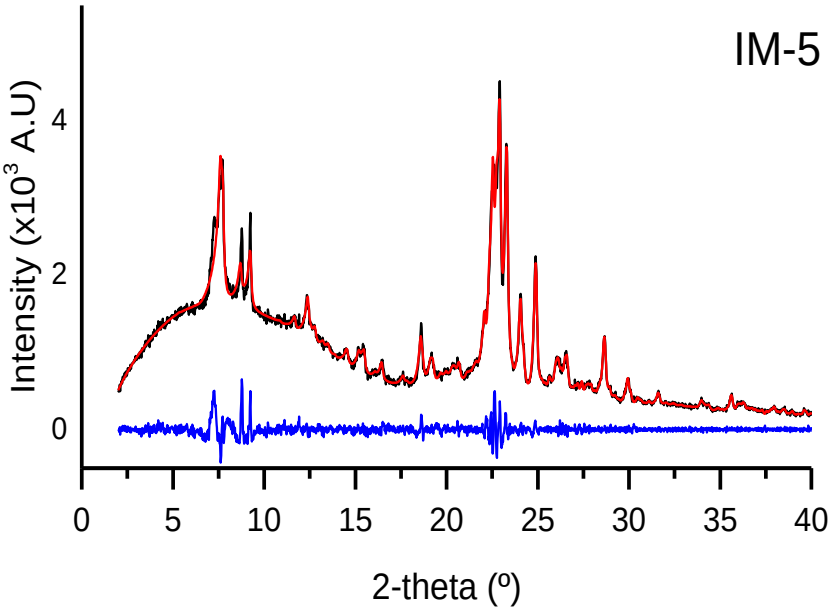

Figure 4. 5: Measured X-ray diffraction pattern of IM-5 sample (black), Pawley-refined XRD curve of IMF framework (red, R_{wp} = 5.86 %), and their difference (blue). The diffractogram was measured by N. Kasian [78].

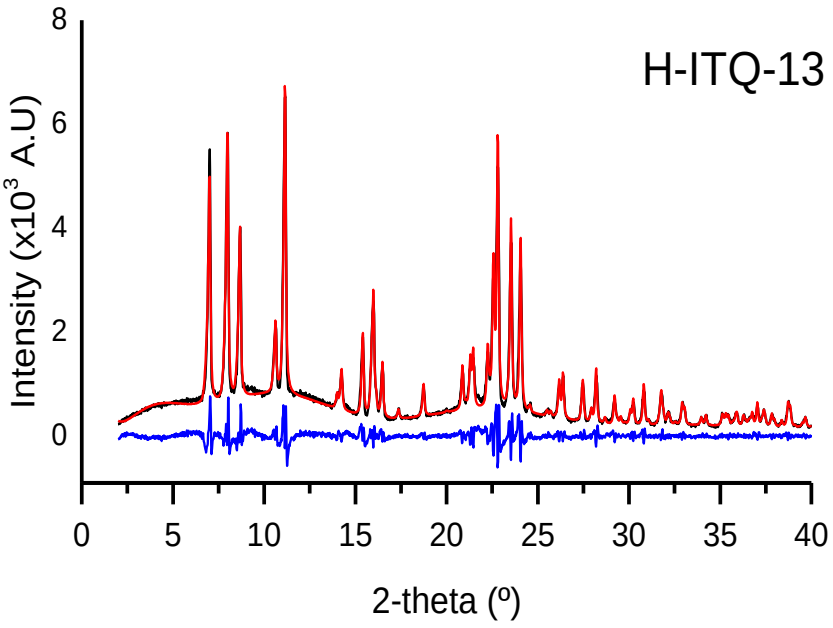

Figure 4. 6: Measured X-ray diffraction pattern of H-ITQ-13 sample (black), Pawley-refined XRD curve of ITH framework (red, R_{wp} = 10.03 %), and their difference (blue). The diffractogram was measured by N. Kasian [78].

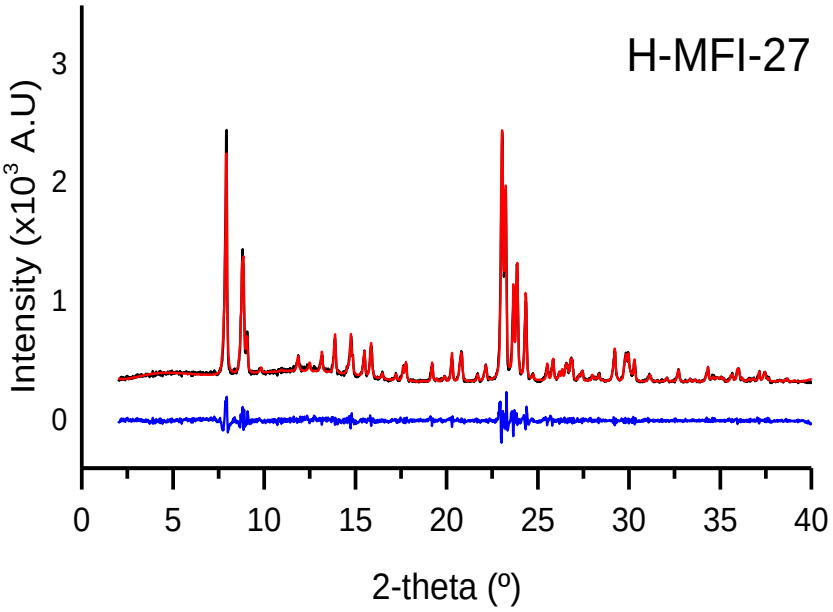

Figure 4. 7: Measured X-ray diffraction pattern of H-MFI-27 sample (black), Pawley-refined XRD curve of MFI framework (red, R_{wp} = 13.37 %), and their difference (blue).

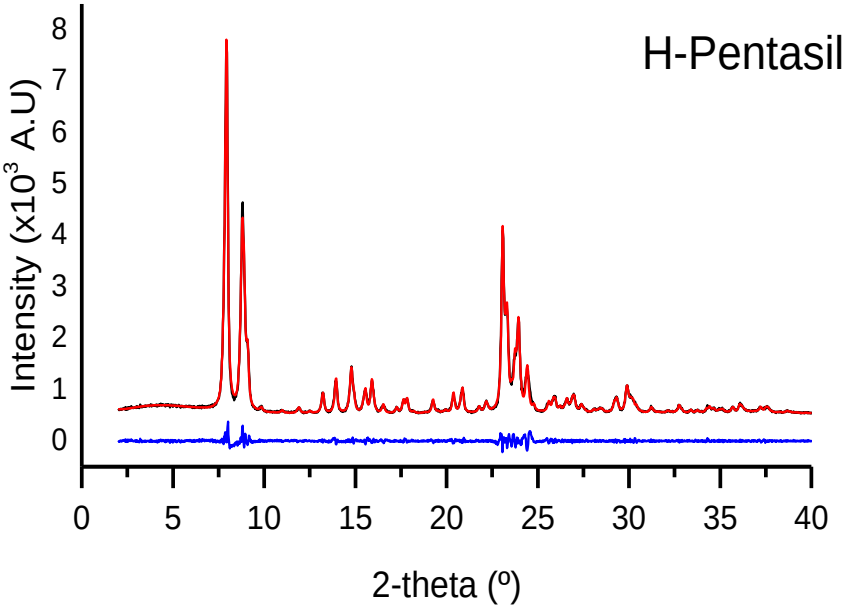

Figure 4. 8: Measured X-ray diffraction pattern of H-Pentasil sample (black), Pawley-refined XRD curve of MFI framework (red, R_{wp} = 9.28 %), and their difference (blue). The diffractogram was measured by S. Etemadi [2].

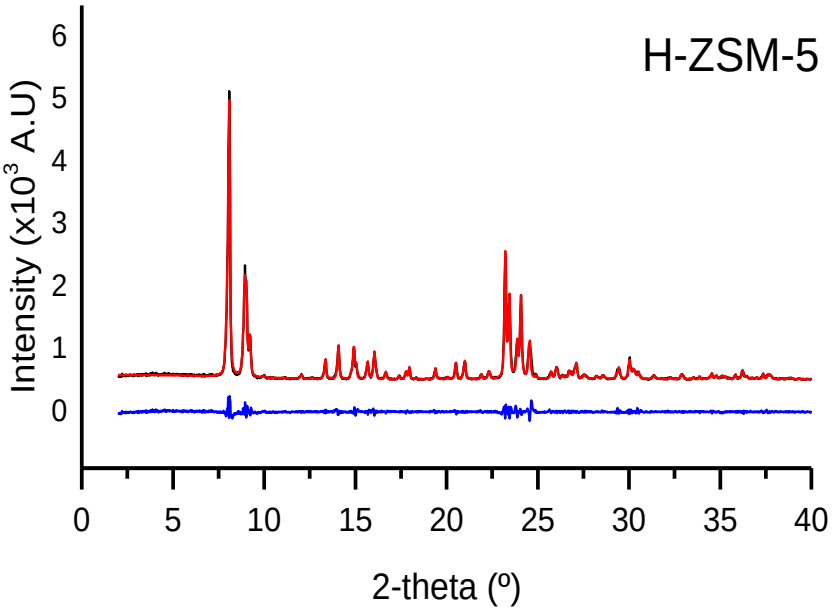

Figure 4. 9: Measured X-ray diffraction pattern of H-ZSM-5 sample (black), Pawley-refined XRD curve of MFI framework (red, R_{wp} = 12.08 %), and their difference (blue).

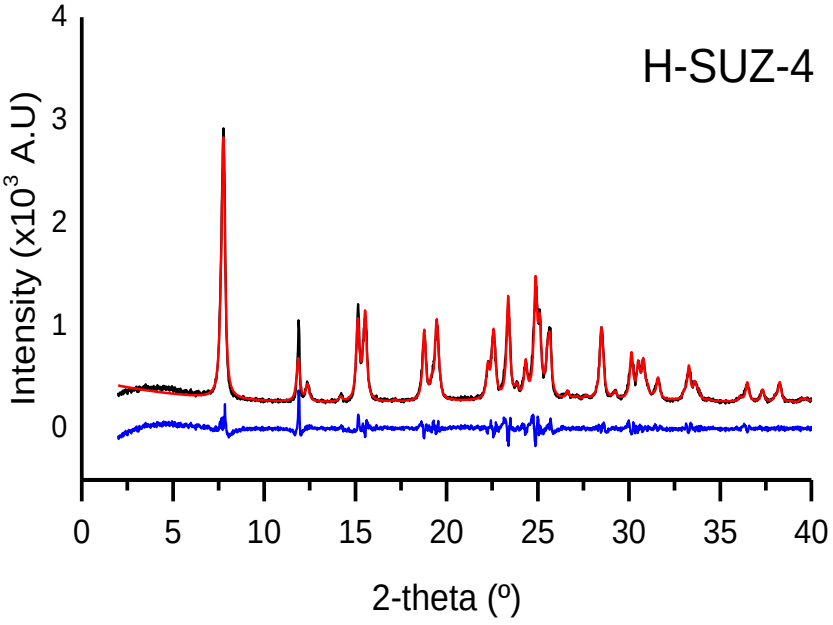

Figure 4. 10 Measured X-ray diffraction pattern of H-SUZ-4 sample (black), Pawley-refined XRD curve of SZR framework (red, R_{wp} = 13.14%), and their difference (blue). The diffractogram was measured by S. Etemadi [2].

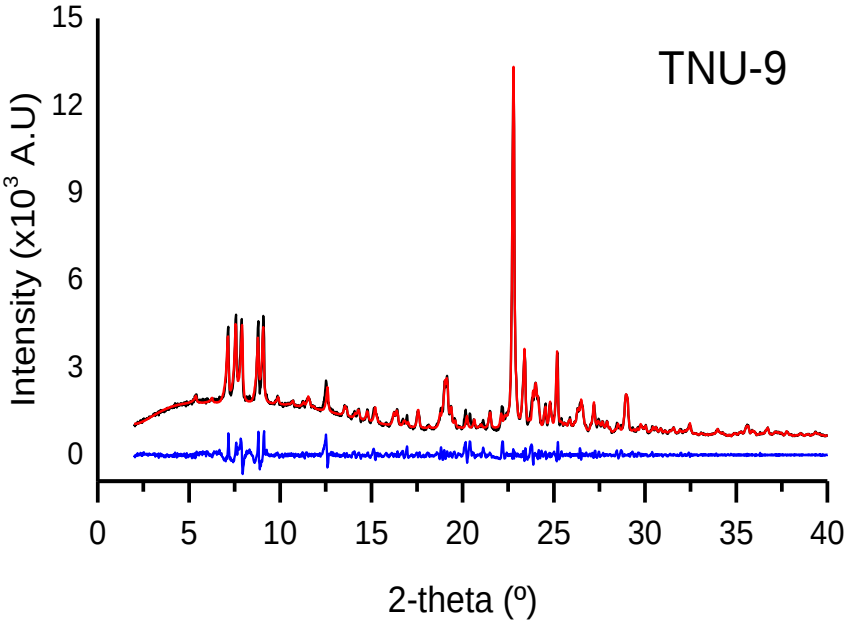

Figure 4. 11: Measured X-ray diffraction pattern of TNU-9 sample (black), Pawley-refined XRD curve of TUN framework (red, R_{wp} = 9.81 %), and their difference (blue). The diffractogram was measured by N. Kasian [78].

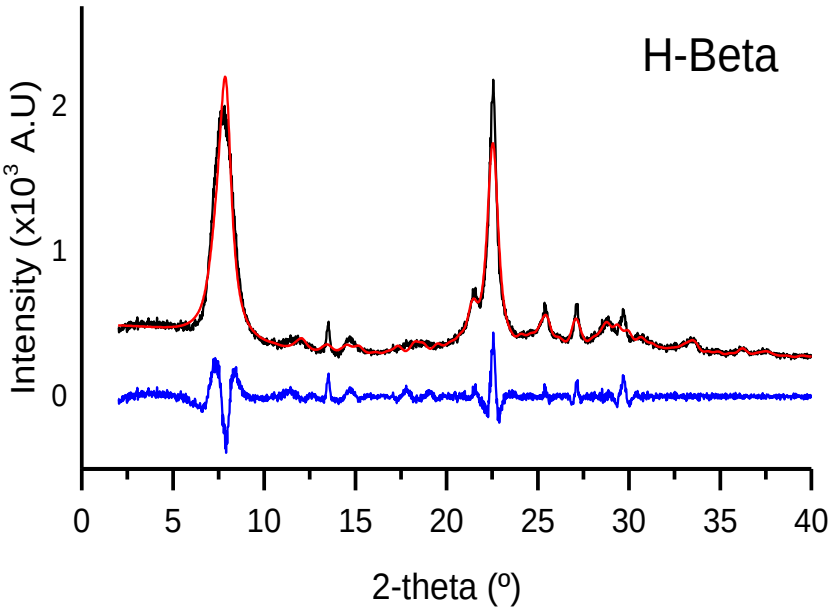

Figure 4. 12: Measured X-ray diffraction pattern of H-Beta sample (black), Pawley-refined XRD curve of *BEA framework (red, R_{wp} = 12.16%), and their difference (blue). The diffractogram was measured by S. Etemadi [2].

4.1.2 SEM

Pictures taken in 2.0 μm and 10.0 μm scales using SEM are presented for each zeolite sample. From the Figure 4. 13 to Figure 4. 24, information regarding morphology and rough size of each zeolite can be acquired.

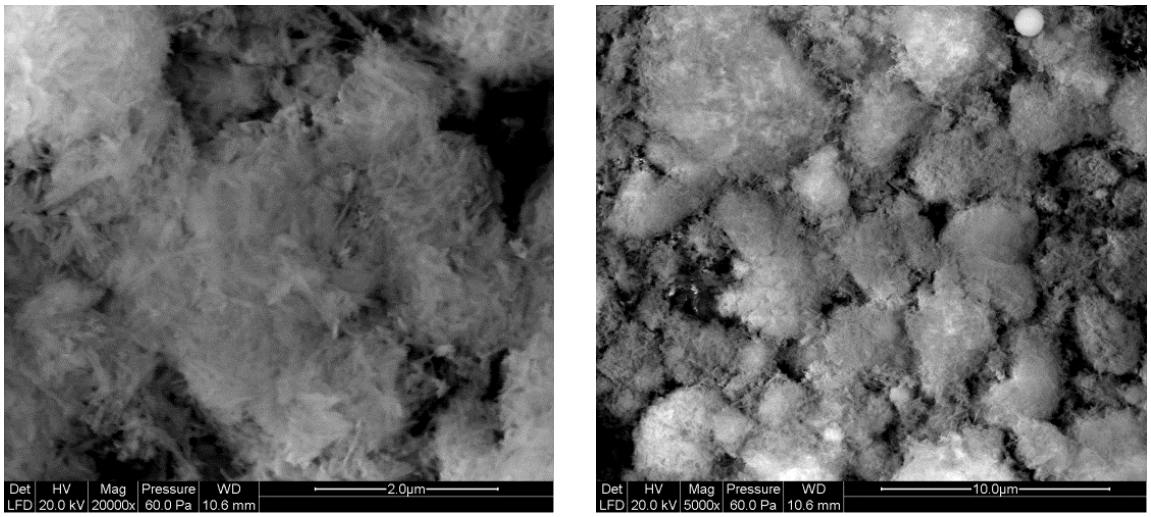

Figure 4. 13: SEM image of H-ZSM-23

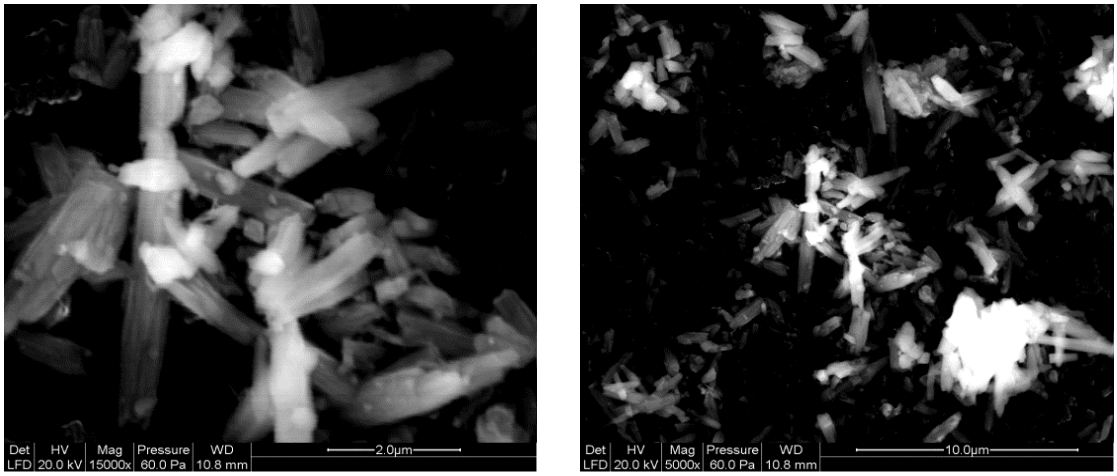

Figure 4. 14: SEM image of H-ZSM-22

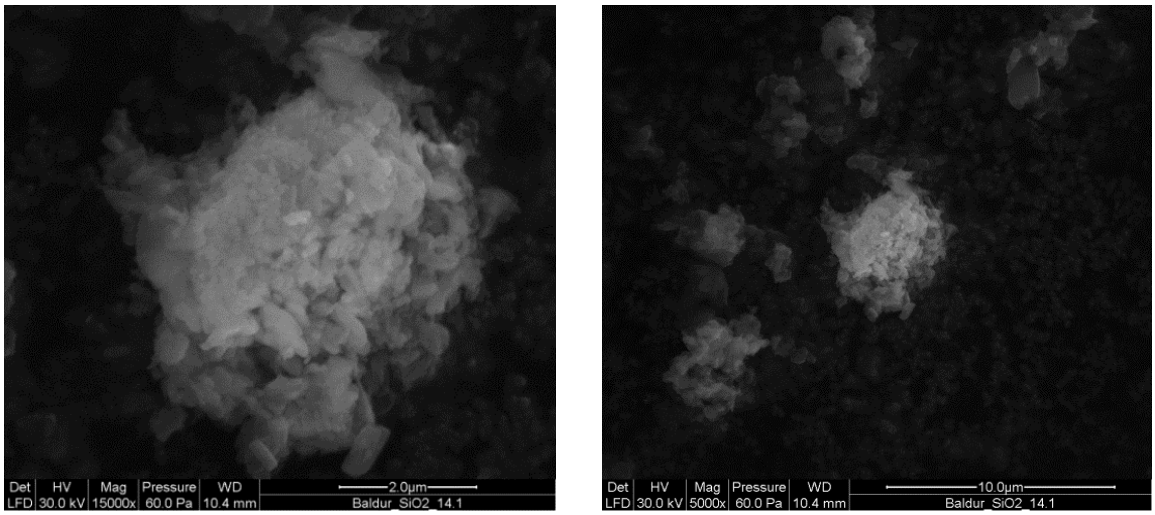

Figure 4. 15: SEM image of H-Mordenite

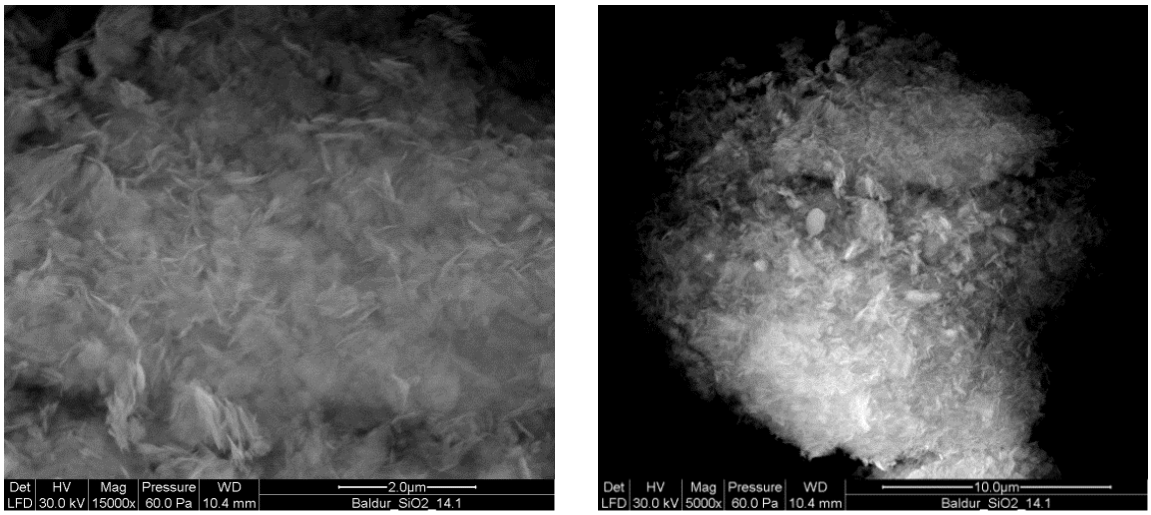

Figure 4. 16: SEM image of H-MCM-22

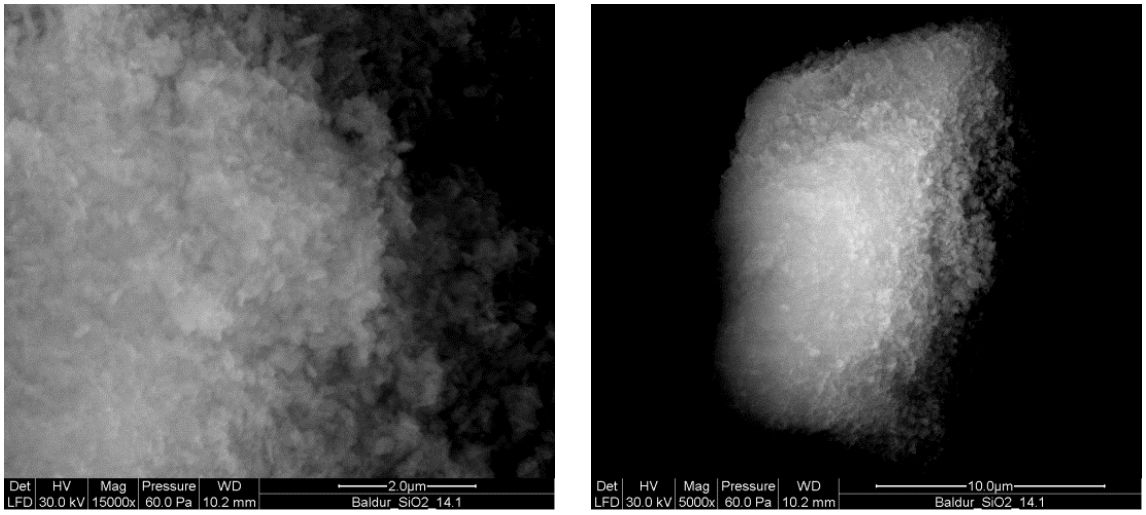

Figure 4. 17: SEM image of H-IM-5

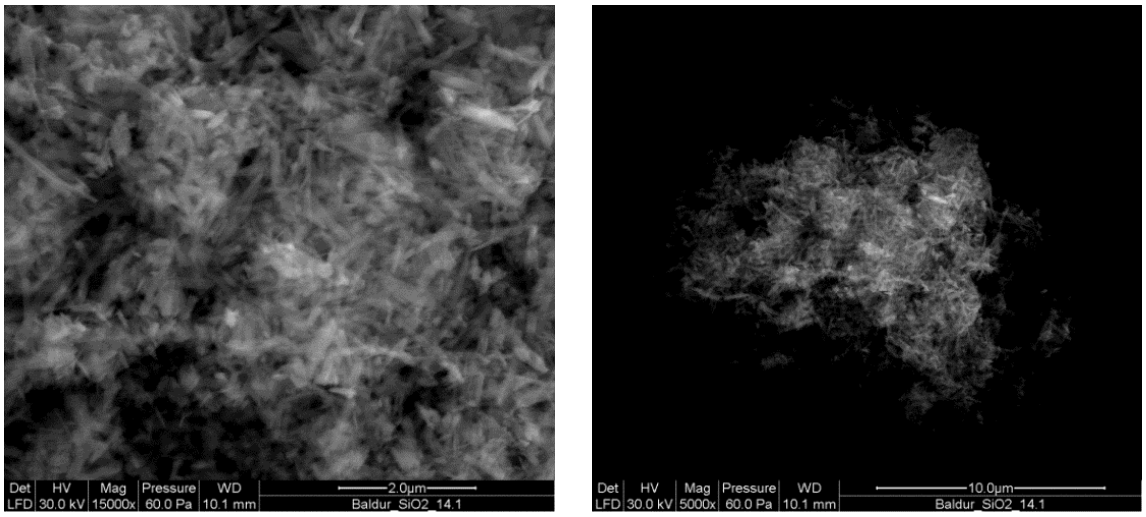

Figure 4. 18: SEM image of H-ITQ-13

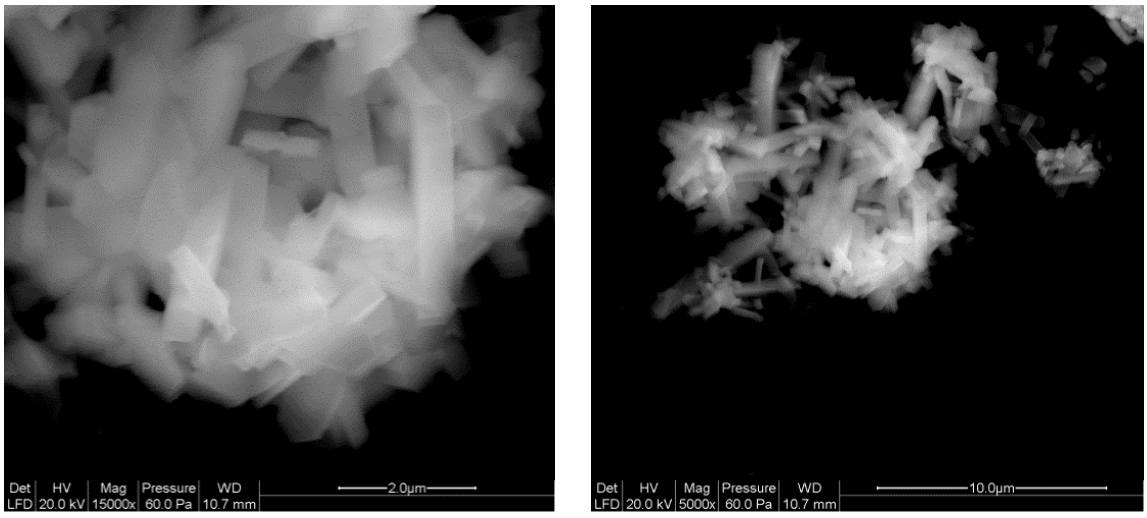

Figure 4. 19: SEM image of H-MFI-27

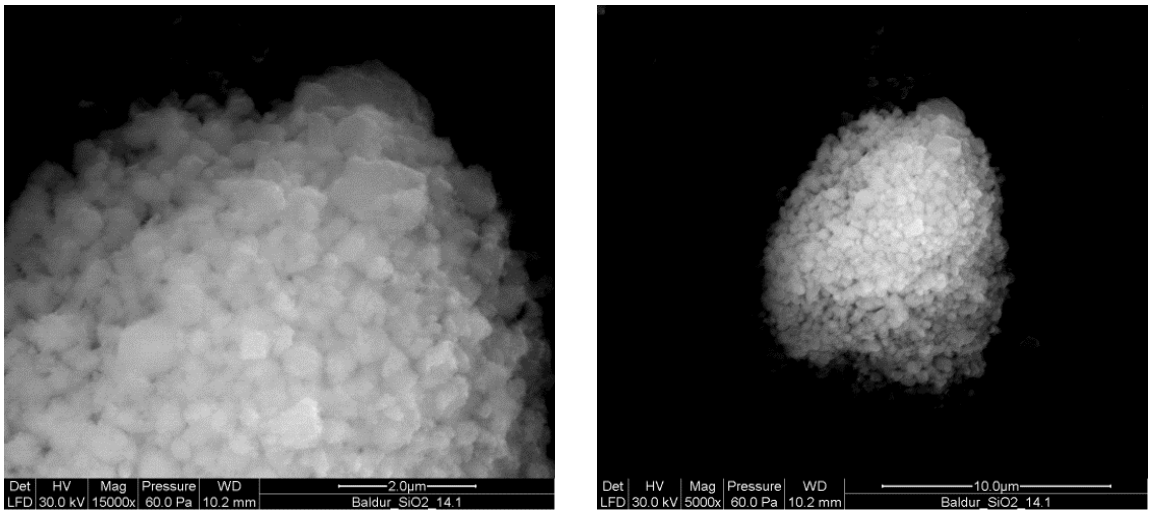

Figure 4. 20: SEM image of H-pentasil

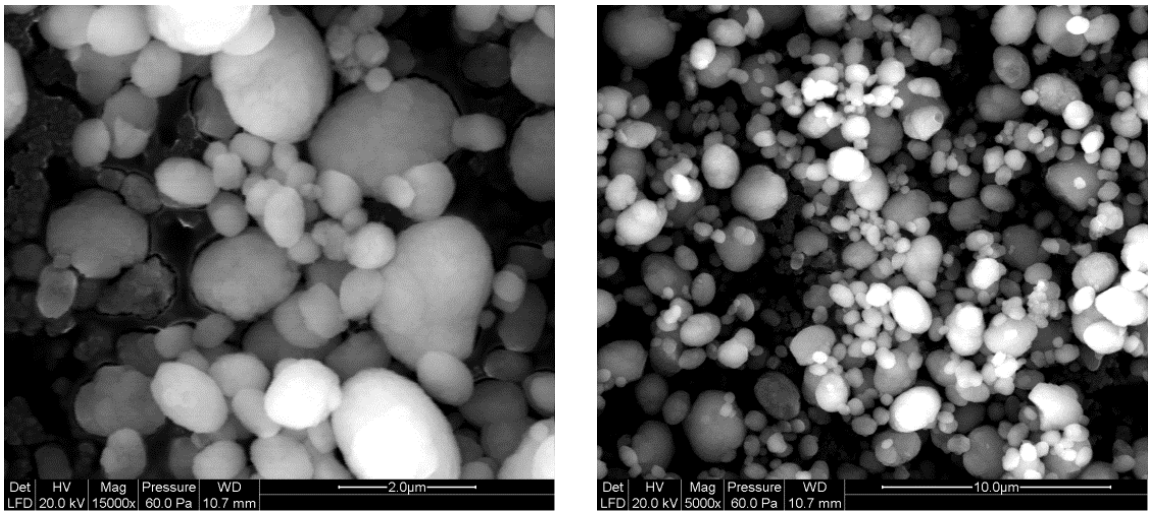

Figure 4. 21: SEM image of H-ZSM-5

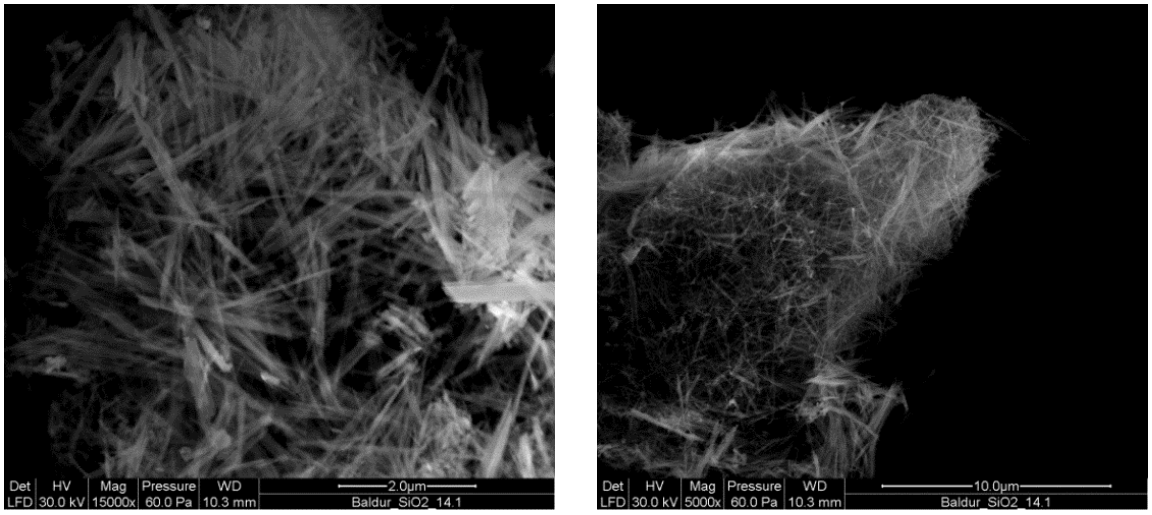

Figure 4. 22: SEM image of H-SUZ-4

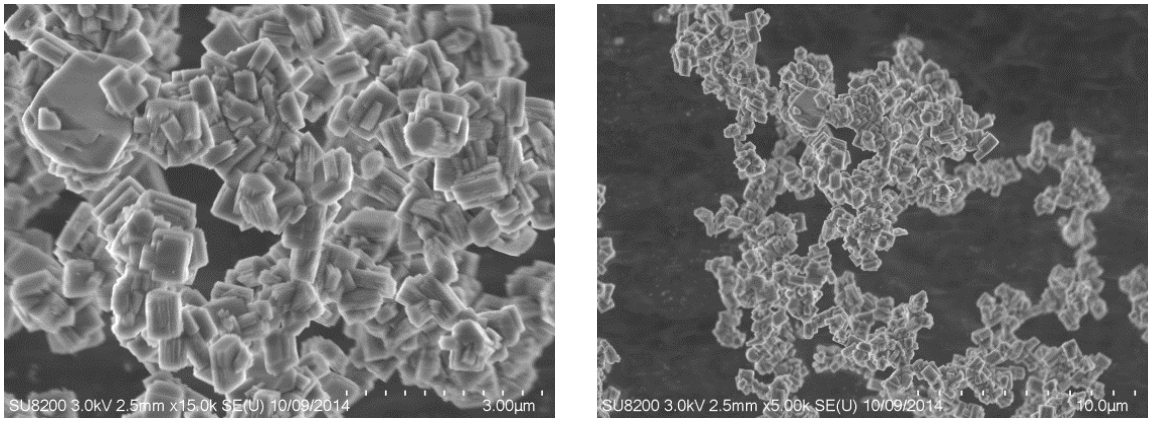

Figure 4. 23: SEM image of H-TNU-9

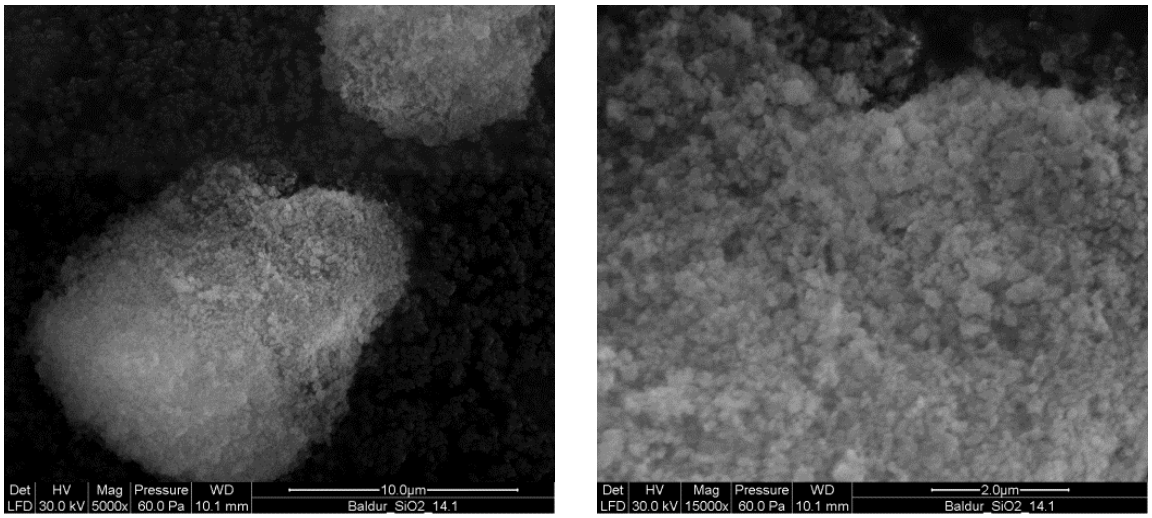

Figure 4. 24: SEM image of H-Beta

The information about Si/Al from the EDS was acquired as well, and the values are compared with the "theoretical" Si/Al values which were provided from manufacturer of the sample. From Table 4. 1, it can be seen that there is no big difference between theoretical Si/Al and that from EDS except for one sample, H-ITQ-13. Since the sample was in-house synthesized, not commercial, there is possibility that Si/Al of synthesized sample is different from the aimed value. Si/Al calculated from pyridine adsorption on H-ITQ-13 is also lower than the theoretical value and quite close to the value from EDS which can support the assumption.

Table 4. 1: Theoretical Si/Al and calculated Si/Al using EDS

		Theoretical Si/Al	Si/Al from EDS
MTT	H-ZSM-23	23	22
TON	H-ZSM-22	45	33
MOR	H-Mordenite	22	15
MWW	H-MCM-22	15	13
IMF	H-IM-5	15	15
ITH	H-ITQ-13	50	30
MFI	H-MFI-27	13.5	15

	H-Pentasil	45	32
	H-ZSM-5	50	40
SZR	H-SUZ-4	8	7
TUN	H-TNU-9	15	13
*BEA	H-Beta	13.5	12

4.1.3 N_2 Adsorption

All of the adsorption isotherm measured in this work shows typical microporous adsorption isotherm [79]. For H-ZSM-22, H-Mordenite and MFI zeolites, one observes hysteresis loop. The hysteresis loop has been considered to be associated with pore condensation into mesoporous (interparticle voids, interconnected pores) [80, 81]. This explains well the reason why MFI zeolites' adsorption isotherms show hysteresis loop behavior. For Mordenite and H-ZSM-22, Coasne et al. studied adsorption isotherm in non-interconnected pores, and they observed hysteresis in well-ordered porous silicon with tubular pores without narrow sections and interconnection [81]. H-TNU-9 sample was measured twice, and the difference in calculated specific BET surface area was 0.7 m^2g^{-1}. From this, we can say that the reproducibility of the technique is reliable.

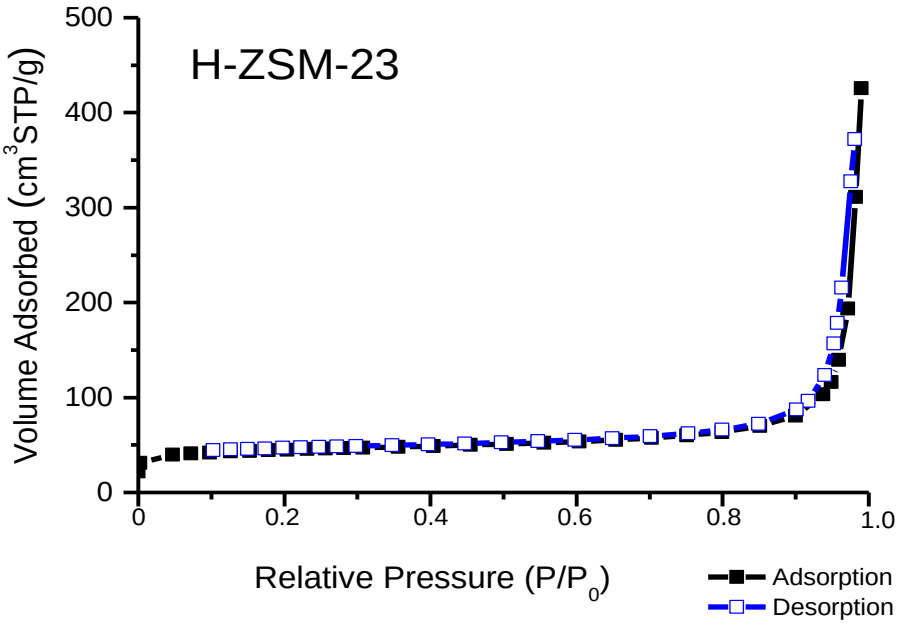

Figure 4. 25: Adsorption Isotherm of H-ZSM-23

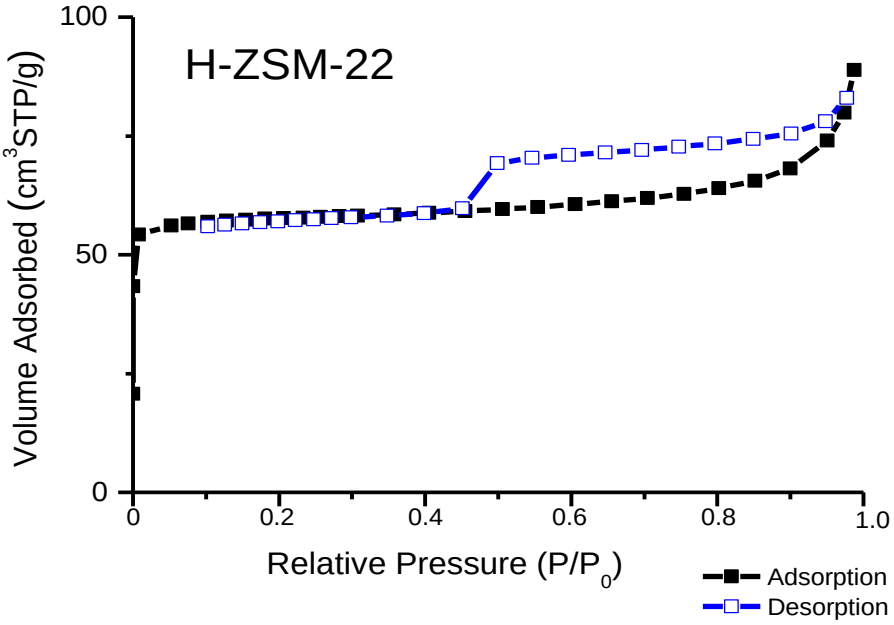

Figure 4. 26: Adsorption Isotherm of H-ZSM-22

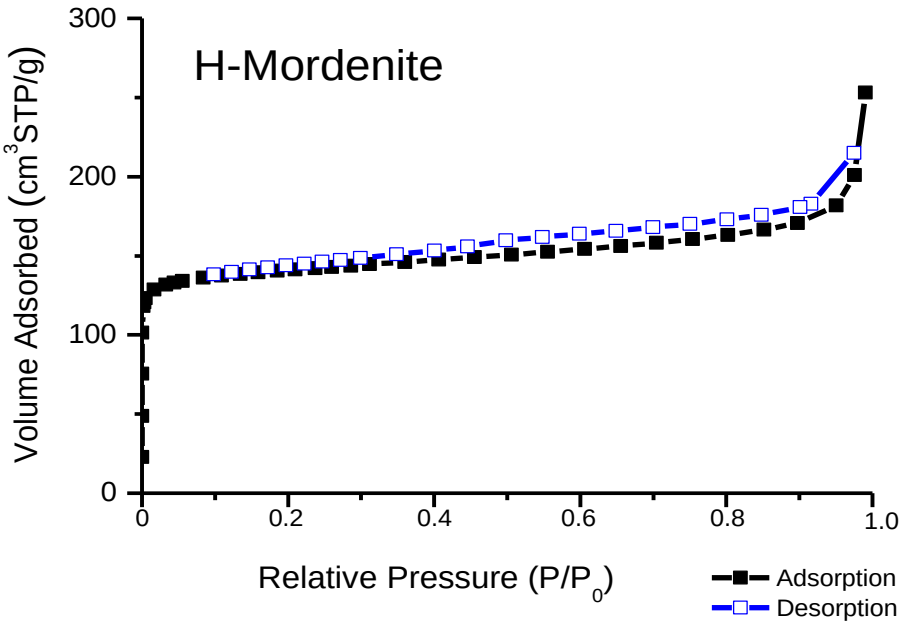

Figure 4. 27: Adsorption Isotherm of H-Mordenite. Experiment performed by S. Etemadi [2].

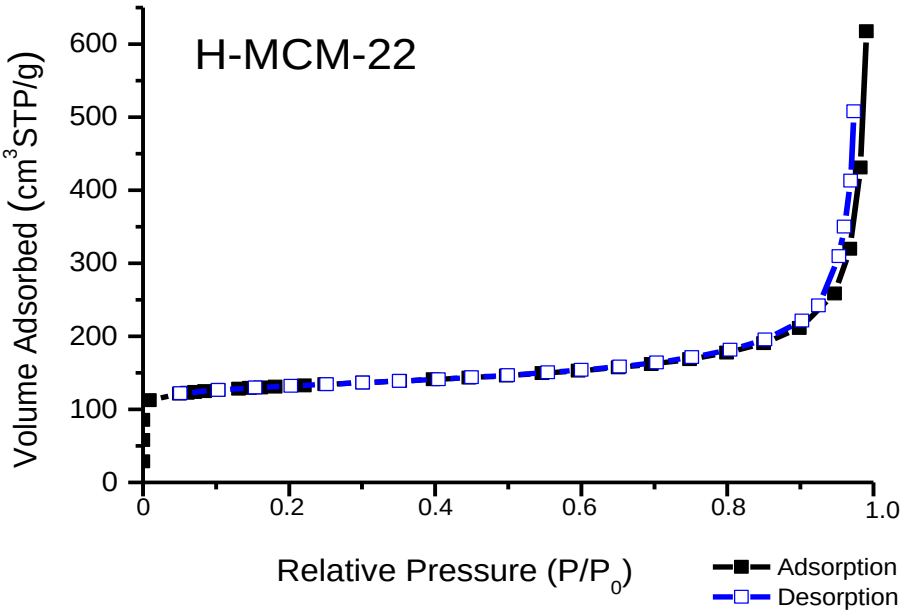

Figure 4. 28: Adsorption Isotherm of H-MCM-22. Experiment performed by S. Etemadi [2].

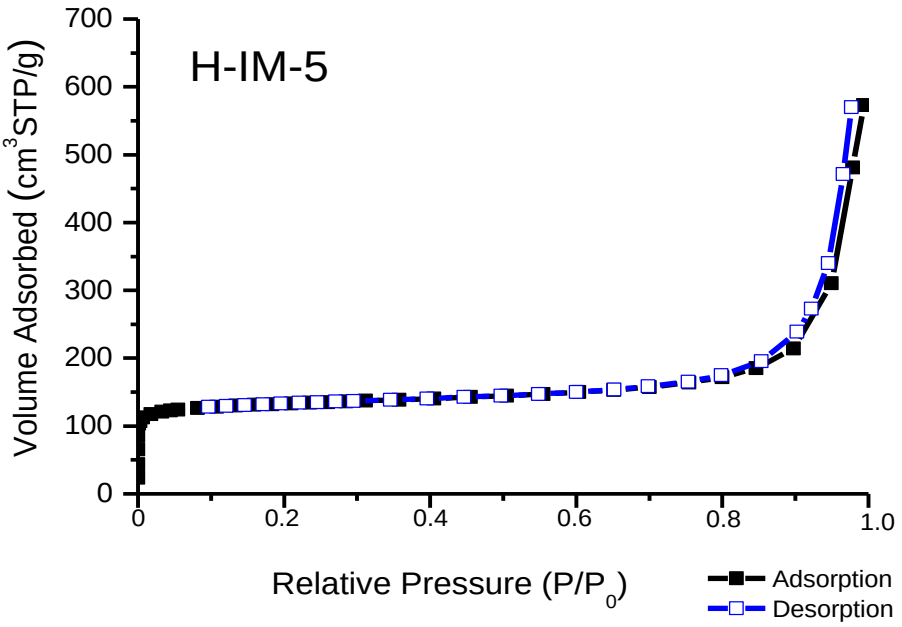

Figure 4. 29: Adsorption Isotherm of IM-5. Experiment performed by N. Kasian [78].

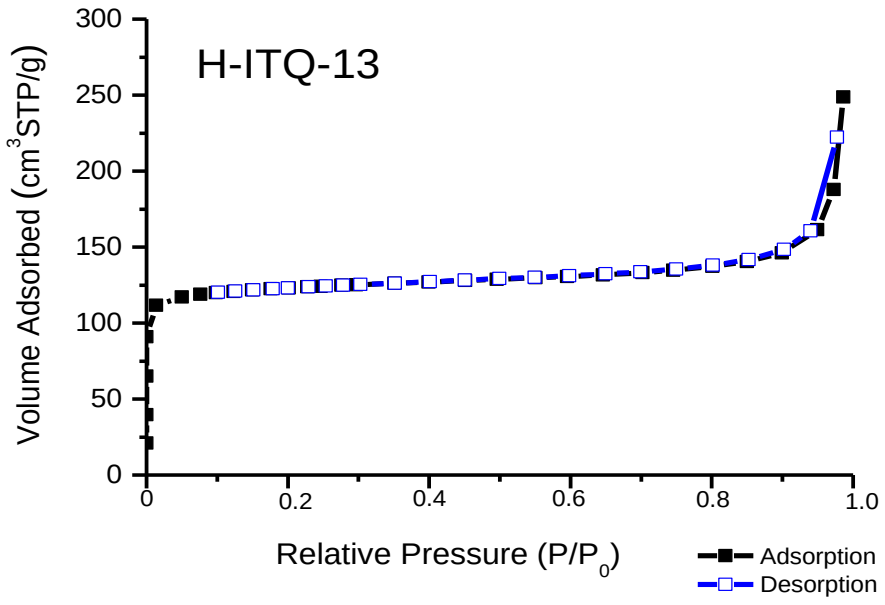

Figure 4. 30: Adsorption Isotherm of H-ITQ-13. Experiment performed by N. Kasian [78].

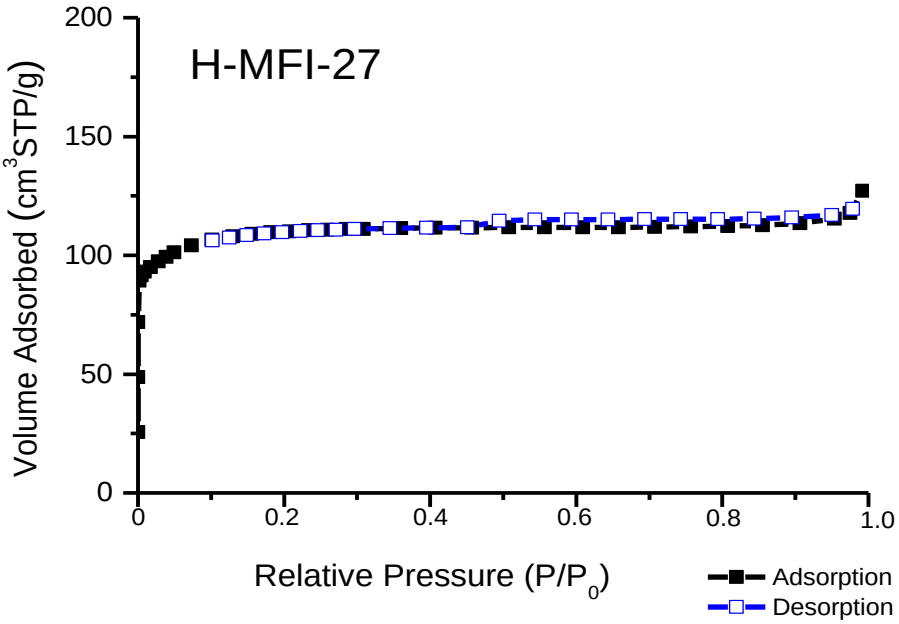

Figure 4. 31: Adsorption Isotherm of H-MFI-27

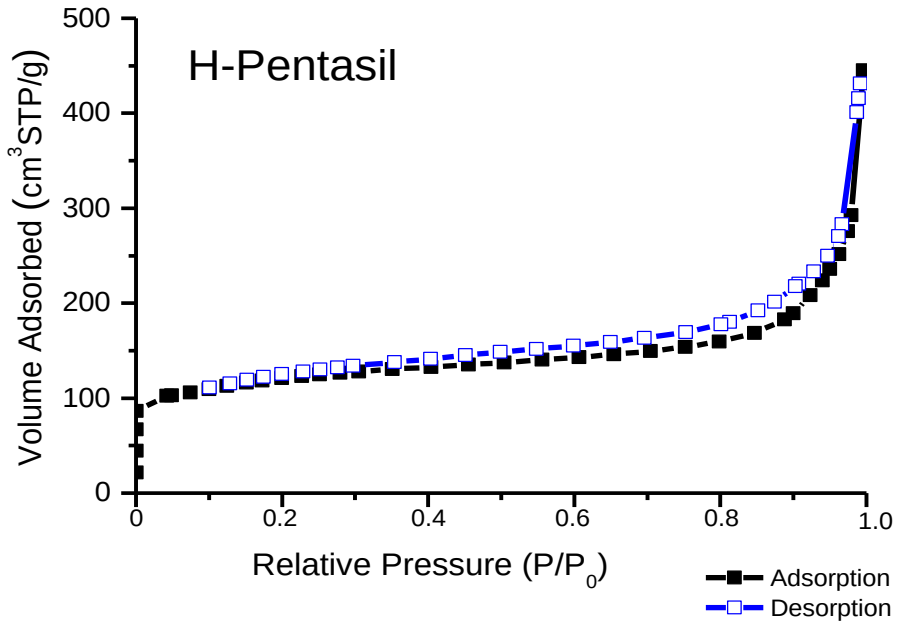

Figure 4. 32: Adsorption Isotherm of H-Pentasil. Experiment performed by S. Etemadi [2].

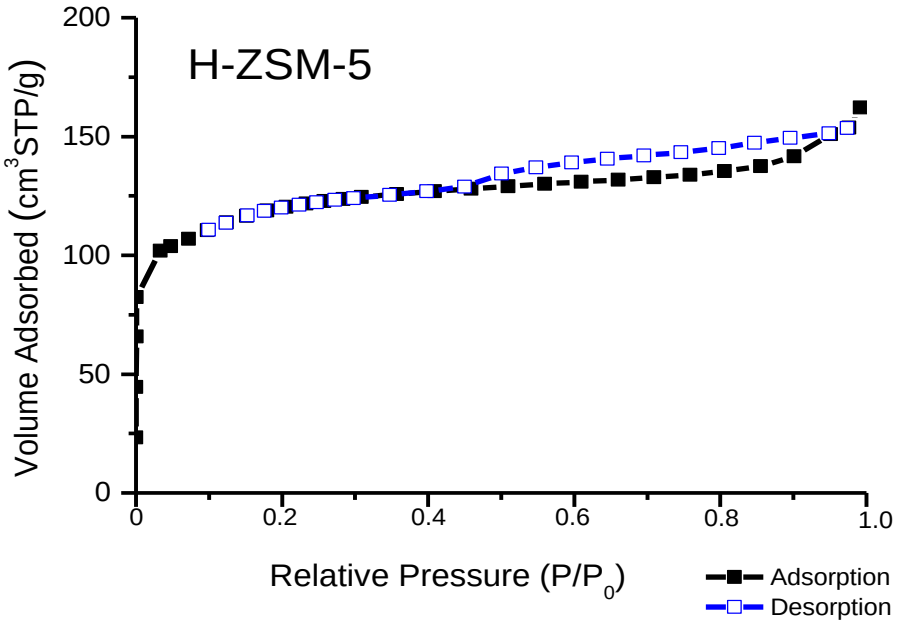

Figure 4. 33: Adsorption Isotherm of H-ZSM-5

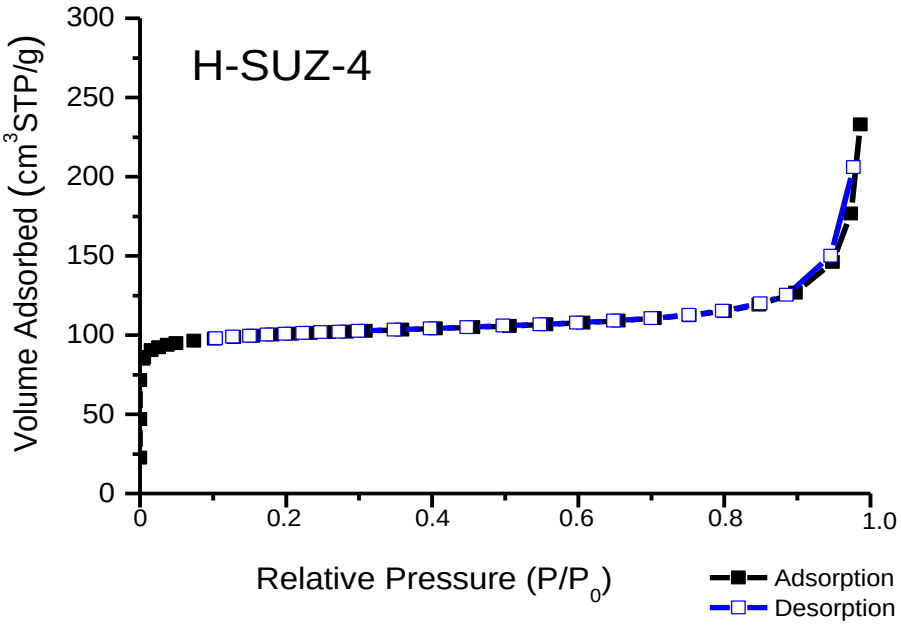

Figure 4. 34: Adsorption Isotherm of H-SUZ-4. Experiment performed by S. Etemadi [2].

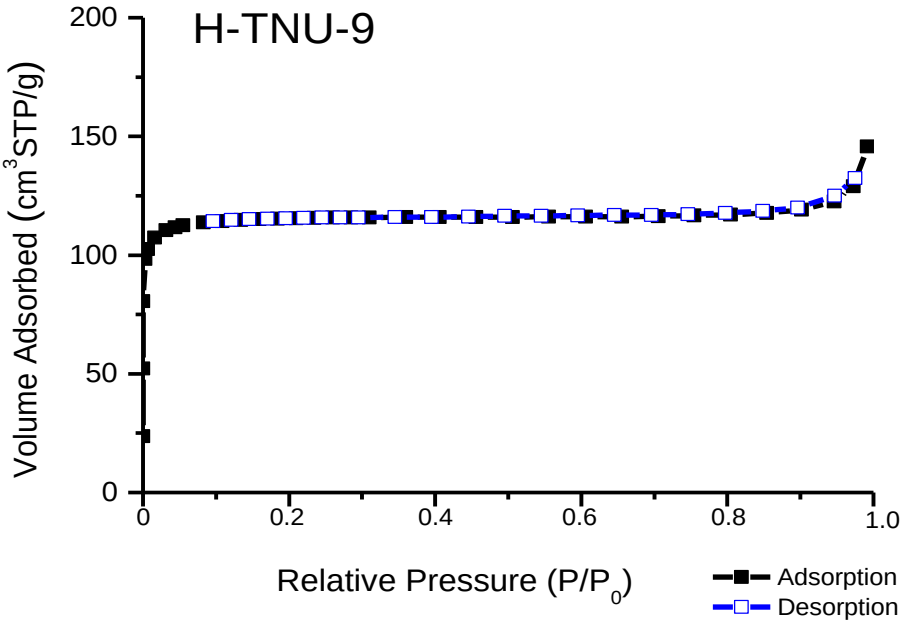

Figure 4. 35: Adsorption Isotherm of H-TNU-9.

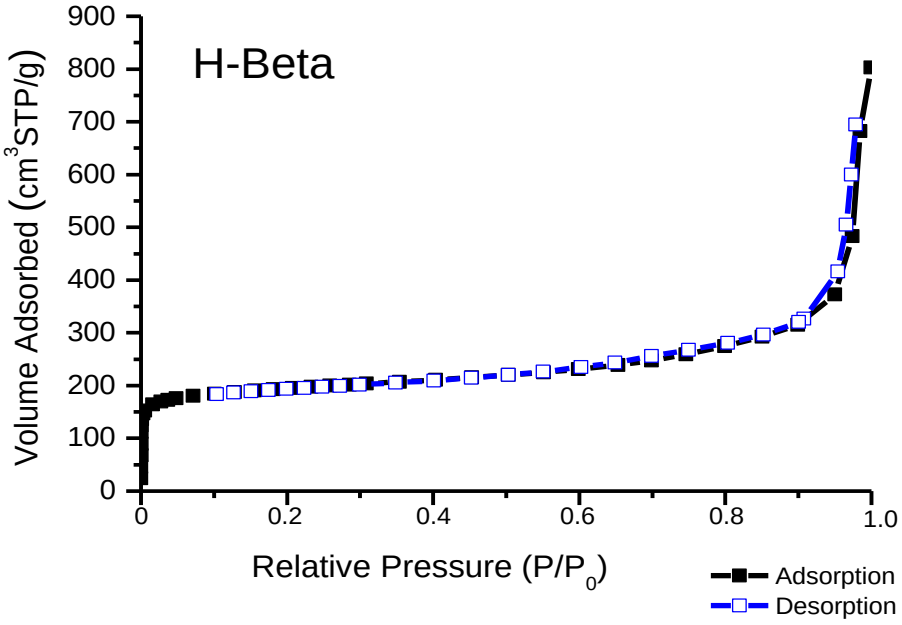

Figure 4. 36: Adsorption Isotherm of H-Beta. Experiment performed by S. Etemadi [2].

As already explained in section 2.1.3, adsorption isotherm can be plotted $p_{rel}/v_{ads}(1-p_{rel})$ against p_{rel} (p/p_0), and linear relationship can be found in lower range of p_{rel}. Specific BET

surface area reported in Table 4. 2 are based on the BET-plots. One of the plots is shown in Figure 4. 37 as an example:

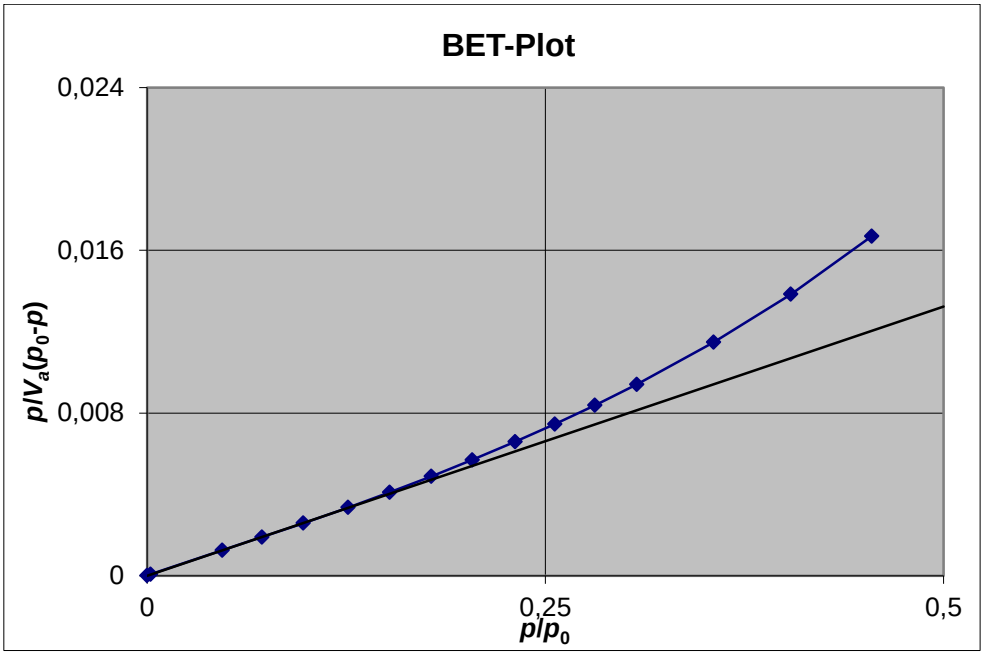

Figure 4. 37: BET plot of H-ZSM-23

Specific BET surface areas measured in this work are in quite good agreement with the values which have been reported [15, 82-85]. Among 12 samples, H-Beta has a largest specific BET surface area and H-ZSM-23 has smallest specific BET surface area. Specific BET surface area of H-Beta is 4 times larger than that of H-ZSM-23. From the H-Beta to H-ZSM-23, the specific BET surface area decreases in order of: H-Beta >> H-Mordenite > H-IM-5 > H-MCM-22 > H-ITQ-13 > H-ZSM-5 > H-Pentasil > H-TNU-9 > H-MFI-27 > H-SUZ-4 > H-ZSM-22 > H-ZSM-23. It is worth noting that the specific BET surface area of H-ZSM-23 sample is extremely low compare to that of other samples. Specific BET surface area for the same H-ZSM-23 sample (Zeolyst, Si/Al =23) reported by Teketel et al. [86] was 115 m^2/g which is even slightly lower than the value measured in this work.

Table 4. 2: Surface Area calculated from BET equation and from other literatures.

		Specific BET Surface Area (m^2g^{-1})	Specific BET Surface Area from other literatures (m^2g^{-1})
MTT	H-ZSM-23	165	115 [15]
TON	H-ZSM-22	217	196 [15]
MOR	H-Mordenite	523	384-485 [84]
MWW	H-MCM-22	479	400, 505 [83]
IMF	H-IM-5	489	425 [82]
ITH	H-ITQ-13	461	413 [82]
MFI	H-MFI-27	419	416 [82]
	H-Pentasil	429	
	H-ZSM-5	431	
SZR	H-SUZ-4	374	346 [15]
TUN	H-TNU-9	424	468 [82]
*BEA	H-Beta	713	608 [85]

4.2 Spectroscopic Investigation

4.2.1 FTIR on zeolites using CO as a probe molecule

For the convenience, the graph of CO adsorption spectra is divided into four parts. Lower-left (1), lower-right (2), upper-left (3), and upper-right (4) parts. Left parts show spectra between 3050 and 3800 cm^{-1} where one can get information of ν(OH). Right parts consist of spectra between 2075 and 2245 cm^{-1} with information from carbon monoxide species. Lower part of graphs is focused on changing in bridging hydroxyl groups while upper parts are focused on changing in silanol groups. It should be noted that the scale in the left side of graph, (1) and (3), and the right side of graph, (2) and (4), are different in each plot.

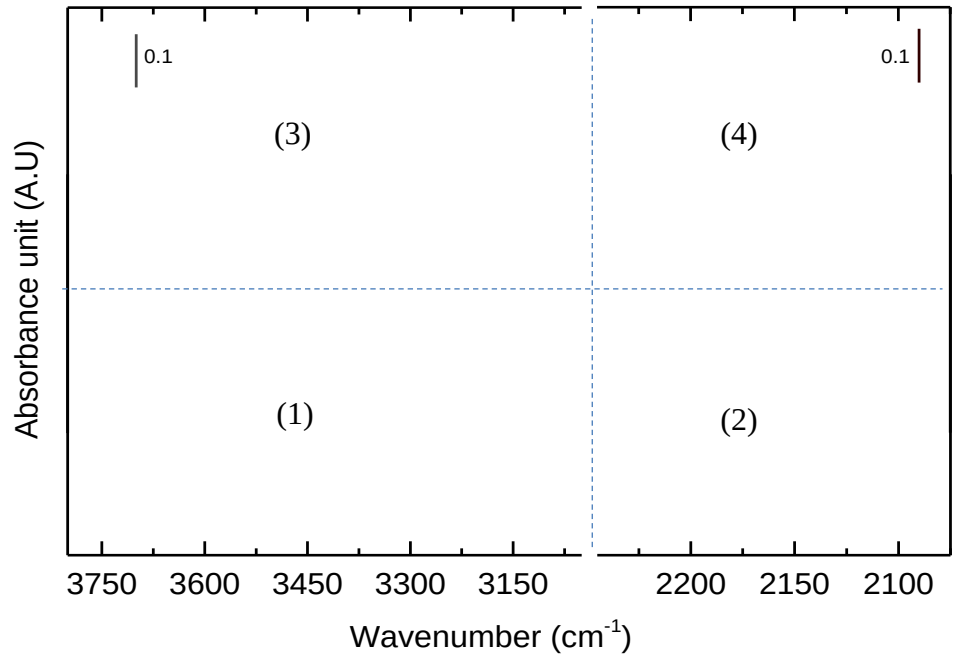

Figure 4. 38: Composition of plots for CO adsorption experiment.

In all plots, red curve is spectrum of the activated clean zeolite sample. Here, clean means 'before contact with carbon monoxide'. As the dosage of the CO increases, the color of spectrum gets darker, and it will become eventually black curve representing the spectrum recorded under maximum dosage of CO.

H-ZSM-23

Spectra recorded during CO adsorption experiment on H-ZSM-23 zeolite are shown in Figure 4. 39. From the red spectrum in the region (1), which is from the activated clean zeolite, silanol and bridging Brønsted acid site peaks are observed at ~3748 cm^{-1} and ~3610 cm^{-1}, respectively. One can see that the silanol band (~3749 cm^{-1}) is asymmetric, tailed towards the lower wavenumber. It is attributed to different silanol groups, isolated and terminal ones. Sharp peak at ~3749 cm^{-1} is for isolated silanols while the tail is because of existence of terminal silanols. A small peak at ~3665 cm^{-1} is assigned to the hydroxyl groups attached to partially EFAl [50].

When interacting with CO, the hydroxyl groups are pertubated. In region (1), one can observe that the bridging Brønsted acid sites band at ~3610 cm^{-1} erodes while a new band at

~3290 cm^{-1} appears ($\Delta\bar{\nu}$ = -320 cm^{-1}). This band has a shoulder at ~3396 cm^{-1}. Assignment of this shoulder is rather controversy. According to Zecchina et al., the shoulder appears because the hydroxyl species on partially EFAl at ~3665 cm^{-1} are pertubated by interaction with CO ($\Delta\bar{\nu}$ = -269 cm^{-1}) [50]. However, there are others who do not agree with them. Knözinger and Huber observed the shoulder appearing on samples where partially EFAl species obviously did not exist at a detectable level. They proposed that the shoulder band is due to heterogeneity of Brønsted acid site where heterogeneity is attributed to inhomogeneous distribution of Al resulting in locally Si/Al ratios different from the average value [51]. Chakarova and Hadjiivanov suggested that split of the shifted OH modes is a Fermi-resonance with the second excited state of δ(OH) which is expected slightly above 3300 cm^{-1} [87]. Because of complexity of the assignment, this shoulder will not be discussed further in depth.

As hydroxyl groups in region (1) are pertubated, new bands at region (2) appear as well. CO forms hydrogen bond with bridging Brønsted acid sites, and the ν(CO) band appears at ~2175 cm^{-1} ($\Delta\bar{\nu}$ = +32 cm^{-1}, compare to CO in gas phase, 2143 cm^{-1}). After hydroxyl group in Brønsted acid sites were consumed in maximum quantity, silanol groups started to get consumed. In region (3), we see that silanol band at ~3748 cm^{-1} got pertubated to lower wavenumber ~3660 cm^{-1} (($\Delta\bar{\nu}$ = -88 cm^{-1}). Decrease of silanol band, though, is very little. Simultaneously, CO adsorbed on silanols shows blue shift to ~2157 cm^{-1} ($\Delta\bar{\nu}$ = +14 cm^{-1}, region (4)).~ 2138 cm^{-1} band is assigned to physisorbed CO inside the zeolite channels [88].

It is noticeable that the band at ~3610 cm^{-1} was not fully eroded during the experiment. It shows that there were bridging Brønsted acid sites which were not consumed upon dosing of CO. There are two possible explanations for this: 1) Either dosage of CO was not enough to interact with all Brønsted acid sites or 2) There are Brønsted acid sites not accessible to CO. Since silanols band started to erode after certain amount of Brønsted acid sites were consumed, 1) has weaker argument. Moreover, we observed that there are certain amounts of Brønsted acid sites not accessible to pyridine under pyridine adsorption experiment. If there is bridging hydroxyls not accessible to CO, they are surely not accessible to pyridine. So, the explanation 2) seems more plausible for now, but further investigation is needed for more concrete explanation.

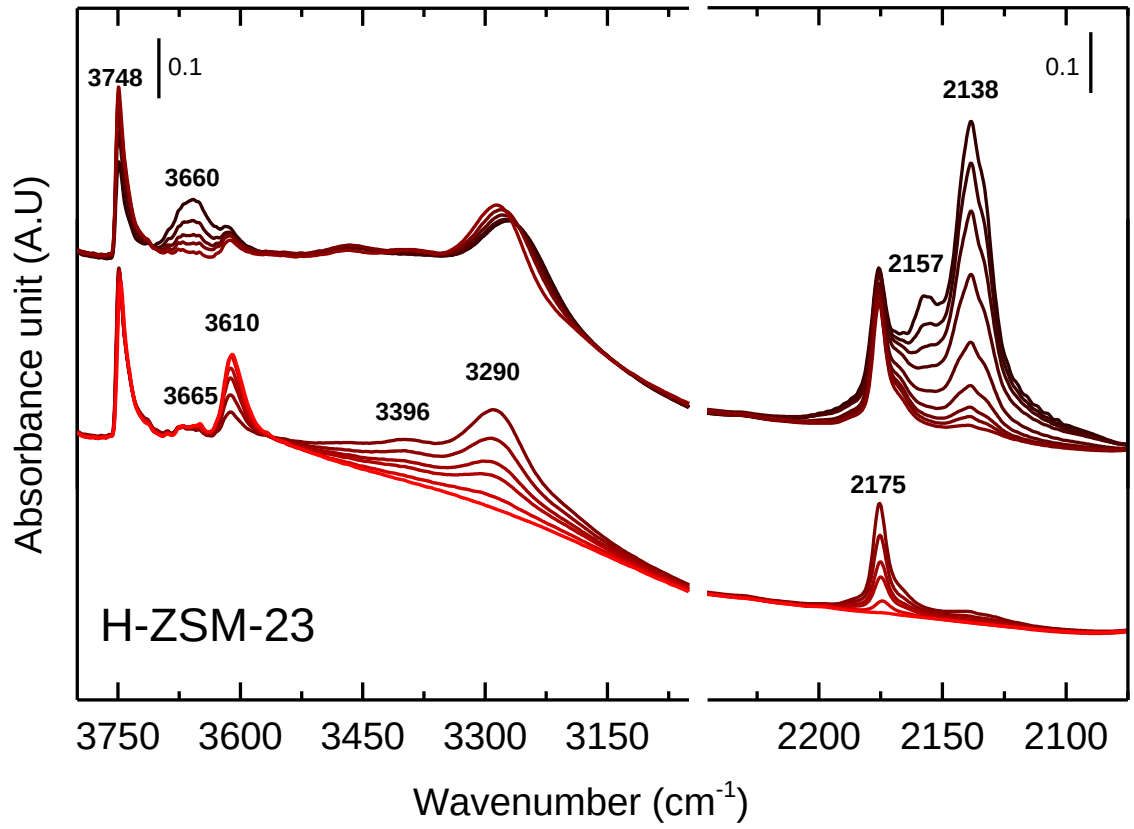

Figure 4. 39: FT-IR spectra of increasing dosages of CO on H-ZSM-23

H-ZSM-22

The recorded spectra of H-ZSM-22 zeolite upon CO adsorption are not much different from that of H-ZSM-23. ν(OH) modes of silanols and bridging Brønsted acid sites appear at ~3747 and ~3605 cm^{-1}, respectively. The existence of hydroxyl species attached to partially EFAl which might be a band at ~3673 cm^{-1} is difficult to confirm because of broad silanol band. Again, broad silanol band, tailed towards lower wavenumber, is due to the terminal silanol groups. Upon CO adsorption, ν(OH) modes from hydroxyl species in bridging Brønsted acid sites were shifted to ~3290 cm^{-1} ($\Delta\bar{\nu}$ = -315 cm^{-1}) while ν(CO) showed blue-shift to ~2175 cm-1 ($\Delta\bar{\nu}$ = +32 cm^{-1}). Afterwards, silanol band got consumed showing red-shift to ~3649 cm^{-1} ($\Delta\bar{\nu}$ = -98 cm^{-1}) with shoulder at ~3567 cm^{-1}, and CO adsorbed on silanols appeared as a band at ~2156 cm^{-1} ($\Delta\bar{\nu}$ = +13 cm^{-1}). This ~3567 cm^{-1} shoulder is due to the pertubated terminal silanols. Broader silanol band in H-ZSM-22 sample compare to that in, for example, H-MCM-22 implies that there are more terminal silanols existing relative to isolated silanols

in H-ZSM-22 which results in rising of shoulder at ~3567 cm^{-1}. This shoulder is often observed from the samples with broad silanol band.

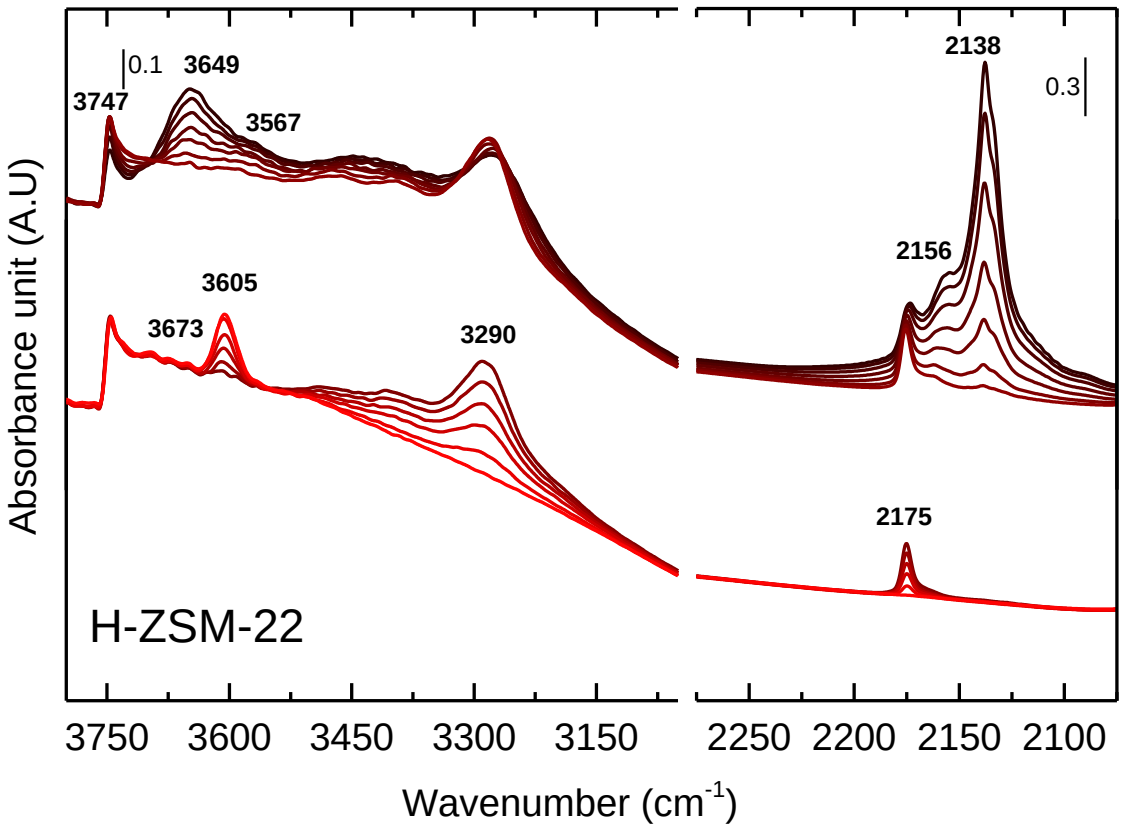

Figure 4. 40: FT-IR spectra of increasing dosages of CO on H-ZSM-22

H-Mordenite

For the case of H-Mordenite, Brønsted acid sites showed shift from ~3610 cm^{-1} to ~3300 cm^{-1} ($\Delta\bar{\nu}$ = -310 cm^{-1}) followed by silanol band shift, from ~3747 cm^{-1} to ~3645 cm^{-1} ($\Delta\bar{\nu}$ = -102 cm^{-1}) with shoulder at ~3580 cm^{-1} due to terminal silanols. A Band for CO adsorbed on Brønsted acid sites is observed at ~2176 cm^{-1} ($\Delta\bar{\nu}$ = +33 cm^{-1}) while that for CO adsorbed on silnols is at ~2156 cm^{-1} ($\Delta\bar{\nu}$ = +13 cm^{-1}). There is also a small band at ~3688 cm^{-1} showing existence of OH species attached to partially EFAl.

There are two new features observed in H-Mordenite compare to previous two samples, H-ZSM-23 and H-ZSM-22. First, a weak band at ~2225 cm^{-1} is observed (Inset of Figure 4. 41).

This band is normally assigned to CO adsorbed on strong Lewis acid sites even though exact species and structures associated are yet fully revealed [50, 88-91]. Another special feature of the H-Mordenite is asymmetric ν(OH) band of bridging Brønsted acid sites at ~3610 cm^{-1}. There is a tail towards the lower wavenumber. This asymmetric band implies that H-Mordenite has two different types of Brønsted acid sites exist in the zeolite. The band can be deconvoluted into two separate ones as in Figure 4. 42, one with the maxima at ~3612 cm^{-1} and another with the maxima at ~3584 cm^{-1}. It was previously reported that the band at higher wavenumber is generated by OH groups in 12-ring channels, and the band at lower wavenumber is component by OH groups in the 8-ring channels [88, 92, 93]. This is because hydroxyl groups in 6- or 8-rings experience a red-shift due to electrostatic interaction with nearest oxygen atoms, and therefore the interaction inversely proportional to the average of the square distances [94, 95]. Upon CO dosing, new bands at ~3300 cm^{-1} and ~3450 cm^{-1} appeared as asymmetric ~3610 cm^{-1} band eroded. ~3300 cm^{-1} band is already assigned to pertubated hydroxyls in Brønsted acid sites, and the ~3450 cm^{-1} is the one with different assignments from different groups. It might be tempting to assign both peaks for pertubated OH groups in two different channels, but it is not that straightforward. First of all, they are too far away from each other considering that ~3610 cm^{-1} band appeared only as asymmetric band, not double. Moreover, ~3450 cm^{-1} band was absent in the experiment performed by Bordiga et al.[88] even though the Brønsted acid band could be deconvoluted into two resolved components. Based on this observation, it is very unlikely that ~3450 cm^{-1} band is originated from OH groups in 8- or 12-ring channels. Therefore, the band holds the complex discussion regarding the assignment. The ~3300 cm^{-1} band may have two components, but their detailed silhouettes are hidden behind the broadness of the band [88]. Regarding CO band at ~2176 cm^{-1}, asymmetric band is observed. However, Bordiga et al.[88] do not think that this assymetry is due to CO adsorbed on different OH groups becuase i) maxima of the band varies slightly depending on CO equilibrium pressure ii) pertubation of ν(CO) is not sensitive enough to discriminate between two types of bridging OH groups.

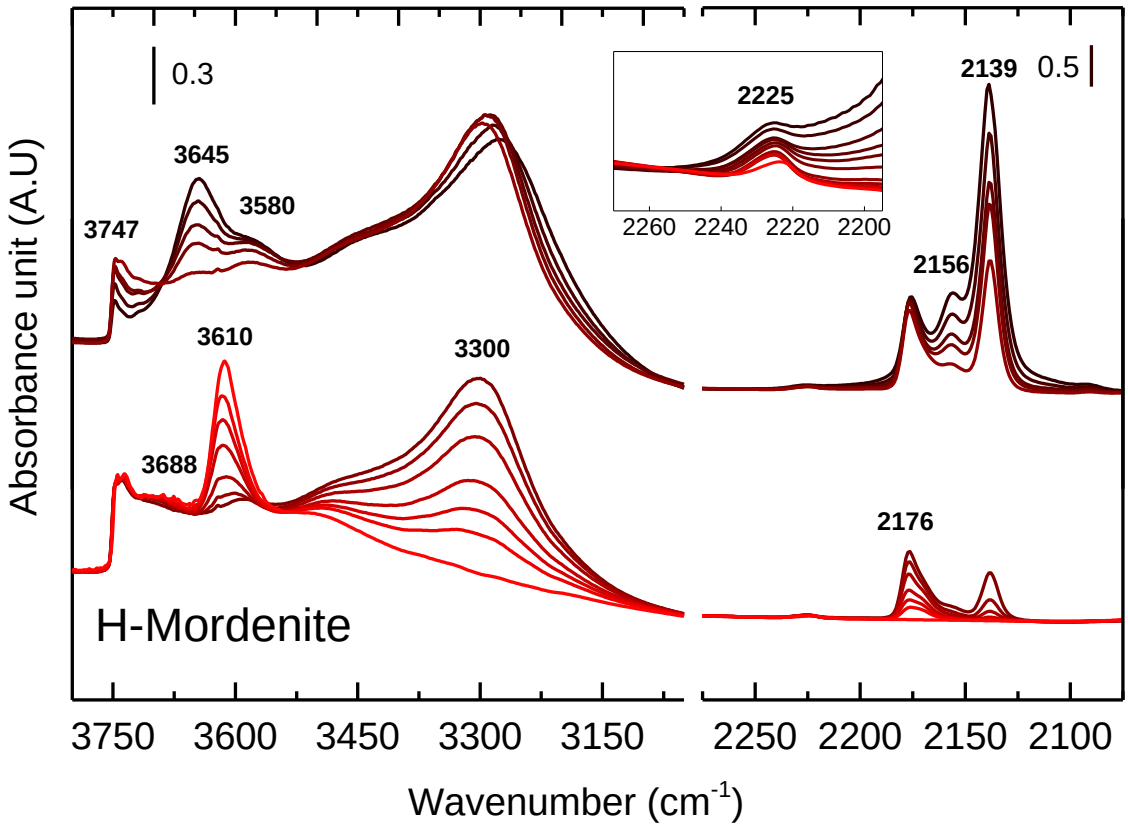

Figure 4. 41: FT-IR spectra of increasing dosages of CO on H-Mordenite. Experiment performed by S. Etemadi [2]

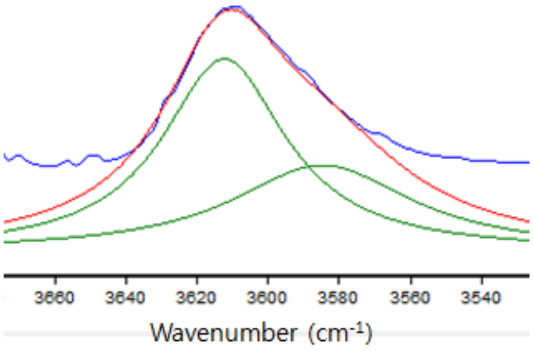

Figure 4. 42: Deconvolution of ~3610 cm^{-1} band using OPUS 7.0 by Bruker Optik GmbH. Blue curve is recorded spectrum of clean and activated H-Mordenite zeolite, green curves are two bands composing ~3610 cm^{-1} band, and red curve is the combination of two red bands.

H-MCM-22

H-MCM-22 has band from hydroxyl groups in silanol at ~3752 cm^{-1}, from hydroxyls in bridging Brønsted acid sites at ~3627 cm^{-1}. A small band for OH species attached to partially EFAl is at ~3672 cm^{-1}. When CO was injected and adsorption occured, Brønsted acid sites was consumed first, and this is shown as pertubated band at ~3303 cm^{-1} ($\Delta\bar{\nu}$ = -324 cm^{-1}). Simultaneously, CO shows blue shift to ~2175 cm^{-1} ($\Delta\bar{\nu}$ = +32 cm^{-1}). After all the Brønsted acid site was consumed, silanol started to get consumed. The silanol band was pertubated to ~3650 cm^{-1} ($\Delta\bar{\nu}$ = -102 cm^{-1}). Since the amount of silanol band interacting with CO, assumed from the band intensity, is little, the band for CO adsorbed on silanol is not easy to detect. However, one can see the small shoulder around ~2158 cm^{-1}, and it is reasonable to assign this to the CO adsorbed on silanol ($\Delta\bar{\nu}$ = +15 cm^{-1}). From the inset of Figure 4. 43, one can confirm the existence of Lewis acid sites.

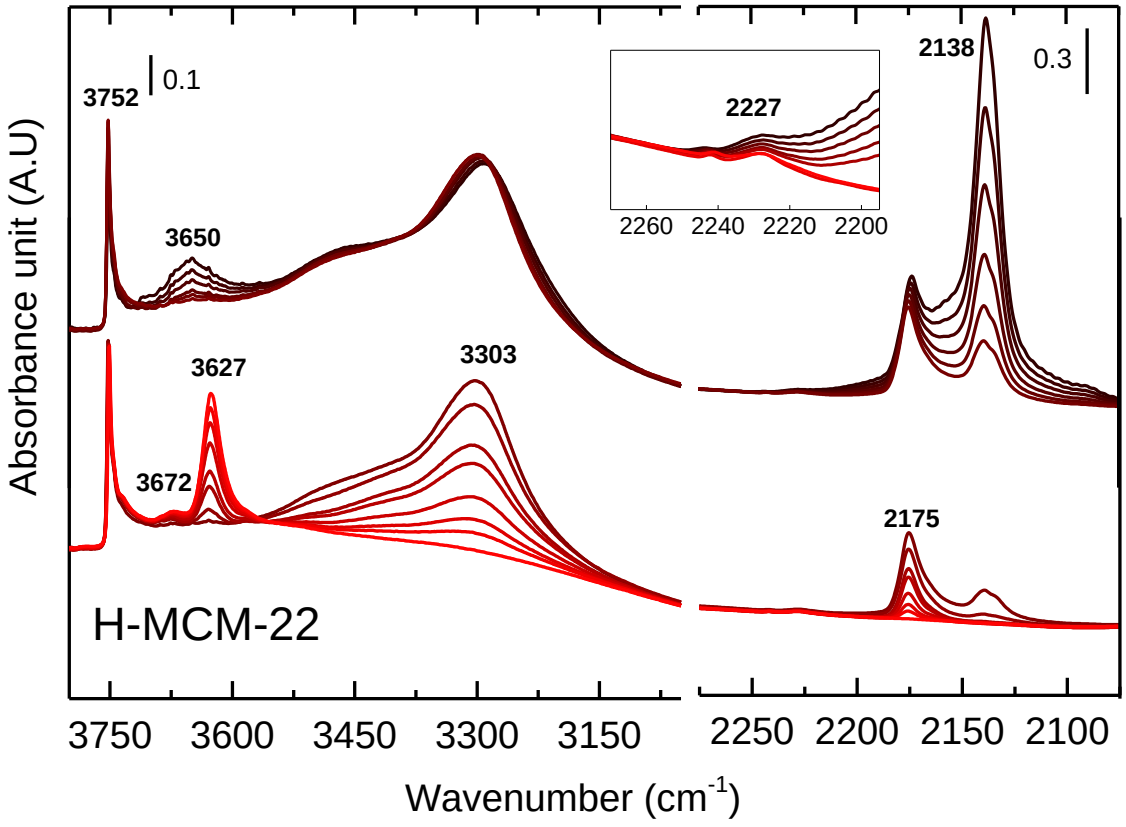

Figure 4. 43:FT-IR spectra of increasing dosages of CO on H-MCM-22

H-IM-5

A clean activated H-IM-5 possesses hydroxyl group from silanol (~3749 cm^{-1}), from bridging Brønsted acid sites (~3615 cm^{-1}), and OH groups attached to partially EFAl (~3672 cm^{-1}). Upon interaction with CO, red shifts of hydroxyl groups were observed. First, as ~3615 cm^{-1} band eroded, a new band at ~3302 cm^{-1} appeared ($\Delta\bar{\nu}$ = -313 cm^{-1}). Corresponding CO stretching band is at ~2175 cm^{-1} ($\Delta\bar{\nu}$ = +32 cm^{-1}). After all Brønsted acid sites interacted with CO, silanol got to interact with CO showing pertubation band at ~3652 cm^{-1} ($\Delta\bar{\nu}$ = -97 cm^{-1}). A weak band at ~2157 cm^{-1} is for the CO adsorbed on silanol groups ($\Delta\bar{\nu}$ = +14 cm^{-1}).

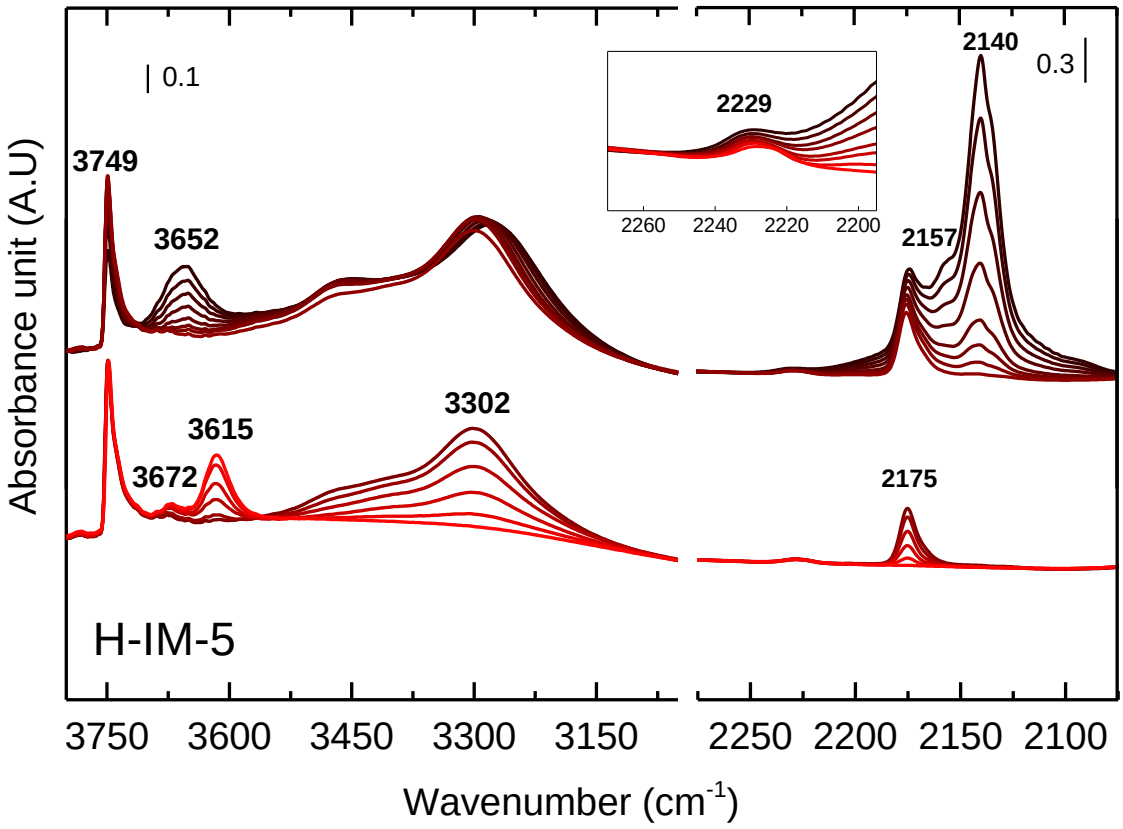

Figure 4. 44: FT-IR spectra of increasing dosages of CO on H-IM-5

H-ITQ-13

Compare to previous samples, it is noticeable that amount of Brønsted acid sites exist in the H-ITQ-13 sample is very little (band at ~3619 cm^{-1}). Comparably, there are quite amount of silanols (~3739 cm^{-1}). A very weak band at ~3670 cm^{-1} can be assigned to the OH groups

attached to the partially EFAl eixst. When CO was introduced to the system, little amount of Brønsted acid sites was consumed first. The stretching vibration of OH appeared at the lower wavenumber, ~3314 cm^{-1} ($\Delta\bar{\nu}$ = -305 cm^{-1}). Since it was very little Brønsted acid sites to interact, equilibrium pressure of CO in the system after all Brønsted acid sites was consumed was low. Band at ~2175 cm^{-1} grew as ~3619 cm^{-1} band eroded, and this band is assigned to CO adsorbed on Brønsted acid sites ($\Delta\bar{\nu}$ = +32 cm^{-1}). As CO equilibrium pressures increased further, quite large portion of silanols were consumed, and the band at ~3646 cm^{-1} appeared ($\Delta\bar{\nu}$ = -93 cm^{-1}). Simultaneously, the band at ~2156 cm^{-1} grew for CO adsorbed on silanols ($\Delta\bar{\nu}$ = +13 cm^{-1}). Because the degree of erosion in silanol band is much larger than that in Brønsted acid sites, the ~2156 cm^{-1} band is higher than ~2175 cm^{-1} band at highest dosage of CO.

In fact, ITH zeolites have heterogeneous acid sites since it has 10- and 9-ring channels. Because of small bridging Brønsted acid band and its perturbation band, however, observation of the heterogeneity from these bands is difficult.

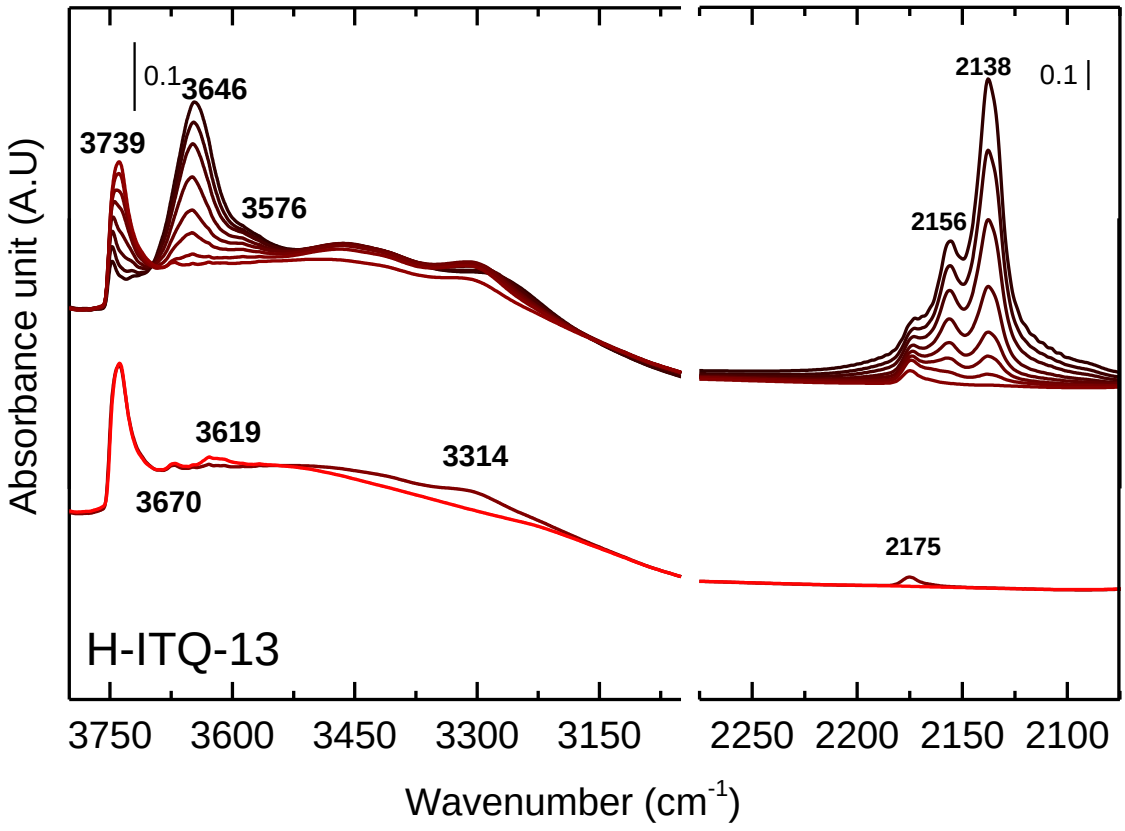

Figure 4. 45: FT-IR spectra of increasing dosages of CO on H-ITQ-13

H-MFI-27

In contrast to the case of H-ITQ-13, H-MFI-27 has very little amount of silanols (~3748 cm^{-1}) but quite large amount of Brønsted acid sites (~3617 cm^{-1}). There is also a little trace of OH-EFAl species at ~3674 cm^{-1}. With CO, Brønsted acid sites first got consumed and the Brønsted band was shifted from ~3617 cm^{-1} to ~3311 cm^{-1} ($\Delta\bar{\nu}$ = -306 cm^{-1}). Corresponding CO stretching appeared at ~2174 cm^{-1} ($\Delta\bar{\nu}$ = +31 cm^{-1}). After all Brønsted band was consumed, silanol was started to get consumed. However, since the intensity of the original band is weak and the amount consumed is not much either, pertubation band appeared very weak at ~3640 cm^{-1} ($\Delta\bar{\nu}$ = -108 cm^{-1}). There is no detectable band around 2155-2160 cm^{-1} which is assigned to stretching mode of CO adsorbed on silanols. This is due to very little amount of silanol consumed as well.

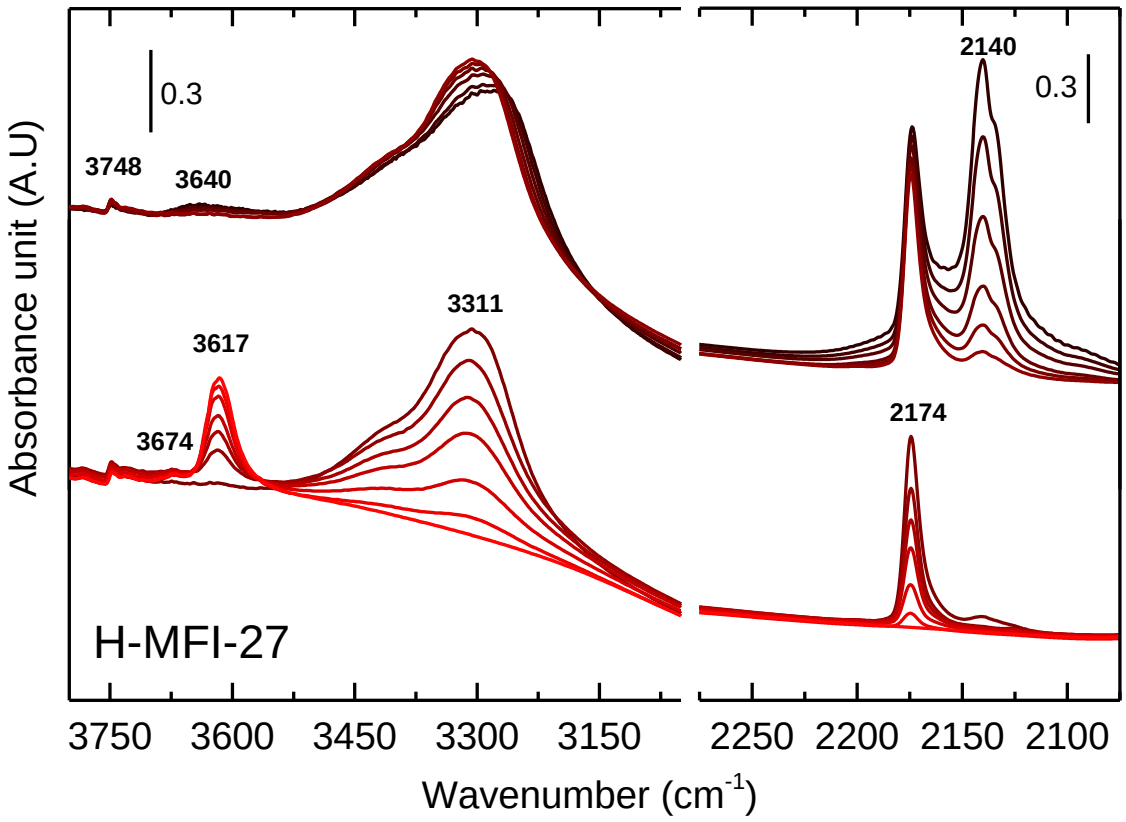

Figure 4. 46: FT-IR spectra of increasing dosages of CO on H-MFI-27.

H-Pentasil

The first thing one can notice from Figure 4. 47 is that H-Pentasil shows more intense silanol band at ~3749 cm^{-1} compare to H-MFI-27 sample. There is a bridging Brønsted acid band at ~3618 cm^{-1}, and OH stretching band for partially EFAl species at ~3666 cm^{-1}. Upon CO dosing, Brønsted acid sites band was pertubated to ~3305 cm^{-1} ($\Delta\bar{\nu}$ = -313 cm^{-1}), and corresponding CO stretching band is found at ~2175 cm^{-1} ($\Delta\bar{\nu}$ = +32 cm^{-1}). Once all Brønsted acid sites was consumed, silanol started to get consumed, and the pertubated OH stretching band appeared at ~3660 cm^{-1} ($\Delta\bar{\nu}$ = -89 cm^{-1}). Corresponding CO stretching is at ~2156 cm^{-1} ($\Delta\bar{\nu}$ = +13 cm^{-1}). Quite large amount of silanol got consumed upon interaction with CO.

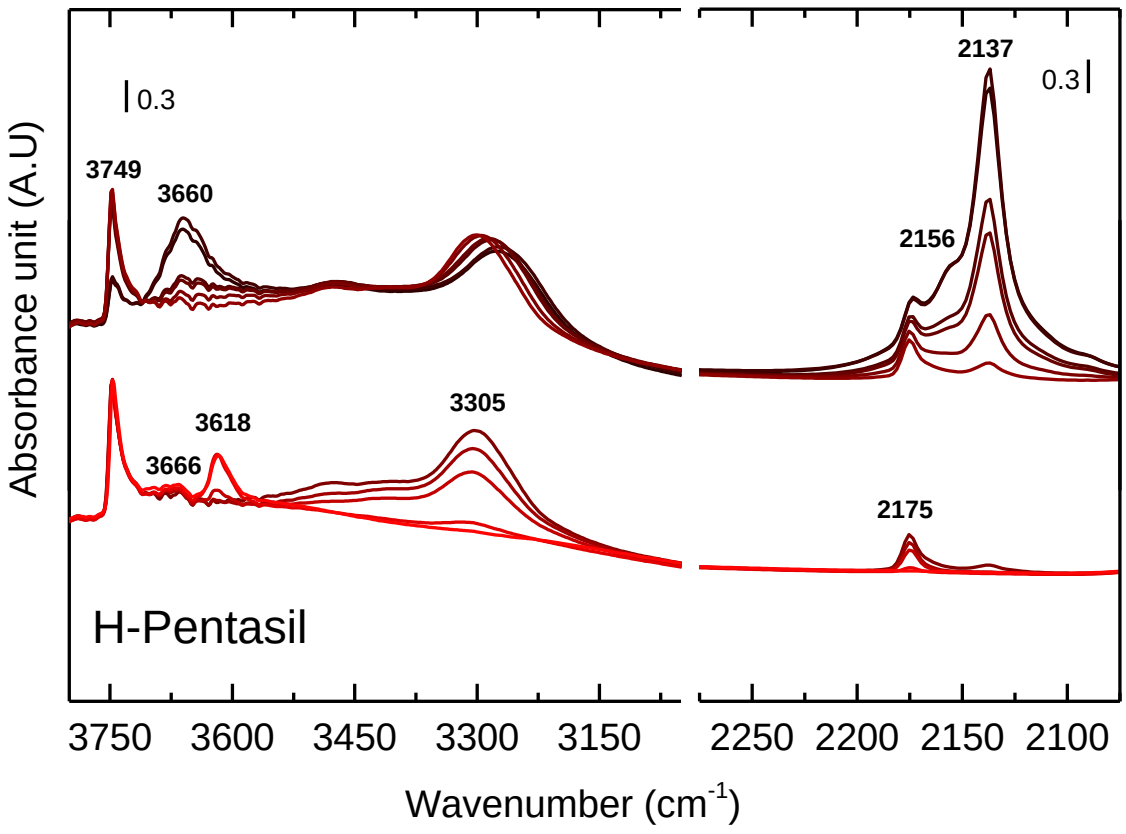

Figure 4. 47: FT-IR spectra of increasing dosages of CO on H-Pentasil. Experiment performed by S. Etemadi [2]

H-ZSM-5

Upon CO adsorption, ν(OH) band of Brønsted acid sites was shifted from ~3619 cm^{-1} to ~3314 cm^{-1} ($\Delta\bar{\nu}$ = -305 cm^{-1}) and corresponding CO band was blue-shifted to ~2175 cm^{-1} ($\Delta\bar{\nu}$ = +32 cm^{-1}). Quite amount of broad silanol band at ~3746 cm^{-1} was consumed as dosage of CO became higher. Shifted band is observed at ~3646 cm^{-1} ($\Delta\bar{\nu}$ = -100 cm^{-1}) with shoulder ~3565 cm^{-1}. Pertubated band at ~3646 cm^{-1} is originated from isolated silanols while shoulder at ~3565 cm^{-1} is originated from terminal silanols. Blue-shifted CO band because of interaction with silanol can be found at ~2155 cm^{-1} ($\Delta\bar{\nu}$ = +12 cm^{-1}).

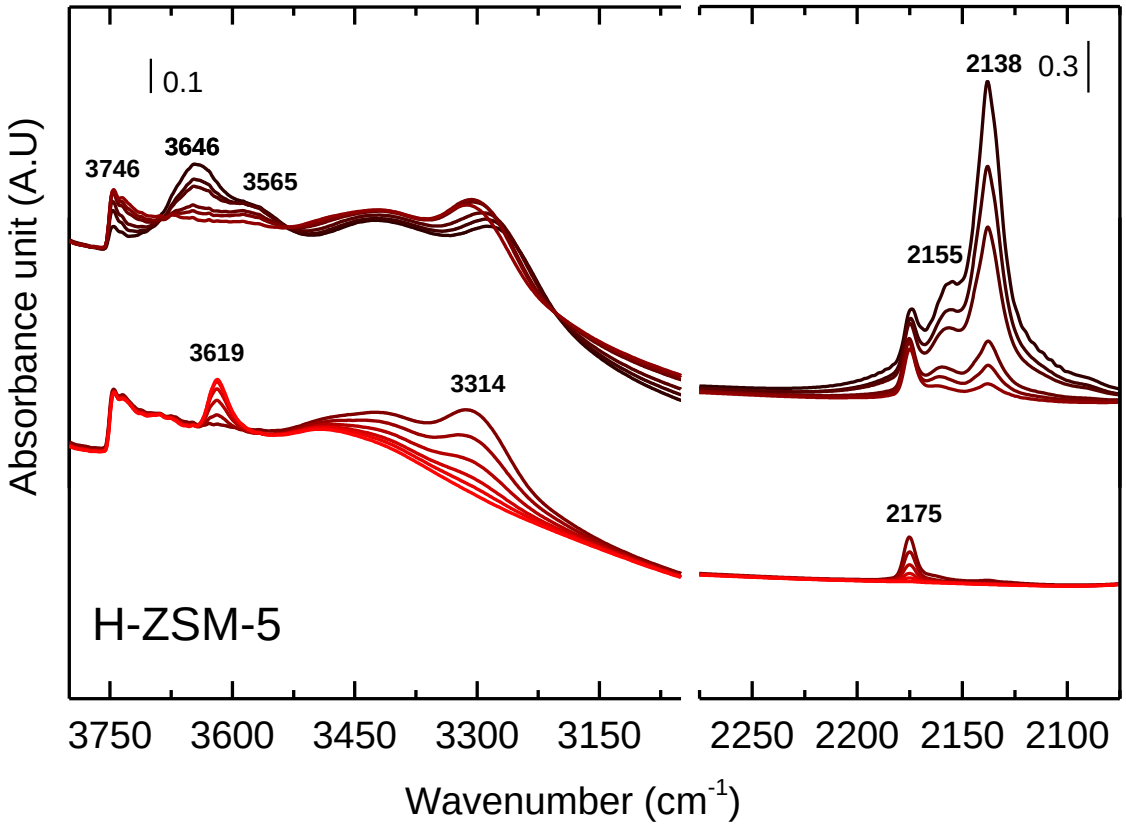

Figure 4. 48: FT-IR spectra of increasing dosages of CO on H-ZSM-5

H-SUZ-4

H-SUZ-4 shows very different bridging Brønsted acid band than all the other samples investigated in this work. It shows clear doublet in the band, and this double is also seen from the pertubated bands. There are two explanations which can possibly explain this: 1)

Heterogeneity of acid sites in SUZ-4 sample 2) Existence of OH-EFAl species. If it is because of the Heterogeneity of acid sites, the doublet can be assigned to OH groups in 10-ring channels (~3651 cm^{-1}) and 8-ring channels (~3613 cm^{-1}), respectively. As discussed earlier for H-Mordenite, band of ν(OH) in small rings such as 8- or 6-rings appears at lower frequency because of electrostatic interaction with the nearest oxygen atoms [94-96]. However, Zholobenko et al.[96] did not observe clear double from the spectra of clean, activated SUZ-4 sample with Si/Al = 6.2. Moreover, they deconstructed OH band of bridging Brønsted acid sites, and got three IR bands at 3565, 3592, and 3610 cm^{-1} which are assigned to OH groups in 6-, 8-, and 10-membered ring, respectively. ~3651 cm^{-1} band is at too high wavenumber to be assigned to the OH groups in 10-ring channels considering experiment result from Zholobenko et al [96]. It makes more sense to assign the ~3651 cm^{-1} band to OH-EFAl species. OH groups in different ring channels may overlap and appear as a band at ~3613 cm^{-1}. Because of high intensity neighbouring OH-EFAl band, it is not easy to see the asymmetry or to deconvolute the ~3613 cm^{-1} band for further analysis in order to investigate heterogeneity of acid sites.

Upon CO adsorption, two new bands appeared as ~3651 and 3613 cm^{-1} band eroded. From the pattern of development of the bands, we can see that ~3317 cm^{-1} band is from pertubated species which originally gave rise to the band at ~3613 cm^{-1} ($\Delta\bar{\nu}$ = -296 cm^{-1}), and ~3483 cm^{-1} is from pertubated OH groups attached to EFAl species. In a same way, from the development pattern of the bands, we can identify that CO adsorbed on Brønsted acid sites gives rise to the ~2173 cm^{-1} band ($\Delta\bar{\nu}$ = +30 cm^{-1}) while CO adsorbed on OH-EFAl species gives rise to the 2163 cm^{-1} band.

Silanols in this sample, as well as in other samples, started to get consumed after Brønsted acid site band was fully eroded. Not all silanols were consumed upon introduction of CO, but some of them interacted with CO resulting in appearance of pertubated ν(OH) band at ~3650 cm^{-1} ($\Delta\bar{\nu}$ = -100 cm^{-1}). Corresponding ν(CO) band is difficult to observe, and it is considered to be shielded by the high intensity bands nearby.

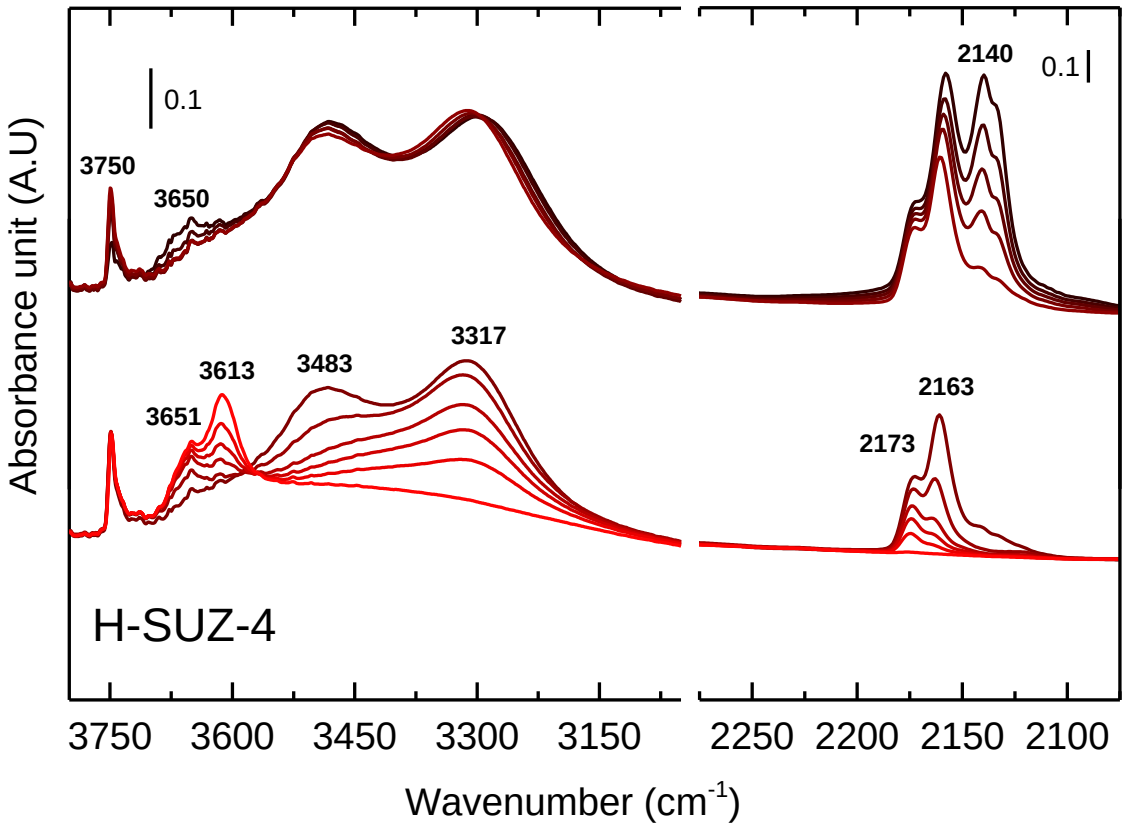

Figure 4. 49: FT-IR spectra of increasing dosages of CO on H-SUZ-4. Experiment performed by S. Etemadi [2]

H-TNU-9

In H-TNU-9, higher intensity of Brønsted acid band (~3618 cm^{-1}) is observed compare to that of silanol (~3749 cm^{-1}). Upon CO interaction, ~3618 cm^{-1} band was shifted to lower wavenumber, ~3297 cm^{-1} ($\Delta\bar{\nu}$ = -321 cm^{-1}), and CO band was shifted to higher wavenumber, ~2175 cm^{-1} ($\Delta\bar{\nu}$ = +32 cm^{-1}). All Brønsted acid sites were consumed and some of silanol got consumed afterwards. The pertubated ν(OH) band of silanol is seen at ~3649 cm^{-1} ($\Delta\bar{\nu}$ = -100 cm^{-1}), and corresponding ν(CO) is at ~2157 cm^{-1} ($\Delta\bar{\nu}$ = +14 cm^{-1}). Existence of ~3670 cm^{-1} and ~2225 cm^{-1} band indicates that there are OH-EFAl species and strong Lewis sites in H-TNU-9, respectively.

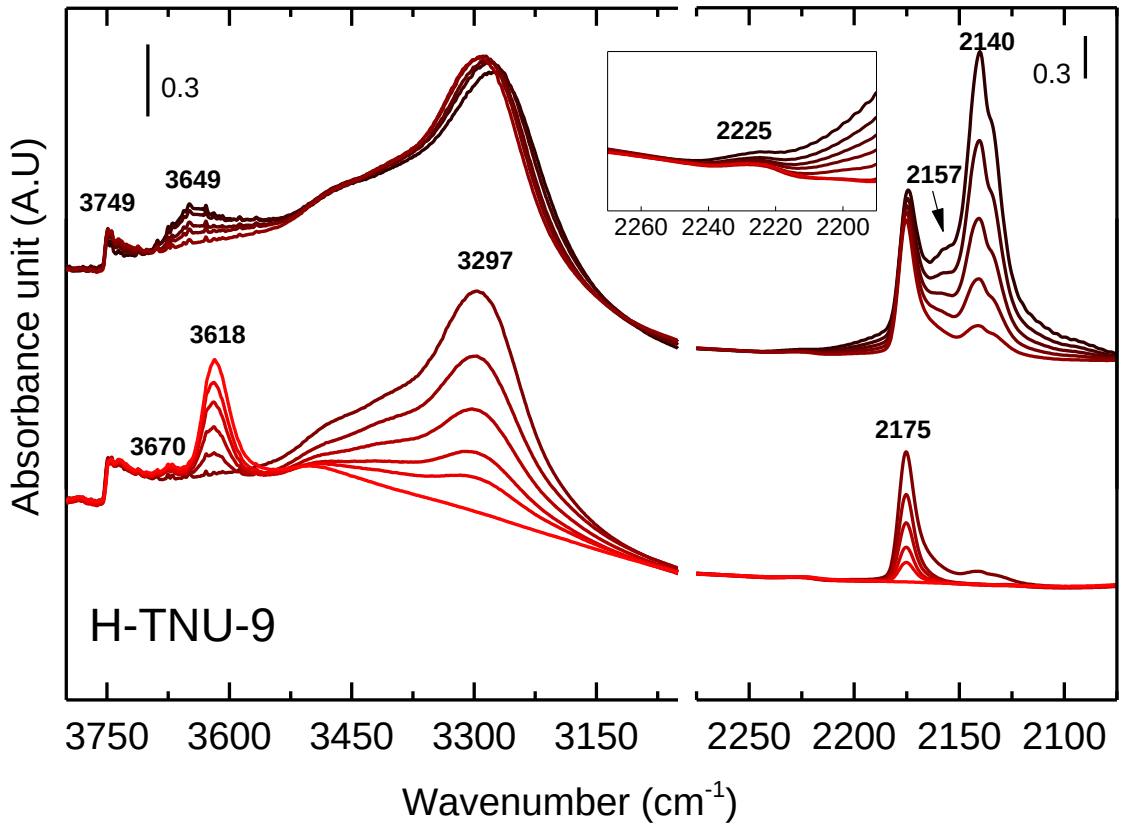

Figure 4. 50: FT-IR spectra of increasing dosages of CO on H-TNU-9

H-Beta

Opposite to H-TNU-9, silanol band at ~3749 cm^{-1} shows much higher intensity compare to Brønsted acid band at ~3611 cm^{-1} in H-Beta. ~3670 cm^{-1} band implies that there are OH-EFAl species in the zeolite sample. When CO was introduced into the system, acid sites started to interact with the molecule. O-H stretching vibration in Brønsted acid sites was pertubated and the experienced red-shift to ~3296 cm^{-1} ($\Delta\bar{\nu}$ = -315 cm^{-1}). CO stretching vibrations underwent blue-shift to ~2176 cm^{-1} ($\Delta\bar{\nu}$ = +33 cm^{-1}). Once all Brønsted acid sites were consumed, then erosion of silanol band started with appearance of a new band at ~3655 cm^{-1}. This can be seen in the region (3) of Figure 4. 51. ~3655 cm^{-1} band is pertubated ν(OH) of silanols ($\Delta\bar{\nu}$ = -94 cm^{-1}). Corresponding CO band is at ~2156 cm^{-1} ($\Delta\bar{\nu}$ = +13 cm^{-1}). ~2228 cm^{-1} band tells us that there are strong Lewis acid sites existing in the H-Beta zeolite.

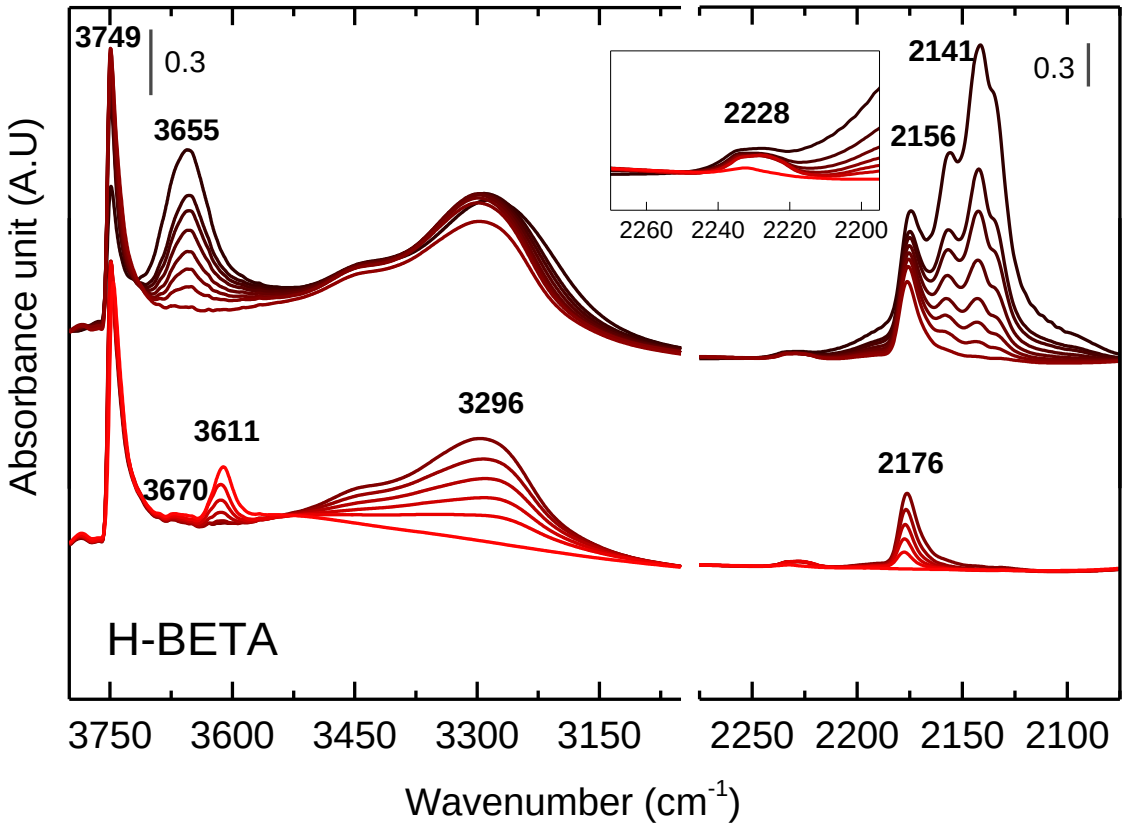

Figure 4. 51: FT-IR spectra of increasing dosages of CO on H-Beta. Experiment performed by S. Etemadi [2]

From Table 4. 3, one can compare acid strength of different zeolites. ν(CO) is less sensitive upon the adsorption of CO than ν(OH) because Δν(CO) varies in much smaller degree than Δν(CO) from zeolite to zeolite. Because of the sensitivity difference, it is common to compare acid strength based on degree of shift of ν(OH) band rather than shift of ν(CO) band. According to degree of red shift of the bands, the of acid strength decreases in following order: H-MCM-22 > H-TNU-9 ≈ H-ZSM-23 > H-ZSM-22 ≈ H-Beta > H-IM-5 ≈ H-Pentasil > H-Mordenite > H-MFI-27 ≈ H-ITQ-13 ≈ H-ZSM-5 > H-SUZ-4. It should be noted that the difference in Δν(OH) values less than 2 cm^{-1} was not considered to be different in acid strength as the resolution of the spectra was 2 cm^{-1}. In other words, it's difficult to say acid strength of H-TNU-9 is stronger than H-ZSM-23 because the difference between their Δν(OH) values (1 cm^{-1}) is smaller than the resolution limit.

Table 4. 3: Shift of ν(CO) and ν(OH_{BA}) band upon adsorption of CO in different zeolites.

		Δν(CO) (cm^{-1})	Δν(OH) (cm^{-1})	ν(OH) (cm^{-1})
MTT	H-ZSM-23	+32	-320	3610 → 3290
TON	H-ZSM-22	+32	-315	3605 → 3290
MOR	H-Mordenite	+33	-310	3610 → 3300
MWW	H-MCM-22	+32	-324	3627 → 3303
IMF	H-IM-5	+32	-313	3615 → 3302
ITH	H-ITQ-13	+32	-305	3619 → 3314
MFI	H-MFI-27	+31	-306	3617 → 3311
	H-Pentasil	+32	-313	3618 → 3305
	H-ZSM-5	+32	-305	3619 → 3314
SZR	H-SUZ-4	+30	-296	3613 → 3317
TUN	H-TNU-9	+32	-321	3618 → 3297
*BEA	H-BETA	+33	-315	3611 → 3296

It is worth noting that the difference in Δν(OH) values between the zeolite with strongest acid strength (H-MCM-22, Δν(OH) = -324 cm^{-1}) and the zeolite with weakest acid strength (H-SUZ-4, Δν(OH) = -296 cm^{-1}) was 28 cm^{-1}. The difference is 10 % of their value. One can argue about whether this is large enough difference to see the clear effect of the acid strength in the reaction that zeolites involve or not. It is difficult to say how much of the difference in Δν(OH) values are large enough for clear comparison of acid strength, but one should be cautious when discuss the acid strength based on the Δν(OH) values.

4.2.2 FTIR on zeolites using pyridine as a probe molecule

Upon adsorption of pyridine on H-form zeolites, most prominent peaks observed are at ~1544, 1490, and 1455 cm^{-1}. The figures presented in this section are mostly focused in the region containing these three bands. ν(OH) region is shown as an inset in order to show the decrease of the bridging OH band and the silanol band.

As mentioned earlier, ~1544 cm^{-1} band is assigned to pyridinium ions adsorbed on Brønsted acid site, and ~1455 cm^{-1} band is assigned to pyridine coordinated to Lewis acid sites [40]. ~1490 cm^{-1} band cannot be assigned to a single site, and it is considered as a combined contribution from pyridinium ion adsorbed on Brønsted acid site and pyridine coordinated to Lewis acid site [97]. Tommy et al.[97] assigned bands at ~1635 and 1621 cm^{-1} to the adsorbed pyridinium ion on Brønsted acid site and pyridine coordinated to Lewis acid site, respectively as well. This is supported by reference [63]. However these two peaks have little relevance to the purpose of pyridine adsorption experiment performed in this work, so they will not be discussed further, and there will be more focus on ~1544 and 1455 cm^{-1} band which are directly related to quantification of acid site density.

In quantification of acid sites using pyridine adsorption technique, a spectrum collected after desorption of pyridine at 150°C is usually used to calculate the total concentration of Brønsted and Lewis acid sites [38, 40, 95, 98]. This is to remove the physisorbed species [95] and pyridine adsorbed on silanol sites as they give rise to the band at ~1439 and 1444 cm^{-1}, respectively. If the contributions from the physisorbed species and pyridine adsorbed on silanol are not excluded, concentration of Lewis acid site would be overestimated, and it is important to remove these species to the maximum extent. In previously studies, 150°C was enough to desorb and remove physisorbed pyridine and pyridine adsorbed on Lewis acid sites from the system [38, 40, 95, 98]. However, 200 °C was needed in our case to exclude the contribution from species other than pyridine interacting with Lewis acid sites. It is because pyridine was flushed with nitrogen for evacuation in this work, while earlier literatures used vacuum line for evacuation of pyridine. Apparently the flushing with nitrogen is less effective than vacuum line, and there were still considerable amount of physisorbed pyridine and pyridine interacting with silanol contributing to the band around 1455 cm^{-1} after evacuation at 150 °C. For example, from the Figure 4. 56, pyridine adsorption experiment results of H-Mordenite, a shoulder at 1444-1440 cm^{-1} still exists after evacuation at 150°C, but the shoulder is not observed in 200°C curve. Moreover, from the concentration plots of Brønsted and Lewis acid, one can observe that extent of decreasing in Lewis acid site concentration from 150°C and 200°C is larger than other intervals. This can interpreted as that much of physisorbed pyridine and pyridine interacting with silanol are desorbed between 150°C and 200°C. Therefore, the temperature spectrum collected after desorption of pyridine at 200°C, instead of 150°C, was chosen for the calculation of total concentration of Brønsted and Lewis acid sites in this work.

One more thing that should be discussed here is Integrated Molar Extinction Coefficient (IMEC). As mentioned earlier, the values of IMEC from different literatures vary in quite large extent [38-49], and different experimental condition is considered for the reason [40]. IMEC values which have been reported are shown in Table 4. 4. To decide which IMEC value has the best fit to our experimental setup, pyridine adsorption experiments on three different MFI samples (H-ZSM-5 and H-MFI-27 which are used in this work, and another ZSM-5 sample from Zeolyst (Si/Al = 25)) were performed twice per sample. Afterwards, the Si/Al ratio was calculated using all values in Table 4. 4 for comparison. It was observed that the calculated Si/Al showed closest values to the theoretical Si/Al when we used the IMEC values (0.73 and 0.64 for 1544 and 1455cm^{-1}, respectively) reported by Selli and Forni [40]. It is not an illogical reasoning to use the IMEC values giving the best match relate to theoretical values when the difference of IMEC values come from the different experimental condition [40]. However, it is for now, and more work should be done to determine IMEC values for our own setup in order to improve the reliability of results from the technique.

Table 4. 4: IMEC values which have been reported in the literatures.

IMEC relative to the absorption band at 1544 cm^{-1} ($cm \cdot \mu mol^{-1}$)	IMEC relative to the absorption band at 1455 cm^{-1} ($cm \cdot \mu mol^{-1}$)	Year	Reference
1.67	2.22	1993	[38]
1.13	1.28	1997	[39]
0.73	0.64	1999	[40]
3.03	3.26	1967	[41]
1.3	1.5	1986	[42]
1.8		1994	[43]
1.1		1995	[44]
0.078	0.269	1996	[45]
0.085		1997	[46]
0.81	1.5	1996	[47]
1.13	1.28	1997	[48]
0.73	1.11	1992	[49]

Desorption spectra plot and the concentration plot are presented for each zeolite sample in the following part of this paper. Since our interest is to quantify Brønsted and Lewis acid sites, no detail of spectra will be discussed unless there is something unusual observed.

H-ZSM-23

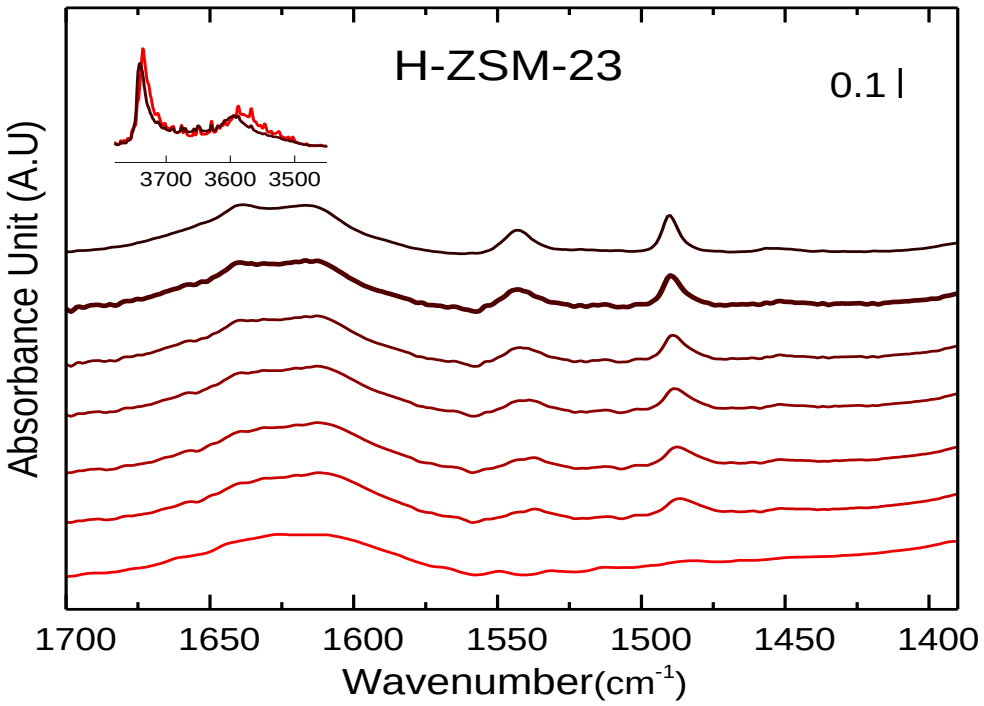

Figure 4. 52: FT-IR spectra under pyridine adsorption experiment on H-ZSM-23. From the top to the bottom: spectrum recorded after evacuation of pyridine at 150°C, 200°C(bold line), 250°C, 300°C, 350°C, 400°C, and clean & activated spectrum of the zeolite at 450°C. ν(OH) region is included as an inset showing spectrum recorded after evacuation of pyridine at 200°C (black) and clean & activated spectrum of the zeolite recorded at 450°C (red).

It is very noticeable that not all Brønsted acid sites were consumed under the pyridine adsorption experiment on H-ZSM-23. From the inset of Figure 4. 52, one can observe that only small amount of Brønsted acid sites interacted with pyridine at 200°C. Injection of pyridine was done for an hour at 150° C in order to make sure that enough pyridine was introduced in the system, but no major change in peaks (~3600, 1544 cm^{-1}) was observed after 30 minutes. At first, it was suspected that pyridine couldn't interact with acid sites in H-ZSM-

23 because pyridine is too big for the 1D-10 ring channel of the zeolite. To confirm this assumption, the calculation was performed and this will be discussed in depth in the section 4.2.3. Concentration of Brønsted acid sites and that of Lewis acid sites which interacted with pyridine were calculated as in other zeolite samples. However, for the H-ZSM-23, this value is more "concentration of Brønsted/Lewis acid sites accessible to pyridine" than total concentration of Brønsted/Lewis acid sites. Because not all the Brønsted acid sites were interacted with pyridine, Si/Al ratio could not be calculated from the integrated area of ~1544 cm^{-1} peak, and the value is not reported in the Table 4. 5 and Table 4. 6.

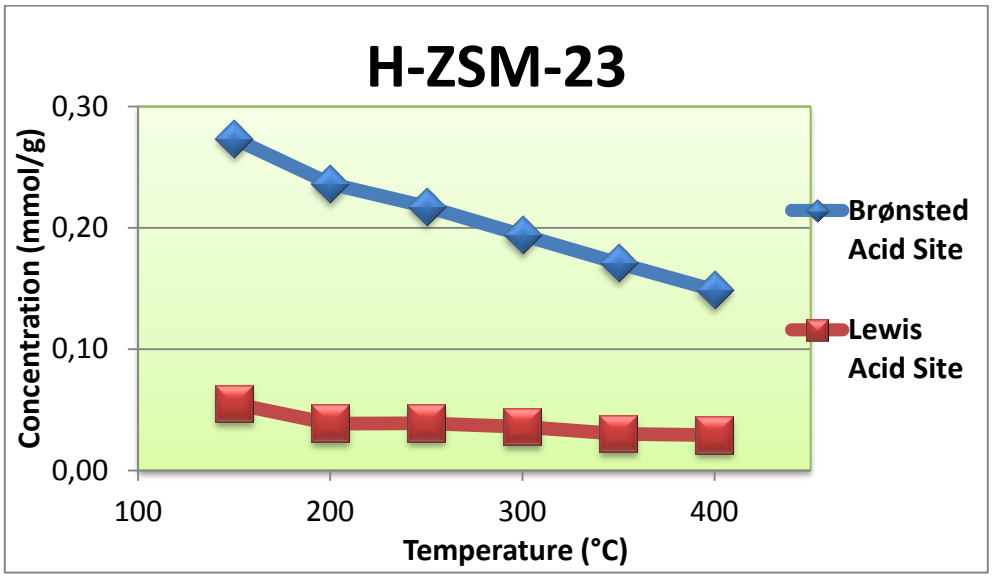

Figure 4. 53: Concentration of bridging Brønsted and Lewis acid site interacting with pyridine on H-ZSM-23 zeolite after evacuation of pyridine at different temperatures.

H-ZSM-22

Different from H-ZSM-23, all Brønsted acid sites were consumed under introduction of pyridine to the system. One can confirm it from the inset of Figure 4. 54. ~1544 cm^{-1} band and ~1455 cm^{-1} band are observable in this experiment as expected, and the concentration change of Brønsted and Lewis acid sites after evacuation of pyridine at different temperature is reported at Figure 4. 55. Since all Brønsted acid sites was consumed, one can calculated the Si to Al ratio of zeolite sample using equations in section 2.2.2, and value is reported in Table 4. 5 and Table 4. 6.

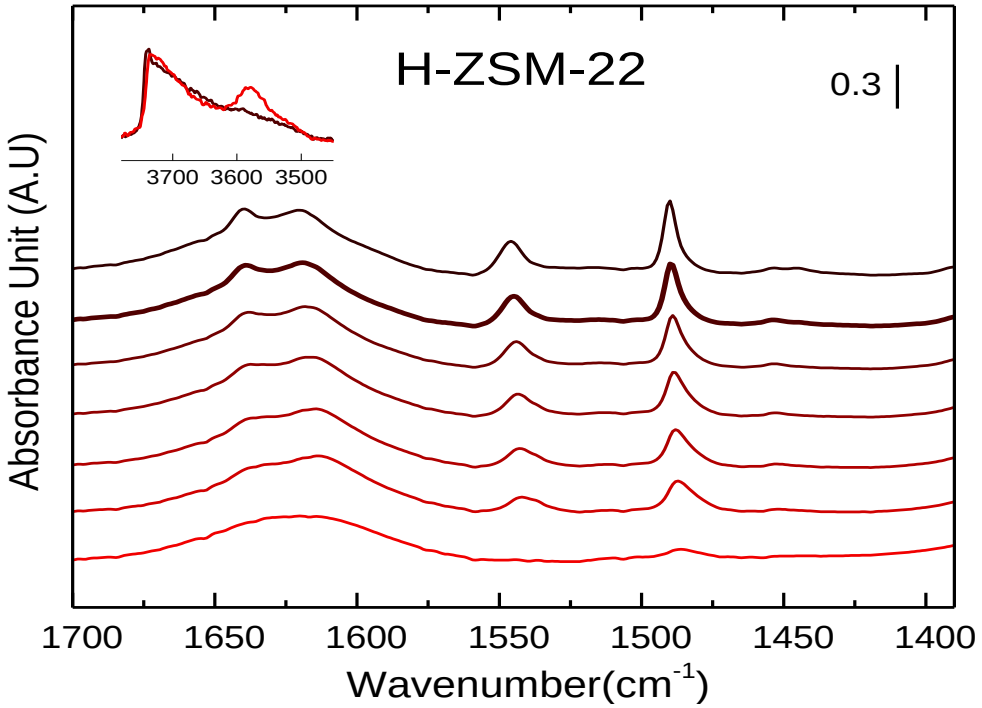

Figure 4. 54: FT-IR spectra under pyridine adsorption experiment on H-ZSM-22. From the top to the bottom: spectrum recorded after evacuation of pyridine at 150°C, 200°C(bold line), 250°C, 300°C, 350°C, 400°C, and clean & activated spectrum of the zeolite at 450°C. ν(OH) region is included as an inset showing spectrum recorded after evacuation of pyridine at 200°C (black) and clean & activated spectrum of the zeolite recorded at 450°C (red).

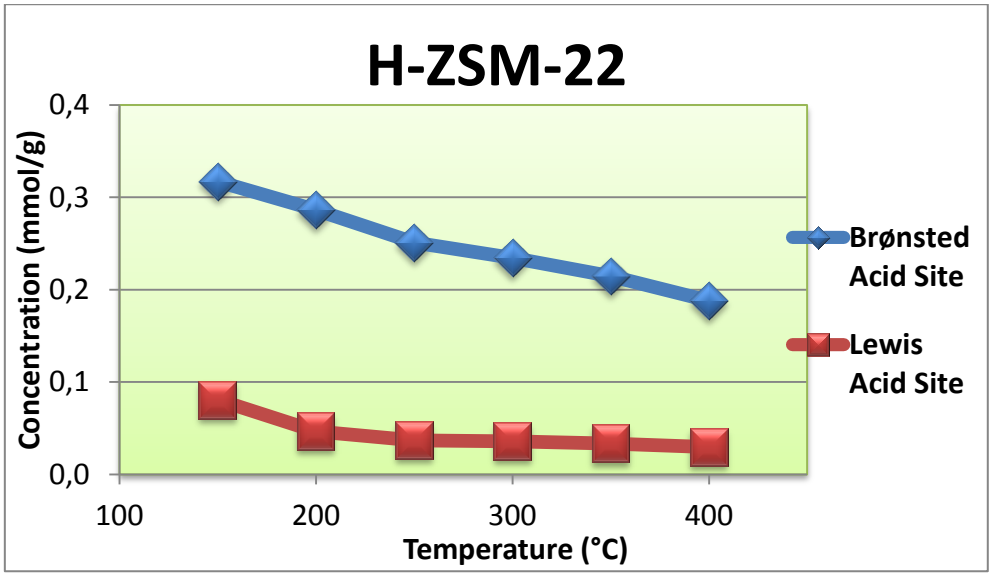

Figure 4. 55: Concentration of bridging Brønsted and Lewis acid site interacting with pyridine on H-ZSM-22 zeolite after evacuation of pyridine at different temperatures.

H-Mordenite

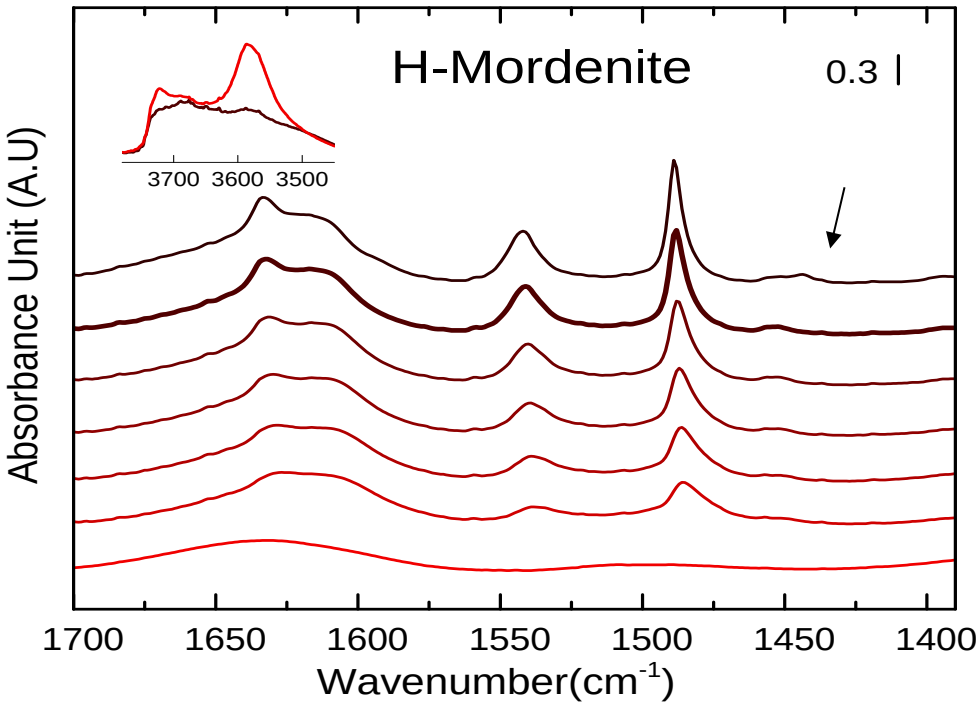

Figure 4. 56: FT-IR spectra under pyridine adsorption experiment on H-Mordenite. From the top to the bottom: spectrum recorded after evacuation of pyridine at 150°C, 200°C(bold line), 250°C, 300°C, 350°C, 400°C, and clean & activated spectrum of the zeolite at 450°C. ν(OH) region is included as an inset showing spectrum recorded after evacuation of pyridine at 200°C (black) and clean & activated spectrum of the zeolite recorded at 450°C (red).

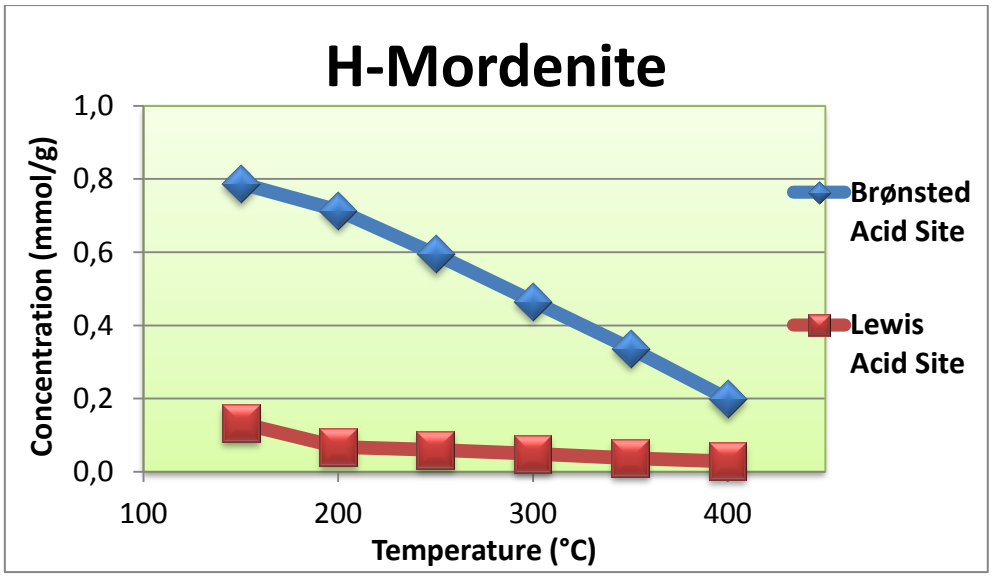

Figure 4. 57: Concentration of bridging Brønsted and Lewis acid site interacting with pyridine on H-Mordenite zeolite after evacuation of pyridine at different temperatures.

In the case of H-Mordenite, decrease in the band at ~3724 cm^{-1} at inset of Figure 4. 56 is observed. This implies that considerable amount of silanols interacted with pyridine. At 150°C desorption, corresponding band originated from pyridine at ~1444 cm^{-1} is marked with an arrow in Figure 4.56. ~1481 cm^{-1} band is expected as well from pyridine adsorbed on silanols, but it is difficult to identify because of high intensity of ~1490 cm^{-1} band. From 200°C and higher desorption temperature, ~1444 cm^{-1} band is absent, and this supports that total concentration of acid sites should be calculated at 200°C desorption spectra, not at 150°C.

H-MCM-22

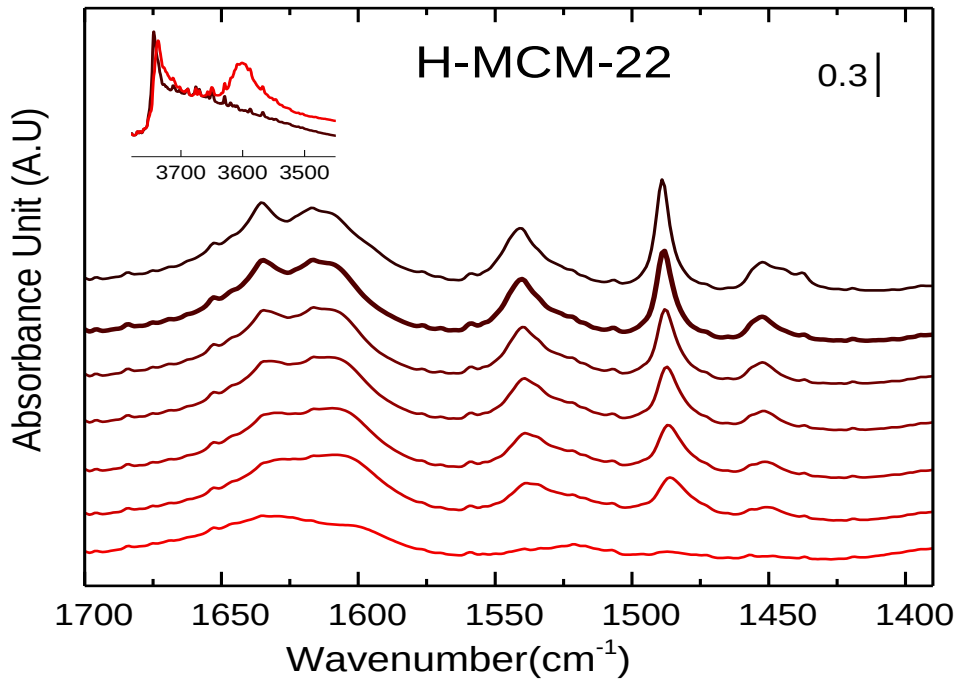

Figure 4. 58: FT-IR spectra under pyridine adsorption experiment on H-MCM-22. From the top to the bottom: spectrum recorded after evacuation of pyridine at 150°C, 200°C(bold line), 250°C, 300°C, 350°C, 400°C, and clean & activated spectrum of the zeolite at 450°C. ν(OH) region is included as an inset showing spectrum recorded after evacuation of pyridine at 200°C (black) and clean & activated spectrum of the zeolite recorded at 450°C (red).

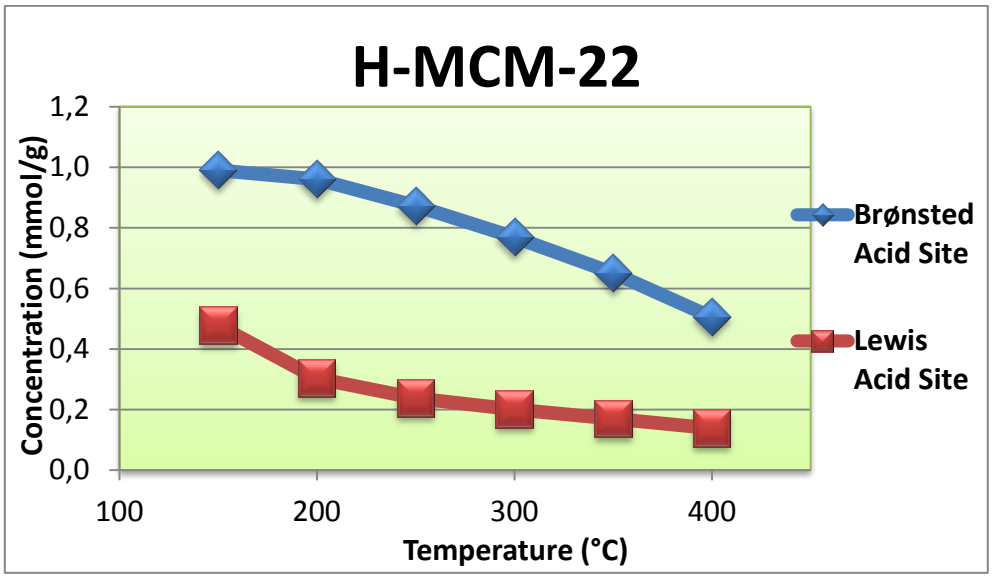

Figure 4. 59: Concentration of bridging Brønsted and Lewis acid site interacting with pyridine on H-MCM-22 zeolite after evacuation of pyridine at different temperatures.

H-IM-5

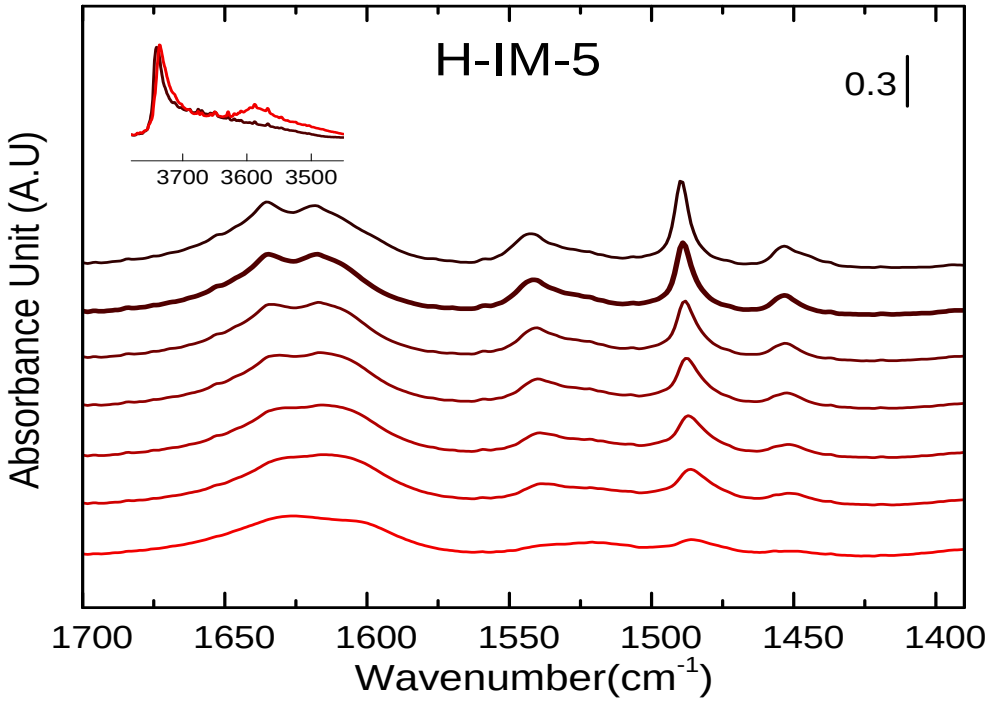

Figure 4. 60: FT-IR spectra under pyridine adsorption experiment on H-IM-5. From the top to the bottom: spectrum recorded after evacuation of pyridine at 150°C, 200°C(bold line), 250°C, 300°C, 350°C, 400°C, and clean & activated spectrum of the zeolite at 450°C. ν(OH) region is included as an inset showing spectrum recorded after evacuation of pyridine at 200°C (black) and clean & activated spectrum of the zeolite recorded at 450°C (red).

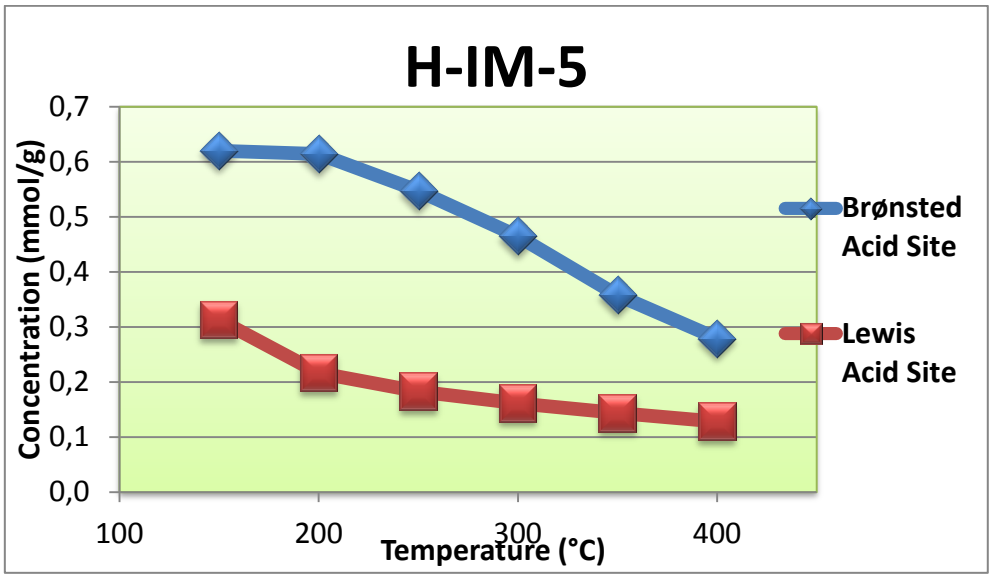

Figure 4. 61: Concentration of bridging Brønsted and Lewis acid site interacting with pyridine on H-IM-5 zeolite after evacuation of pyridine at different temperatures.

H-ITQ-13

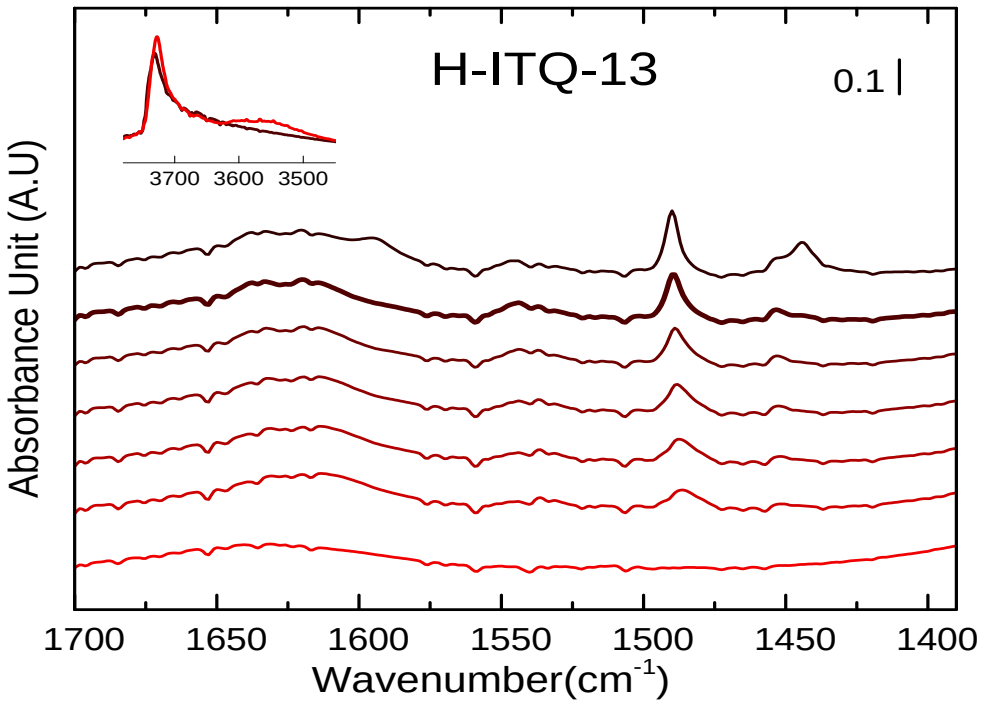

Figure 4. 62: FT-IR spectra under pyridine adsorption experiment on H-ITQ-13. From the top to the bottom: spectrum recorded after evacuation of pyridine at 150°C, 200°C(bold line), 250°C, 300°C, 350°C, 400°C, and clean & activated spectrum of the zeolite at 450°C. ν(OH) region is included as an inset showing spectrum recorded after evacuation of pyridine at 200°C (black) and clean & activated spectrum of the zeolite recorded at 450°C (red).

For the case of H-ITQ-13, the concentration of bridging Brønsted acid site at 150°C is lower than the concentration at 200°C (Figure 4. 63). It is because of the spectrum measured at 150 °C is broader than spectrum measured at 200 °C, and their difference in integral area is not large. Moreover, noise in the spectra was quite severe, which makes it difficult to decide the start and the end of the ~1544 cm^{-1} band. The reason why the ~1544cm^{-1} band at 150°C is broader than 200 °C can be explained by hydrogen bonding between pyridinium ion and conjugate base, $zeolite^-$. Here the expression conjugate base zeolite- is used to explain the status of zeolite after it transferred the hydrogen to pyridine under acid-base reaction [59]. At the lower temperature, the less evacuation of pyridine happens, so one can expect more hydrogen bonds between pyridinium ion and conjugate base $zeolite^-$. It is known fact that hydrogen bonds contribute to broadening of absorbance band, and this applies to what we observe in the case of pyridine adsorption experiment on H-ITQ-13 zeolite. It should be also noted that inaccuracy factors exist in integration process of the band. Under the five consecutive integration of the spectrum recorded after evacuation of pyridine at 150°C, five different integration results were obtained in the range of 1.152 ~ 1.236 which leads to the concentration of bridging Brønsted acid site in the range of 0.344 ~ 0.368 mmol/g catalyst with standard deviation of 0.010. Even though the concentration difference at 150°C and 200°C (0.053 mmol/g) is larger than the standard deviation calculated, we still cannot rule out the possibility of error made in the process of integration.

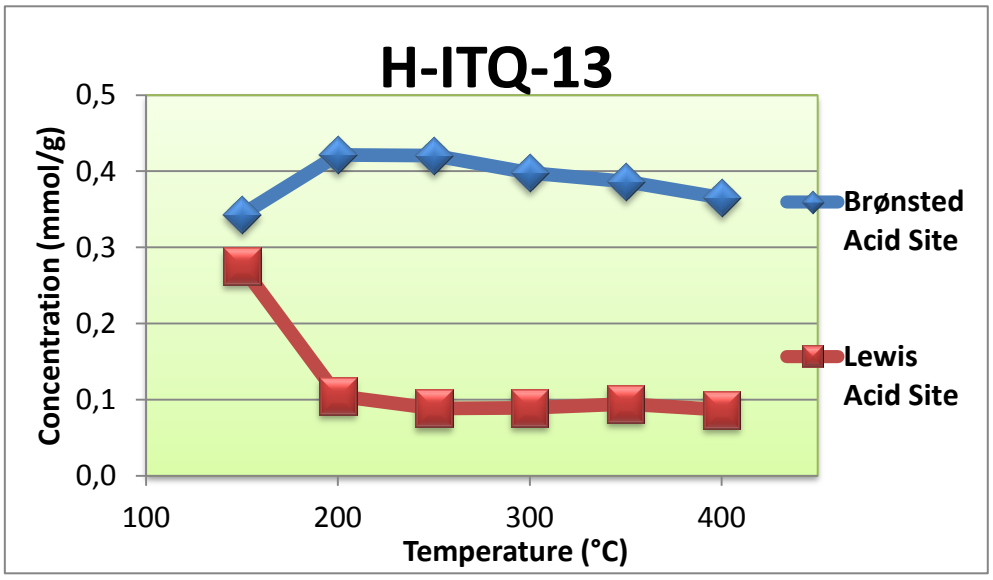

Figure 4. 63: Concentration of bridging Brønsted and Lewis acid site interacting with pyridine on H-MFI-27 zeolite after evacuation of pyridine at different temperatures.

H-MFI-27

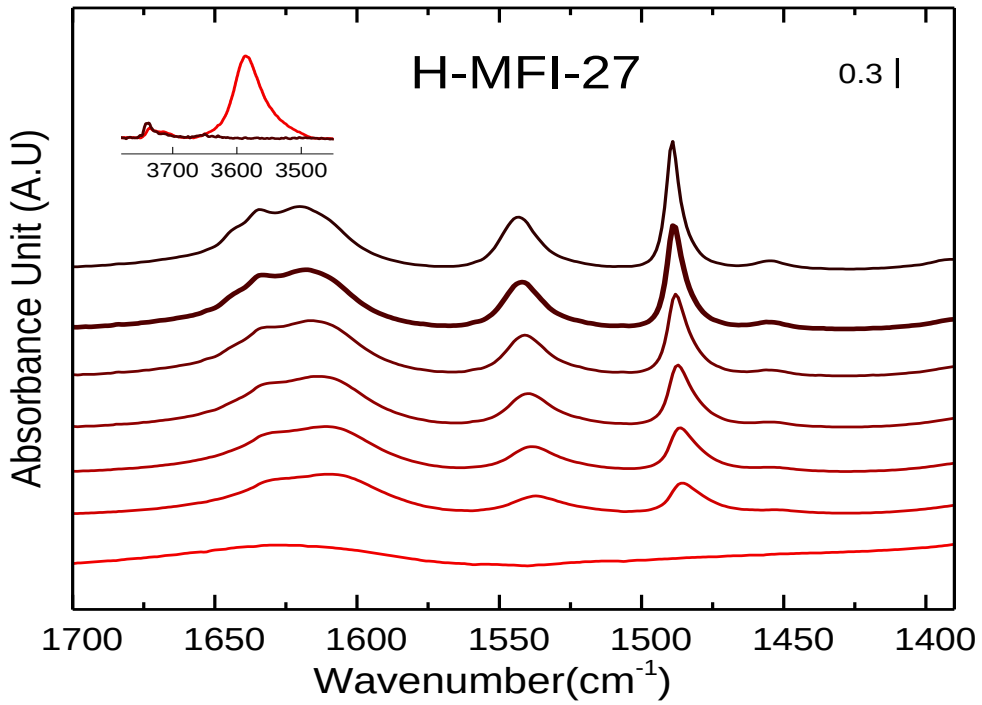

Figure 4. 64: FT-IR spectra under pyridine adsorption experiment on H-MFI-27. From the top to the bottom: spectrum recorded after evacuation of pyridine at 150°C, 200°C(bold line), 250°C, 300°C, 350°C, 400°C, and clean & activated spectrum of the zeolite at 450°C. ν(OH) region is included as an inset showing spectrum recorded after evacuation of pyridine at 200°C (black) and clean & activated spectrum of the zeolite recorded at 450°C (red).

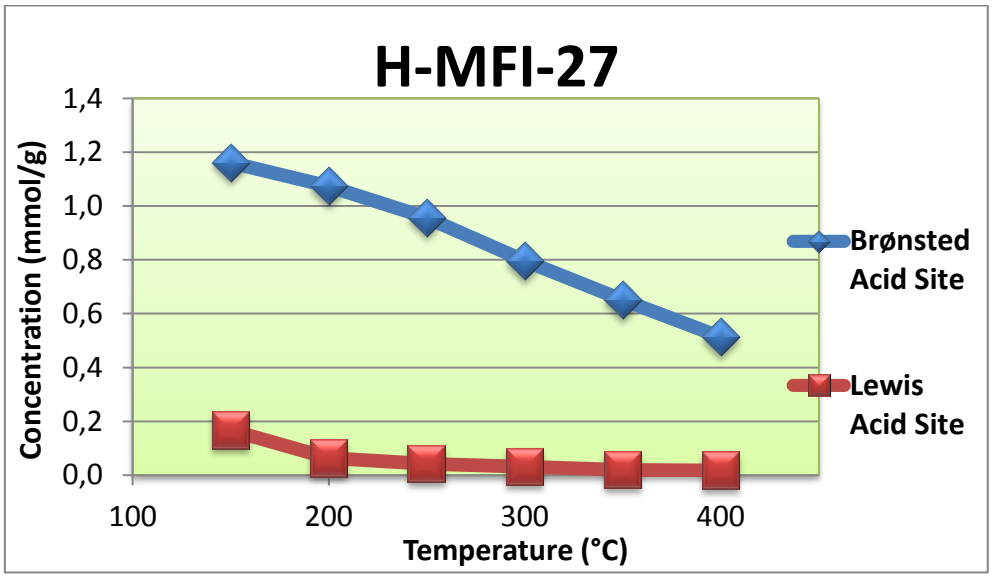

Figure 4. 65: Concentration of bridging Brønsted and Lewis acid site interacting with pyridine on H-MFI-27 zeolite after evacuation of pyridine at different temperatures.

H-Pentasil

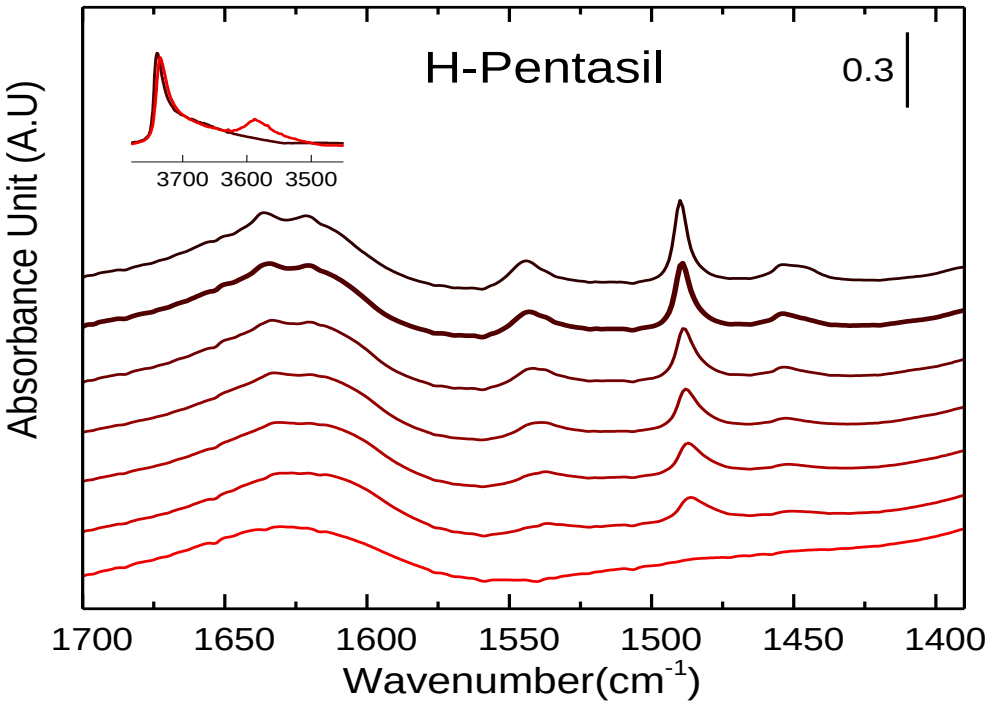

Figure 4. 66: FT-IR spectra under pyridine adsorption experiment on H-Pentasil. From the top to the bottom: spectrum recorded after evacuation of pyridine at 150°C, 200°C(bold line), 250°C, 300°C, 350°C, 400°C, and clean & activated spectrum of the zeolite at 450°C. ν(OH) region is included as an inset showing spectrum recorded after evacuation of pyridine at 200°C (black) and clean & activated spectrum of the zeolite recorded at 450°C (red).

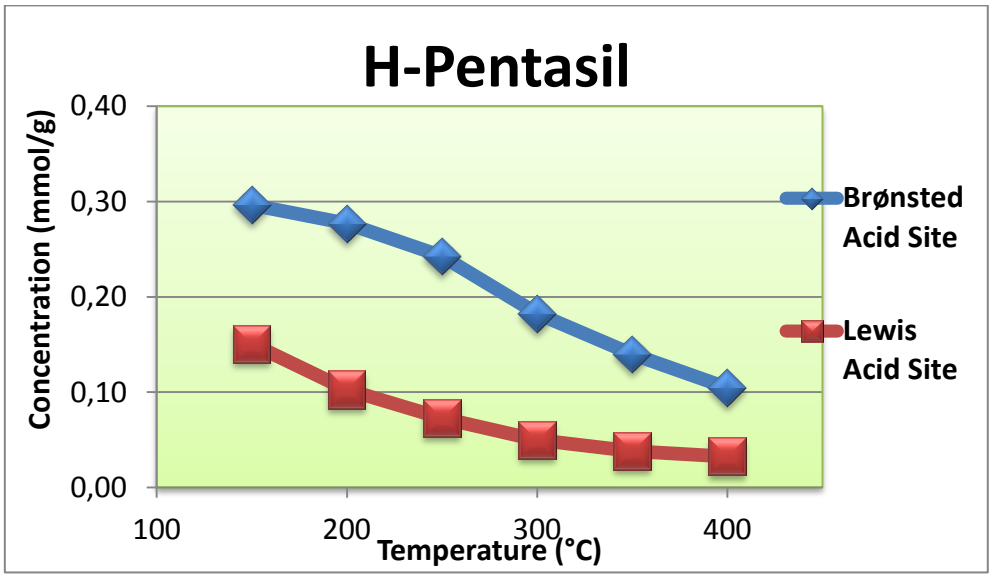

Figure 4. 67: Concentration of bridging Brønsted and Lewis acid site interacting with pyridine on H-Pentasil zeolite after evacuation of pyridine at different temperatures.

H-ZSM-5

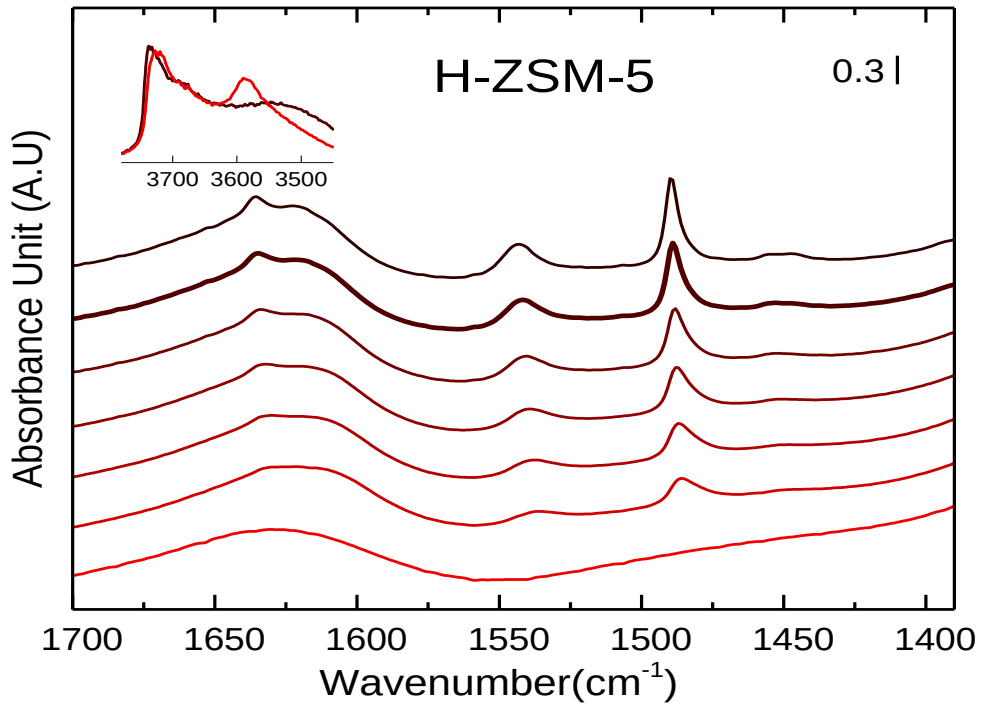

Figure 4. 68: FT-IR spectra under pyridine adsorption experiment on H-ZSM-5. From the top to the bottom: spectrum recorded after evacuation of pyridine at 150°C, 200°C(bold line), 250°C, 300°C, 350°C, 400°C, and clean & activated spectrum of the zeolite at 450°C. ν(OH) region is included as an inset showing spectrum recorded after evacuation of pyridine at 200°C (black) and clean & activated spectrum of the zeolite recorded at 450°C (red).

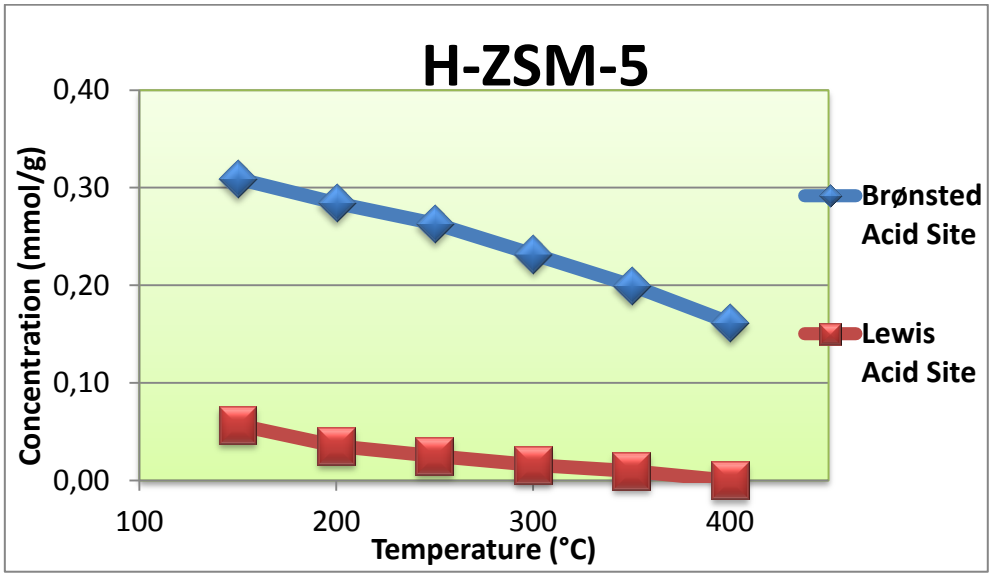

Figure 4. 69: Concentration of bridging Brønsted and Lewis acid site interacting with pyridine on H-ZSM-5 zeolite after evacuation of pyridine at different temperatures.

H-SUZ-4

As it happened for H-ZSM-23, but in more severe degree, there were Brønsted acid sites in H-SUZ-4 which were not consumed under introduction of pyridine. More specifically, there is nearly no erosion in Brønsted acid band seen from the inset of Figure 4.70. There are very weak bands which seem like being at ~1544, 1490, and 1455 cm^{-1}, but it is difficult to affirm because of strong noise in the spectrum.

Since H-SUZ-4 has two different channel types, 10- and 8-memebered ring channels, it was suspected that hydroxyls in 8-membered ring channels are inaccessible to pyridine. It was reported before that isobutene cannot reach the acid sites located in 8-membered ring channels [96]. If that is the case for isobutane, it is very possible that the access to the hydroxyls in 8-membered ring for pyridine is prevented too. The calculation was performed to test the assumption. More detail will be discussed in section 4.2.3.

Because the ~1544 and 1455cm^{-1} bands are not clearly distinguishable from the noise, the concentration plot was not made for H-SUZ-4.

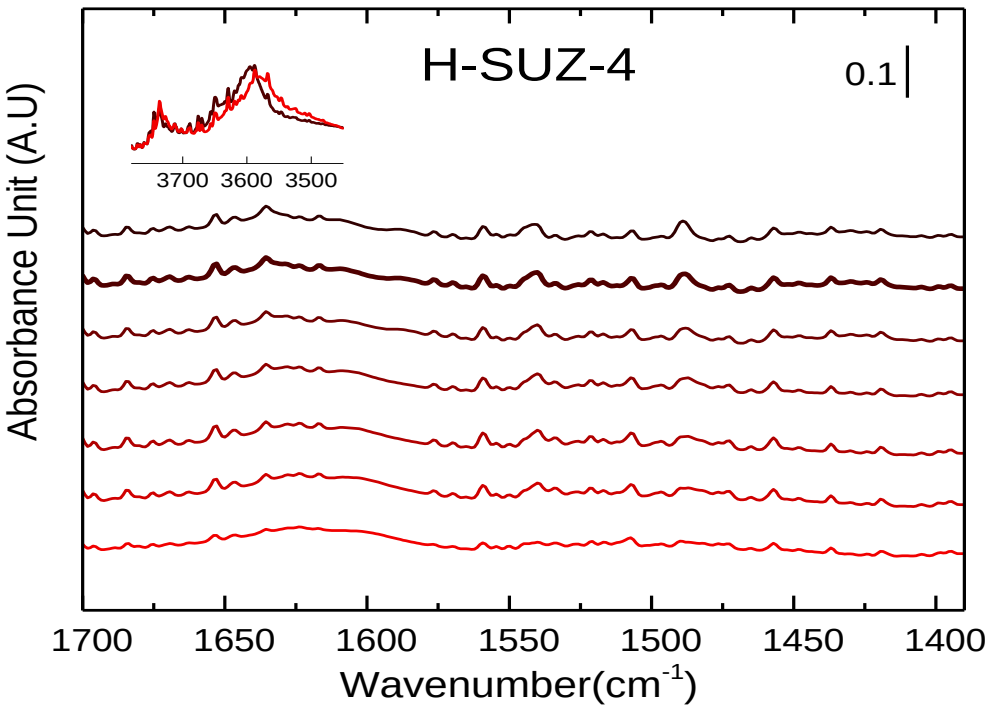

Figure 4. 70: FT-IR spectra under pyridine adsorption experiment on H-SUZ-4. From the top to the bottom: spectrum recorded after evacuation of pyridine at 150°C, 200°C(bold line), 250°C, 300°C, 350°C, 400°C, and clean & activated spectrum of the zeolite at 450°C. ν(OH) region is included as an inset showing spectrum recorded after evacuation of pyridine at 200°C (black) and clean & activated spectrum of the zeolite recorded at 450°C (red).

H-TNU-9

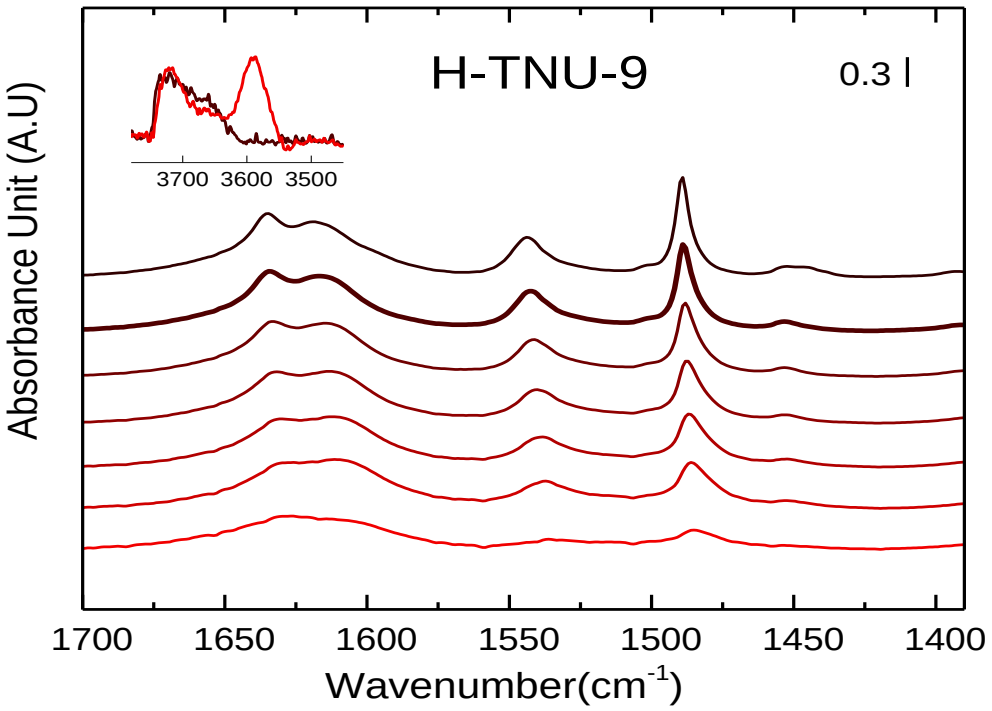

Figure 4. 71: FT-IR spectra under pyridine adsorption experiment on H-TNU-9. From the top to the bottom: spectrum recorded after evacuation of pyridine at 150°C, 200°C(bold line), 250°C, 300°C, 350°C, 400°C, and clean & activated spectrum of the zeolite at 450°C. ν(OH) region is included as an inset showing spectrum recorded after evacuation of pyridine at 200°C (black) and clean & activated spectrum of the zeolite recorded at 450°C (red).

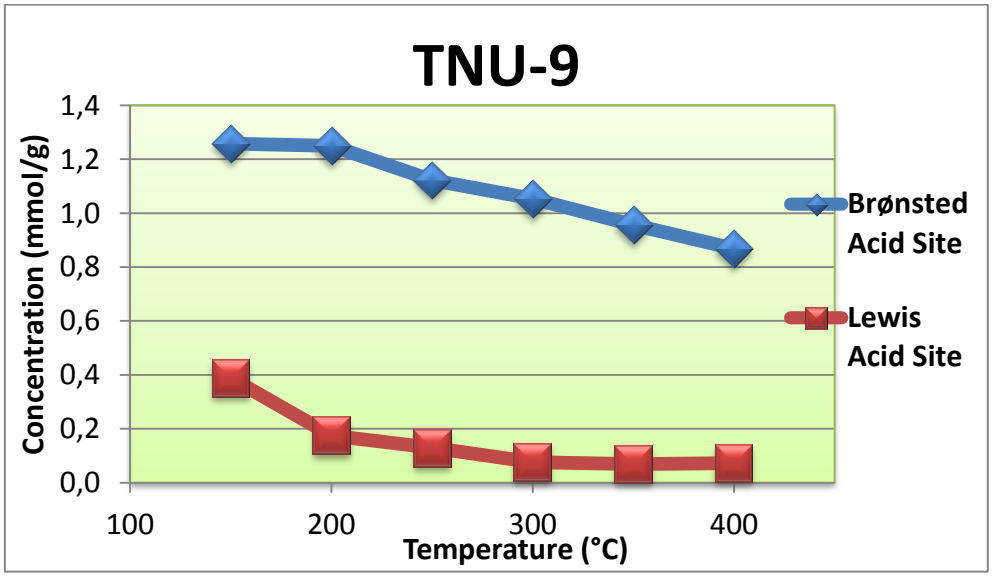

Figure 4. 72: Concentration of bridging Brønsted and Lewis acid site interacting with pyridine on H-TNU-9 zeolite after evacuation of pyridine at different temperatures.

H-Beta

H-Beta sample shows same trend in concentration change as in H-ITQ-13. Concentration of bridging Brønsted acid site interacting with pyridine at 150°C is smaller than at 200°C. Possible reasons already discussed for H-ITQ-13 can be applied to explain the observation in Figure 4. 74 as well.

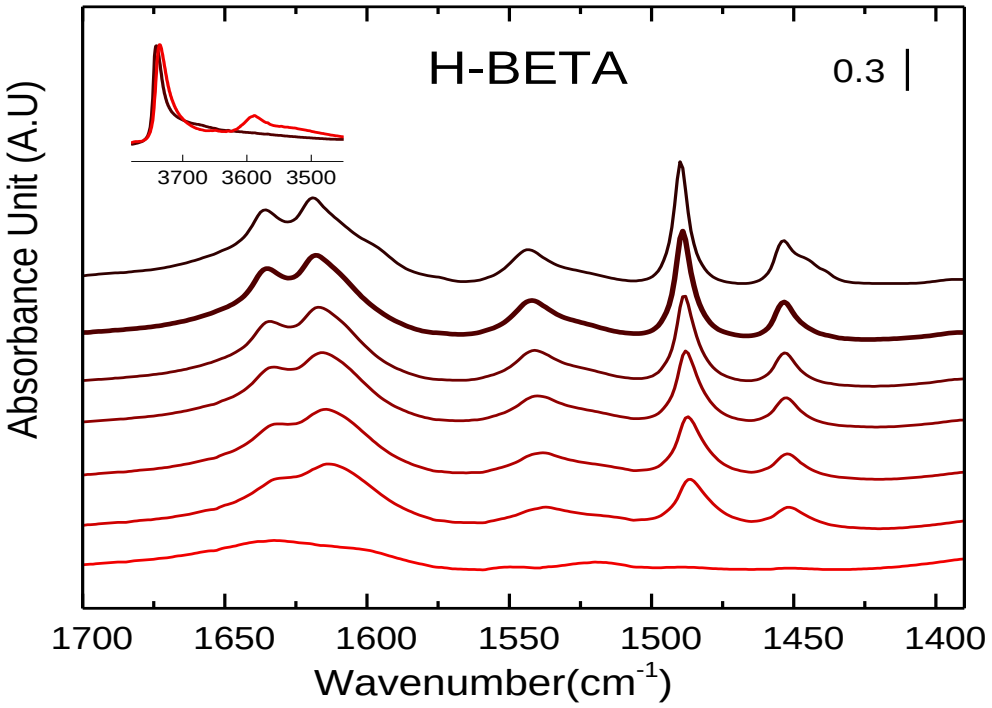

Figure 4. 73: FT-IR spectra under pyridine adsorption experiment on H-BETA. From the top to the bottom: spectrum recorded after evacuation of pyridine at 150°C, 200°C(bold line), 250°C, 300°C, 350°C, 400°C, and clean & activated spectrum of the zeolite at 450°C. ν(OH) region is included as an inset showing spectrum recorded after evacuation of pyridine at 200°C (black) and clean & activated spectrum of the zeolite recorded at 450°C (red).

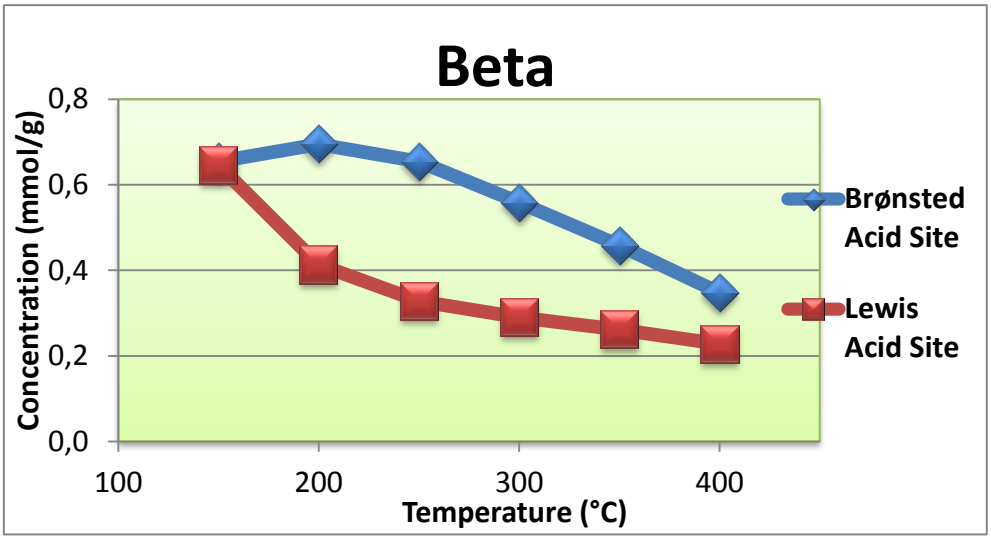

Figure 4. 74: Concentration of bridging Brønsted and Lewis acid site interacting with pyridine on H-Beta zeolite after evacuation of pyridine at different temperatures.

Table 4. 5: Concentration of Brønsted and Lewis acid site, and calculated Si/Al for all 12 samples based on pyridine adsorption experiment

Framework code	Sample	Total concentration of Brønsted acid site (C_{BA})	Total concentration of Lewis acid site (C_{LA})	Si/Al calculated ($=\frac{16.6-C_{BA}-C_{LA}}{C_{BA}+C_{LA}}$)
MTT	H-ZSM-23	0.236	0.039	
TON	H-ZSM-22	0.287	0.047	**49**
MOR	H-Mordenite	0.714	0.068	**20**
MWW	H-MCM-22	0.960	0.303	**12**
IMF	H-IM-5	0.614	0.216	**19**
ITH	H-ITQ-13	0.422	0.105	**31**
MFI	H-MFI-27	1.074	0.063	**14**
	H-Pentasil	0.277	0.103	**43**
	H-ZSM-5	0.284	0.035	**51**
SZR	H-SUZ-4			
TUN	H-TNU-9	1.250	0.175	**11**
*BEA	H-Beta	0.695	0.414	**14**

Total concentration of Brønsted acid sites, that of Lewis acid sites, and calculated Si/Al for each sample is listed in Table 4. 5. It is no wonder that the sample with low Si/Al ratio shows higher concentration of (Brønsted) acid site since the assumption of this whole experiment is that an acid site is generated under a replacement of Si with Al. When it comes to the total concentration of Brønsted acid site (C_{BA}) in each zeolite sample, it decreases in following order: H-TNU-9 > H-MFI-27 > H-MCM-22 > H-Mordenite > H-Beta > H-IM-5 > H-ITQ-13 > H-ZSM-22 > H-ZSM-5 > H-Pentasil. H-ZSM-23 and H-SUZ-4 could not be included because not all Brønsted acid site were consumed upon pyridine adsorption experiment.

In Table 4. 6, Si/Al values from different sources are listed. Theoretical Si/Al value was provided by manufacturer of each sample, EDS was the measured by using Energy Dispersive X-ray Spectroscopy technique. One can see that values from EDS and pyridine adsorption are not much different from theoretical values, except H-ITQ-13 zeolite. For H-ITQ-13, the discussion can be found in section 4.1.2.

Table 4. 6: Comparison of theoretical Si/Al, Si/Al from EDS and Si/Al calculated from pyridine adsorption experiment.

Framework Type	Sample	Theroetical Si/Al	EDS	Si/Al calculated from pyridine adsorption
MTT	H-ZSM-23	23	22	
TON	H-ZSM-22	45	33	49
MOR	H-Mordenite	22	15	20
MWW	H-MCM-22	15	13	12
IMF	H-IM-5	15	15	19
ITH	H-ITQ-13	50	30	31
MFI	H-MFI-27	13.5	15	14
	H-Pentasil	45	32	43
	H-ZSM-5	50	40	51
SZR	H-SUZ-4	8	7	
TUN	H-TNU-9	15	13	11
*BEA	H-Beta	12.5	12	14

4.2.3 Calculation regarding pyridine adsorption on zeolite

Calculation was initially performed to find the reason why not all the Brønsted acid sites was consumed under introduction of pyridine to H-ZSM-23 and H-SUZ-4. H-ZSM-22 was included in the calculation for comparison. Calculated energy for each species and adsorption energy are shown in Table 4. 7 - Table 4. 10. Different cases with different location of acid sites were calculated, and they are numbered with Roman numerals. Figures of optimized geometry of all cases are found in Appendix C. It should be reminded that the calculation was performed as a small side-project in this work, and no extensive calculation in all possible locations or possible combination of Brønsted acid sites inside of unit cell was carried out. It was more to get rough idea about the spatial availability of pores in H-ZSM-23 and H-SUZ-4.

Table 4. 7: Adsorption energy (eV) of a pyridine on H-ZSM-23 and H-ZSM-22 with and without Brønsted acid sites.

Zeolite	Case #	Energy of Pyridine (Lattice: 14Å) (eV)	Energy of zeolite without an acid site (eV)	Energy of zeolite with a single acid site in two joint unit cell (eV)	Energy of zeolite with pyridine adsorbed (eV)	Adsorption Energy (eV)
H-ZSM-23	I-a	-1125.7	-47298.6		-48425.1	-0.7
	I-b	-1125.7		-47263.5	-48391.3	-2.1
H-ZSM-22	I-a	-1125.7	-47299.7		-48425.8	-0.4
	I-b	-1125.7		-47264.5	-48391.3	-1.9

Table 4. 7 shows calculation result of adsorption energy of a pyridine on zeolite with and without an acid site. This was to see whether a pyridine can interact with a Brønsted acid site located inside of the 10-ring channel of the zeolites. To observe sorely the effect spatial factor, it is needed to avoid the interaction between pyridines in neighboring cells. Therefore, for the case with an acid site, one acid site per two joint unit cells was placed and the calculation was performed. Comparing the adsorption energy for the case without and with a Brønsted acid

site shows us both adsorption energies, without and with a Brønsted acid site. From the values reported, it can be said that the system of a pyridine in the H-ZSM-23 zeolite is actually more stable compare to that of a pyridine in the H-ZSM-22 zeolite. This implies that our original hypothesis, pyridine might be too big for 10-ring of H-ZSM-23 zeolite, is not supported by calculation results. For the H-SUZ-4, it was confirmed that pyridine can interact with a Brønsted acid site in 10-ring pore, but not with the acid site in 8-ring pore (Table 4. 8).

Table 4. 8: Adsorption energy (eV) of a pyridine on a Brønsted acid site at different location in 8- and 10-ring of H-SUZ-4.

	Case #	Energy of Pyridine (Lattice: 14Å) (eV)	Energy of zeolite with a single acid site in two joint unit cell (eV)	Energy of zeolite with pyridine adsorbed on acid site (eV)	Adsorption Energy (eV)
H-SUZ-4 with one acid site per two joint unit cell	10-ring I	-1125.7	-70912.7	-72040.4	-2.1
	10-ring II	-1125.7	-70912.6	-72039.9	-1.7
	8-ring I	-1125.7	-70912.3	-72035.5	2.5
	8-ring II	-1125.7	-70912.7	-72035.7	2.7
	8-ring III	-1125.7	-70912.7	-72035.7	2.6

Since our hypothesis did not turned out to be plausible, another hypothesis was established and tested. H-ZSM-23 has lower Si/Al compare to the H-ZSM-22, which means more Al in the system. According to the chemical formula of each zeolite provided by International Zeolites Association (IZA) [14], Si/Al=45 of H-ZSM-22 corresponds to one OH group per two joint unit cells while Si/Al=23 of H-ZSM-23 corresponds to one OH group per one unit cell of the zeolite. Therefore, for the H-ZSM-23, the situation where acid sites are close to each other and pore of the zeolite becomes too crowded to accommodate two pyridine molecules can happen. So, two acid sites were located in two joint unit cell, and the adsorption energy calculations were carried out with one pyridine molecule in the system and two molecules in the system. Results are presented in Table 4. 9.

Table 4. 9: Adsorption energy (eV) of pyridine(s) on two Brøsnsted acid in H-ZSM-23 and H-ZSM-22.

Zeolite	Case #	# of pyridine in the system	Energy of Pyridine (Lattice: 14Å) (eV)	Energy of zeolite with a single acid site in two joint unit cell (eV)	Energy of zeolite with pyridine adsorbed on acid site (eV)	Adsorption Energy (eV)
H-ZSM-23 with two acid site per two joint unit cell	II	Py x1	-1125.7	-47228.5	-48355.9	-1.7
		Py x2	-1125.7	-47228.5	-49483.1	-3.3
	III	Py x1	-1125.7	-47228.3	-48356.1	-2.1
		Py x2	-1125.7	-47228.3	-49482.1	-2.4
	IV	Py x1	-1125.7	-47227.9	-48356.0	-2.5
		Py x2	-1125.7	-47227.9	-49480.5	-1.3

For the case II, the adsorption energy with two pyridine molecules adsorbed on the acid sites are lower than that with one pyridine molecule. For the case III, the adsorption energy is lower for the case with two pyridine molecules adsorbed than one, but the difference is only 0.3 eV. The distance of O-H bond was checked in order to see whether proton transfer was happened or not in this case. Distance between O and H in geometry optimized H-ZSM-23 in the case III was 0.980 Å for both hydroxyl groups. Upon geometry optimization with pyridine, the distance became 2.497 Å and 2.866 Å implying that proton transfer from both hydroxyl groups to pyridine molecules occurred. The last case, IV, adsorption energy became higher as another pyridine was added in the system. OH distance of two hydroxyl groups upon geometry optimization with two pyridine molecules was 2.311 Å and 0.989 Å indicating only one pyridine got protonated. However, The two acid sites were located in two neighboring oxygen, and this was supposed to be the least favored scenario for two pyridine adsorbed on two Brønsted acid sites as the possibility of the two sites sit right next to each other does not seem high at all inside of the two joint unit cell. Moreover, similar condition, two acid sites located in two neighboring oxygen, was calculate for H-SUZ-4 (Table 4. 10, 10-ring VII case) as well. However, the adsorption energy with 2 pyridine in the system was lower than 1 pyridine in the system. From the bond length as well, we could confirm that protons were transferred from both acid sites to two pyridine molecules in the case of H-SUZ-4. In general, in 10-rings of H-SUZ-4 zeolites, two pyridine molecules seem to be adsorbed on two different

Brønsted acid sites in the joint unit cells without problem judging from the calculation results in Table 4. 10.

From the calculation results, we confirmed that a single pyridine molecule can interact with Brønsted acid sites in 10-rings of H-ZSM-23 and that of H-SUZ-4. The Brønsted acid sites located in 8-ring of H-SUZ-4 are the only ones inaccessible to pyridine. Even the adsorption of two pyridines on two different Brønsted acid sites in the two joint unit cells in H-ZSM-23 and H-SUZ-4 seem possible for the most of cases. Then how can we explain the behavior we observed from pyridine adsorption on these two samples? For H-SUZ-4, Teketel reported that 10-ring channels are only accessible from the edge of the needle-like crystal while 8-ring channels are accessible from the sides of the needle-like crystal [15]. This can lead to the situation where many of pyridine molecules try to get access from the sides of the needle-like crystal where 8-ring channels locate. There is also a possibility that outstandingly low Si/Al of H-SUZ-4 (8) resulting in too many Brønsted acid sites in the unit cell might not give enough space for pyridines to interact with all acid sites.

Table 4. 10: Adsorption energy (eV) of pyridine(s) on two Brønsted acid sites in H-SUZ-4.

Zeolite	Case #	# of pyridine in the system	Energy of Pyridine (Lattice: 14Å) (eV)	Energy of zeolite with a single acid site in two joint unit cell (eV)	Energy of zeolite with pyridine adsorbed on acid site (eV)	Adsorption Energy (eV)
H-SUZ-4 with two acid site per two joint unit cell	10-ring IV	Py x1	-1125.7	-70877.7	-72005.2	-1.8
		Py x2	-1125.7	-70877.7	-73131.2	-2.2
	10-ring V	Py x1	-1125.7	-70877.4	-72004.8	-1.8
		Py x2	-1125.7	-70877.4	-73131.8	-3.0
	10-ring VI	Py x1	-1125.7	-70877.6	-72005.0	-1.8
		Py x2	-1125.7	-70877.6	-73132.6	-3.7
	10-ring VII	Py x1	-1125.7	-70877.4	-72005.4	-2.3
		Py x2	-1125.7	-70877.4	-73131.4	-2.6

For H-ZSM-23, none of the hypothesis made earlier seem plausible. Moreover, there were Brønsted acid sites which were not consumed upon CO adsorption. From the calculation, we saw that the pyridine can interact with the Brønsted acid sites in 10-ring channel, and this means that CO should be able to interact with those acid sites as well. This issue might be related to diffusion of probe molecule along the H-ZSM-23 channel which is not smooth, rather bumpy (Figure 1. 5), side pockets in H-ZSM-23 or very low surface area of the sample (Table 4. 2). However, it could not be tested in this work any further. Surely more investigation is needed to find reasonable explanation for our observation from pyridine and CO adsorption on H-ZSM-23 and H-SUZ-4.

4.2.4 In situ FTIR on zeolites during the MTH reaction

In this section, assignment of the appearing band upon introduction of MeOH to the system was done mainly based on the Table 4. 11 and Table 4. 12. Three plots are presented for each sample, 1) spectra which were recorded after 0h, 1h, 2h, 3h and 4h of TOS, 2) subtracted version of recorded spectra after 0, 1, 2, 3 and 4 hours of TOS (each spectrum was subtracted by the clean zeolite spectrum which corresponds to after-0h-of-TOS spectrum), and 3) MeOH conversion and product selectivity relative to TOS. Plot 1) and 2) are grouped together and shown as a figure for each zeolite sample. It is more straightforward to see how much of acid sites was consumed during MeOH introduction in plot 1) while it is easier to see the new appearing bands in plot 2). As mentioned earlier, the spectra plots can be separated into three regions for analysis, ν(OH) (3800-3400 cm^{-1}), ν(CH) (3200-2800 cm^{-1}) and ν(CC)/ δ(CH) (1700-1300 cm^{-1}). As we are introducing MeOH to the system, absorption bands originated from many of the methoxy species such as methoxy adsorbed on silanol, Brønsted acid sites and EFAl are observed in the ν(CH) region. ν(CC)/δ(CH) region is mainly used for analysis related to coke.

Regarding plot 3), we can compare the plots with the conversion and products distribution observed in catalytic testing performed by Etemadi [2]. For all samples, it was observed that conversion at initial stage of the reaction from this work is too low, and the decrease rate in conversion from this work was different relative to the catalytic testing results shown in Appendix A. This is due to the experimental setup. Since the reaction was carried out using Specac HTHP cell which has much larger volume compare to the sample wafer, there were

quite amount of bypassing MeOH in the system without having any contact with the catalyst. As conversion was calculated from amount of MeOH and dimethyl ether (DME) detected by the GC-MS-FID, high quantity of bypassing MeOH led to lower conversion value. This affected values of the calculated conversion for all samples. High level of detected MeOH in GC-MS-FID in all samples can be seen in Figure B. 2 and Figure B. 4 in Appendix B.

Table 4. 11: Assignment of IR band related to MTH reaction in region 2), 3200-2800 cm^{-1}.

IR band (cm^{-1})	Assignments	Reference
3200-3000	**Aromatic CH stretching modes**	[67]
	3070 cm^{-1} : ν(CH) in polyalkenes or aromatics	[73]
	3109, 3083, 3058, 3045 cm^{-1}: benzene	[66]
2970-2850	**CH stretching modes of paraffinic species**	[67]
	2958-2955 cm^{-1} : $\nu_{as}(CH_3)$	[67, 73]
	2926 cm^{-1} : $\nu_{as}(CH_2)$	[67]
	2929-2932 cm^{-1} : methylation products	[66]
	2872 cm^{-1} : $\nu_{s}(CH_3)$	[67]
	2856 cm^{-1} : $\nu_{s}(CH_2)$	[67]
	2960-2956, 2857-2855 cm^{-1} : Methoxy on Silanols (CH_3OSi)	[66, 99, 100]
	2978, 2867 cm^{-1} : Methoxy on bridging Brønsted acid sties ($SiOCH_3Al$)	[99]
	2968(2980), 2865(2868) cm^{-1} : Methoxy on Al ($AlOCH_3$)	[99]([100])
2387-2377	**Secondary and tertiary carbenium ions**	[67, 101, 102]

Table 4. 12: Assignment of IR band in region 3), 1700-1300cm^{-1}.

IR band (cm^{-1})	Assignments	Reference
1670	**Stretching vibration of C=C in alkenes**	[73]
1620-1580 1440-1480	**Carboxylate surface species**	[67]
1620-1570	**Highly unsaturated polyenes and condensed aromatics**	[67]
	1600-1580 cm^{-1} : coke bands	[67, 68, 74]
	1604 cm^{-1} : H-tetramethylbenzene^{+}	[103]
	1600 cm^{-1}: H-hexymethylbenzene^{+}	[71]
1580-1550	**allylic species**	[67]
1540-1510	**alkylnaphthalenes**	[67]
1530–1500	**alkyl, alkenyl and cycloolefinic carbocations**	[67]
	1505 cm^{-1} : Dienyl carbocations	
	1535 cm^{-1} : Monoenyl carbocations	
1515-1490	**C =C of neutral and cationic polyene, non-condensed aromatics**	[67]
1490-1420, 1390-1360	**CH bending modes of paraffinic species**	[67]
	1390-1360 cm^{-1} : $\delta_s(CH_3)$ of isopropyl or tertiary butyl groups	[67]
	1485 cm^{-1} : $\delta_{as}(CH_3)$	[67]
	1468 cm^{-1} : $\delta_{as}(CH_2)$	[67]
	1382 cm^{-1} : $\delta_s(CH_3)$	[67]
	1359 cm^{-1} : $\delta_s(CH_2)$	[67]

H-ZSM-23

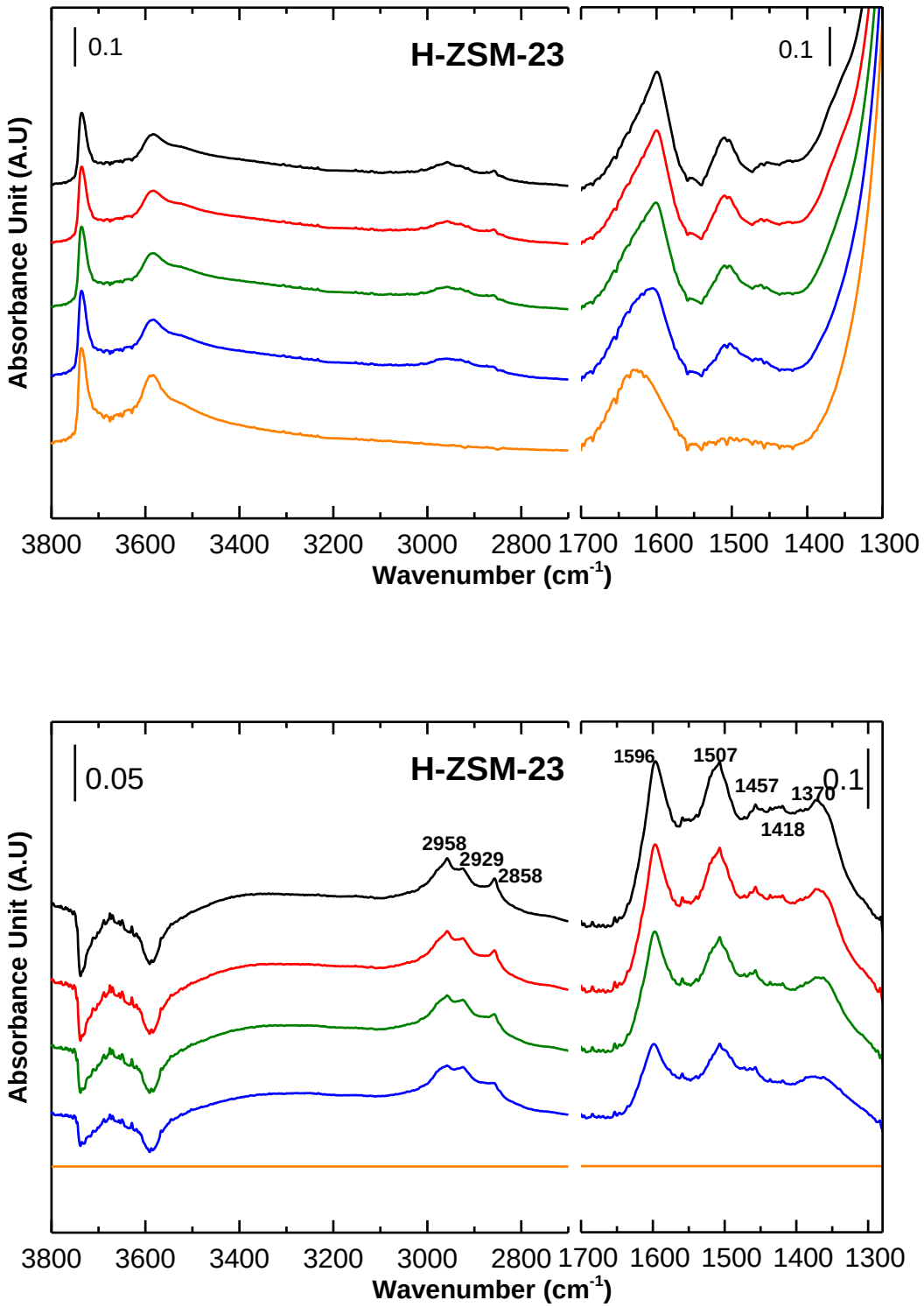

Figure 4. 75: In situ FTIR Spectra of the H-ZSM-23 zeolite obtained before introducing MeOH (yellow), after 1h (blue), 2h (green), 3h (red) and 4h (black) of contact with MeOH at 400°C and WHSV = 2.0gg^{-1}h^{-1}. (Upper) recorded spectra (Lower) clean zeolite spectrum subtracted spectra.

From the subtracted spectra, a few different bands appear upon contact with MeOH. Starting from coke peaks at the right side of the graph, one can observe ~1596 and 1370 cm^{-1} bands. As already mentioned at section 2.2.3, ~1596 cm^{-1} band is commonly referred to as a "coke band" which is related to condensed aromatic species. ~1370 cm^{-1} band is assigned to bending mode of CH_3 of isopropyl or tertiary butyl which might be attached to aromatic coke species by Bauer and Karge [67]. Study of deactivated H-ZSM-23 showed the residual hydrocarbon species up to three-ring aromatic species [86], and this implies that it is spatially possible for isopropylbenzene or tert-butylbenzene to exist inside of the pores in the H-ZSM-23. Intensity of these two bands is steadily increases as contact time increases, and these two bands together will be called as "coke bands" hereinafter. Besides of the coke bands, in ν(CC)/δ(CH) region, ~1507 cm^{-1} band is observed with high intensity. Interestingly, similar band is observed in H-ZSM-22, which has one-dimensional 10-ring channel system as H-ZSM-23, but no other samples. Karge, Nieβen and Bludau [69] earlier related the ~1507 cm^{-1} band to coke which is in form of linear, branched saturated or allylic hydrocarbons. Weak bands at ~1457 and 1418 cm^{-1} are from CH bending modes of paraffinic species. Park and Seo [68] previously assigned a band appearing at ~1465 cm^{-1} to the active intermediates formed in the pores based on the observation that the band grew rapidly in the initial period and maintained the steady level of intensity throughout the reaction. In our case, the band at ~1457 and 1418 cm^{-1} seem to behave similar with the ~1465 cm^{-1} band of Park and Seo. Both band appeared after 4 minutes of MeOH contact, and the intensity growth was leveled off for the rest of the experiment. Based on this observation, we can assign both bands to the active aliphatic intermediate species [67, 68].

In ν(CH) region, bands at ~2958, 2929, and 2858 cm^{-1} appear during contact with MeOH. They are all from paraffinic species. ~2958 and 2858 cm^{-1} bands are assigned to asymmetric and symmetric stretching band of methoxy groups on silanols, respectively [66, 99, 100], and ~2929 cm^{-1} is asymmetric stretching band of CH_2 from the methylation products [66]. Symmetric stretching band of CH_2 from the same species is supposed to appear at ~2856 cm^{-1}, and it is possible that the band overlaps with ~2858 cm^{-1} band. Methoxy groups on Brønsted acid sites which give absorption band at ~2980 cm^{-1} is difficult to observe even though the erosion of the Brønsted band is seen from the spectra (Figure 4. 75). From the most of the samples, the bands from methoxy adsorbed on Brønsted acid sites were difficult to observe compare to the band from methoxy on silanols. This will be discussed in detail at the end of this section regarding this matter. There is no obvious trace of aromatic species (bands at

3200-3000 cm^{-1}) in this region, and this is not consistent with existence of the band at ~1596 cm^{-1}. This will be also explained in more detail at the end of this section, after spectra of all samples are examined.

It should be noted that the ν(OH) bands for Brønsted acid sites and silanols did not consumed much after 4 hours of contact with MeOH even though the conversion decreases to 1/3 of its starting value. It can be related to blockage of the zeolite pore openings by the coke species in mono-dimensional zeolites [104-106]. Blockage of the zeolite pore can prevent MeOH from getting into the channels of H-ZSM-23 and interacting with active sites. Therefore, there will be active sites existing inside of the pores which give absorption band in IR spectroscopy, but inaccessible to MeOH for the reaction.

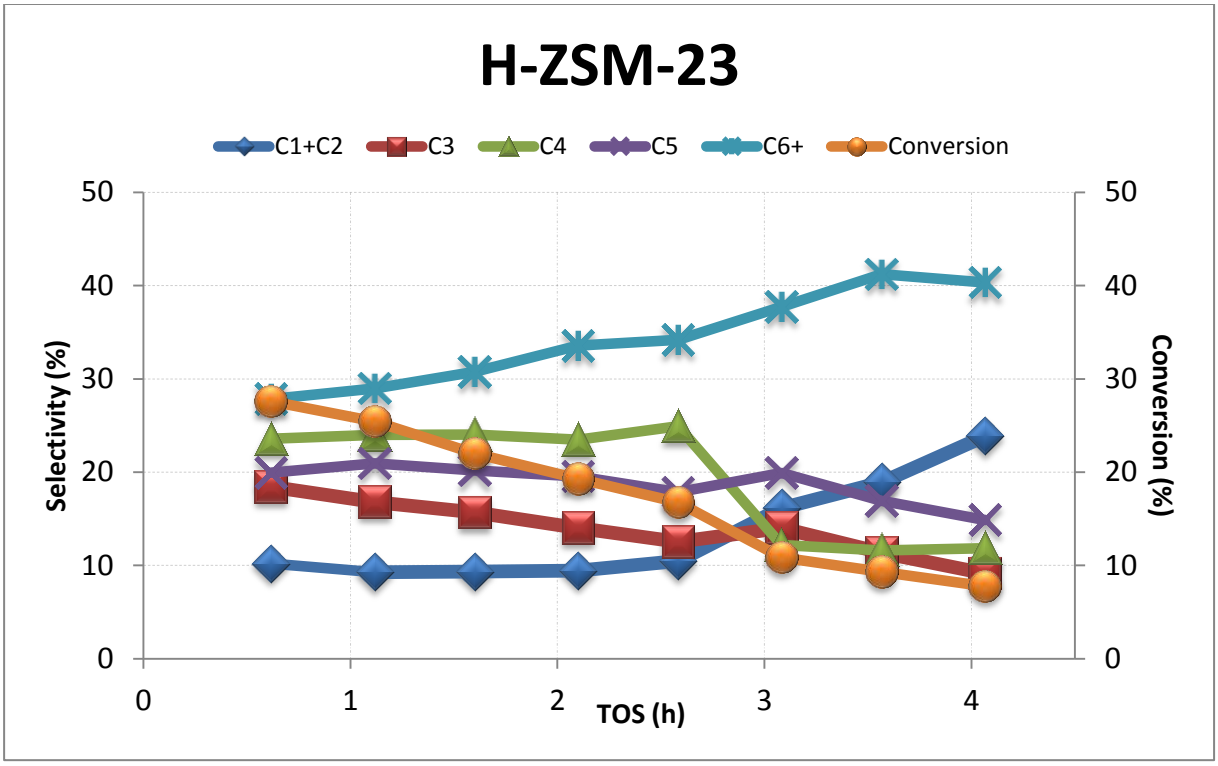

Figure 4. 76: Methanol conversion and product selectivity during MTH reaction at 400°C and WHSV = 2.0gg^{-1} h^{-1} as a function of TOS in H-ZSM-23 zeolite.

During 4 hours of MeOH contact, we can clearly see that conversion drops as a function of time from GC-MS-FID effluent analysis (Figure 4. 76). However, conversion at initial stage of the reaction is too low (28%). This is due to the bypassing MeOH mentioned earlier in this section. Product selectivity seems to show similar trend as in the result from catalytic testing

in Figure A. 1. Result from catalytic testing, in fact, provides more detail regarding product selectivity. For example, aromatic and aliphatic C_{6+} species can be discriminated from each other in catalytic testing result as well as alkyl and alkenyl C_4 products. Based on catalytic testing result, C_4 products reported here in Figure 4. 76 are mostly alkenyl species, and C_6 products are mostly aliphatic species. Overall, ZSM-23 shows high selectivity towards olefin product (C_3-C6) and low selectivity towards ethane, which implies that MTH reaction in H-ZSM-23 favors the cycle of olefin methylation and cracking [15, 104].

H-ZSM-22

In-situ spectra recorded during MTH reaction on the H-ZSM-22 zeolite are similar to those of H-ZSM-23. Existence of ~1594 and 1362 cm^{-1} band, coke bands, and their intensity growth over increasing time can be observed from Figure 4. 77. As in H-ZSM-23, the intensity of ~1594 cm^{-1} is much lower compare to spectra of other fast deactivating zeolites during MTH reaction (Figure 4. 101). For H-ZSM-22, the intensity of this peak is even lower than that of H-ZSM-23. ~1506 cm^{-1} band is characteristic only for H-ZSM-23 and H-ZSM-22 which implies the existence of linear or branched saturated or allylic hydrocarbons. Another band at ~1457 cm^{-1} is similar to the band at same wavenumber in H-ZSM-23, and thought to be originated from active aliphatic intermediate species. In ν(CH) region, methoxy on silanols gives rise to the bands at ~2958 and 2857 cm^{-1}, and asymmetric stretching of CH_2 from the methylation products [66] gives rise to the band at ~2925 cm^{-1}. Its corresponding symmetric stretching at ~2856 cm^{-1} band, again, might overlap with the band from methoxy on silanols. In the case of H-ZSM-22, the shoulder around ~2977 cm^{-1} which is suspected to be from asymmetric stretching of methoxy adsorbed on bridging Brønsted acid sites is observed. Its corresponding symmetric stretching is normally observed at ~2867 cm^{-1} where contribution from other species makes the interpretation of the peak difficult.

As in H-ZSM-23, ν(OH) band of Brønsted acid sites kept a bit of intensity in H-ZSM-22 even though conversion decreased to 1/3 level of initial conversion. This can be explained in the same way, blockage of pore opening by the coke species [104-106].

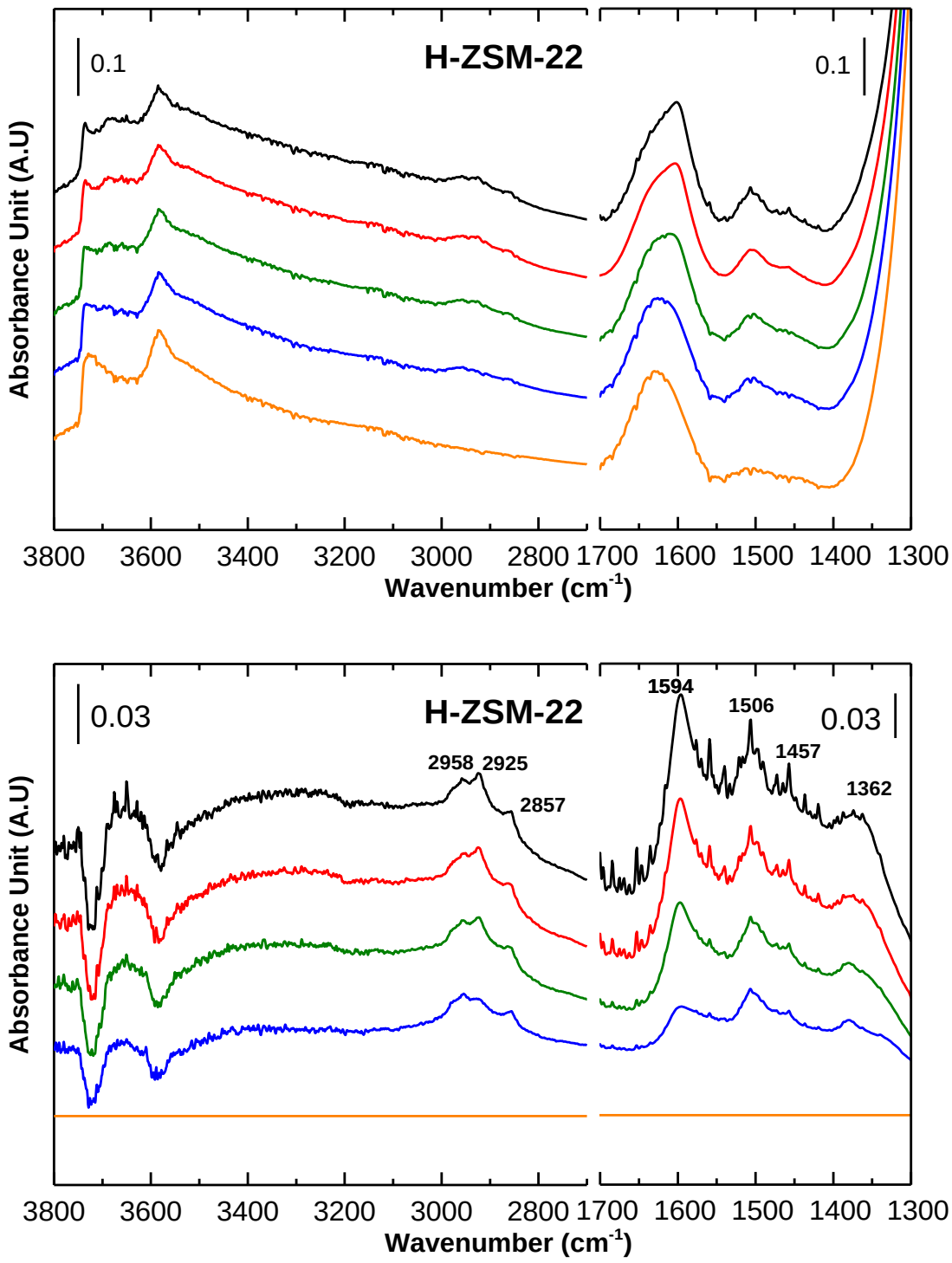

Figure 4. 77: In situ FTIR Spectra of the H-ZSM-22 zeolite obtained before introducing MeOH (yellow), after 1h (blue), 2h (green), 3h (red) and 4h (black) of contact with MeOH at 400°C and WHSV = 2.0$gg^{-1}h^{-1}$. (Upper) recorded spectra (Lower) clean zeolite spectrum subtracted spectra.

Conversion of MTH reaction over H-ZSM-22 shows also similar trend to that over H-ZSM-23. We see decrease of conversion, even though overall conversion is considerably low compare to catalytic testing result due to bypassing MeOH. C_{6+} products shown in Figure 4. 78 are mostly aliphatic species, and C_4 products are mostly alkenyl species judging from the Figure A. 3. According to the catalytic testing result, H-ZSM-22 reaches to the full deactivation faster than H-ZSM-23, but both of the zeolites show similar product distribution during the reaction such as low aromatic products selectivity, high selectivity towards C_3-C_6 olefins, and low selectivity towards ethene which is strong evidence that alkene cracking/methylation cycle is preferred in MTH reaction over H-ZSM-22 and H-ZSM-23 zeolite [15, 104].

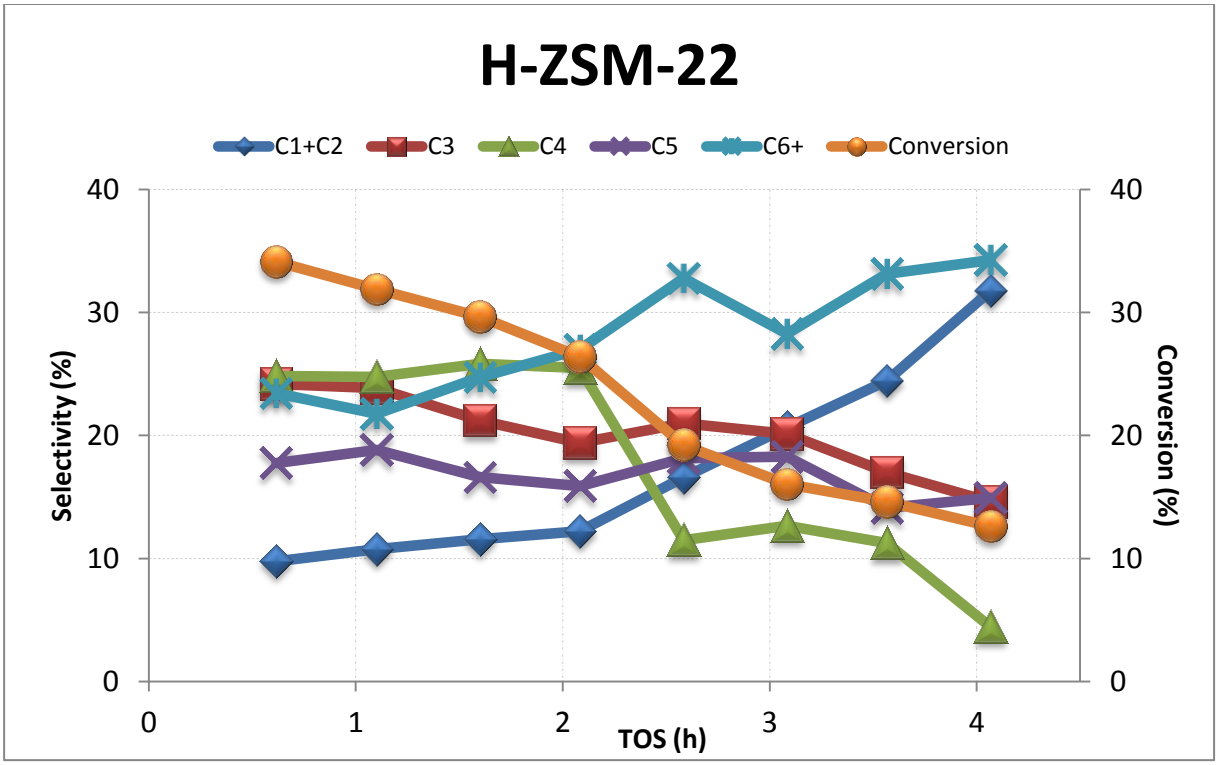

Figure 4. 78: Methanol conversion and product selectivity during MTH reaction at 400°C and WHSV = 2.0gg^{-1} h^{-1} as a function of TOS in H-ZSM-22 zeolite.

H-Mordenite

From upper panel of the Figure 4. 79, it is seen that almost all Brønsted acid sites were consumed during 4 hours of MTH reaction. Subtracted spectra show development of several peaks. In ν(CC)/δ(CH) region, the coke bands are seen at ~1587 and 1375 cm^{-1}. ~1506 cm^{-1}

band which was quite prominent in H-ZSM-23 and H-ZSM-22 zeolite is absent in H-Mordenite. Instead, a weak band at ~1500 cm^{-1} is observed. Assignment of this band is rather difficult since paraffinic species, olefinic species of neutral and cationic polyene, and non-condensed aromatics can all be candidates. ~1423 cm^{-1} can be said to be from CH bending modes of paraffinic species.

In ν(CH) region, a new band at ~3119 cm^{-1} that was absent in one-dimensional 10-ring zeolite is observed. This band is from aromatic species. There is very asymmetric band at ~2929 cm^{-1}. Considering the asymmetry, one can suspect that the band consists of several components. The one gives highest intensity, which may have maxima around ~2929 cm^{-1} is from methylation products [66]. From the quite amount of consumption in hydroxyl groups in silanols and Brønsted acid sites upon MeOH injection, it is natural to expect some amount of methoxy species adsorbed on those acid sites. Therefore, asymmetry is most likely caused by the ν(CH) band of methoxy adsorbed on silanol and Brønsted acid sites. This can be supported by the observation that the maxima of the band at shorter contact time with MeOH, after 1 hour, was at ~2960 cm^{-1} and it shifted towards the ~2929 cm^{-1} as contact time increased to 4 hours. ~2864 cm^{-1} band, which is absent in H-ZSM-23 and H-ZSM22, is observed in H-Mordenite. This band is from methoxy groups on EFAl [99]. It was confirmed from CO adsorption that there are strong Lewis sites existing in H-Mordenite (Figure 4. 41), and it is plausible to say that the EFAl species who contributed to the rise of ~2225 cm^{-1} band upon CO adsorption gave the rise to ~2864 cm^{-1} band upon contact with MeOH. One can argue that this ~2864 cm^{-1} band is located too close to ~2858 and 2867 cm^{-1} band which are assigned to methoxy adsorbed on silanols and Brønsted acid sites, respectively. It is highly possible that the bands overlap and make interpretation and assignment quite difficult. However, the observation of 2864-2868 cm^{-1} band only in H-Mordenite, H-MCM-22, H-IM-5 and H-TNU-9 which are five out of six samples which showed band at 2225-2229cm^{-1} in CO adsorption gives a good reason to assign ~2864 cm^{-1} band appearing during MTH reaction over H-Mordenite to methoxy adsorbed on EFAl species. Of course the possibility that ~2864 cm^{-1} band consists of more than one band is still open. In fact, the existence of CH asymmetric stretching band from methoxy adsorbed on silanols gives an expectation to find CH symmetric stretching band around ~2858 cm^{-1}, and this band might overlap with ~2864 cm^{-1} band.

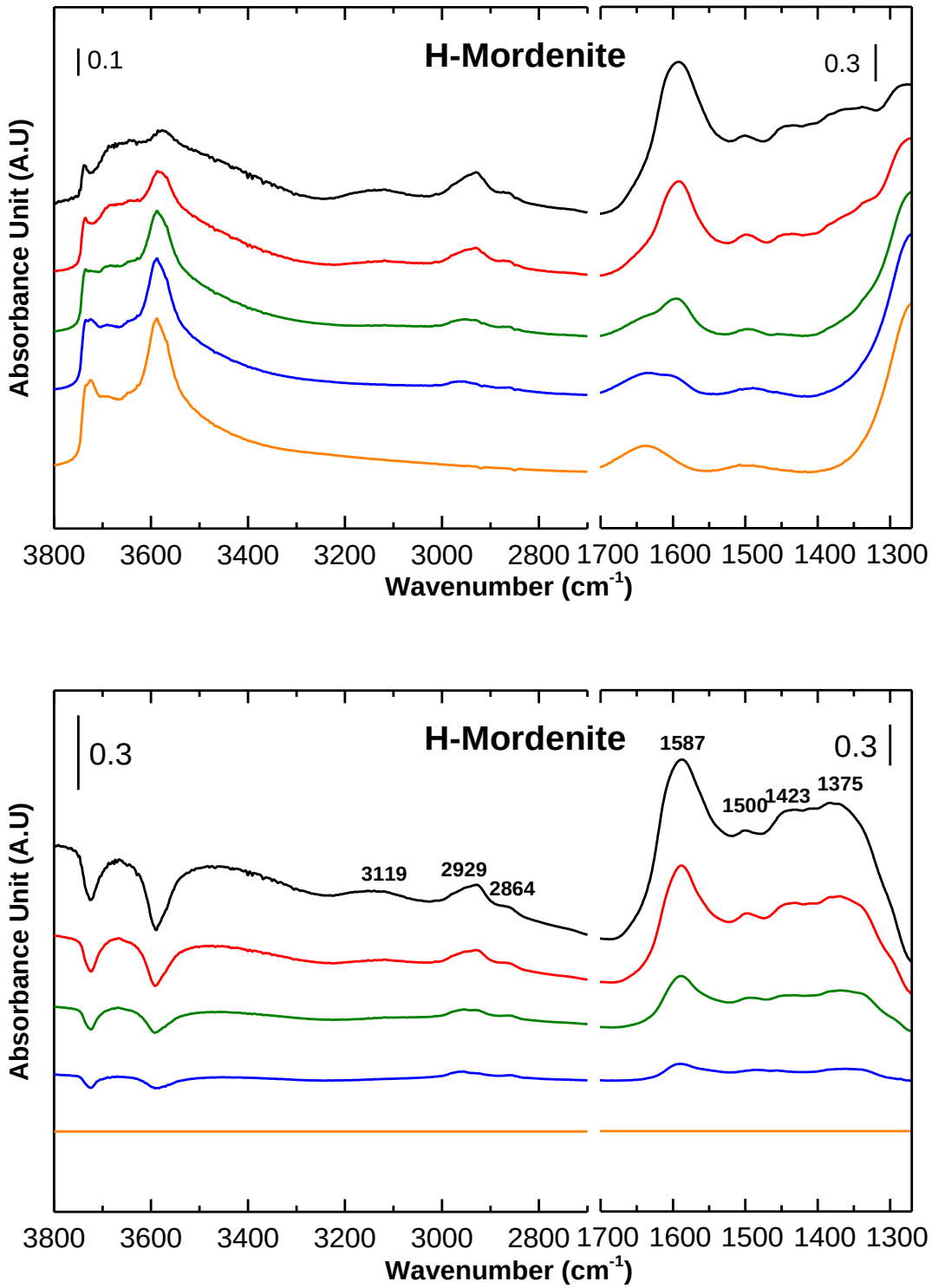

Figure 4. 79: In situ FTIR Spectra of the H-Mordenite zeolite obtained before introducing MeOH (yellow), after 1h (blue), 2h (green), 3h (red) and 4h (black) of contact with MeOH at 400°C and WHSV = 2.0$gg^{-1}h^{-1}$. (Upper) recorded spectra (Lower) clean zeolite spectrum subtracted spectra.

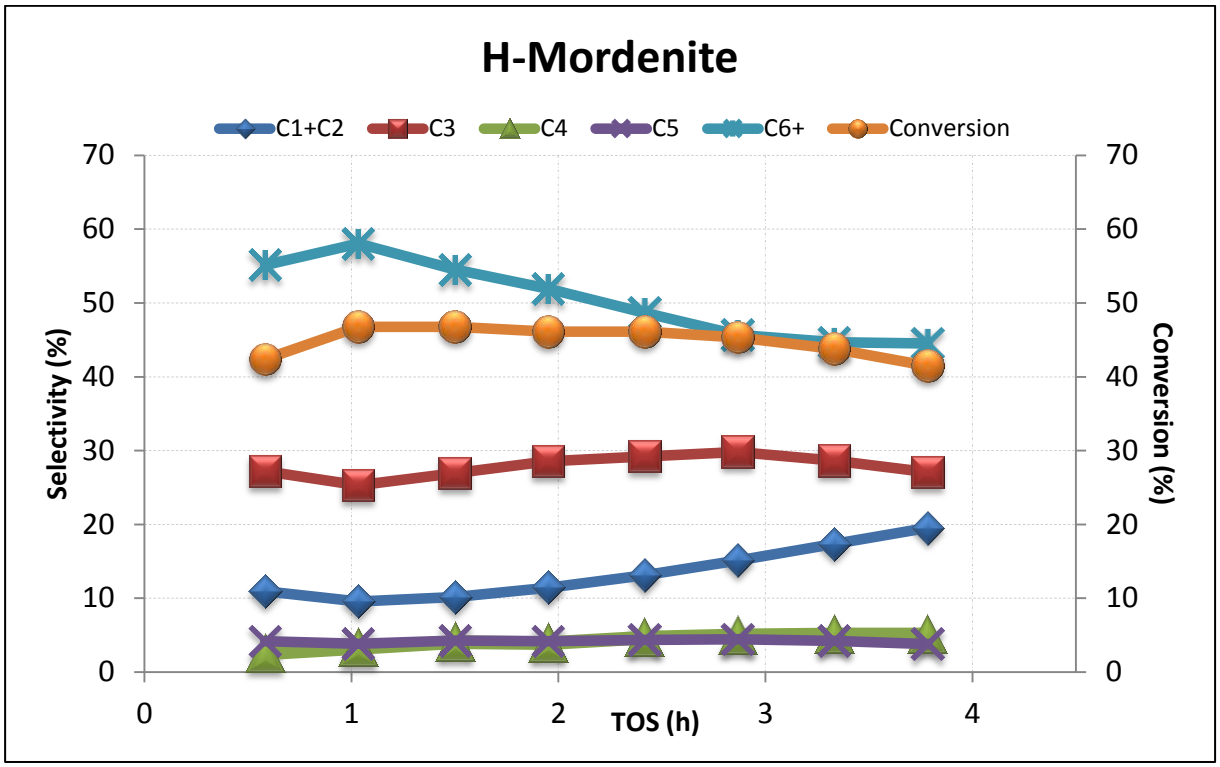

Figure 4. 80: Methanol conversion and product selectivity during MTH reaction at 400°C and WHSV = 2.0gg^{-1} h-^{1} as a function of TOS in H-Mordenite zeolite.

H-Mordenite is known to deactivate rapidly [107], and this can be confirmed from catalytic testing result (Figure A. 5). However, the conversion plot in Figure 4. 80 does not show the sign of total deactivation even after almost 4 hours of contact with MeOH. It is partly because of lower partial pressure of MeOH in IR experiment setup compare to catalytic bed experiment setup. Decreasing partial pressure of MeOH leads to enhanced olefin selectivity and less coke deposition [107, 108]. However, it is still strange since we see the decrease in conversion in H-ZSM-23 and H-ZSM-22 from GC-MS-FID instrument connected to transmission IR cell. According to catalytic testing, these two samples deactivate less rapidly compare to H-Mordenite. Moreover, from normalized spectra comparison in Figure 4. 101, it is seen that coke bands of the H-Mordenite is quite intense compare to other samples. Actually, they are second most intense after H-SUZ-4. Another possible explanation is inaccurate GC-MS-FID analysis performed for H-Mordenite. The detail setting of GC-MS-FID experiment was changed after measuring only H-Mordenite because of unclear peak identification. Some of the peaks were combined together and it was difficult to identify and quantify the peaks. So, H-Mordenite shows different retention time, and peaks especially

around MeOH is very difficult to distinguish. It is possible that the conversion calculation was affected by this, and gave somewhat wrong values. Without more experimental investigation, it is difficult to explain why conversion of H-Mordenite from GC-MS-FID instrument connected to HTHP IR cell shows such behavior in full extent.

H-MCM-22

Now we move on to two-dimensional zeolite, H-MCM-22. Quite amount of Brønsted acid sites were consumed after four hours of MTH reaction over H-MCM-22, but not all of them. Subtracted spectra show bands developed in ν(CC)/δ(CH) region and ν(CH) region. As three other previous samples, two coke bands appear, at ~1598 and 1345 cm^{-1} in the ν(CC)/δ(CH) region. Interestingly, the lower frequency coke band of H-MCM-22 is seen ~1345 cm^{-1} while that of one-dimensional zeolites (H-ZSM-23, H-ZSM-22, and H-Mordenite) were at between ~1375 and 1362 cm^{-1}. CH bending mode of methyl groups usually appear at 1380-1370 cm^{-1}, that of gem-dimethyl or iso- species appear at 1370-1365 cm^{-1}, that of trimethyl or tert-butyl species at ~1365 cm^{-1} and that of methanylylidene(-CH=) at 1350-1330 cm^{-1} [109, 110]. Therefore, it is tempting to say that the lower frequency coke band in H-MCM-22 is originated from methanylylidene (-CH=) species while the coke band in one-dimensional zeolites is from methyl groups. Shoulders at ~1374, 1323 cm^{-1} and weak bands at ~1493, ~1450 cm^{-1} from complex mixture of carbonaceous species are observed as well. Absence of ~1507 cm^{-1} band is another clear difference between H-MCM-22 and one-dimensional 10-memebered ring channel zeolites, and this is indication of the absence of linear or branched saturated or allylic hydrocarbons [69].

In ν(CH) region, trace of aromatic species is seen from a broad band at ~3078 cm^{-1}. ~2864 cm^{-1} band can be primarily assigned to methoxy groups adsorbed on EFAl from the fact that existence of strong Lewis acid sites was confirmed from CO adsorption experiment (Figure 4. 43). There is a possibility that methoxy adsorbed on silanols and Brønsted acid sites contribute to the band as well since their bands appear at the wavenumber not far from ~2864 cm^{-1}. One can see that intensity of ~2932 cm^{-1} band increases as contact increases. After one hour of contact with MeOH, ~2932 cm^{-1} band showed similar intensity with ~2979 cm^{-1} band. The intensity, however, of ~2932 cm^{-1} band grew faster afterwards resulting in higher intensity compare to ~2979 cm^{-1} band. ~2932 cm^{-1} band is assigned to the asymmetric

stretching band of CH_2 from the methylation products [66]. ~2979 cm^{-1} band is at pretty much exactly where we expect the methoxy adsorbed on Brønsted acid sites to be even though the shape of the band is not sharp implying the composition of several bands from methoxy species adsorbed on silanol and EFAl. Relatively high intensity decrease in Brønsted band compare to silanol band could lead to more clear appearance of ~2979 cm^{-1} band which was not the case for the samples discussed already.

The catalytic testing result which carried out in the similar experimental condition, especially the temperature-wise, could not be found. However, similarities in composition and the reaction pattern of the retained material during the MTH reaction in the H-MCM-22 and H-Beta zeolites were reported by Bjørgen et al. [111]. For example, higher methylbenzenes such as heheptamethylbenzene cation (heptaMB$^+$) and hexamethylmethylenecyclohexadiene (HMMC) function as reaction intermediates in the MTH reaction over both zeolites [111]. Lacarriere et al. [112] studied the MTH reaction over H-MCM-22 (Si/Al = 18) at 450°C and WHSV = 2.0 $gg^{-1}h^{-1}$, and they observed that catalytic lifetime was around 7 hours. Production distribution reported is in fact somewhat similar to the result shown in Figure 4. 82. Amount of ethylene in products is quite large in the early stage of the reaction, but it decreases as the time increases. Instead, C_{3+} products become more abundant after initial stage of the reaction implying that methylation-cracking mechanism is favored after initial stage of reaction is passed. Selectivity of aromatic products increases as time passes as well. Aromatic species are considered to be involved into successive hydrogen transfer reactions leading to coke formation and deactivation of catalyst [112].

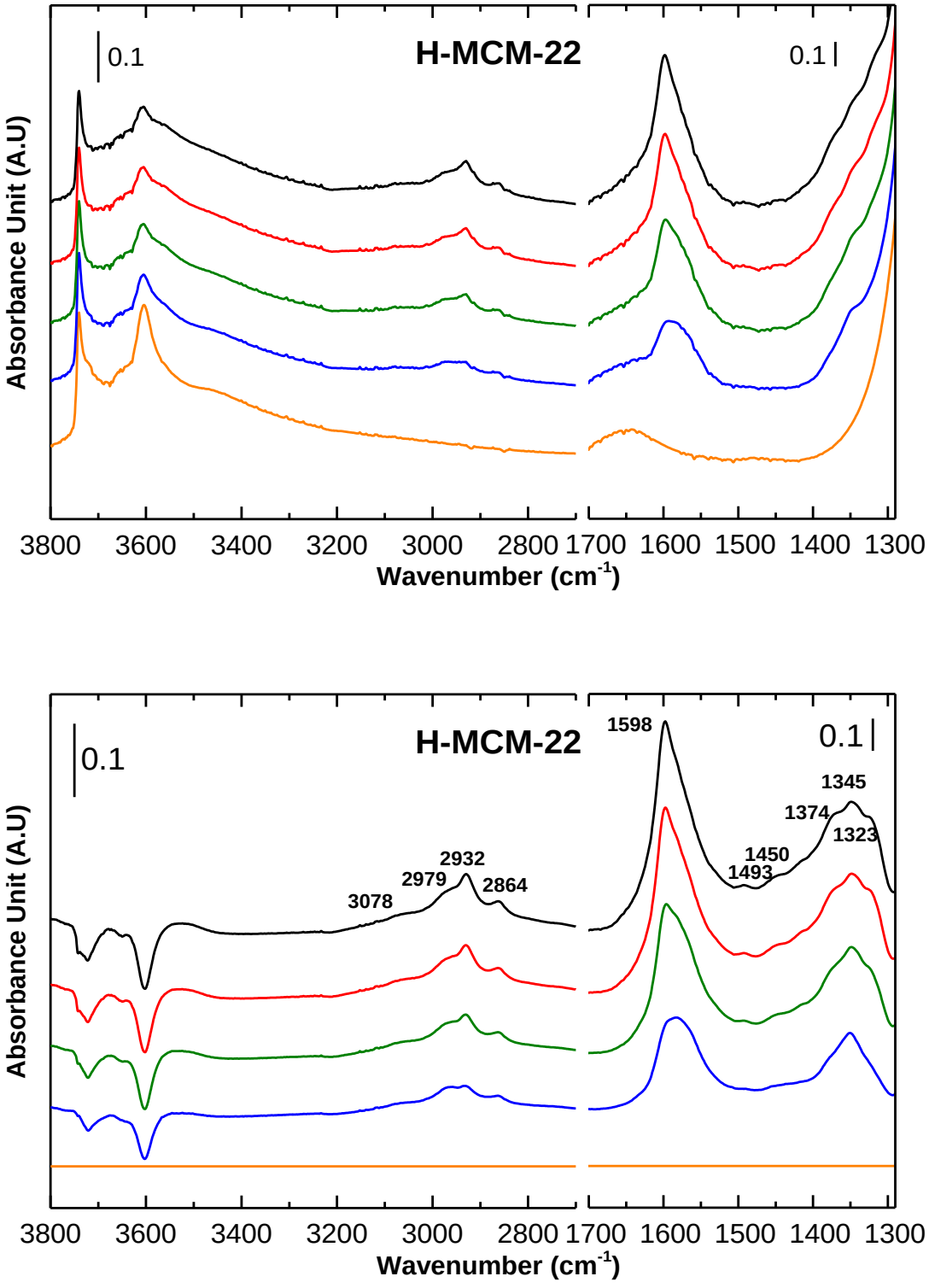

Figure 4. 81: In situ FTIR Spectra of the H-MCM-22 zeolite obtained before introducing MeOH (yellow), after 1h (blue), 2h (green), 3h (red) and 4h (black) of contact with MeOH at 400°C and WHSV = 2.0gg^{-1}h^{-1}. (Upper) recorded spectra (Lower) clean zeolite spectrum subtracted spectra.

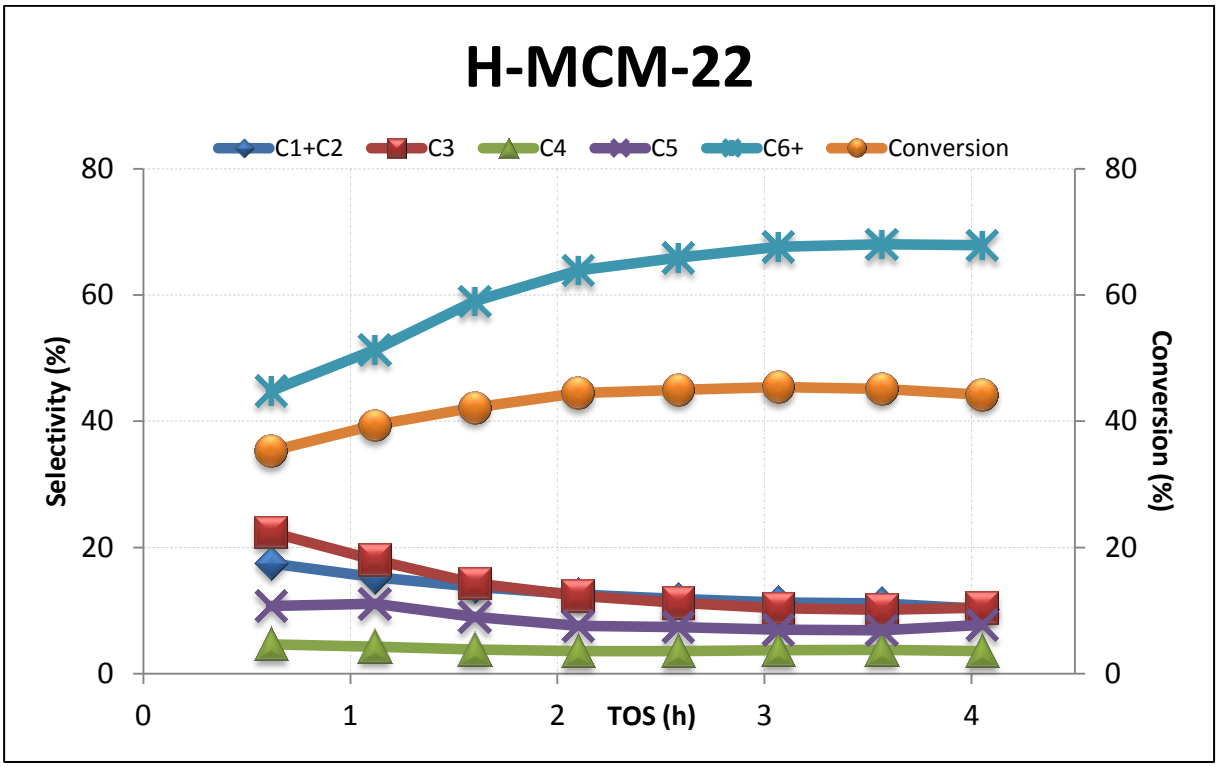

Figure 4. 82: Methanol conversion and product selectivity during MTH reaction at 400°C and WHSV = 2.0gg^{-1} h-^{1} as a function of TOS in H-MCM-22 zeolite.

H-IM-5

Hereinafter, zeolites with three-dimensional channel systems will be discussed. First, we start from H-IM-5 zeolite. During MTH reaction over H-IM-5, coke bands are seen at ~1585 and ~1359 cm^{-1}. Shoulder at ~1385 cm^{-1} and a weak band at ~1430 cm^{-1} are originated from paraffinic species. ~2929 cm^{-1} band in ν(CH) region is from the methylation products. . ~3116 cm^{-1} band indicates that there are aromatic species in the system. Shoulder at ~2969 cm^{-1} and a weak band at ~2868 cm^{-1} can be primarily assigned to methoxy on EFAl. Observation of ~2229 cm^{-1} band from CO adsorption experiment supports the high possibility of existence of EFAl species in the H-IM-5 zeolite. However, the bands we observe are the products of several overlapping band, and the contributors can be the methoxy adsorbed on silanol (2960-2956 and 2857-2855 cm^{-1}) and methoxy adsorbed on Brønsted acid sites (~2978 and 2867 cm^{-1}).

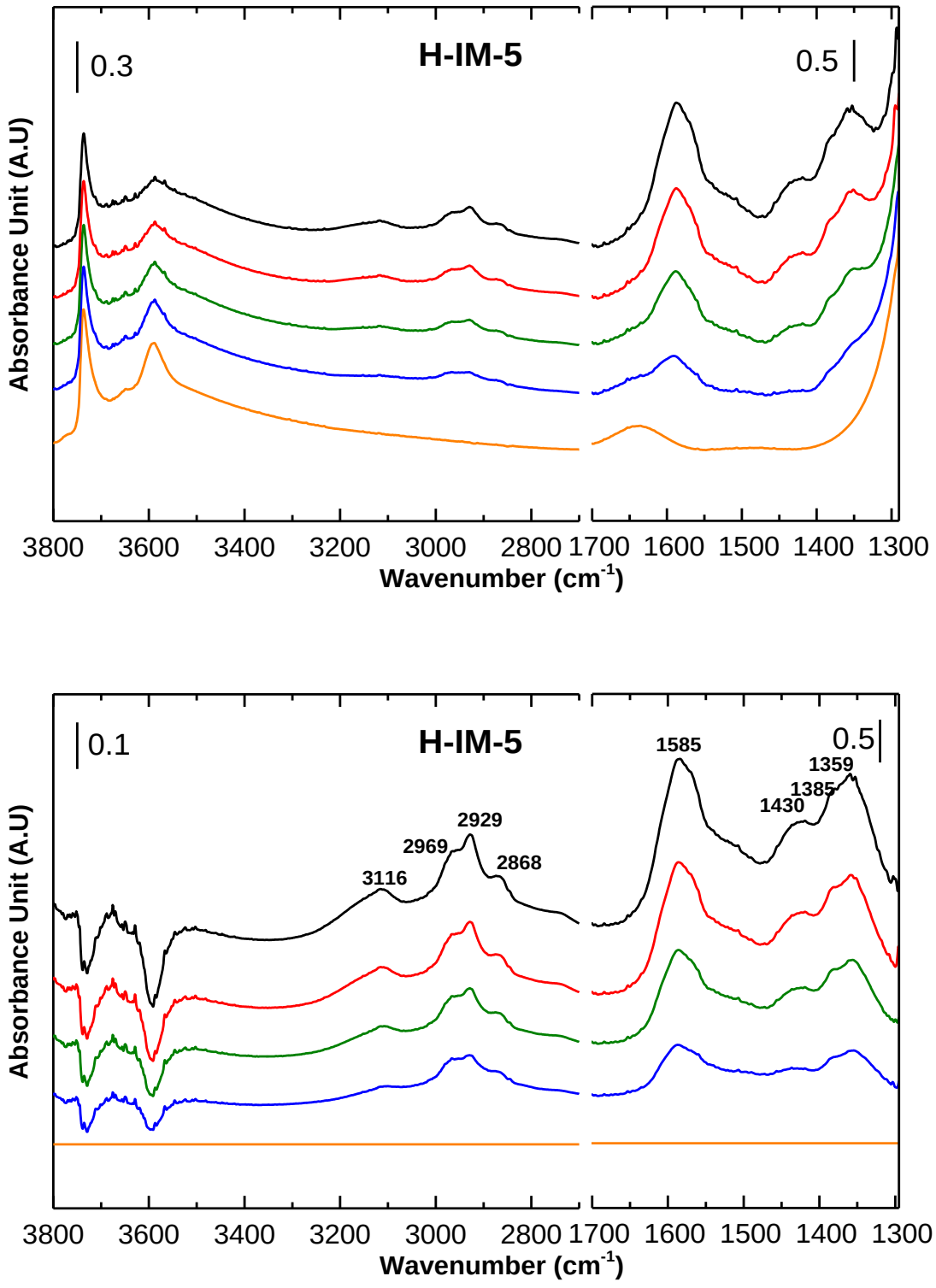

Figure 4. 83: In situ FTIR Spectra of the H-IM-5 zeolite obtained before introducing MeOH (yellow), after 1h (blue), 2h (green), 3h (red) and 4h (black) of contact with MeOH at 400°C and WHSV = 2.0gg^{-1}h^{-1}. (Upper) recorded spectra (Lower) clean zeolite spectrum subtracted spectra.

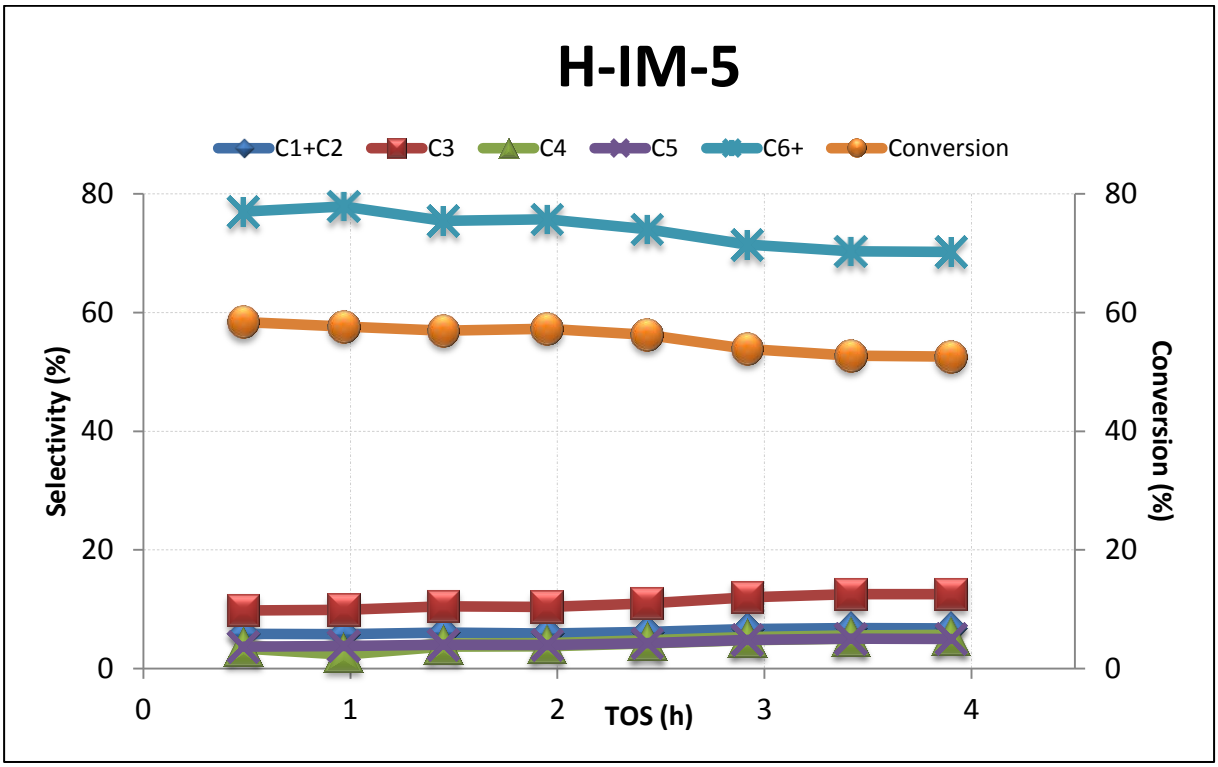

Figure 4. 84: Methanol conversion and product selectivity during MTH reaction at 400°C and WHSV = 2.0gg^{-1} h^{-1} as a function of TOS in H-IM-5 zeolite.

It was found out by W. Skistad [82] that IM-5 and TNU-9 zeolites showed similar gas effluent selectivity with H-ZSM-5 zeolite in MTH reaction, but TNU-9 and IM-5 had lower catalytic stability than H-ZSM-5 at 350°C and WHSV =9.0 $gg^{-1}h^{-1}$. Larger aromatic species which were allowed to form in large cavities of H-TNU-9 and H-IM-5 was pointed out as a possible reason for low stability. Aromatics containing two, three and four benzene rings among the entrapped species were observed after the end of the experiment at the condition mentioned above. Catalytic testing result carried out by S. Etemadi [2] showed that catalyst lifetime of H-IM-5 sample at 400°C, WHSV = 2$gg^{-1}h^{-1}$ condition is around 28 hours (Figure A. 7) and aliphatic C_{6+} and C_3 species are most abundant among products.

H-ITQ-13

In spectroscopy technique-wise, H-ITQ-13 is a good sample to confirm whether some of the ν(CH) band assignments being used in this work is proper or not. It is because that H-ITQ-13 has much intense silanol band compare to Brønsted band, relatively long catalytic lifetime

(Figure A. 10, [113]) which can be related to less coking during four hours of MTH reaction, low selectivity towards aromatic products, and no strong Lewis acid species detected from CO adsorption. That is, with minimized contribution from of other factors, one can study the bands arising mainly due to silanols and the MTH intermediates or products using spectra of H-ITQ-13 zeolite.

In the ν(CH) region, ~2954 and 2856 cm^{-1} band which are from methoxy on silanol groups are clearly observed. ~2924 cm^{-1} band is less clear, but still able to observe. This band is related to methylation products formed during the MTH reaction. The band at 3200-3000 cm^{-1} from CH stretching of aromatics is absent.

In the ν(CC)/δ(CH) region, the coke bands at ~1590 and 1341 cm^{-1} are seen. ~1590 cm^{-1} band is originated from aromatic species while ~1341 cm^{-1} band is from methanylylidene (-CH=) species. ~1341 cm^{-1} band is quite broad in shape implying that the band consists of several components which are from complex hydrocarbon species. The intensity of ~1458 cm^{-1} band shows little changes during the MTH reaction, and this can leads to the assignment of the peak to active aliphatic intermediate species even though overlapping with other bands are highly possible judging from the very broadness of the band.

Effluent analysis from the GC-MS-FID connected directly to the IR cell and two separate analyses from the catalytic testing performed by S. Etemadi [2] (Figure A. 9, Figure A. 10) and by Skistad [113] show similar result except the early stage product selectivity (TOS = 0.5-1.5 h) and overall conversion level reported from GC-MS-FID connected directly to the IR cell (Figure 4. 86). As discussed earlier, the overall conversion is much lower when the experiment was performed at HTHP cell due to considerable amount of bypassing MeOH. Because of this factor, it is more reliable to refer results from catalytic testing for the overall discussion of product selectivity and conversion. H-ITQ-13 is slightly less stable than ZSM-5, but it is fourth most stable zeolite after three MFI samples (H-MFI-27, H-Pentasil, H- ZSM-5) among the samples investigated in this work. Regarding the product distribution, high selectivity towards C_3 and C_{6+} aliphatic species and relatively low selectivity towards aromatic species were observed. W. Skistad [113] described the product spectrum of H-ITQ-13 as “intermediate of H-ZSM-5 and H-ZSM-22”.

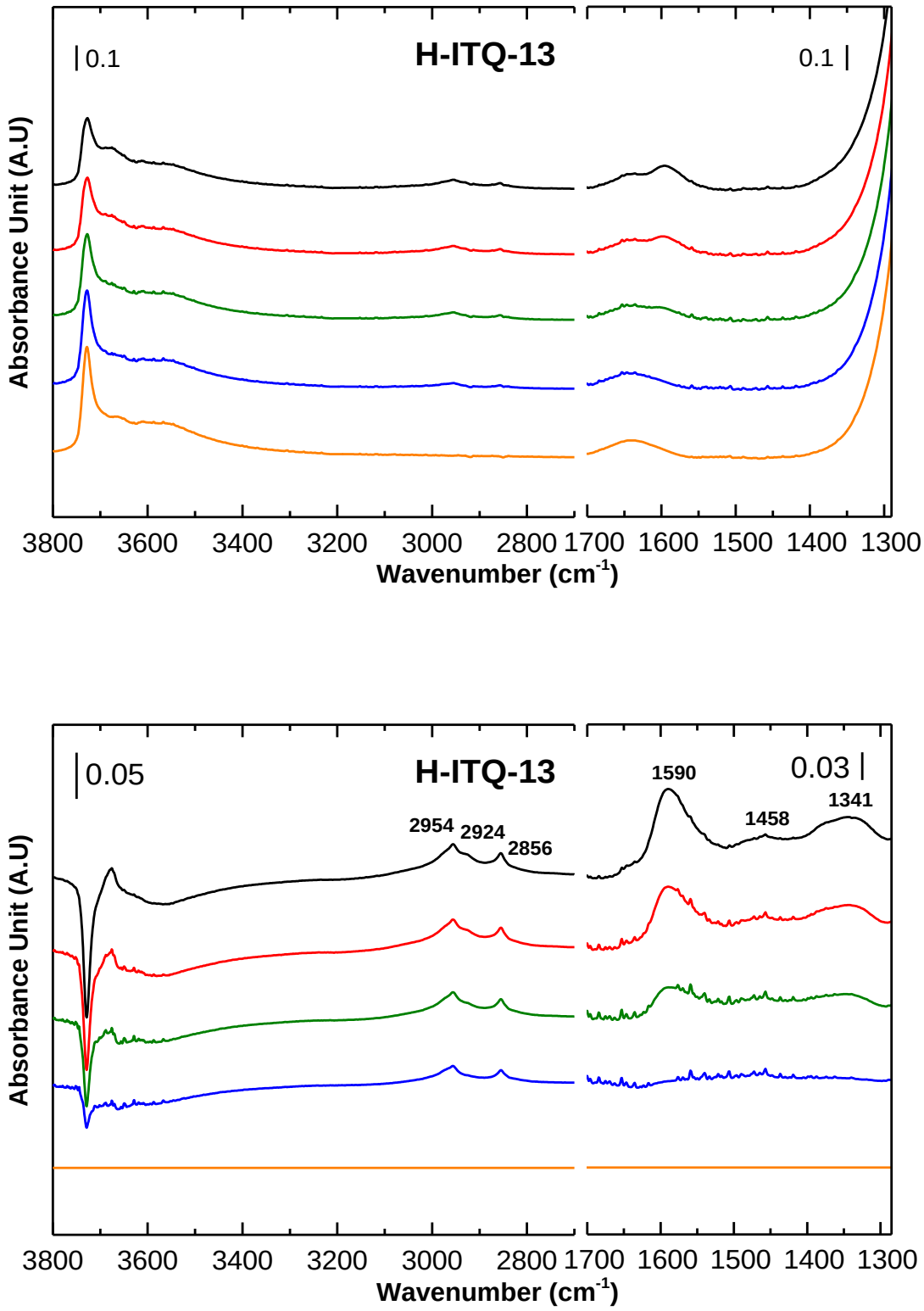

Figure 4. 85: In situ FTIR Spectra of the H-ITQ-13 zeolite obtained before introducing MeOH (yellow), after 1h (blue), 2h (green), 3h (red) and 4h (black) of contact with MeOH at 400°C and WHSV = 2.0gg^{-1}h^{-1}. (Upper) recorded spectra (Lower) clean zeolite spectrum subtracted spectra.

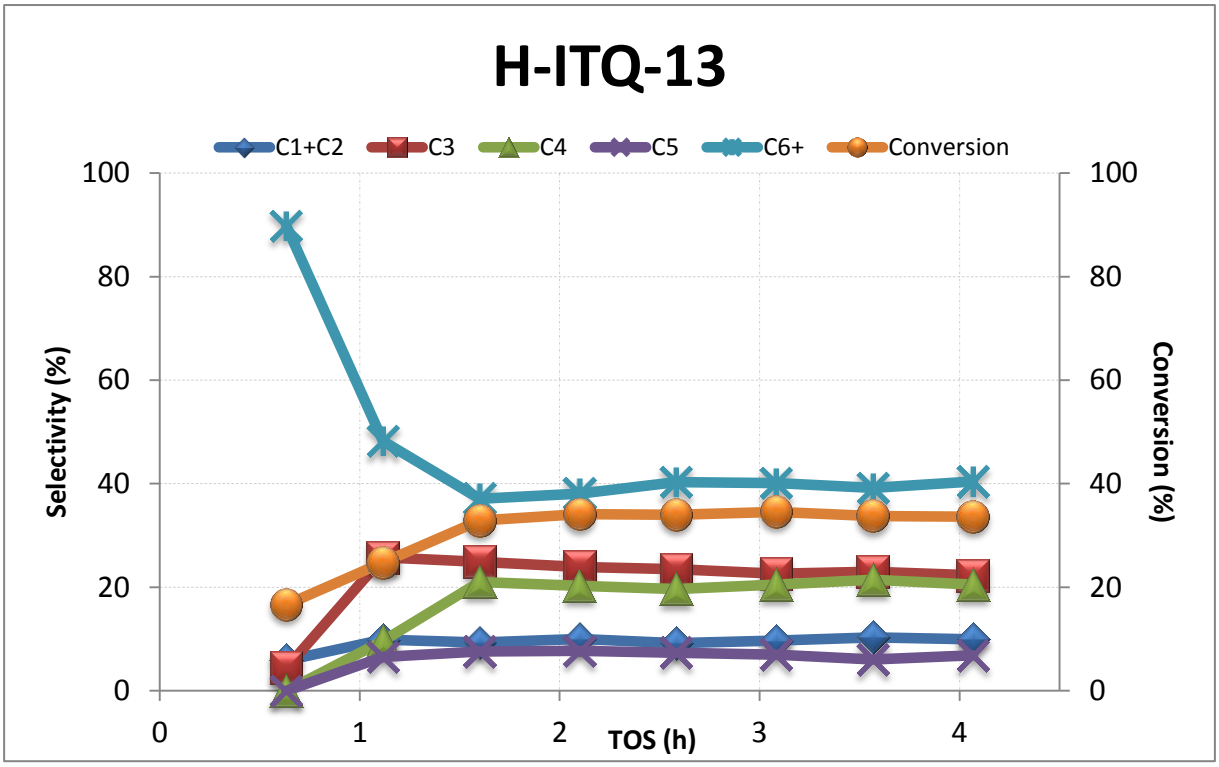

Figure 4. 86: Methanol conversion and product selectivity during MTH reaction at 400°C and WHSV = 2.0gg^{-1} h-^{1} as a function of TOS in H-ITQ-13 zeolite.

MFI (ZSM-5) zeolites

Three H-ZSM-5 zeolites with different Si/Al ratio, named H-MFI-27 (Si/Al = 13.5), H-Pentasil (Si/Al = 45) and H-ZSM-5 (Si/Al = 50), are investigated in this work, and they will be discussed together for better comparison between samples. Having same material with same topology with different acidic features such as acid strength and acid concentration provides a great opportunity to investigate how these features affects the MTH reaction over H-ZSM-5 with minimized contribution from other sources even though the two variables (acid strength and density) cannot be studied separately in the given selection of samples. Si/Al and acidic properties of three samples which were obtained from CO and pyridine adsorption experiment are presented in Table 4. 13. One can see that the acid strength decreases in order of H-Pentasil > H-MFI-27 ≈ H-ZSM-5 while total concentration of Brønsted acid sites decreases in order of H-MFI-27 » H-ZSM-5 ≈ H-Pentasil.

Table 4. 13: Acidic properties of three MFI samples investigated in this work.

	Theoretical Si/Al	Acid Strength (Δν(OH) in CO adsorption) (cm^{-1})	Total concentration of bridging Brønsted acid sites from pyridine adsorption (mmol/g catalyst)
H-MFI-27	13.5	-306	1.074
H-Pentasil	45	-313	0.277
H-ZSM-5	50	-305	0.284

Starting from the analysis of in-situ FTIR spectra, Figure 4. 87 and Figure 4. 88 are provided for the convenience of comparison of spectra of different samples. In the ν(CH) region (Figure 4. 87), one can see the clear difference with ~3119 cm^{-1} band between the zeolites. The zeolite with low Si/Al, H-MFI-27 is the only one shows the band at ~3119 cm^{-1} which is originated from CH stretching mode of aromatic species. Another difference is intensity of 2926-2930 cm^{-1} band which is from methylation products. H-MFI-27 definitely shows the highest intensity of the band indicating more methylation product in the system. ~2957 and 2858 cm^{-1} band are observed in H-Pentasil and H-ZSM-5 but not in H-MFI-27. These bands are from methoxy adsorbed on silanol groups, and the absence of the band in H-MFI-27 can be explained by significantly low intensity of silanol band in clean H-MFI-27 zeolite spectrum. Instead, a band at ~2975 cm^{-1} is observed in H-MFI-27 which can possibly be assigned to methoxy adsorbed on Brønsted acid sites. ~2913 cm^{-1} band in H-MFI-27 is from CH stretching modes of paraffinic species, but no further specific assignment can be made for now. In ν(CC)/δ(CH) region shown in Figure 4. 88, clear difference in intensity of coke bands is seen. This implies that there are more coke-related species in H-MFI-27 than the two other samples.

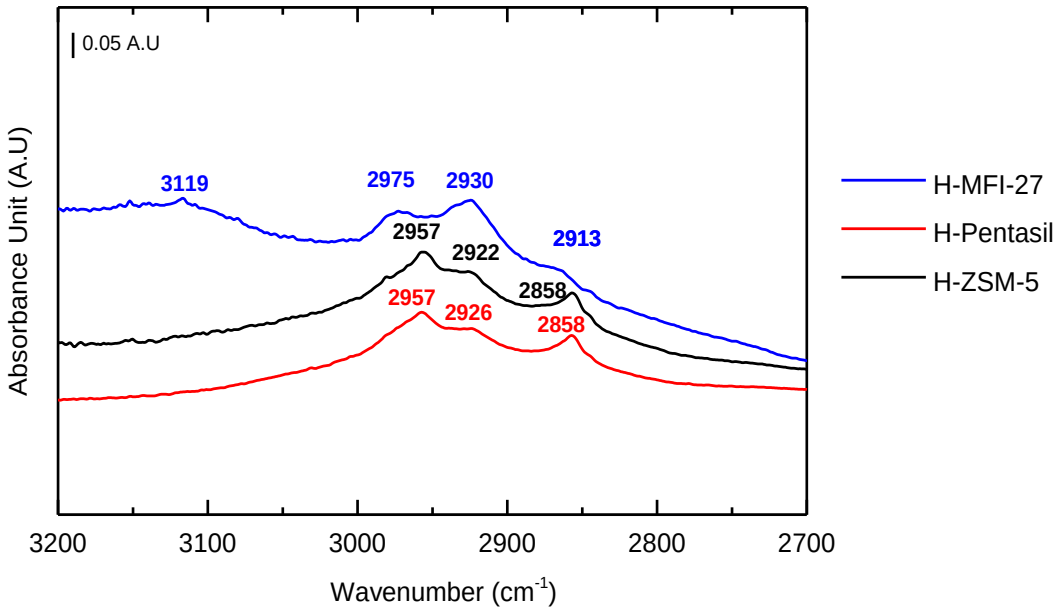

Figure 4. 87: Normalized spectra of H-MFI-27, H-Pentasil, and H-ZSM-5 after 4 hours of contact with MeOH. Each spectrum is subtracted by its activated zeolite spectrum. Only ν(CH) region is shown.

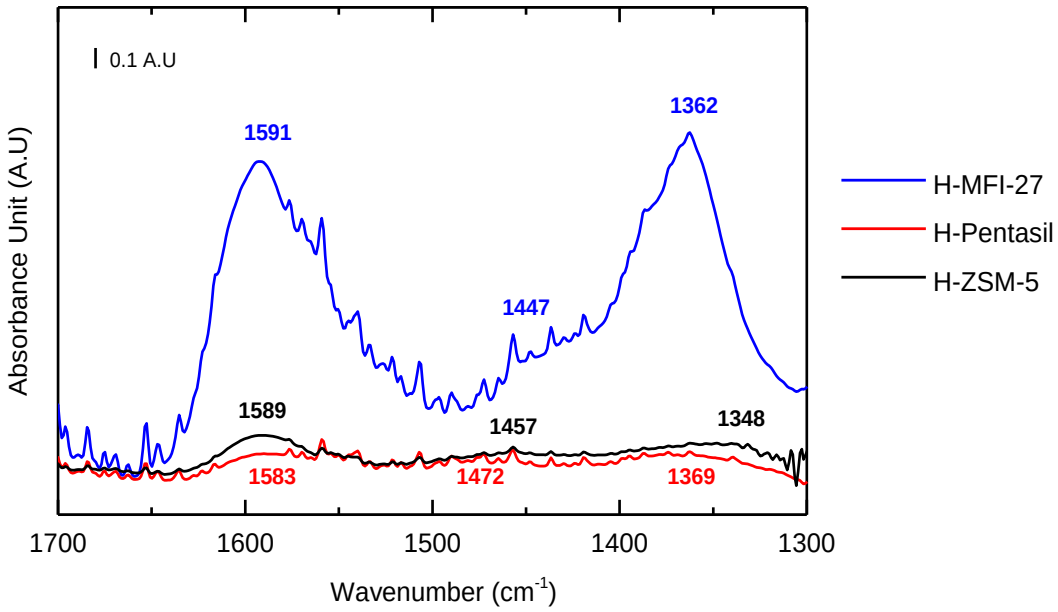

Figure 4. 88: Normalized spectra of H-MFI-27, H-Pentasil, and H-ZSM-5 after 4 hours of contact with MeOH. Each spectrum is subtracted by its activated zeolite spectrum. Only ν(CC)/δ(CH) region is shown.

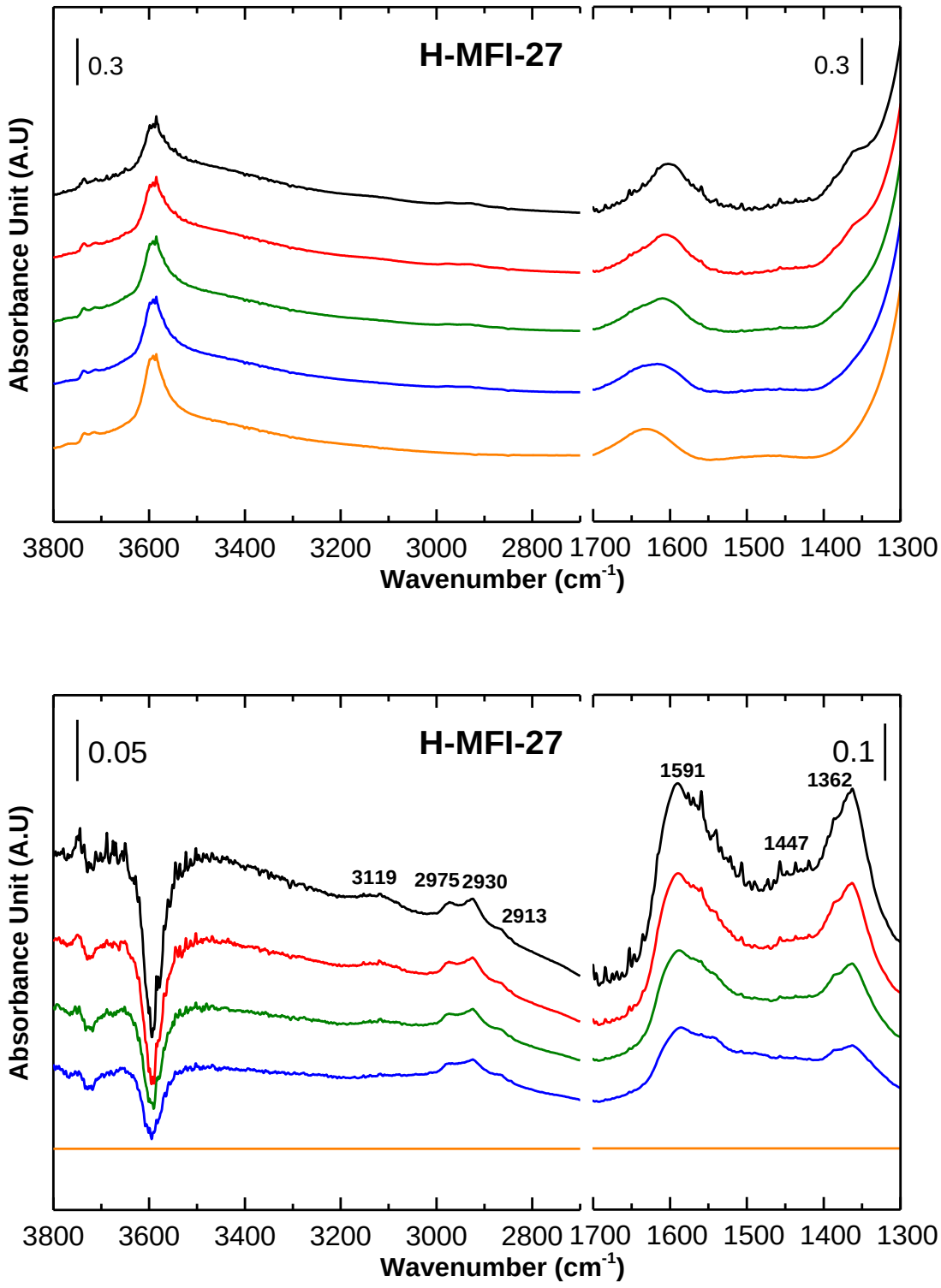

Figure 4. 89: In situ FTIR Spectra of the H-MFI-27 zeolite obtained before introducing MeOH (yellow), after 1h (blue), 2h (green), 3h (red) and 4h (black) of contact with MeOH at 400°C and WHSV = 2.0gg^{-1}h^{-1}. (Upper) recorded spectra (Lower) clean zeolite spectrum subtracted spectra.

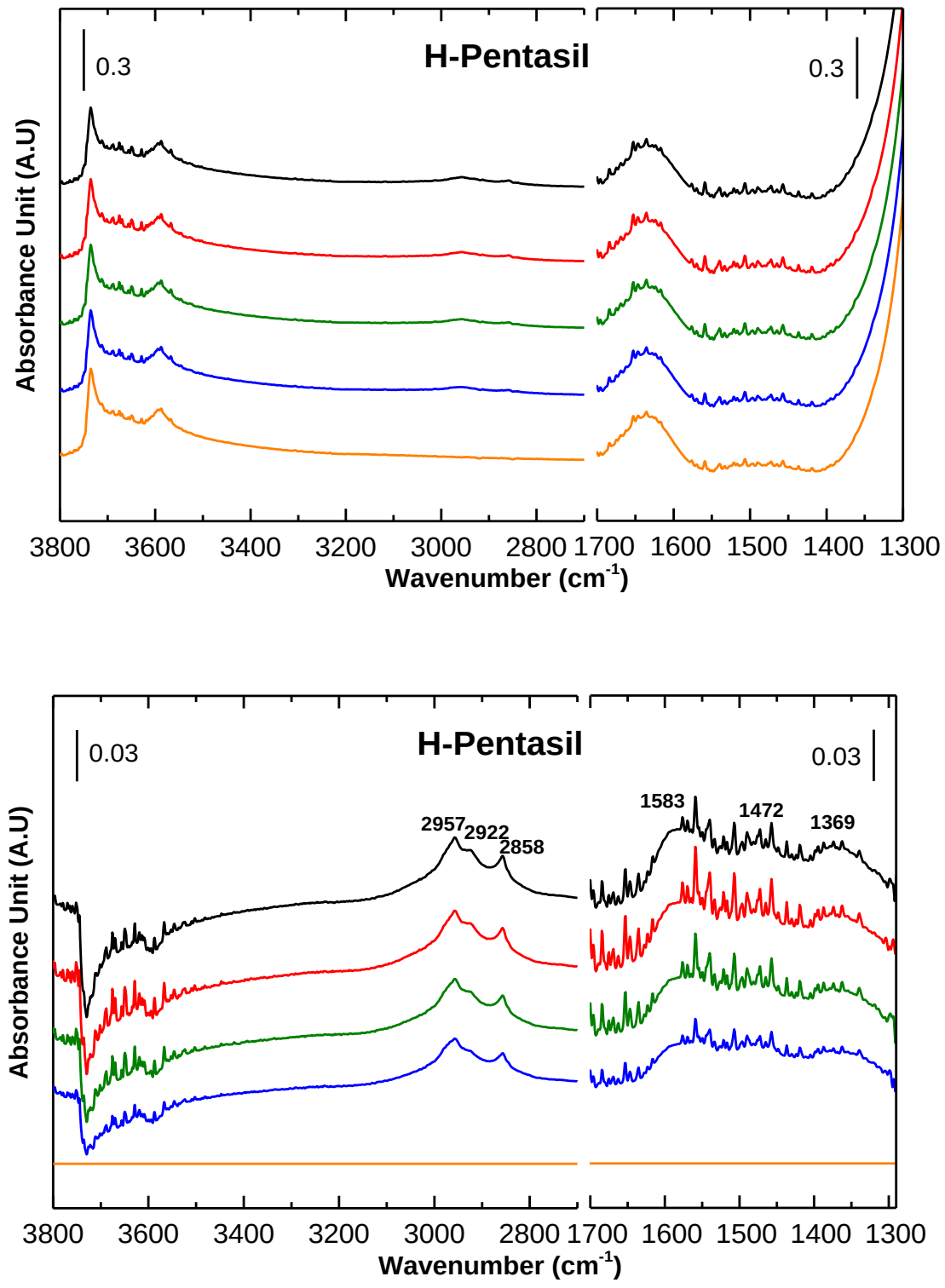

Figure 4. 90: In situ FTIR Spectra of the H-Pentasil zeolite obtained before introducing MeOH (yellow), after 1h (blue), 2h (green), 3h (red) and 4h (black) of contact with MeOH at 400°C and WHSV = 2.0gg^{-1}h^{-1}. (Upper) recorded spectra (Lower) clean zeolite spectrum subtracted spectra.

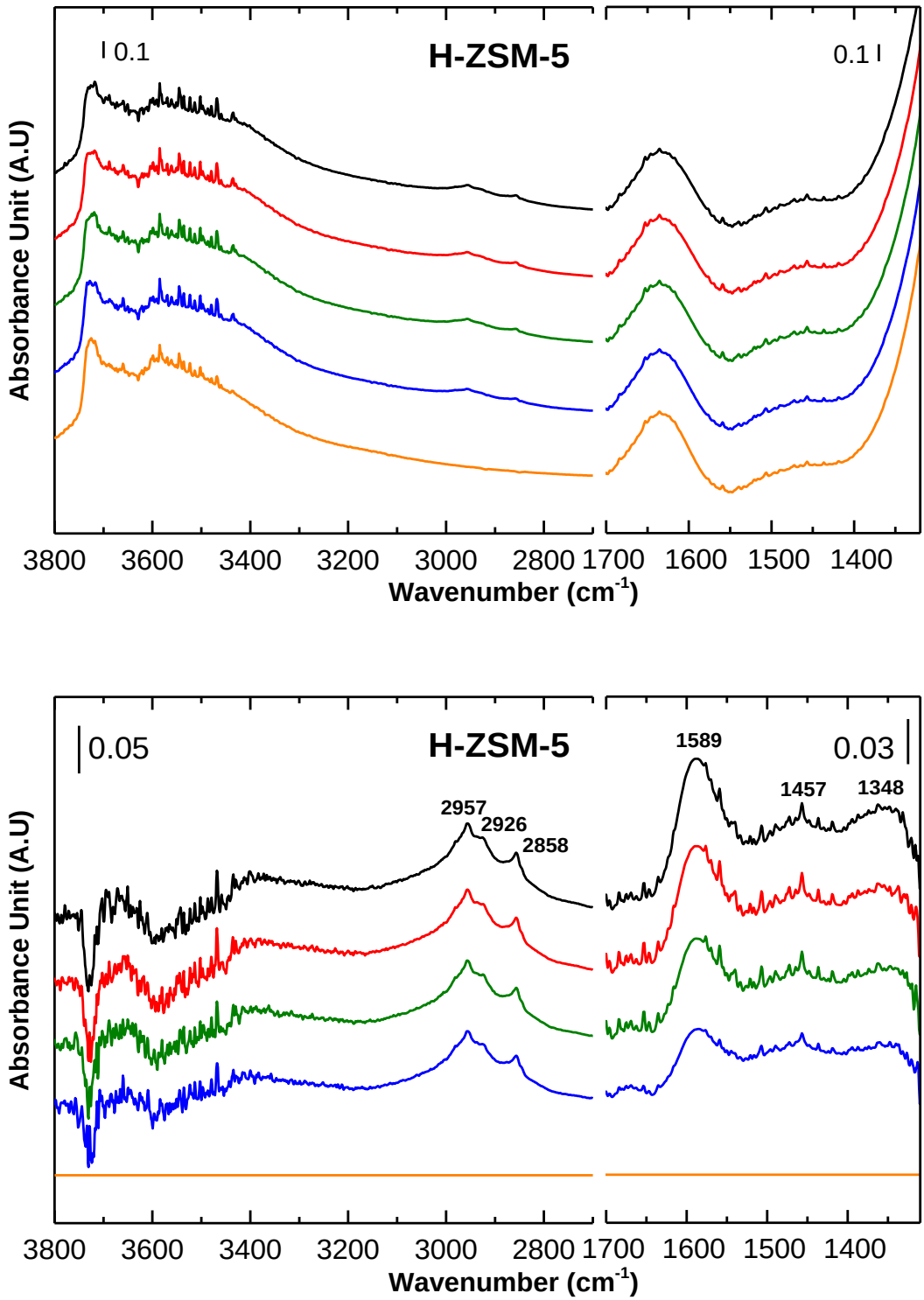

Figure 4. 91: In situ FTIR Spectra of the H-ZSM-5 zeolite obtained before introducing MeOH (yellow), after 1h (blue), 2h (green), 3h (red) and 4h (black) of contact with MeOH at 400°C and WHSV = 2.0gg^{-1}h^{-1}. (Upper) recorded spectra (Lower) clean zeolite spectrum subtracted spectra.

It was reported that the selectivity of propene and ethene increases as the Si/Al ratio of ZSM-5 increases in butene catalytic cracking reaction [114]. That can be applied to the MFI zeolites in MTH reaction, but only to the relationship between propene selectivity and the Si/Al. From H-MFI-27 to H-ZSM-5, one observes that the C_3 selectivity increases as Si/Al increases. As methane selectivity is significant low compare to other products ([115, 116], Figure A. 11, Figure A. 12), the C_1+C_2 curve in Figure 4. 92 - Figure 4. 94 can be interpreted as a C_2 curve. Then, we can find opposite trend in ethene compare to C_3 products. C_2 curve decreases as the Si/Al of MFI samples increases. This is not surprising considering the fact that ethene formation goes through different cycle than other higher alkenes [21]. That is, propene which is mainly formed from alkene cycle in Dual cycle concept can show similar trend as in butene catalytic cracking reaction as methylation and cracking is the main mechanism in the cycle while ethene shows different trend as its formation is not related to the alkene cycle but to arene cycle. Supporting this, increase of C_4 and C_5 product selectivity with increasing of Si/Al is observed as well. Without proper catalytic testing results of these three samples, it is difficult to see the trend in product selectivity of aromatic species as the effluent analysis done in this work does not clearly distinguish the aromatics from aliphatic C_{6+} products. With information about relation between Si/Al and product selectivity of aromatic products, behave of C_2 products in MFI zeolites with different Si/Al could have been explained more in depth. From the observation from the effluent analysis, it was seen that products from alkene cycle becomes more abundant as the Si/Al of MFI zeolite increases. Reversely speaking, arene cycle is more favored when Si/Al is low in MFI zeolites.

Guisnet et al.[117] once wrote expected role of the acidity characteristics as: "*(i) the stronger the acidic sites, the faster the chemical steps and the more pronounced the retention of coke precursors and coke molecules, hence the faster the coking rate; (ii) the higher the density of the acid sites, thus the closer these sites are to each other, the larger the number of successive chemical steps undergone by reactant molecules along the diffusion path within the zeolite crystallites and the more favorable the condensation reactions, hence the faster the coking rate."* From Figure 4. 88 and Table 4. 13, we can see that the coke bands of H-MFI-27 show highest intensity while those of H-ZSM-5 and H-Pentasil show relatively low intensity. There was no big difference in intensity of the coke bands between H-ZSM-5 and H-Pentasil. This is very similar to the order of total bridging Brønsted acid concentration of three samples, H-MFI-27 » H-ZSM-5 ≈ H-Pentasil. The difference in acid strength between three samples is probably not large enough to show clear difference in the coke formation during the MTH

reaction. They only differ 8 cm^{-1} (~3% of its value) in Δν(OH) values. Therefore, this comparison between H-MFI-27, H-ZSM-5 and H-Pentasil can be considered to mainly see the relation between total bridging Brønsted acid concentration and the coke formation in MFI zeolites, and we could find meaningful relation between them.

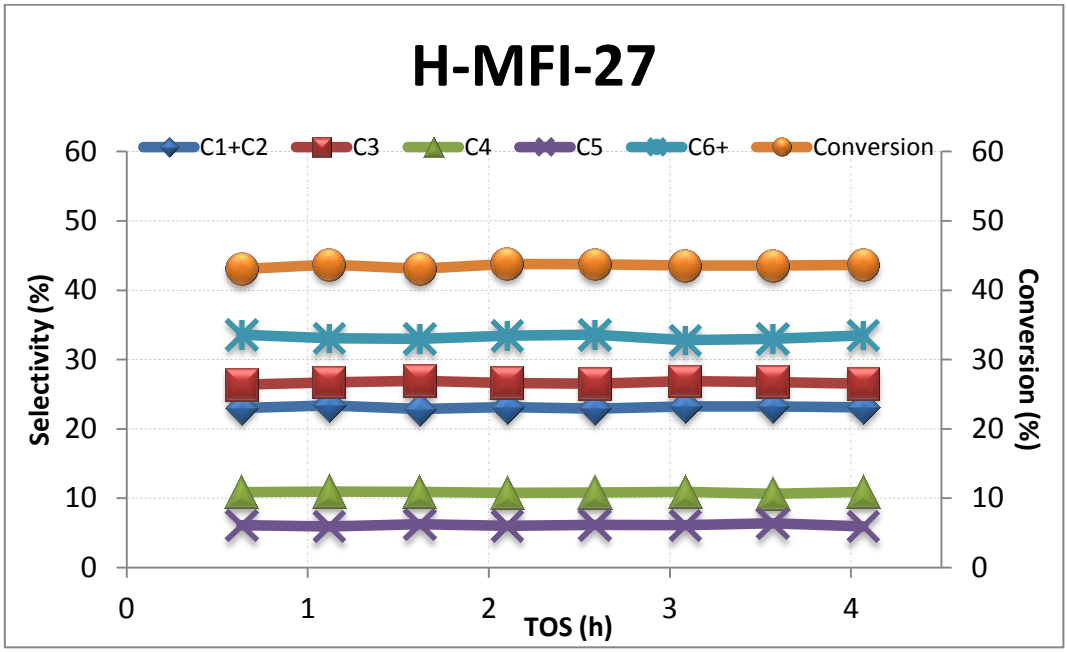

Figure 4. 92: Methanol conversion and product selectivity during MTH reaction at 400°C and WHSV = 2.0gg^{-1} h^{-1} as a function of TOS in H-MFI-27 zeolite.

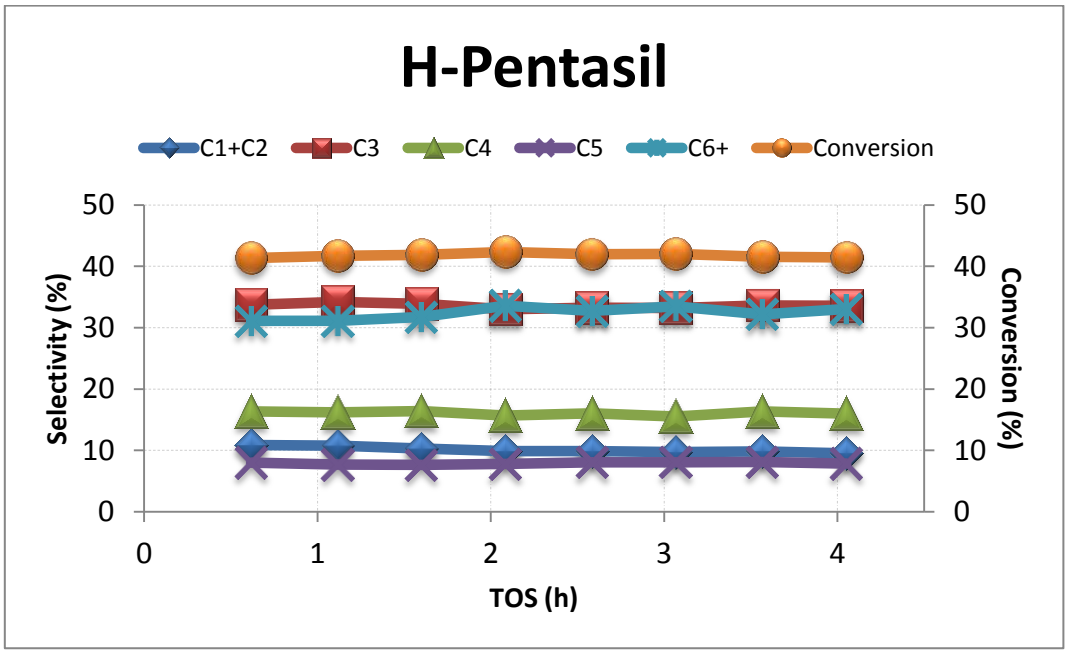

Figure 4. 93: Methanol conversion and product selectivity during MTH reaction at 400°C and WHSV = 2.0gg^{-1} h^{-1} as a function of TOS in H-Pentasil zeolite.

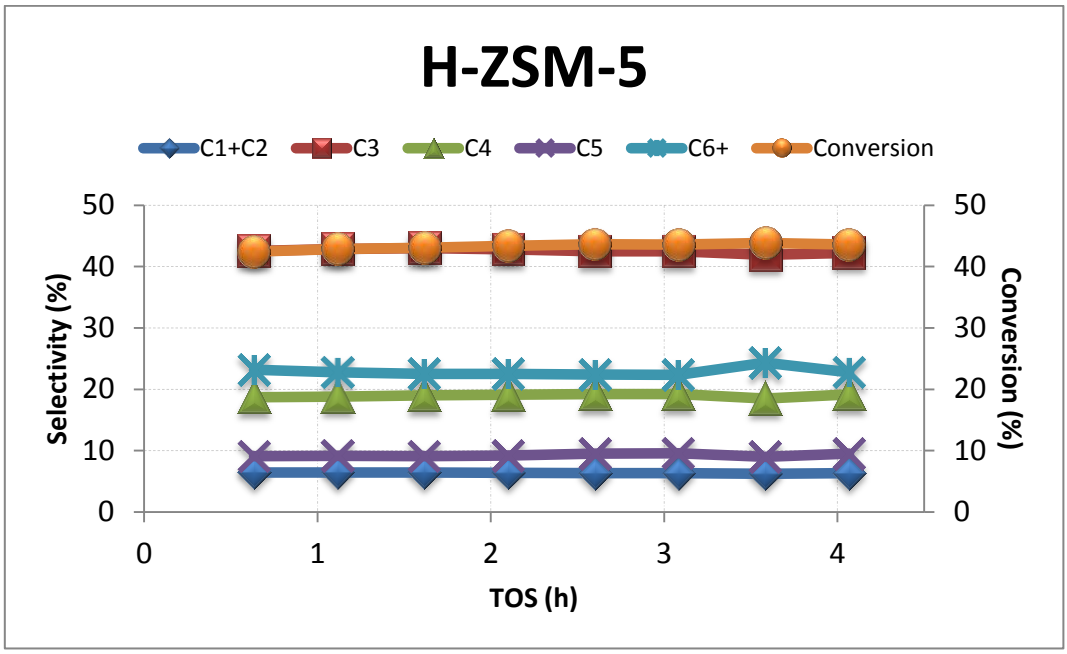

Figure 4. 94: Methanol conversion and product selectivity during MTH reaction at 400°C and WHSV = 2.0gg^{-1} h-^{1} as a function of TOS in H-ZSM-5 zeolite.

H-SUZ-4

SUZ-4 zeolite shows quite different spectra and products distribution during the MTH reaction. ~1587 and 1377 cm-1 band in the ν(CC)/δ(CH) region can be assigned as the coke bands as usual. However, prominent band at ~1540 cm^{-1} which is higher in intensity than ~1587 cm^{-1} band has not been observed from other samples studied in this work. This band is assigned to alkylnaphthalenes [67]. The sample used in this work was tested by Teketel [15] at 400°C and WHSV = 2.0 gg^{-1}h^{-1}, and the sample was fully deactivated after 30 minutes on stream. The sample in the IR cell did not show complete deactivation even after 4 hours on stream, and this might be due to the volume issue of the cell and the sample which is discussed earlier and the lower partial pressure. Teketel [15] observed that the product selectivity of SUZ-4 is very similar to that of SAPO-34 which is CHA type material with 8-membered ring. The opening of the ring has size of 3.8x3.8 Å [14]. It was observed by Hereijgers et al. [118] that methylnaphthalene became the most abundant retained hydrocarbons after longest time on stream at 350°C and WHSV = 6.2 gg^{-1}h^{-1} during MTO reaction over H-SAPO-34. Even though direct evidence of existence of alkylnaphthalenes in the MTH reaction overH-SUZ-4 is not available, the possibility can be deduced from the logic above.

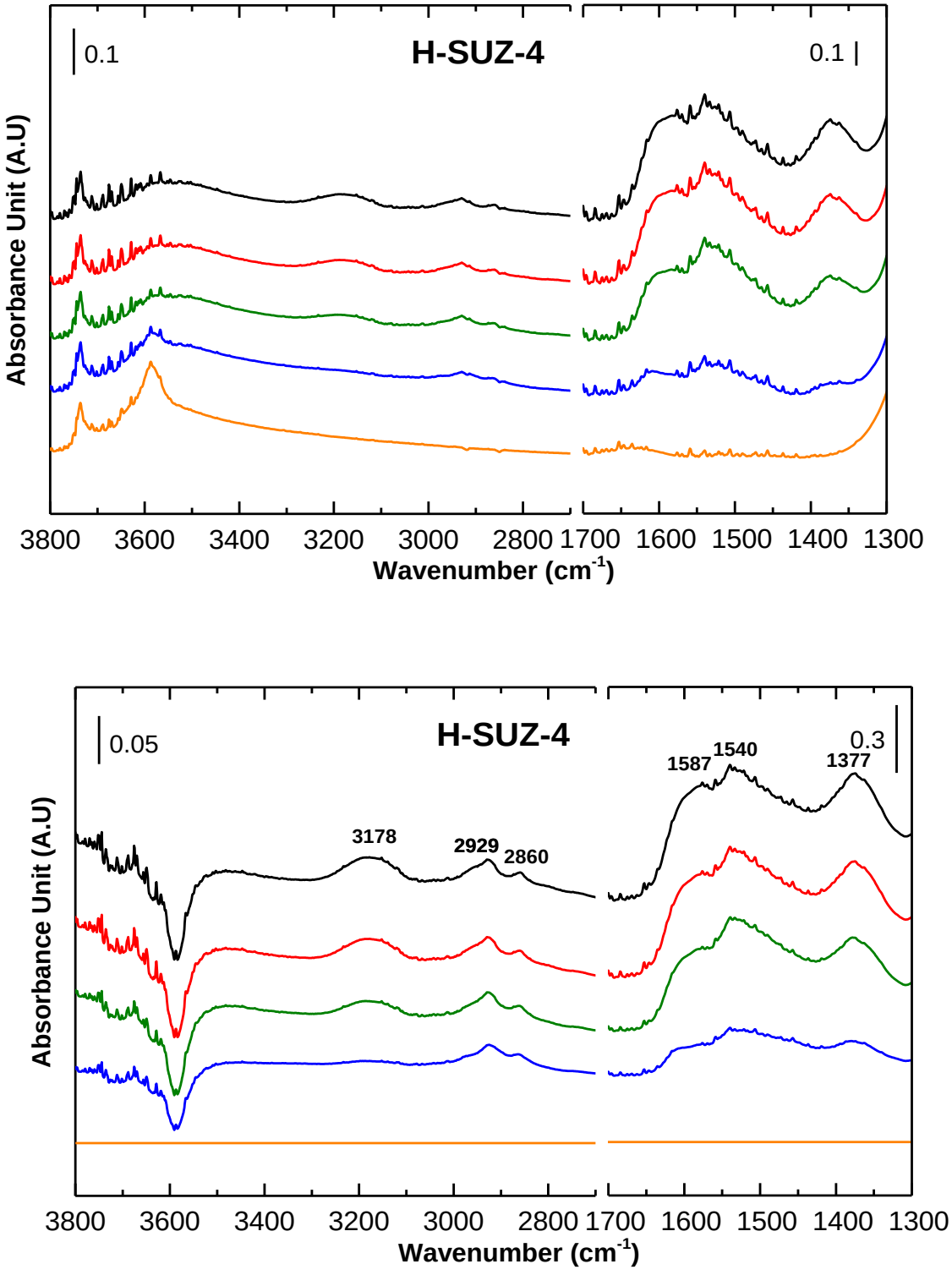

Figure 4. 95: In situ FTIR Spectra of the H-SUZ-4 zeolite obtained before introducing MeOH (yellow), after 1h (blue), 2h (green), 3h (red) and 4h (black) of contact with MeOH at 400°C and WHSV = 2.0gg^{-1}h^{-1}. (Upper) recorded spectra (Lower) clean zeolite spectrum subtracted spectra.

In ν(CH) region, one can observe a band from aromatic species, at ~3178 cm^{-1}, and a band from methylation product, at ~2929 cm^{-1}. It is noticeable, in the ν(OH) region, that decrease in Brønsted band is much severe compare to that in silanol band.

Regarding products distribution, catalytic testing result shows high product selectivity towards light hydrocarbons such as C_2 and C_3 [15] at full conversion. The observation that the three-dimensional 10-membered ring H-SUZ-4 zeolite shows similar production distribution with three-dimensional 8-membered ring H-SAPO-34 led Teketel to suggest that shape selectivity of H-SUZ-4 is induced by crystal morphology, not framework topology [15].

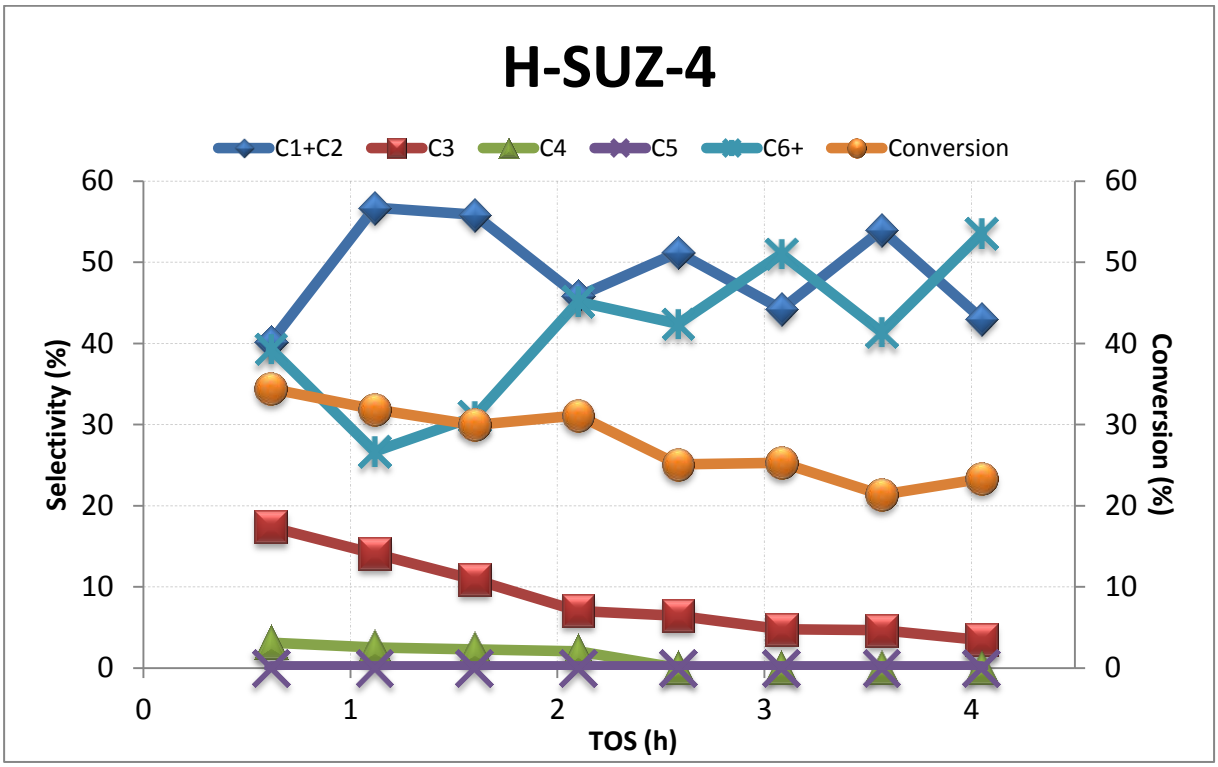

Figure 4. 96: Methanol conversion and product selectivity during MTH reaction at 400°C and WHSV = 2.0gg^{-1} h^{-1} as a function of TOS in H-SUZ-4 zeolite.

H-TNU-9

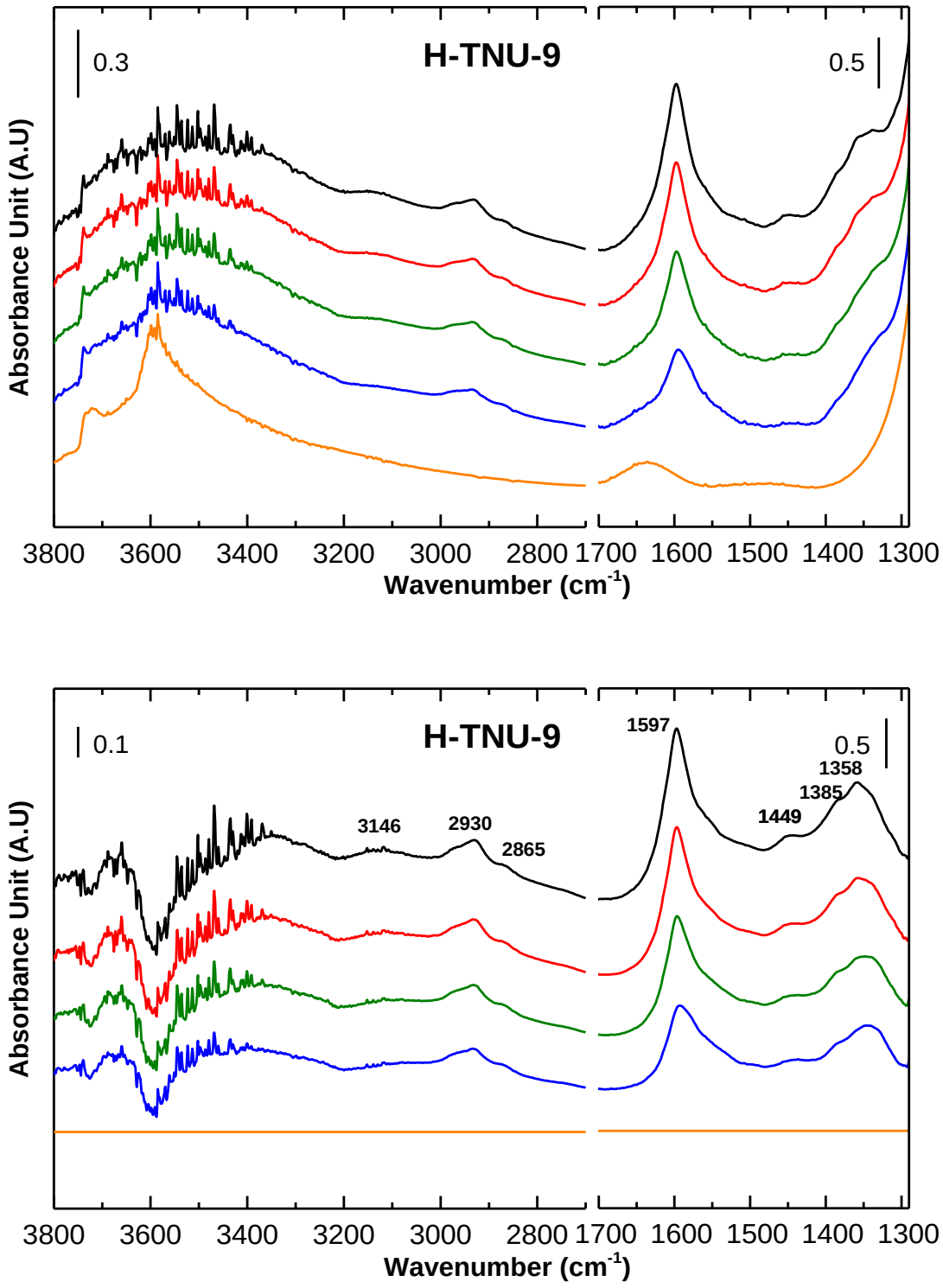

Figure 4. 97: In situ FTIR Spectra of the H-TNU-9 zeolite obtained before introducing MeOH (yellow), after 1h (blue), 2h (green), 3h (red) and 4h (black) of contact with MeOH at 400°C and WHSV = 2.0gg^{-1}h^{-1}. (Upper) recorded spectra (Lower) clean zeolite spectrum subtracted spectra.

FTIR spectra of H-TNU-9 during the MTH reaction at 400°C and WHSV = 2.0 $gg^{-1}h^{-1}$ is presented in Figure 4. 97. Sharp shape of the band at ~1597 cm^{-1} for aromatic coke species is noticeable feature of the H-TNU-9 compare to other zeolites studied in this work. ~1358 cm^{-1}, another coke band, is from bending mode of CH_3 of isopropyl or tertiary butyl which might be attached to aromatic coke species. There is a small shoulder at ~1385 cm^{-1} and a weak band at ~1449 cm^{-1} from paraffinic species. ~3146 cm^{-1} band is for aromatic species, ~2930 cm^{-1} is for methylation products, and ~2865 cm^{-1} can be assigned to methoxy adsorbed on EFAl with contribution from methoxy adsorbed on Brønsted acid sites. The existence of the strong Lewis acid sites was observed from CO adsorption (Figure 4. 50). Almost all Brønsted acid sites were consumed during 4 hours of contact with MeOH.

It was mentioned earlier that H-TNU-9, H-IM-5 and H-ZSM-5 shows similar products distribution [82]. However, effluent analysis from this work does not show similarity in products distribution between H-TNU-9 (Figure 4. 98) and H-IM-5 (Figure 4. 84). H-IM-5 shows very high selectivity towards C_{6+} species and low selectivity towards C_1-C_5 species while H-TNU-9 shows moderate selectivity towards both C_{6+} and C_3 species. The reason cannot be found at this level without catalytic testing result of H-TNU-9 with same experimental condition as in H-IM-5, and more thorough investigation in products distribution is needed further.

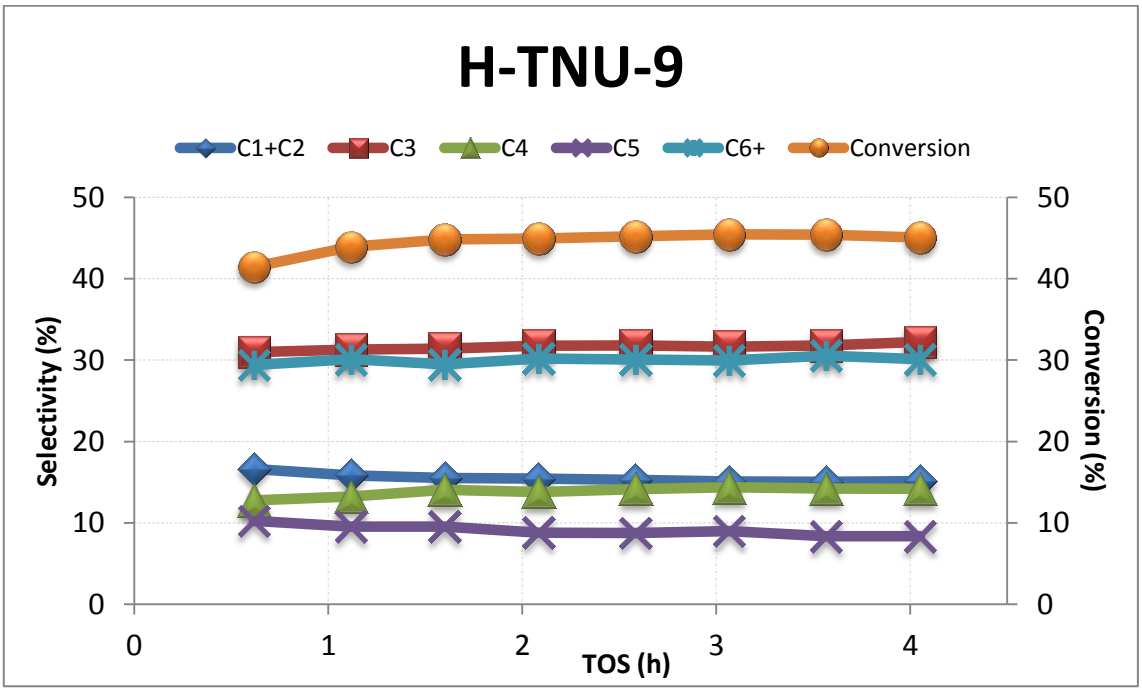

Figure 4. 98: Methanol conversion and product selectivity during MTH reaction at 400°C and WHSV = 2.0gg^{-1} h^{-1} as a function of TOS in H-TNU-9 zeolite.

H-Beta

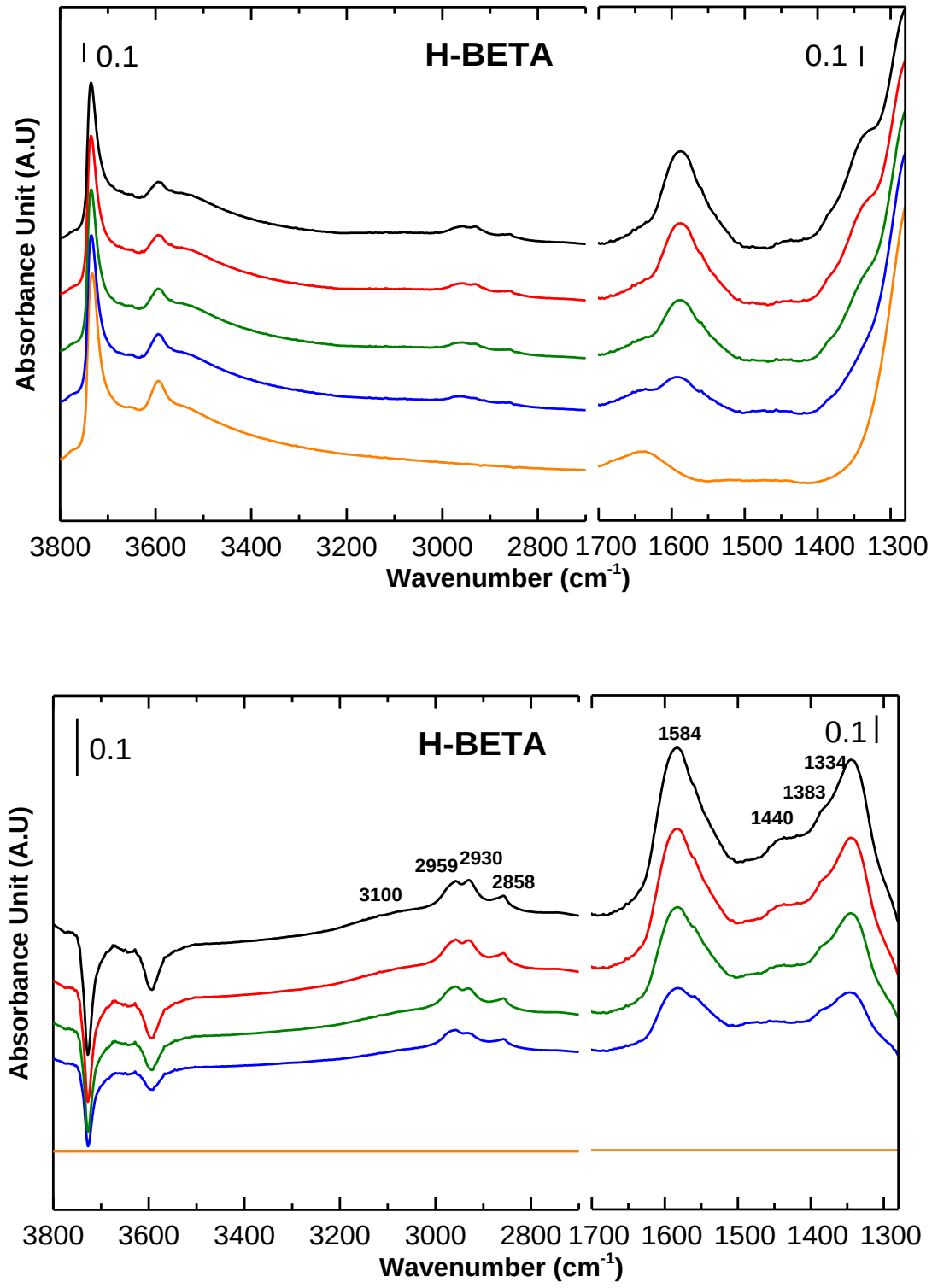

Figure 4. 99: In situ FTIR Spectra of the H-Beta zeolite obtained before introducing MeOH (yellow), after 1h (blue), 2h (green), 3h (red) and 4h (black) of contact with MeOH at 400°C and WHSV = 2.0gg^{-1}h^{-1}. (Upper) recorded spectra (Lower) clean zeolite spectrum subtracted spectra.

Three-dimensional 12-membered ring system zeolite, H-Beta was also investigated for MTH reaction with in-situ FTIR spectroscopy. From the Figure 4. 99, one can observe bands appearing upon consumption of silanol and Brønsted band. In the ν(CH) region, two most prominent bands, coke bands, at ~1584 and 1334 cm^{-1} are seen. ~1383 and 1440 cm^{-1} are from paraffinic species. In the ν(CC)/δ(CH) region, ν(CH) band of aromatic species appears at ~3100 cm^{-1}. ~2959 and 2858 cm^{-1} bands are asymmetric and symmetric CH stretching of methoxy adsorbed on silanols, respectively. Clear appearance of these species is consistent with the observation of relatively large intensity decrease in silanol band compare to Brønsted band. From the CO adsorption (Figure 4. 51), existence of strong Lewis acid sites was confirmed. Bands from methoxy adsorbed on EFAl species are expected at ~2968 and 2865 cm^{-1}, and they seem to contribute to the broadness of ~2959 and 2858 cm^{-1} band. Methylation product band is observed at ~2930 cm^{-1}.

H-Beta is known to favor the arene cycle in Dual-cycle concept with having higher benzenes such as penta- to heptaMB^{+} and HMMC as reaction intermediates [23, 111]. Because of the nature of the cycle, H-Beta has higher selectivity towards propene compare to ethene. It is difficult to observe the propene/ethene ratio from GC-MS-FID analysis in this work as the C_1 and C_2 are represented by only one curve. It is more straightforward from the catalytic testing result in Figure A. 14 [2] Propene is more abundant compare to ethene until conversion capacity of the zeolites gets quite low, and this is in good agreement with arene cycle being favored.

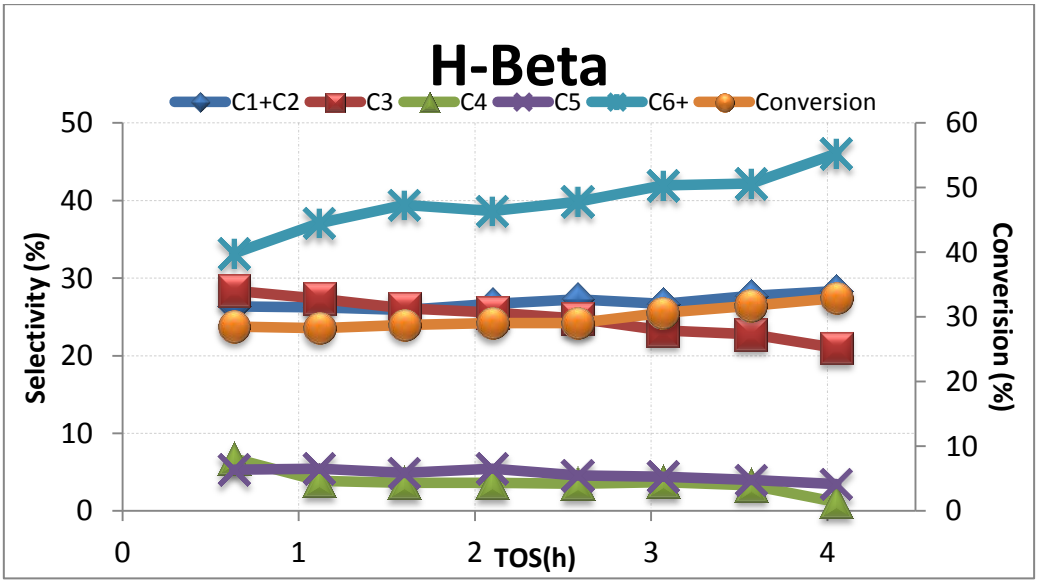

Figure 4. 100: Methanol conversion and product selectivity during MTH reaction at 400°C and WHSV = 2.0gg^{-1} h^{-1} as a function of TOS in H-Beta zeolite.

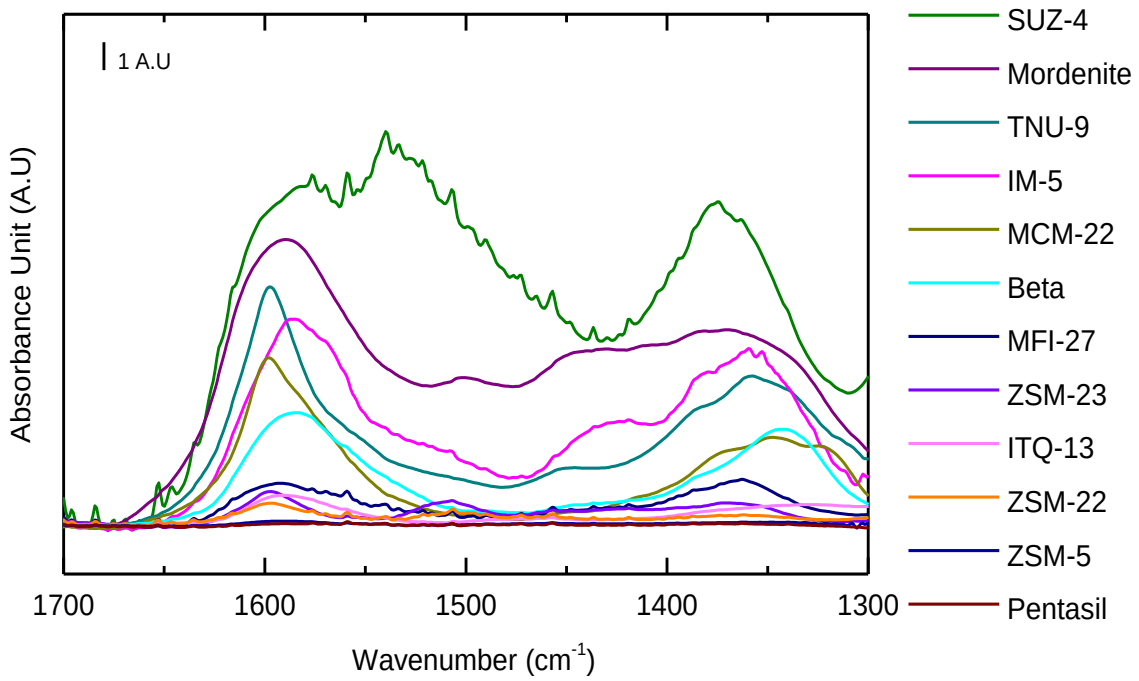

Figure 4. 101: Normalized FTIR spectra of all 12 samples after 4 hours of contact with MeOH. Every spectrum is subtracted by its activated zeolite spectrum.

To see the relation between intensity of the coke bands and the coke formation [69], all spectra from samples after 4 hours of contact with MeOH were normalized and plotted together in Figure 4. 101. It shows, actually, surprisingly good agreement between catalyst lifetime and the intensity of coke bands except for the one-dimensional 10-ring zeolites (H-ZSM-23 and H-ZSM22). One can compare the order of intensity in coke bands as in the legend of Figure 4. 101 to the catalyst lifetime of each zeolite in Table 4. 14. It should be noted the time for full deactivation provided for H-TNU-9, H-MCM-22 and H-Pentasil is at different reaction condition. For H-ZSM-5 and H-Pentasil, from what we observed from comparing three MFI samples, we assume that these two samples have longer lifetime than H-MFI-27. For H-ZSM-23 and H-ZSM-22, the reason for strange behavior, showing low intensity in the coke bands even though they deactivate rapidly, can be explained by their topology. Blockage of the zeolite pore openings by the coke species in mono-dimensional zeolites can happen [104-106] and the blockage of the zeolite pore mouth can prevents MeOH from getting into the channels of H-ZSM-23 and H-ZSM-22 interacting with active sites. This is consistent with the observation that not much of Brønsted acid sites and silanols got consumed after 4 hours of contact with MeOH even though the conversion decreases to 1/3 of

its starting value. Comparing to the case where hydrocarbon residue accumulated inside of large pores considered as coke species, the amount of the coke species needed in H-ZSM-23 and H-ZSM-22 to block the pore opening would be much less than those accumulated in large pores of zeolites. Therefore, the intensity of the coke bands for H-ZSM-23 and H-ZSM-22 can be much smaller than other rapidly deactivating zeolites even though their lifetime is quite short. Even though the papers [104-106] say the pore blockage can happen in "mono-dimensional zeolites", one can see clearly that the coke band of H-Mordenite behaves differently from that of one-dimensional 10-ring zeolites. Bjørgen et al. [111] reported earlier that it is the same hydrocarbon compounds which are formed and retained in the H-Beta, H-MCM-22 and H-Mordenite. Even though H-Mordenite is one-dimensional zeolite, still its pore is large (12-ring channel system) and it behaves like other large pore zeoiltes, not other one-dimensional zeolites.

Table 4. 14: List of sample in order of highest intensity of coke band to lowest intensity of the band examined by in situ FTIR spectroscopy during the MTH reaction (four hours on stream) and the time for full deactivation for each sample at given condition.

Sample	Catalyst lifetime (hour)	Catalytic testing condition	Reference
H-SUZ-4	~0.5	400°C, WHSV = 2.0$gg^{-1}h^{-1}$	[15]
H-Mordenite	~3	400°C, WHSV = 2.0$gg^{-1}h^{-1}$	[2]
H-TNU-9	~15	*350°C, WHSV = 9.0 $gg^{-1}h^{-1}$*	[82, 116]
H-IM-5	~28	400°C, WHSV = 2.0$gg^{-1}h^{-1}$	[2]
H-MCM-22	~7	*450°C*, WHSV = 2.0$gg^{-1}h^{-1}$	[112]
H-Beta	~11	400°C, WHSV = 2.0$gg^{-1}h^{-1}$	[2]
H-MFI-27			
H-ZSM-23	~10	400°C, WHSV = 2.0$gg^{-1}h^{-1}$	[2]
H-ITQ-13	~66	400°C, WHSV = 2.0$gg^{-1}h^{-1}$	[2]
H-ZSM-22	~7	400°C, WHSV = 2.0$gg^{-1}h^{-1}$	[2]
H-ZSM-5			
H-Pentasil	>115	400°C, *WHSV = 10.0$gg^{-1}h^{-1}$*	[2]

For the comparison of difference in appearance of bands during the MTH reaction, the ν(CH) region and ν(CC)/δ(CH) region for all 12 samples are plotted together in Figure 4. 102 and Figure 4. 103. There are some characteristic features observed:

In ν(CH) region,

- Aromatic CH stretching mode at 3200-3000 cm^{-1} only appears in H-Mordenite, H-MCM-22, H-IM-5, H-SUZ-4, H-TNU-9 and H-Beta which are with higher intensity in coke band. Possible explanation for this observation is 1) the nature of the aromatic species existing in zeolites which show high intensity of coke bands are somewhat different from those existing in zeolites which show low intensity of coke bands. For example, the coke band at 1600-1580 cm^{-1} is due to the ν(CC) while the band at 3200-3000 cm^{-1} is due to the ν(CH). 1600-1580 cm^{-1} band was observed for all samples but not 3200-3000 cm^{-1} band. The more substituted benzene ring is, the less ν(CH) from aromatic species is available which can leads to lower intensity in 3200-3000 cm^{-1}. 2) Molar extinction coefficient of two bands, 1600-1580 and 3200-3000 cm^{-1}, are very different in values. In this case, the comparison of the two bands becomes less meaningful. It is difficult to say in which hypothesis is more plausible at this level of study and further investigation is needed, for example, identification of hydrocarbon residue species in wafer which was used in in-situ MTH reaction spectroscopy experiment in different time on stream.

- Relatively clear ~2865 cm^{-1} band is observed for the samples in which existence of strong Lewis sites were observed from CO adsorption experiment. This is in good agreement with the assignment of this band, symmetric CH stretching of methoxy adsorbed on EFAl. Corresponding asymmetric stretching band, ~2968 cm^{-1}, on the other hand, is not as clear as symmetric band as it overlaps with bands from other species.

- From the most of the sample, the CH stretching band from methoxy adsorbed on Brønsted acid sites was not clearly observed. It is opposite of the clear observation of ~2865 cm^{-1} band in zeolite samples with strong Lewis acid sites. It can be due to 1) overlapping with other methoxy species adsorbed on silanol and EFAl. 2) lower molar extinction coefficient of the band compare to the band of methoxy species adsorbed on other acid sites. 3) Active involvement of Brønsted acid sites in MTH reaction.

Brønsted acid sites have most active role in MTH reaction, in a way that hydrocarbon formation is initiated by the generation of methoxy groups at Brønsted acid sites while methanol at silanol and EFAl sites play no direct role in hydrocarbon formation [99]. In this case, it can be assumed that methoxy groups on Brønsted acid sites actively get involved in further reaction for hydrocarbon formation resulting in small absorption band in FTIR spectra.

In ν(CC)/δ(CH),

- Intensity of coke bands at 1600-1580 and 1390-1360 cm^{-1} shows good correlation with catalytic lifetime (Figure 4. 101 and Table 4. 14).

- One of the coke bands, 1390-1360 cm^{-1} band, seems to appear at slightly lower wavenumber as well. The more detailed assignment for the bands in this region can be made [109, 110].

  1380-1370 cm^{-1} : CH bending modes of methyl groups
  1370-1365 cm^{-1} : CH bending modes of gem-dimethyl and iso-species
  ~1365 cm^{-1} : CH bending modes of trimethyl or ter-butyl species
  1350-1330 cm^{-1} : CH bending modes of methanylylidene(-CH=)

- High intensity ~1507 cm^{-1} band is only observed in one-dimensional 10-ring zeolites, H-ZSM-23 and H-ZSM-22. Karge, Nieβen and Bludau [69] earlier related the ~1507 cm^{-1} band to coke which is in form of linear, branched saturated or allylic hydrocarbons.

- H-SUZ-4 shows unique band at ~1540 cm^{-1}, which is originated from alkylnaphthalenes. From the extremely short lifetime of H-SUZ-4 (0.5 hours in catalytic testing, [15]), similar product selectivity of SUZ-4 to SAPO-34 [15], and methylnaphthalene being the most abundant retained hydrocarbons after longest time on stream at 350°C and WHSV = 6.2 $gg^{-1}h^{-1}$ during MTO reaction over H-SAPO-34 [118], possible existence of alkylnaphthalenes during MTH reaction over H-SUZ-4 can be deduced. This can support the assignment made for ~1540 cm^{-1} band.

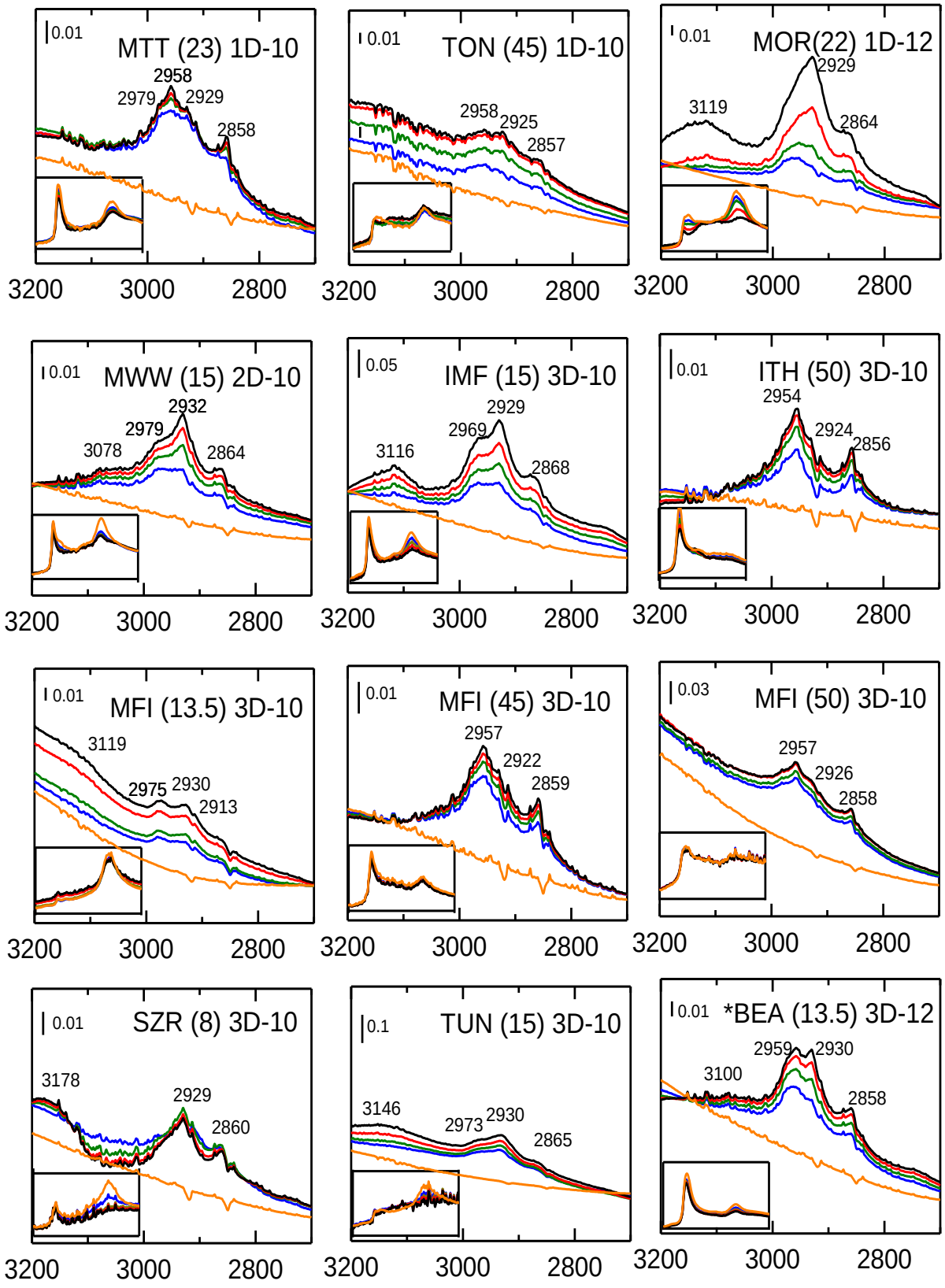

Figure 4. 102: Comparison of ν(CH) region spectra of all 12 samples between 0-4hours of contact with MeOH at 400°C, WHSV = 2.0 $gg^{-1}h^{-1}$. Yellow(TOS =0h) , blue (TOS =1h), green (TOS =2h), red (TOS =3h), and black (TOS =4h) curves are shown.

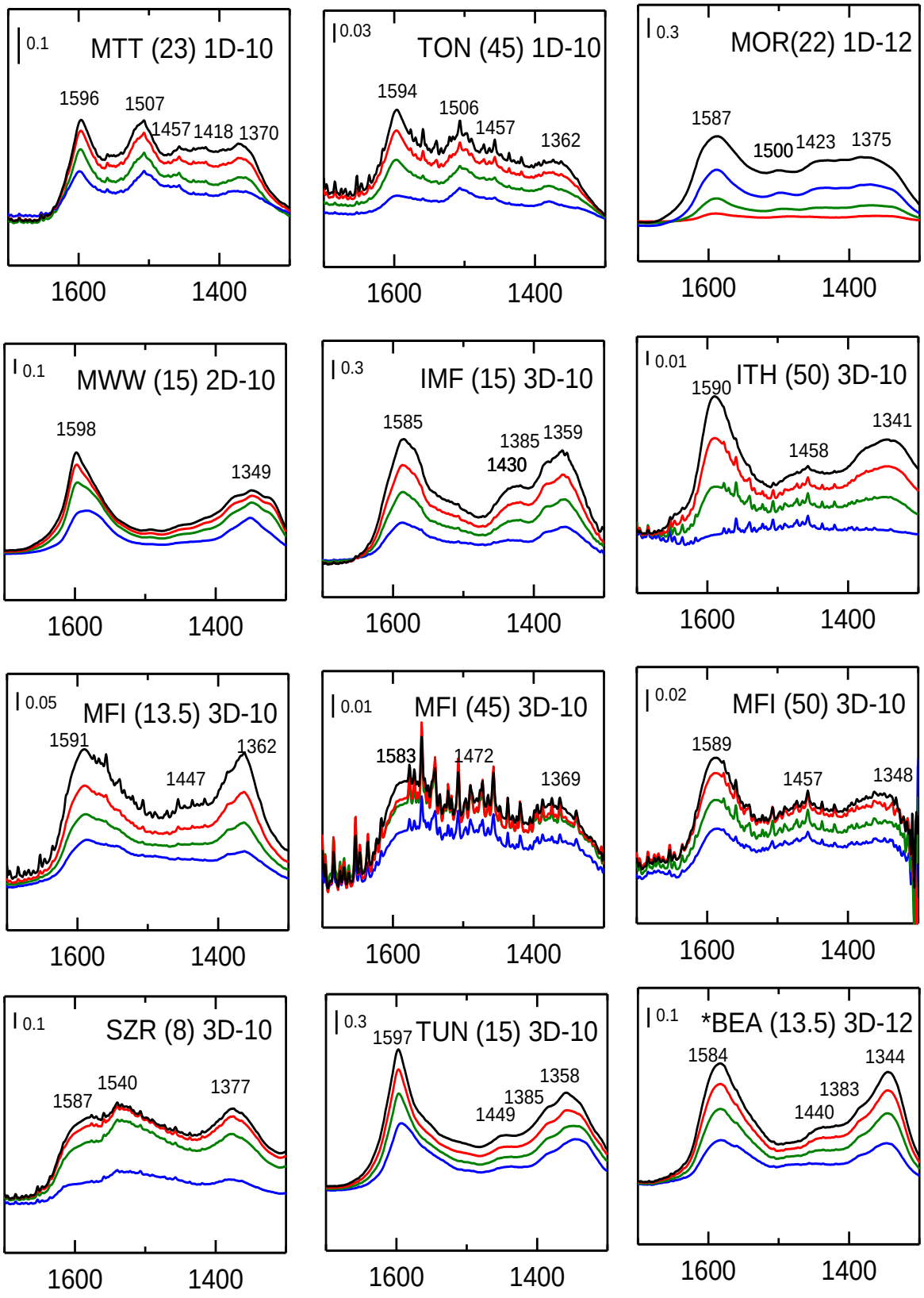

Figure 4. 103: Comparison of ν(CH) region spectra of all 12 samples between 1-4 hours of contact with MeOH at 400°C, WHSV = 2.0 gg-1h-1. Every spectrum is subtracted by its clean zeolite spectrum. . Blue (TOS =1h), Green (TOS =2h), Red (TOS =3h), and Black (TOS =4h) curves are shown.

5 Conclusion & Further Work

From the aspect of the technique used in this work,

- Pyridine adsorption technique for quantification of acid sites and calculation of Si/Al value was established during this work thanks to S. Chavan, and the technique seem to give reasonable value of Si/Al. However, different IMEC values have been reported from different groups [38-49], and different experimental condition is considered to be the reason [40]. Measuring and finding our own IMEC value from the set-up we have in the group would be a great help to achieve more reliable results of concentration of acid sites and Si/Al. Also, more investigation is needed for H-ZSM-23 and H-SUZ-4 samples in order to find good explanation for the part of Brønsted acid sites which did not interact with pyridine (even with CO in the case of H-ZSM-23).

- In-situ FTIR on zeolites during the MTH reaction showed its possibility as a promising method for the study of MTH reaction in different zeolites. It can be more powerful tool when used with effluent analysis. However, in this work, there were quite a lot of amount of bypassing MeOH without contact with catalyst in side of the cell. This can be improved by using Diffuse Reflectance Infrared Fourier Transform (DRIFT) spectroscopy where DRIFT cell can accommodate catalytic beds a few millimeters thick [119]. Also, complementary techniques can be used related to the in situ FTIR spectroscopy. For example, dissolution of spent catalysts would give valuable information regarding coke species. Assignment of the bands can be improved as well by FTIR spectroscopy study of simpler system with compounds found during the MTH reaction.

Regarding the findings from this work,

- From the comparison between three MFI zeolites, relation between acid concentration and the intensity of coke bands was seen. That is, the higher acid concentration in the zeolite is, the higher coke bands it shows during the MTH reaction. Then, from Figure 4. 101, the relation between the intensity of the coke bands and the catalyst lifetime was established. However, one-dimensional 10-ring zeolites, H-ZSM-23 and H-ZSM-23 were exceptions, and this is because the deactivation of the samples is occurred by blockage of pore mouth. That is,

deactivation in these samples can happen with much smaller amount of coke species compare to other zeolite samples studied in this work.

- From Figure 5. 1**,** one can see information about the intensity of coke bands, Si/Al, acid strength, acid concentration and catalyst lifetime of each zeolite studied in this work. Correlation is observed among intensity of coke bands, Si/Al, Brønsted acid concentration and catalyst lifetime (if one does not consider the H-ZSM-23 and H-ZSM-22). For the zeolites with higher Brønsted acid concentration which implies more Al in the system resulting in low Si/Al, the shorter lifetime is generally observed which indicates faster coke formation and accumulation resulting in higher intensity of coke bands. Meaningful relation between acid strength and the rest of the parameters could not be found. However, this does not mean that acid strength can be completely ruled out from the list of parameters affecting the MTH reaction. The technique used to investigate the acid strength, CO adsorption experiment, uses the degree of perturbation in OH band of Brønsted acid sites, and the difference in $\Delta\nu$(OH) between the zeolite with strongest acid strength (H-MCM-22, $\Delta\nu$(OH) = -324 cm^{-1}) and the zeolite with weakest acid strength (H-SUZ-4, $\Delta\nu$(OH) = -296 cm^{-1}) was 28 cm^{-1}. The difference is only 10% of their value while the difference in Brønsted acid concentration is much bigger between samples. For example, the Brønsted acid concentration of H-TNU-9 (C_{BA}= 1.250 mmol/g catalyst), which shows highest Brønsted acid concentration, is 4.5 times higher than the Brønsted acid concentration of H-Pentasil which shows lowest Brønsted acid concentration (C_{BA}= 0.277mmol/g catalyst). So, it could be the case that the acid strength between chosen twelve samples are not widely distributed enough to see the clear effect of the acid strength in MTH reaction. Therefore, further study more deeply focused on effect of acid strength on the MTH reaction is needed. For example, one can study a series of zeolites/zeotypes with similar acid concentration and topology but significantly different in acid strength.

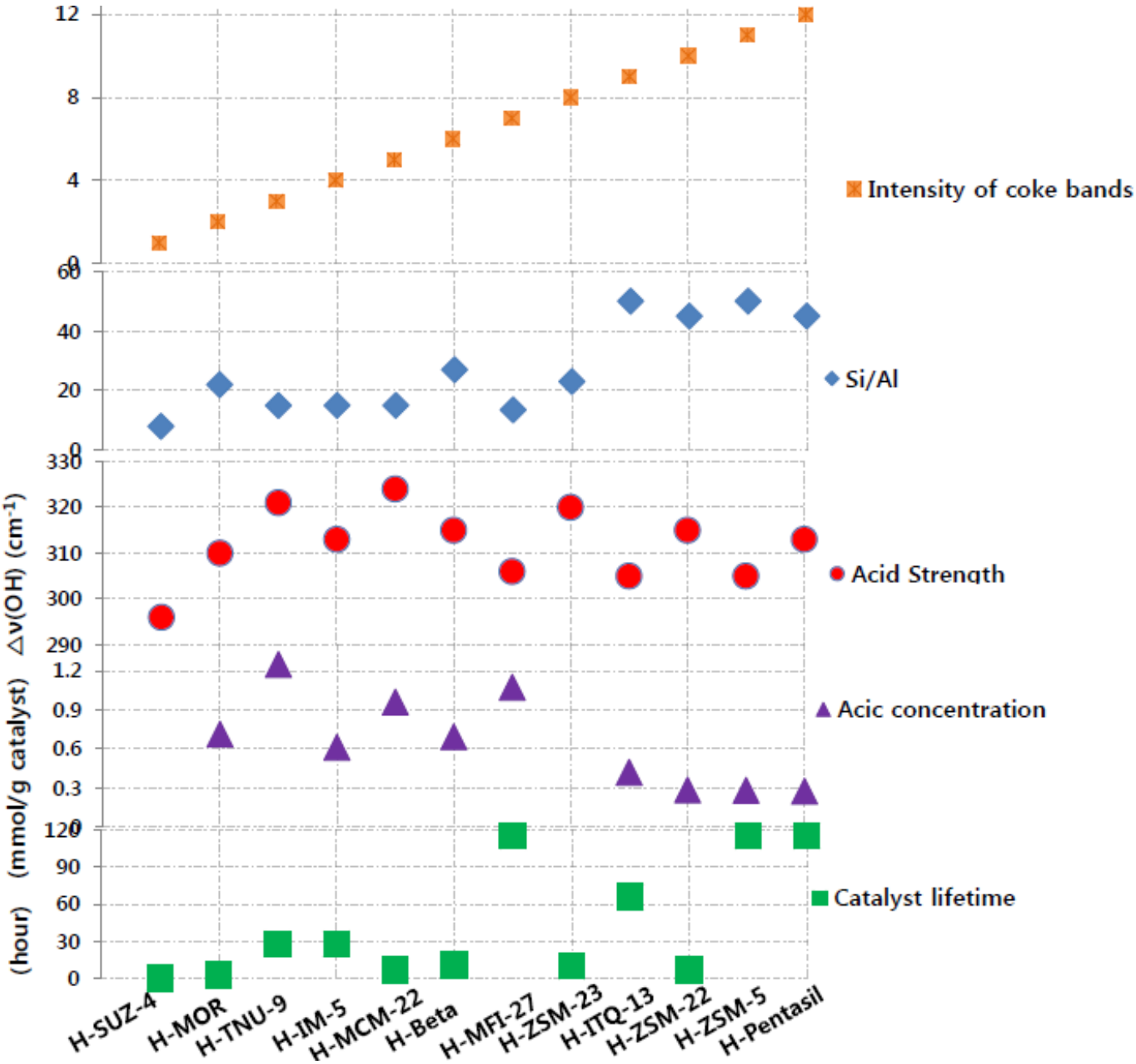

Figure 5. 1: Plot of intensity of coke bands (highest intensity =1 , lowest intensity =12), Si/Al, acid strength (Δν(OH) from CO adsorption experiment), total Brønsted acid concentration (calculated from pyridine adsorption experiment) and catalytic lifetime given in Table 4. 14. The order of samples presented is the order of decreasing intensity in coke bands. It should be noted that the catalyst lifetime of H-TNU-9 was set to same as that ofH-IM-5 measured by Etemadi [2] based on the similarity between the samples reported by Skistad [82]. Catalyst lifetime of H-MCM-22 (7 hours) is at the experimental condition of 450°C and WHSV = 2.0 $gg^{-1}h^{-1}$ [112]. For H-ZSM-5 and H-MFI-27, it was roughly assumed that the lifetime of these zeolites would be similar to that of H-Pentasil measured by catalytic testing performed by Etemadi [2].

Appendix A

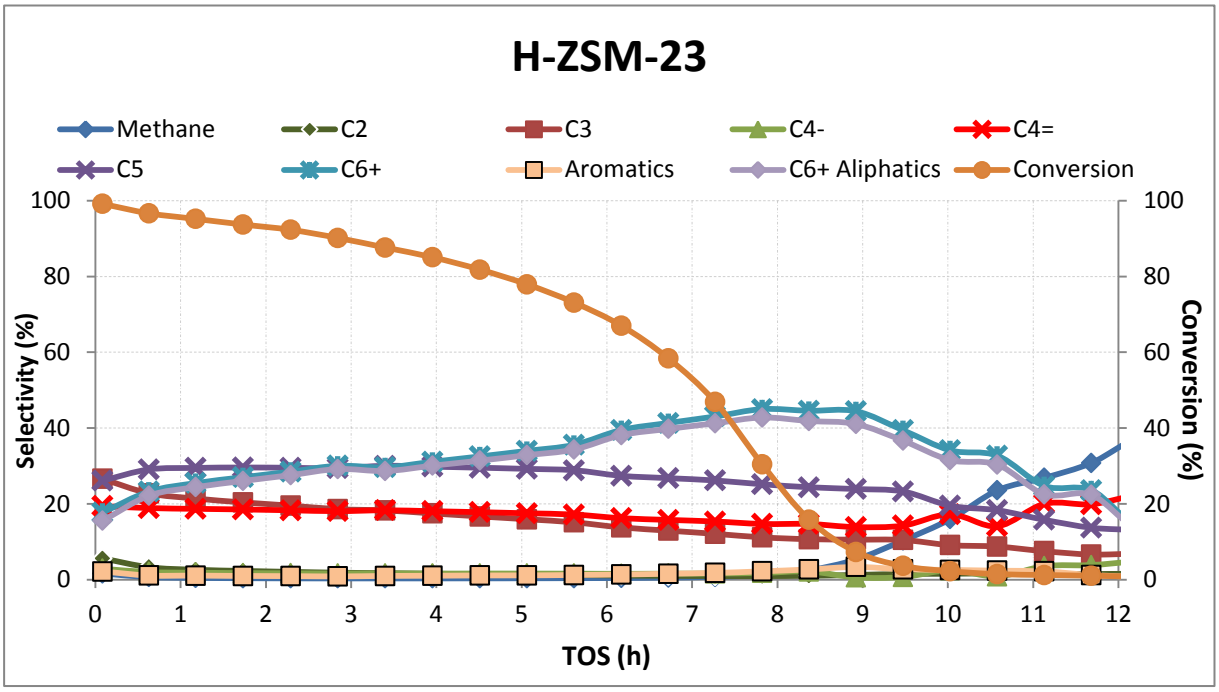

Figure A. 1: Methanol conversion and product selectivity as a function of TOS in H-ZSM-23 during MTH reaction carried out in a fixed bed reactor at 400°C, WHSV = 2.0 $gg^{-1}h^{-1}$. Experiment performed by S. Etemadi [2].

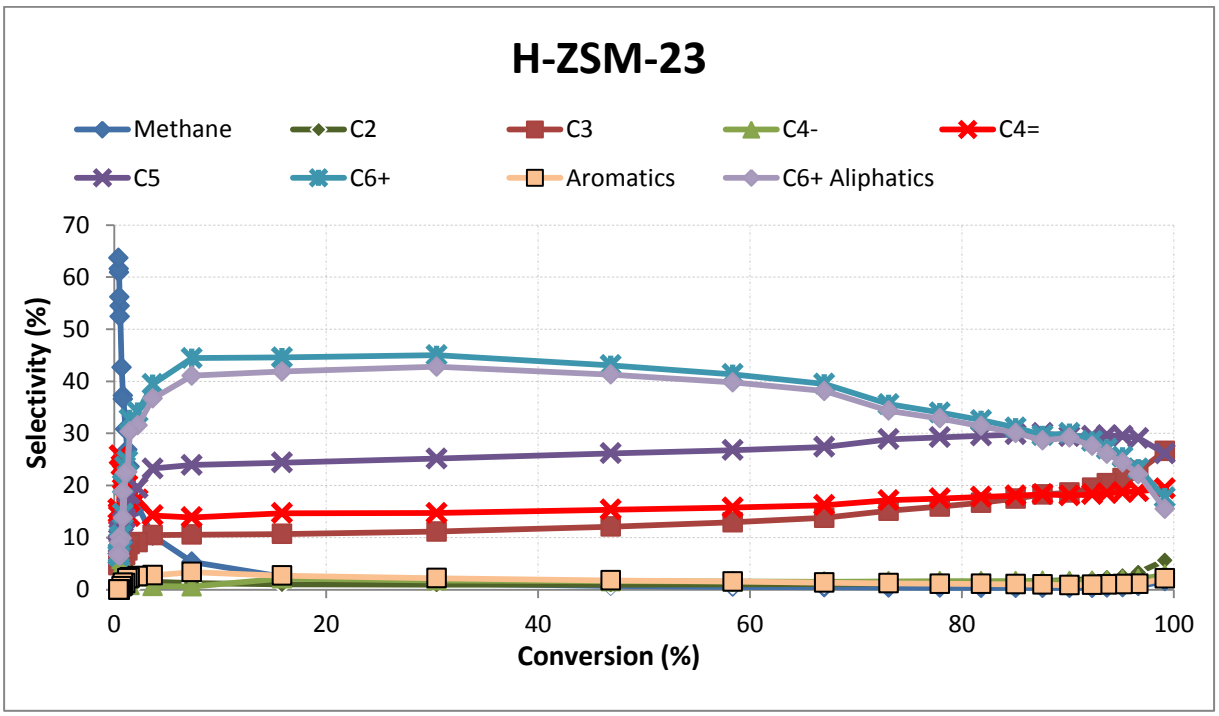

Figure A. 2: Product selectivity as a function of conversion in H-ZSM-23 during MTH reaction carried out in a fixed bed reactor at 400°C, WHSV = 2.0 $gg^{-1}h^{-1}$. Experiment performed by S. Etemadi [77].

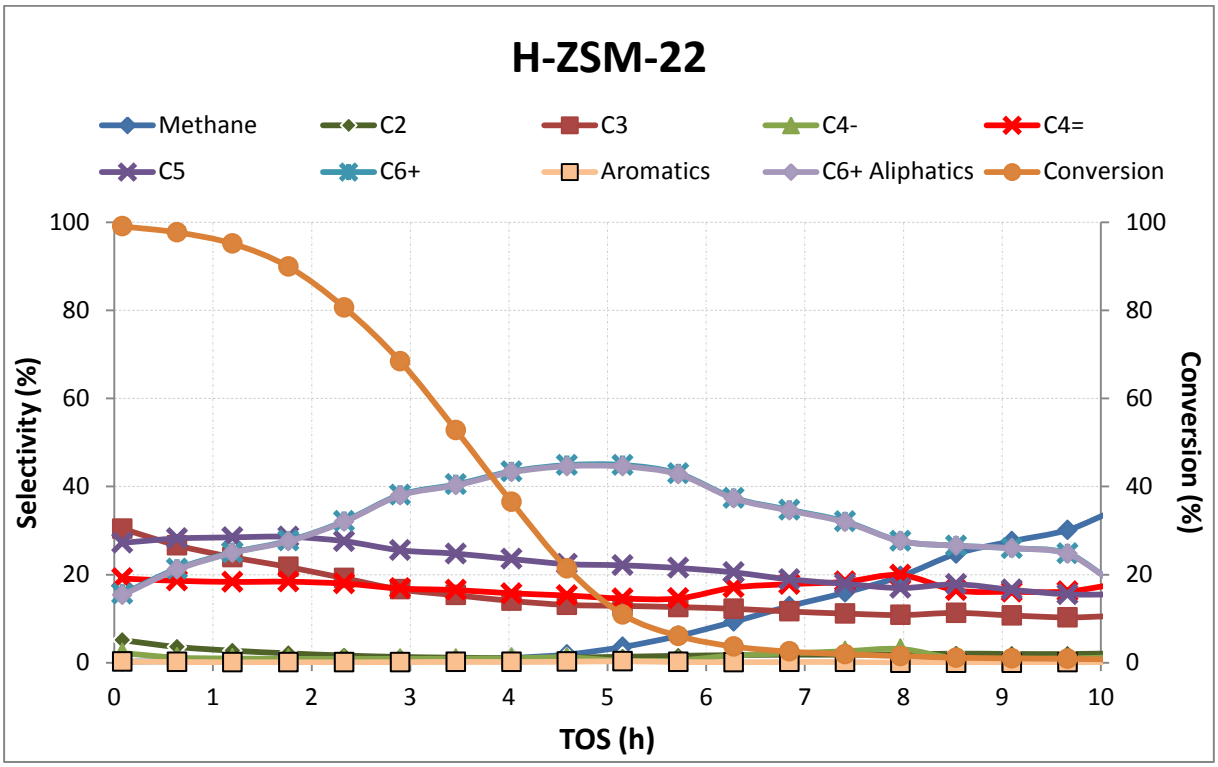

Figure A. 3: Methanol conversion and product selectivity as a function of TOS in H-ZSM-22 during MTH reaction carried out in a fixed bed reactor at 400°C, WHSV = 2.0 gg-1h-1. Experiment performed by S. Etemadi [2].

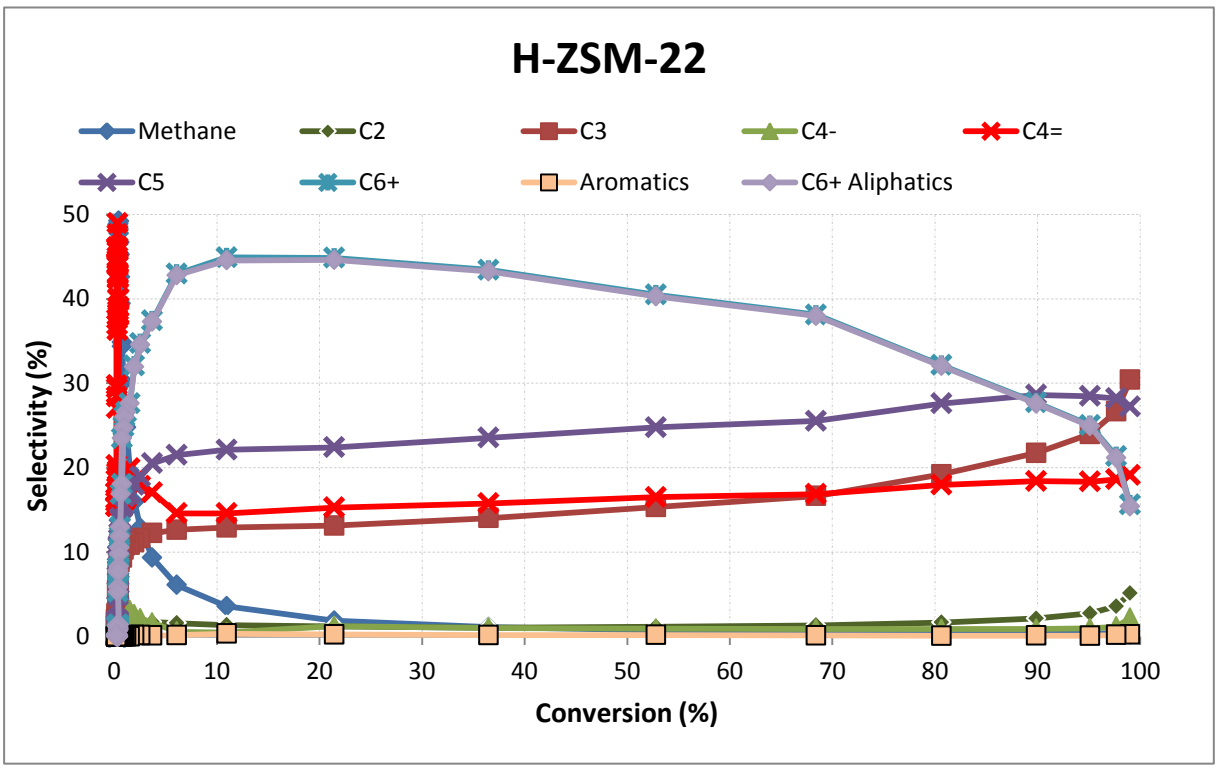

Figure A. 4: Product selectivity as a function of conversion in H-ZSM-22 during MTH reaction carried out in a fixed bed reactor at 400°C, WHSV = 2.0 $gg^{-1}h^{-1}$. Experiment performed by S. Etemadi [2].

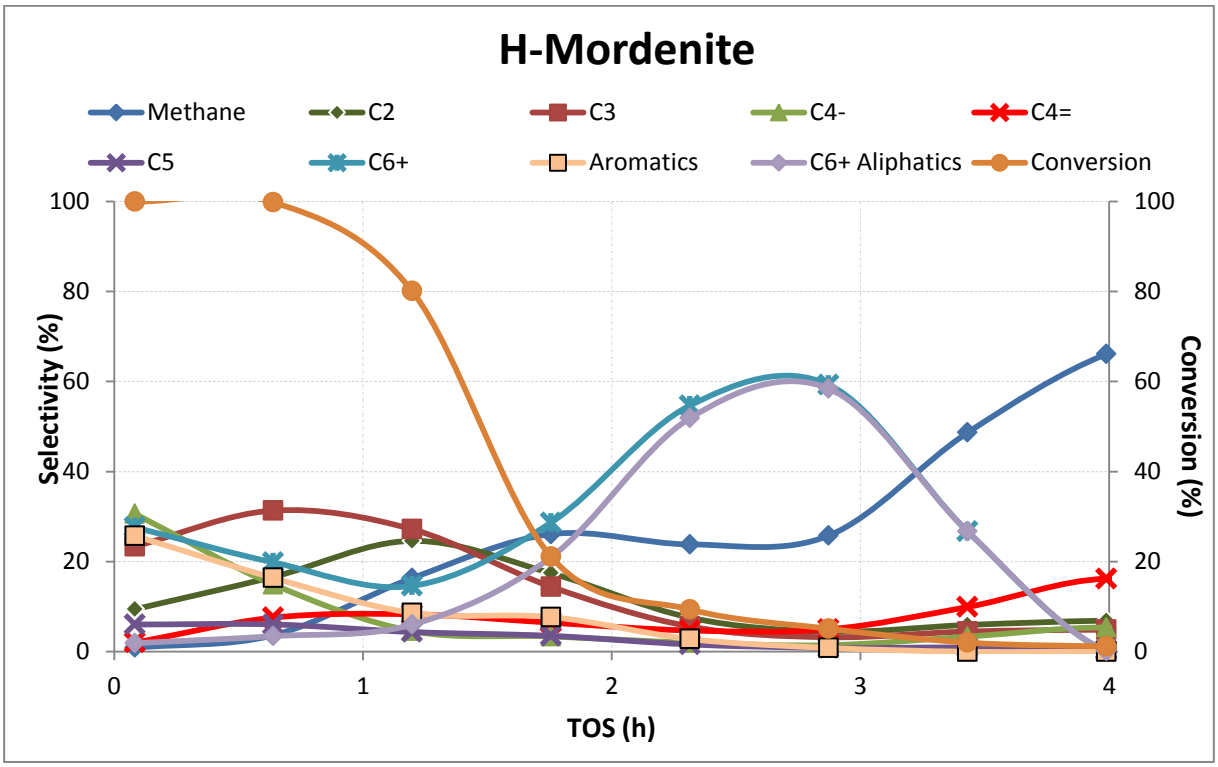

Figure A. 5: Methanol conversion and product selectivity as a function of TOS in H-Mordenite during MTH reaction carried out in a fixed bed reactor at 400°C, WHSV = 2.0 gg-1h-1. Experiment performed by S. Etemadi [2].

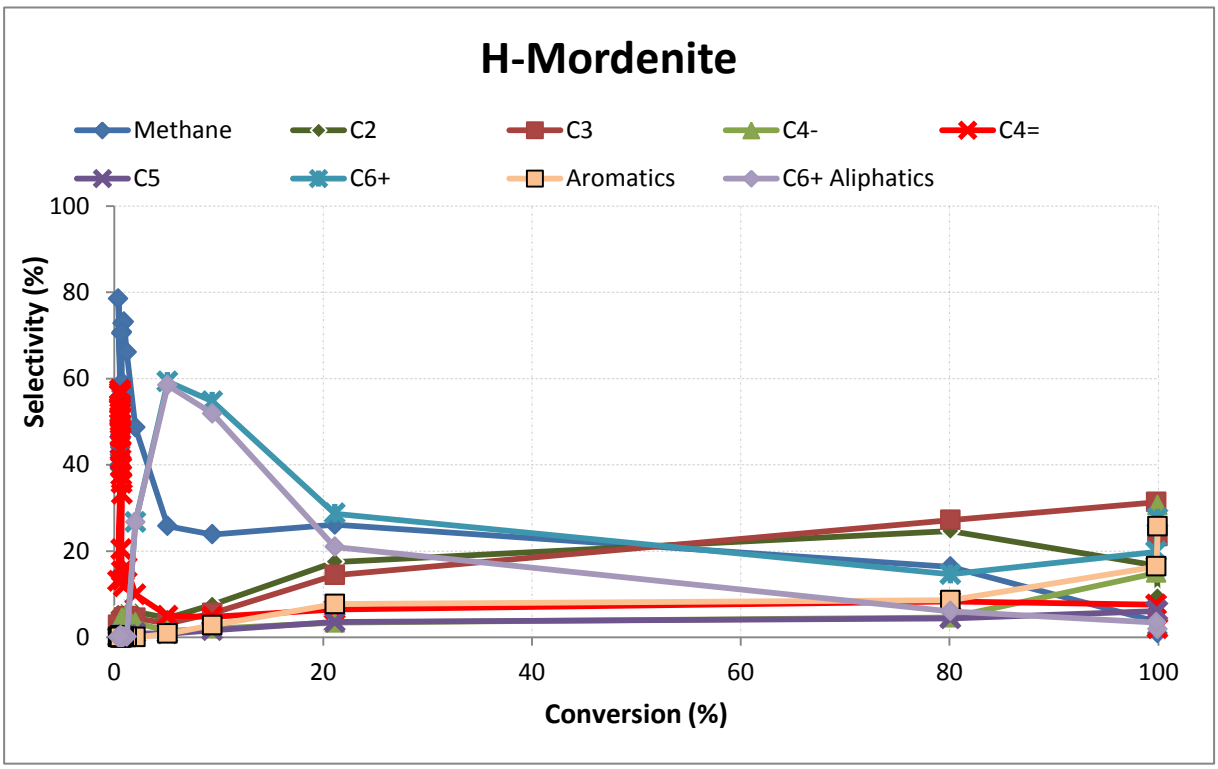

Figure A. 6: Product selectivity as a function of conversion in H-Mordenite during MTH reaction carried out in a fixed bed reactor at 400°C, WHSV = 2.0 $gg^{-1}h^{-1}$. Experiment performed by S. Etemadi [2].

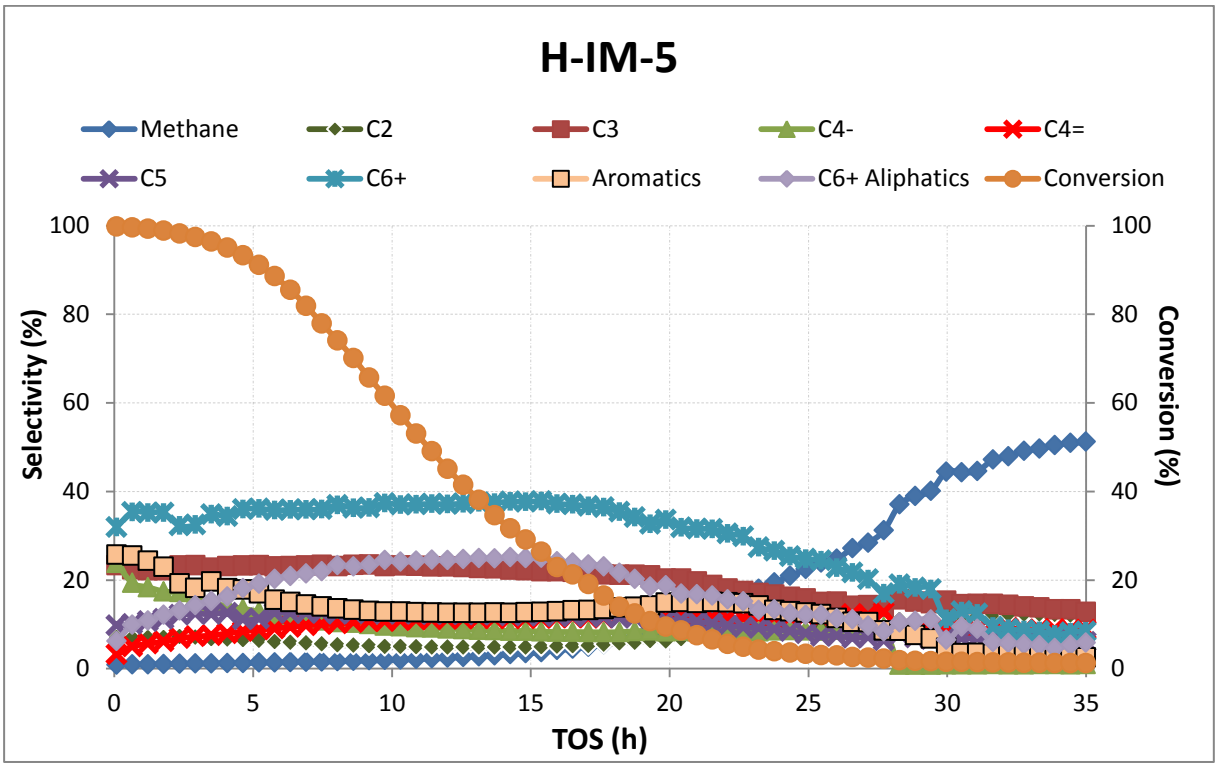

Figure A. 7: Methanol conversion and product selectivity as a function of TOS in H-IM-5 during MTH reaction carried out in a fixed bed reactor at 400°C, WHSV = 2.0 $gg^{-1}h^{-1}$. Experiment performed by S. Etemadi [2].

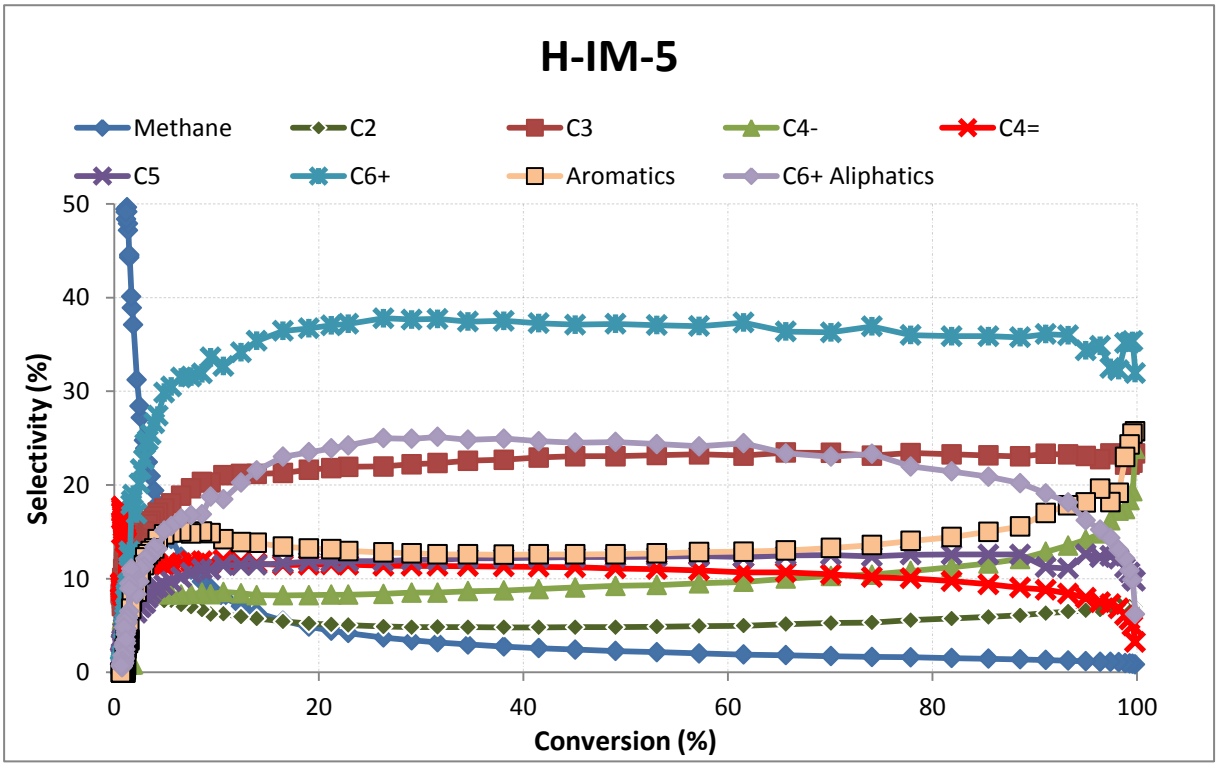

Figure A. 8: Product selectivity as a function of conversion in H-IM-5 during MTH reaction carried out in a fixed bed reactor at 400°C, WHSV = 2.0 $gg^{-1}h^{-1}$. Experiment performed by S. Etemadi [2].

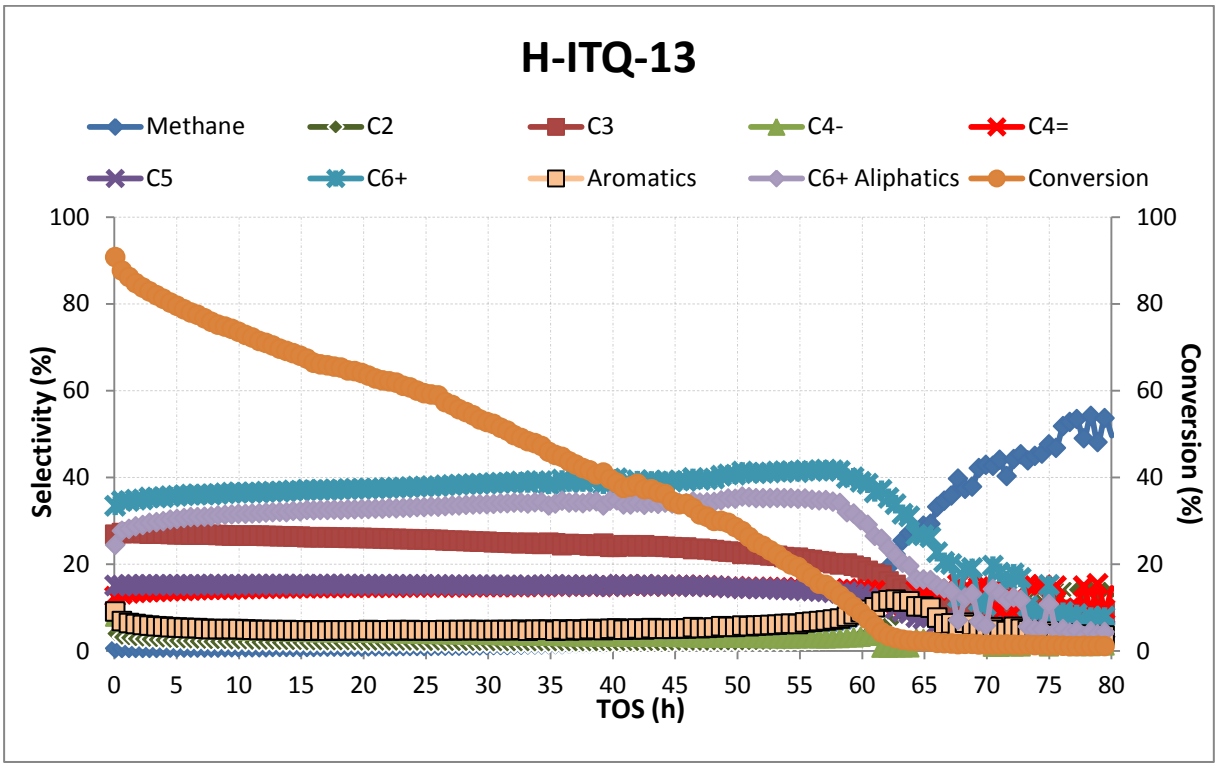

Figure A. 9: Methanol conversion and product selectivity as a function of TOS in H-ITQ-13 during MTH reaction carried out in a fixed bed reactor at 400°C, WHSV = 2.0 $gg^{-1}h^{-1}$. Experiment performed by S. Etemadi [2].

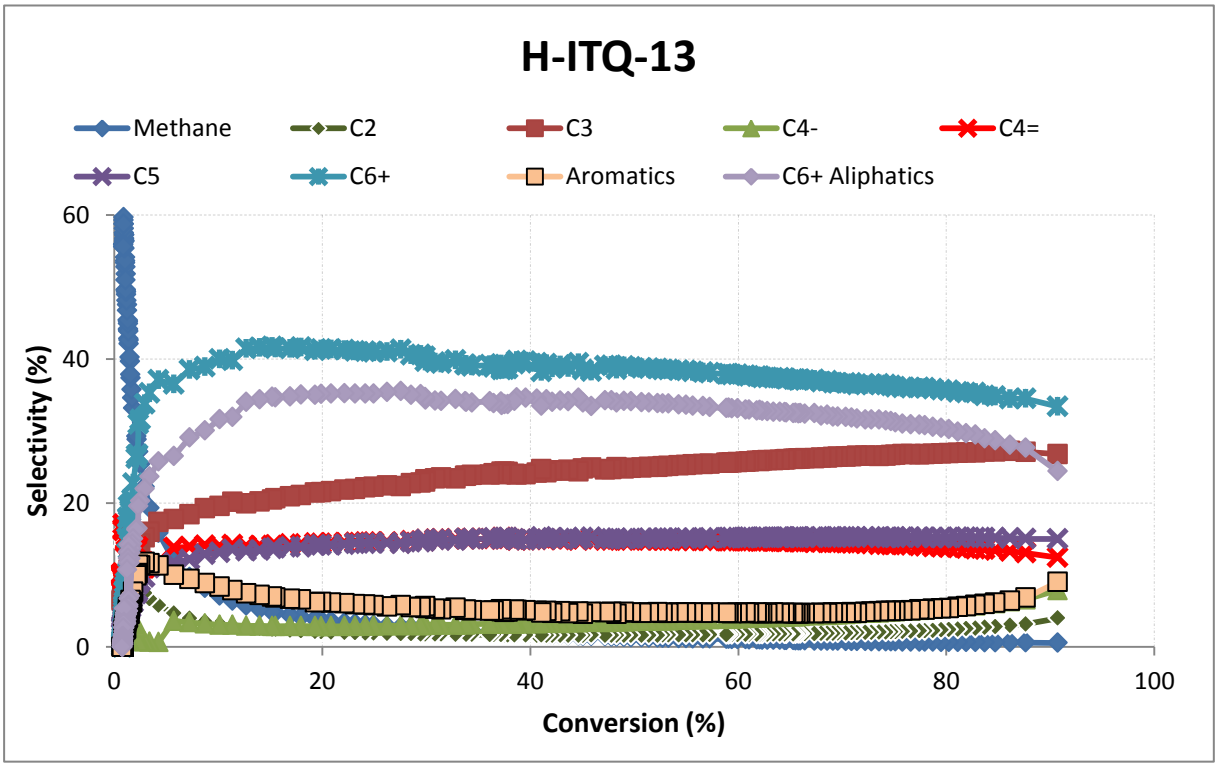

Figure A. 10: Product selectivity as a function of conversion in H-ITQ-13 during MTH reaction carried out in a fixed bed reactor at 400°C, WHSV = 2.0 $gg^{-1}h^{-1}$. Experiment performed by S. Etemadi [2].

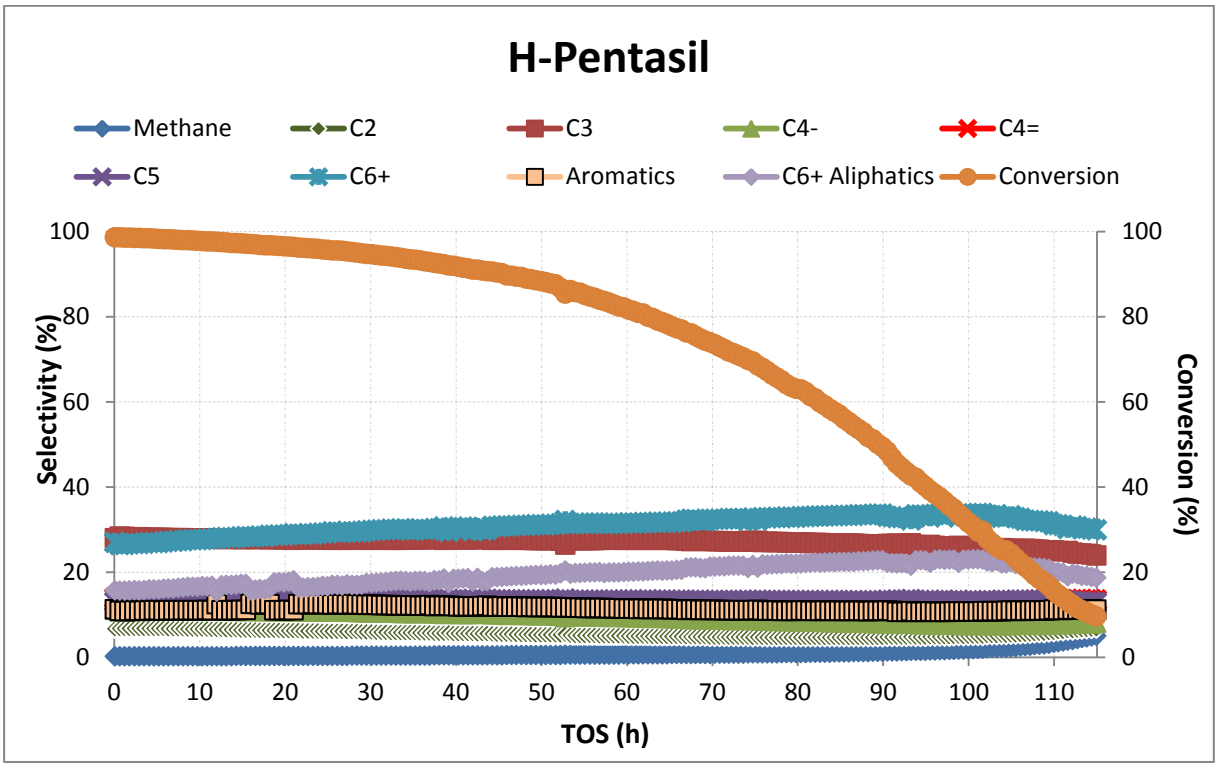

Figure A. 11: Methanol conversion and product selectivity as a function of TOS in H-Pentasil during MTH reaction carried out in a fixed bed reactor at 400°C, WHSV = 10.0 $gg^{-1}h^{-1}$. Experiment performed by S. Etemadi [2].

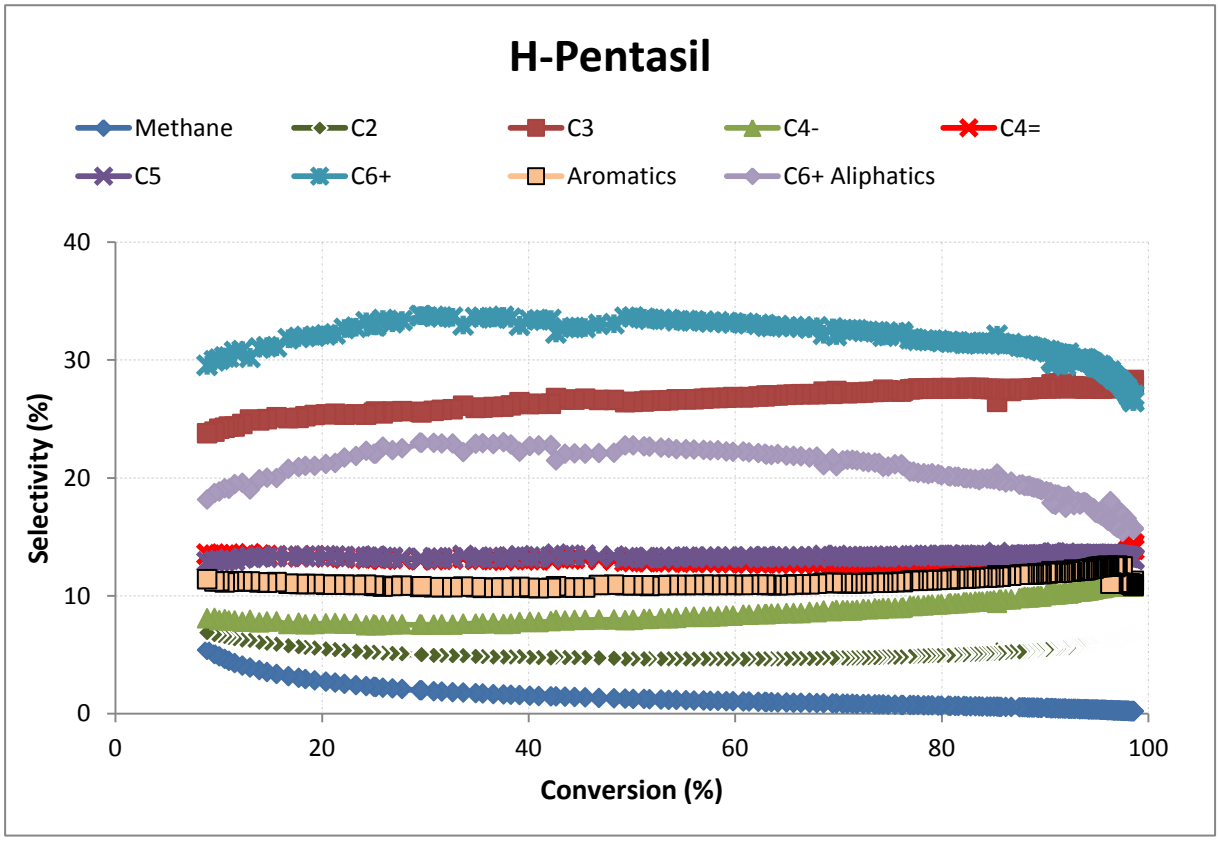

Figure A. 12: Product selectivity as a function of conversion in H-Pentasil during MTH reaction carried out in a fixed bed reactor at 400°C, WHSV = 10.0 $gg^{-1}h^{-1}$. Experiment performed by S. Etemadi [2].

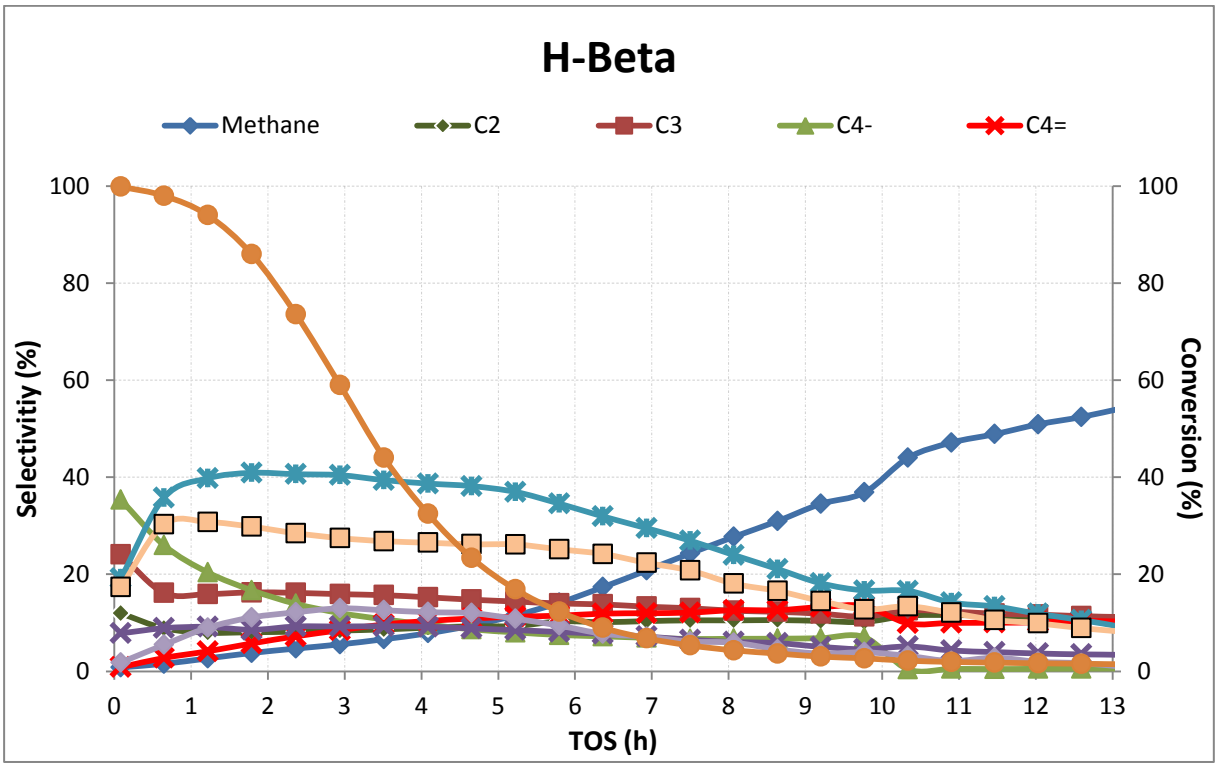

Figure A. 13: Methanol conversion and product selectivity as a function of TOS in H-Beta during MTH reaction carried out in a fixed bed reactor at 400°C, WHSV = 2.0 $gg^{-1}h^{-1}$. Experiment performed by S. Etemadi [2].

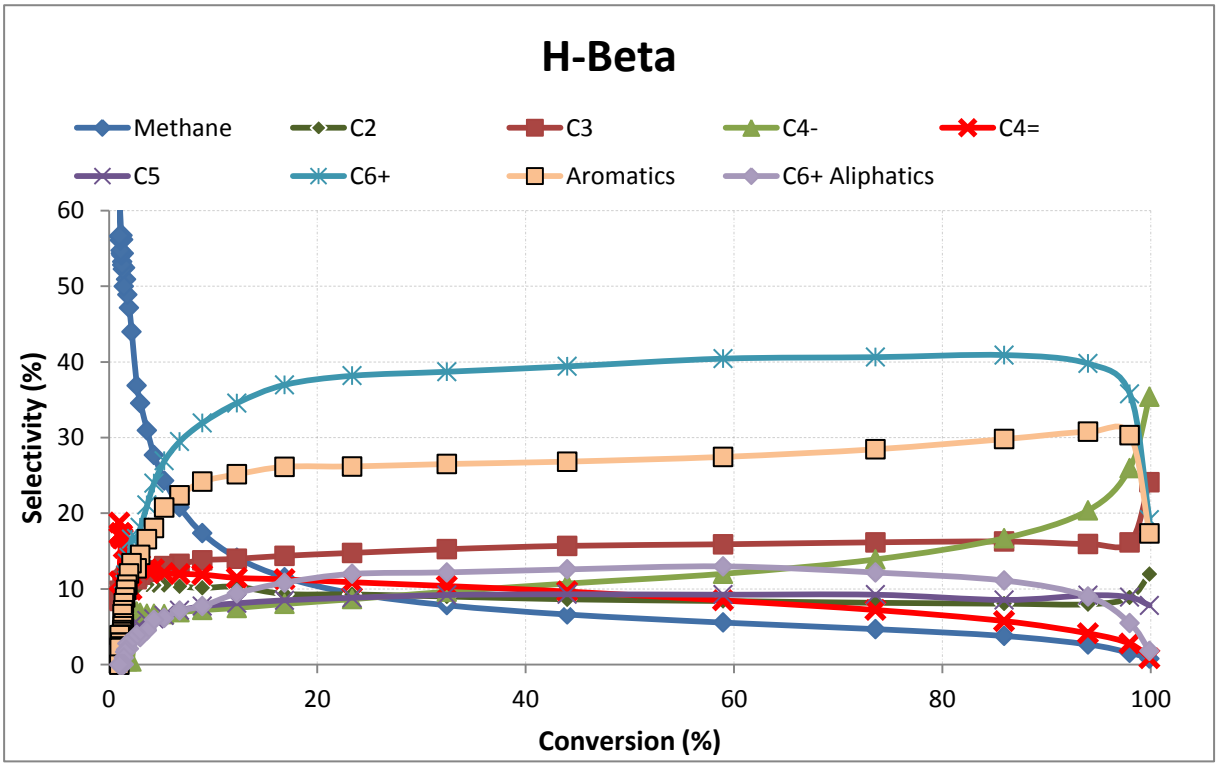

Figure A. 14: Product selectivity as a function of conversion in H-Beta during MTH reaction carried out in a fixed bed reactor at 400°C, WHSV = 2.0 $gg^{-1}h^{-1}$. Experiment performed by S. Etemadi [2].

Appendix B

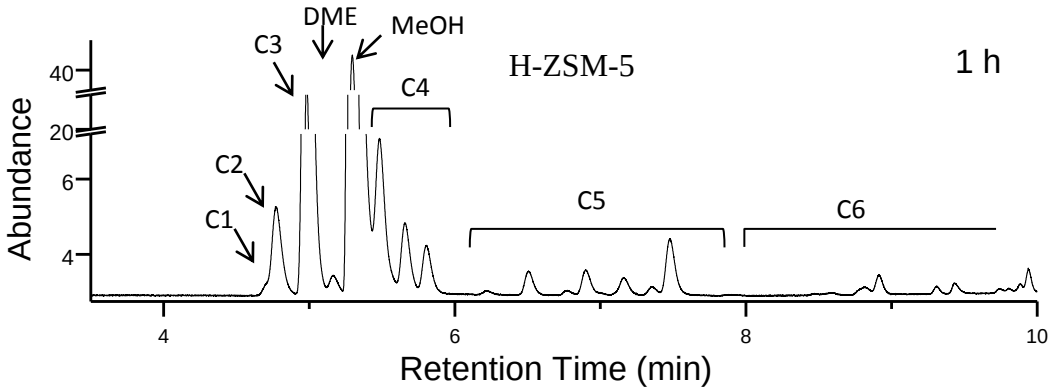

Figure B. 1: Example chromatogram of the H-ZSM-5 zeolite after 1 hour of contact with MeOH. Only the range of 3 ≤ retention time (min) ≤ 10 is shown.

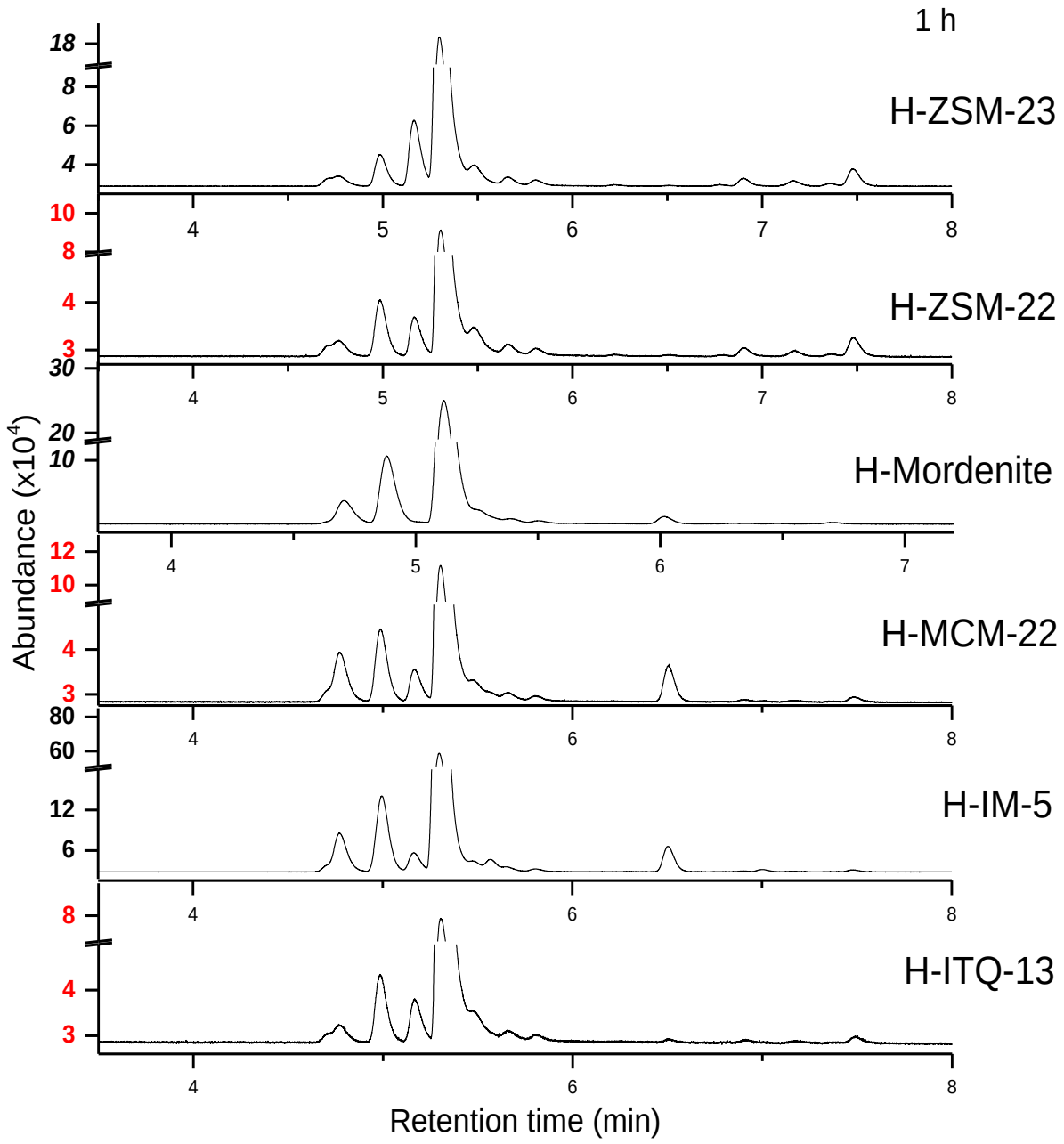

Figure B. 2: Chromatograms of the H-ZSM-23, H-ZSM-22, H-Mordenite, H-MCM-22, H-IM-5 and H-ITQ-13 after 1 hour of contact with MeOH. Only the range of 3 ≤ retention time (min) ≤ 8 is shown. The rest of the range is presented in Figure B. 3. The chromatogram of the H-Mordenite shows different retention time for the products compare to the rest of the samples because of different setting in GC-MS-FID instrument.

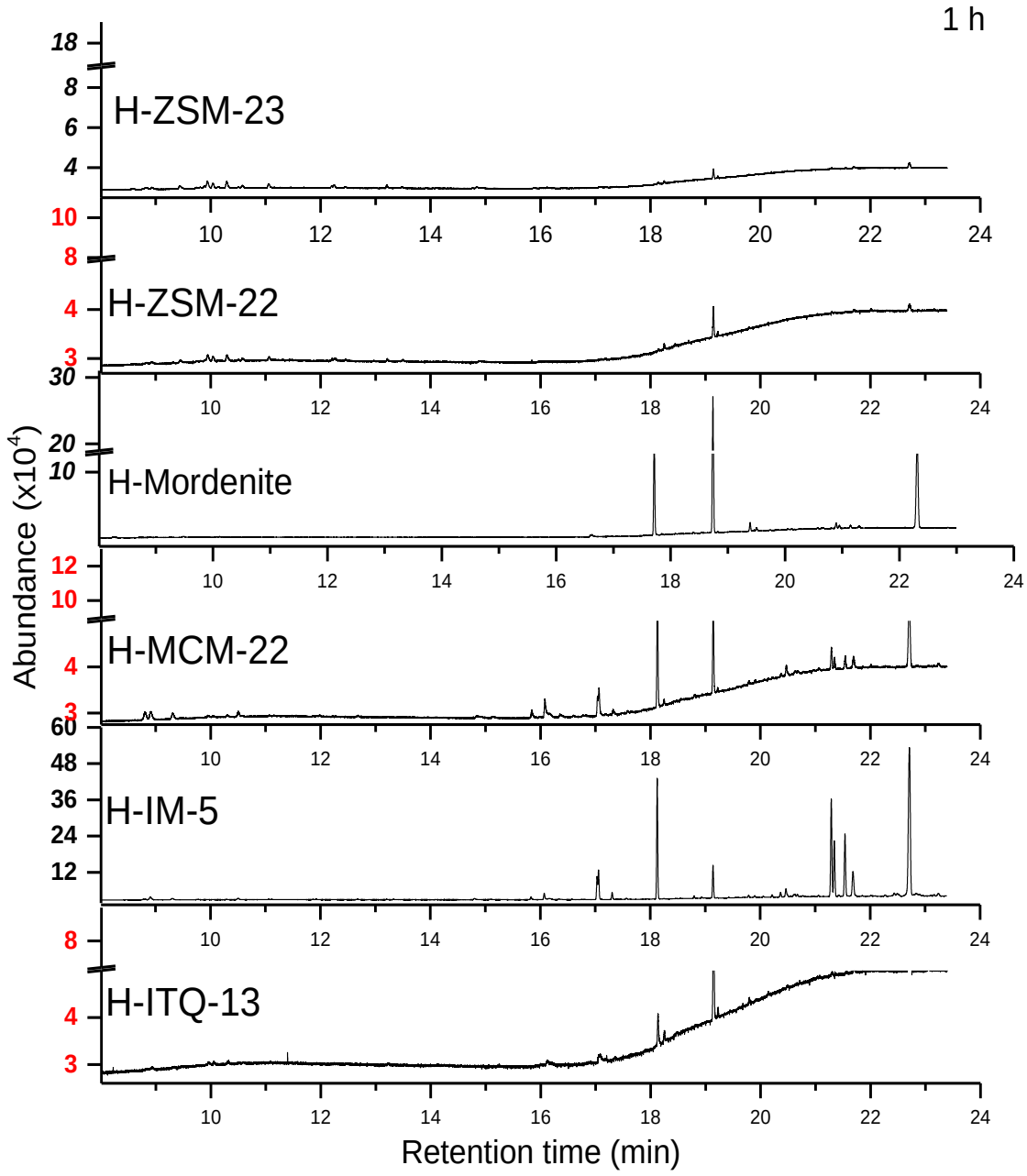

Figure B. 3: Chromatograms of the H-ZSM-23, H-ZSM-22, H-Mordenite, H-MCM-22, H-IM-5 and H-ITQ-13 after 1 hour of contact with MeOH. Only the range of 8 ≤ retention time (min) ≤ 24 is shown. The lower range is presented in Figure B. 2. The chromatogram of the H-Mordenite shows different retention time for the products compare to the rest of the samples because of different setting in GC-MS-FID instrument.

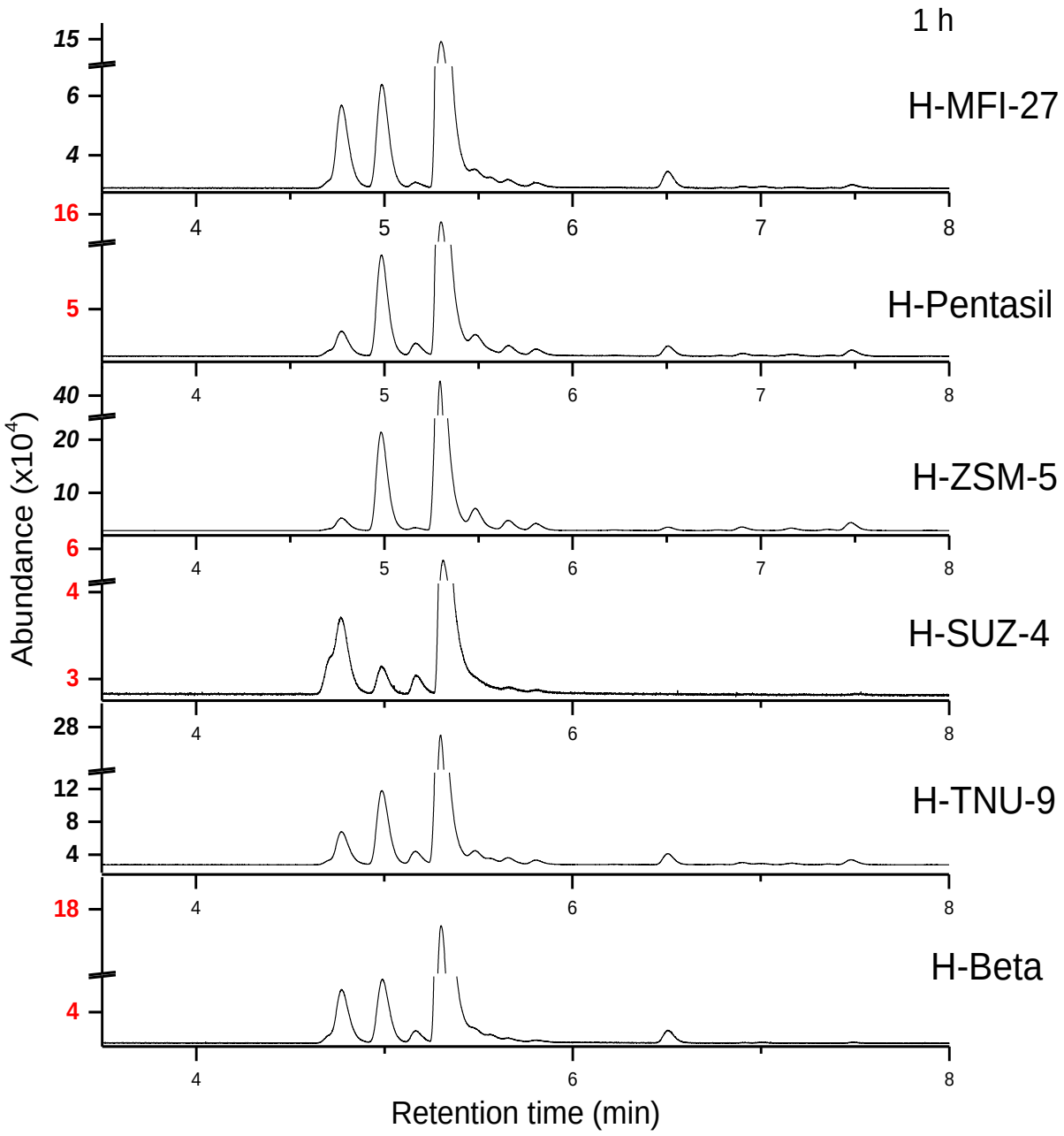

Figure B. 4: Chromatograms of the H-MFI-27, H-Pentasil, H-ZSM-5, H-SUZ-4, H-TNU-9 and H-Beta after 1 hour of contact with MeOH. Only the range of 3 ≤ retention time (min) ≤ 8 is shown. The rest of the range is presented in Figure B. 5.

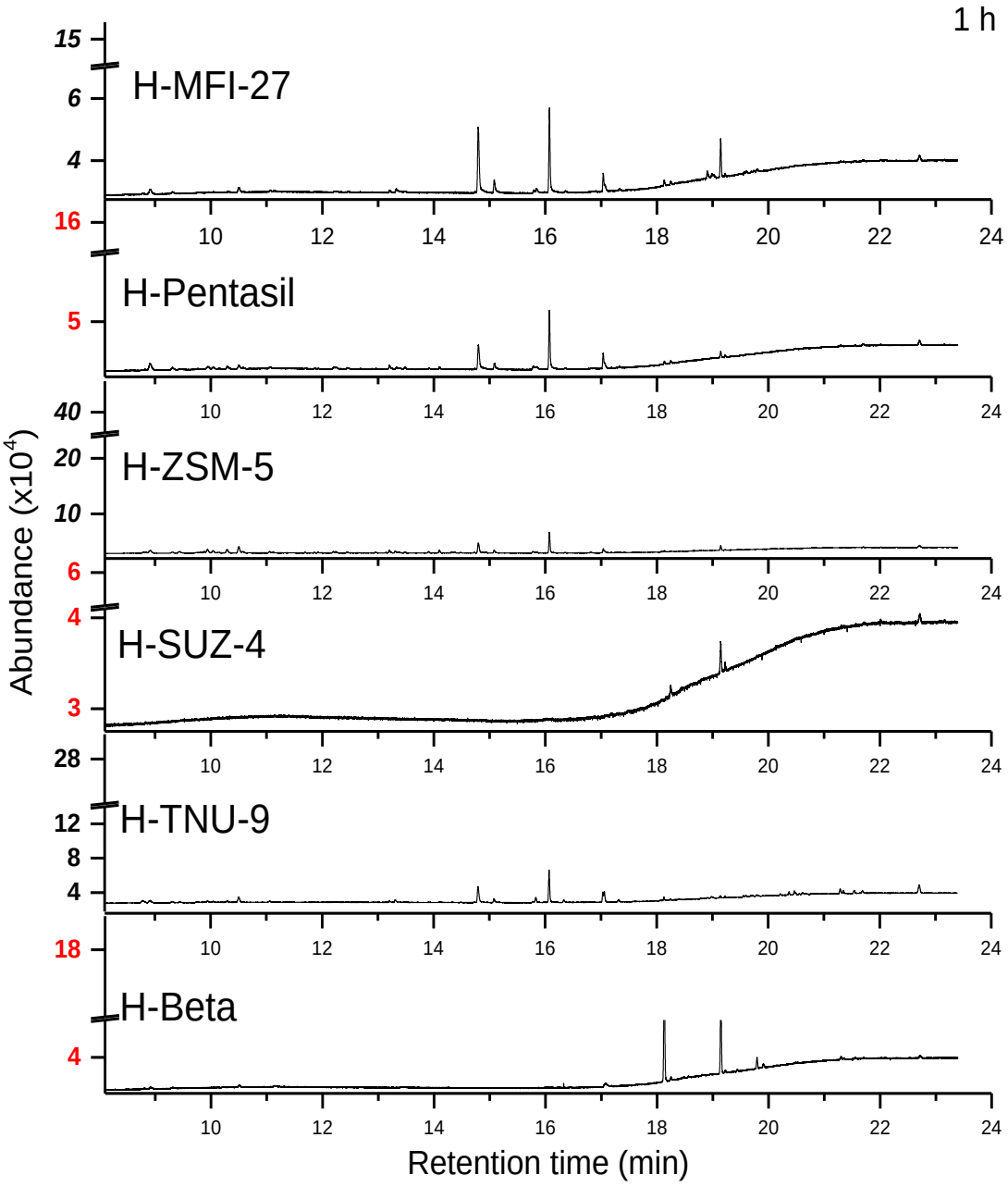

Figure B. 5: Chromatograms of the H-MFI-27, H-Pentasil, H-ZSM-5, H-SUZ-4, H-TNU-9 and H-Beta after 1 hour of contact with MeOH. Only the range of 8 ≤ retention time (min) ≤ 24 is shown. The lower range is presented in Figure B. 4.

Appendix C

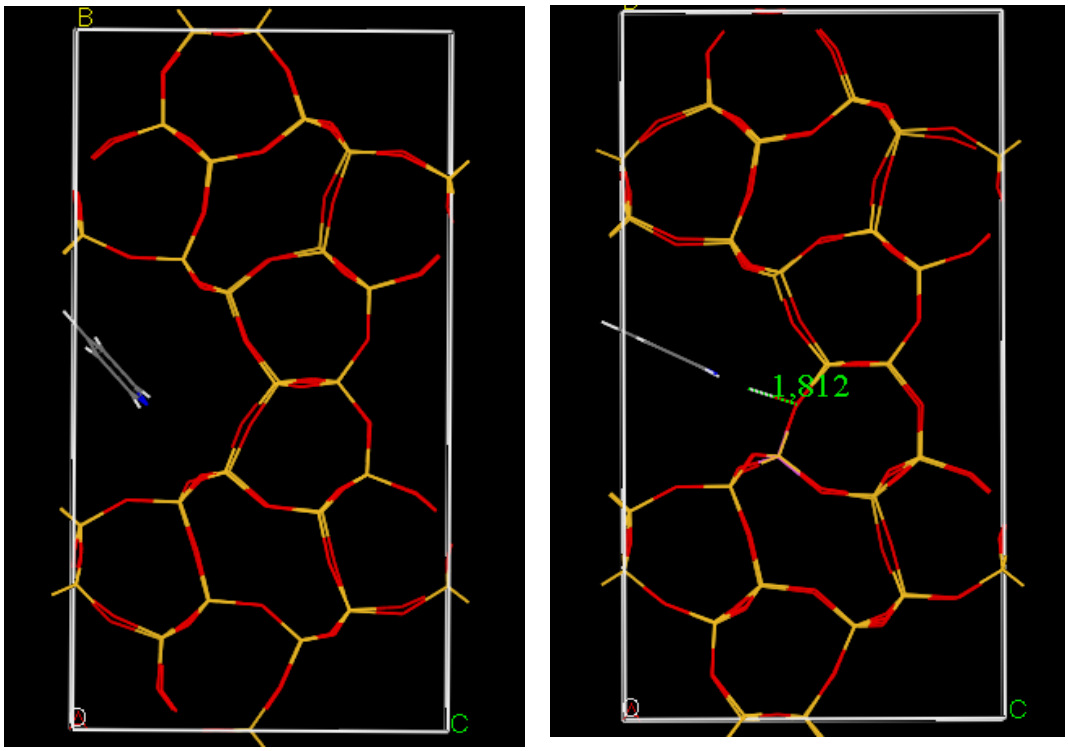

Figure C. 1: Illustration of (Left) H-ZSM-23 I-a, , a pyridine molecule interacting with the zeolite (two joint unit cells) without acid site (Right) H-ZSM-23 I-b, a pyridine molecule interacting with the zeolite (two joint unit cells) with an acid site. The result of the case calculation is in Table 4. 7. Green number is a distance between O-H in hydroxyl group.

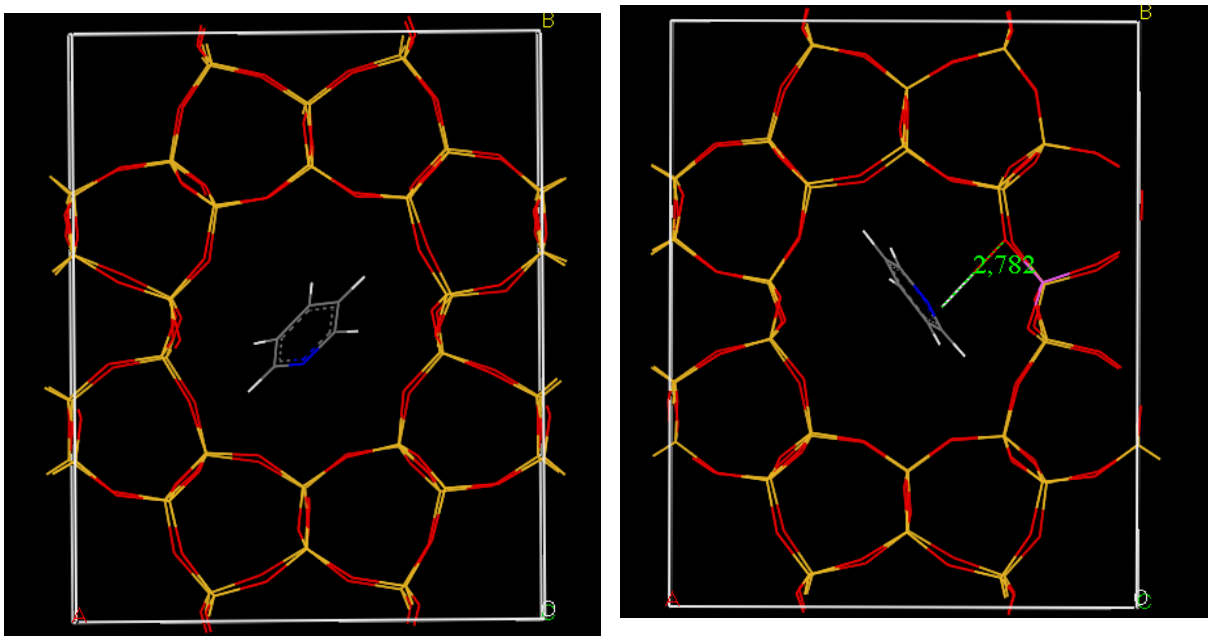

Figure C. 2: Illustration of (Left) H-ZSM-22 I-a, a pyridine molecule interacting with the zeolite (two joint unit cells) without acid site (Right) H-ZSM-22 I-b, a pyridine molecule interacting with the zeolite (two joint unit cells) with an acid site. The result of the case calculation is in Table 4. 7. Green number is a distance between O-H in hydroxyl group.

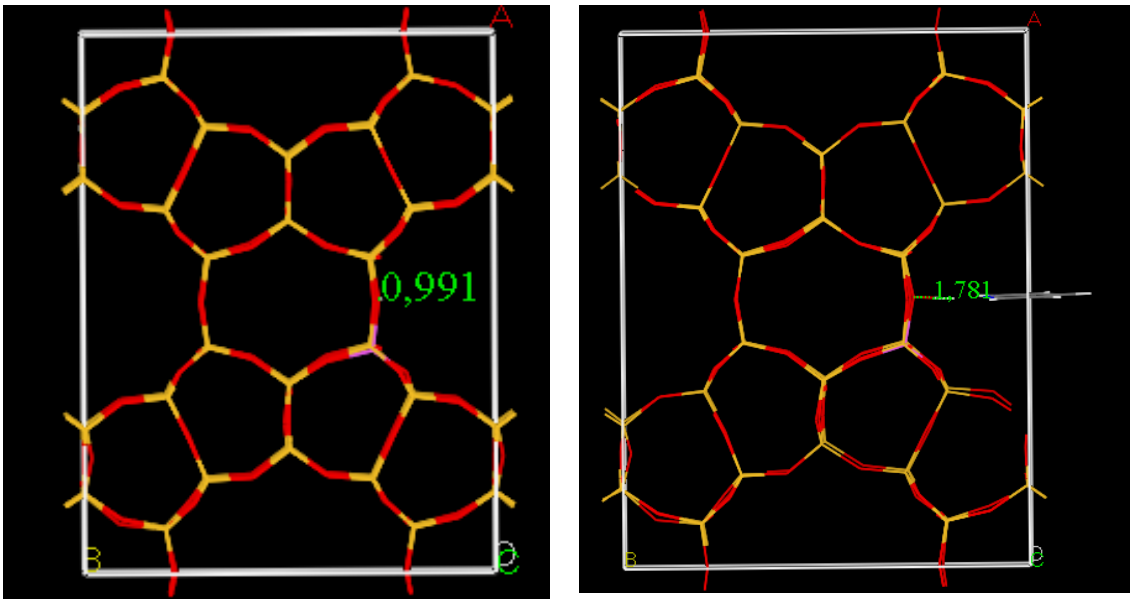

Figure C. 3: Illustration of H-SUZ-4 10-ring I case calculation result in Table 4. 8. (Left) The zeolite (two joint unit cells) with a single acid site (Right) The zeolite (two joint unit cells) with a single acid site interacting with a pyridine. Green number is a distance between O-H in hydroxyl group.

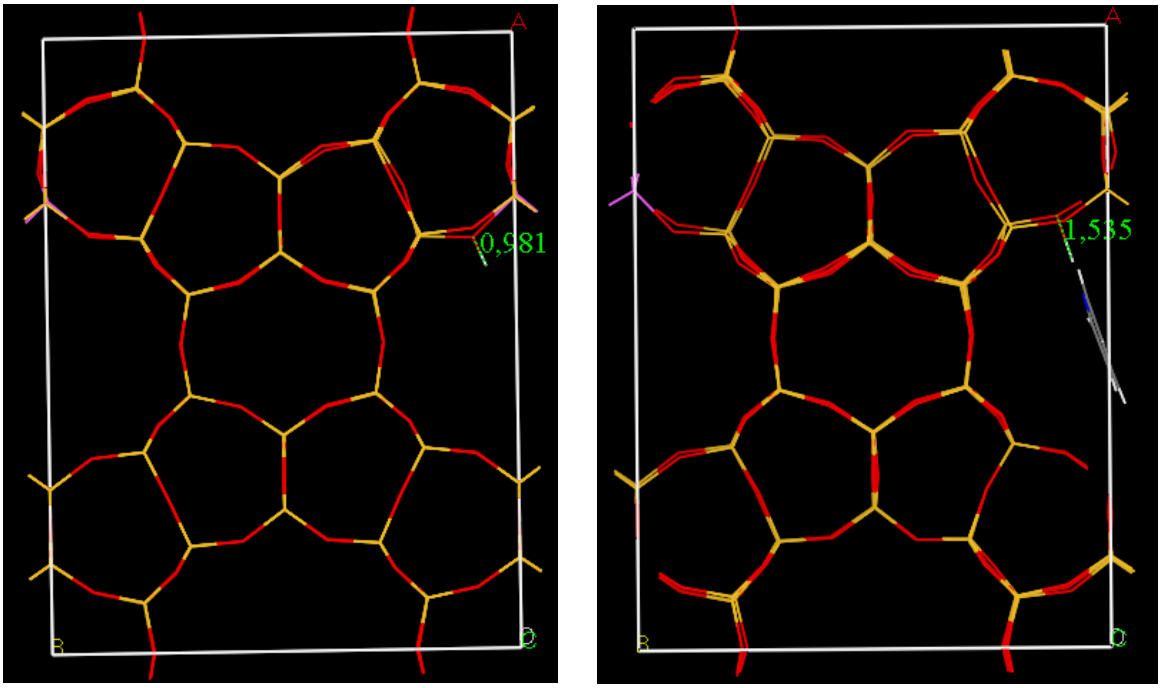

Figure C. 4: Illustration of H-SUZ-4 10-ring II case calculation result in Table 4. 8. (Left) The zeolite (two joint unit cells) with a single acid site (Right) The zeolite (two joint unit cells) with a single acid site interacting with a pyridine. Green number is a distance between O-H in hydroxyl group.

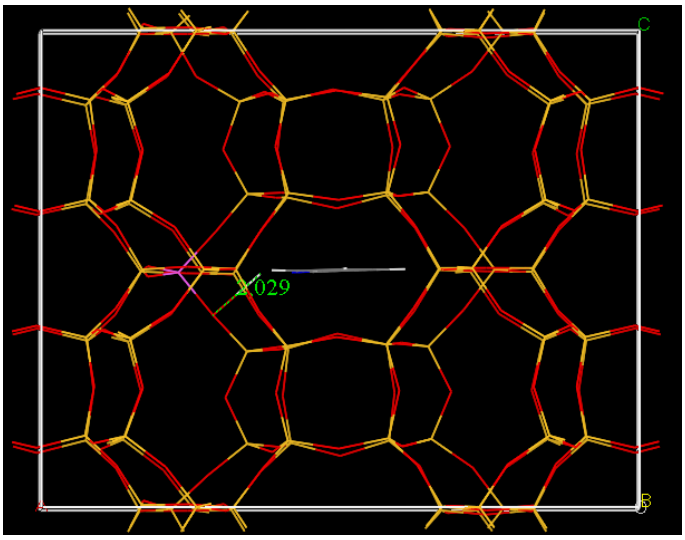

Figure C. 5: Illustration of H-SUZ-4 8-ring I case calculation result in Table 4. 8. H-SUZ-4 with a single acid site in the zeolite (two joint unit cells) interacting with a pyridine. Green number is a distance between O-H in hydroxyl group.

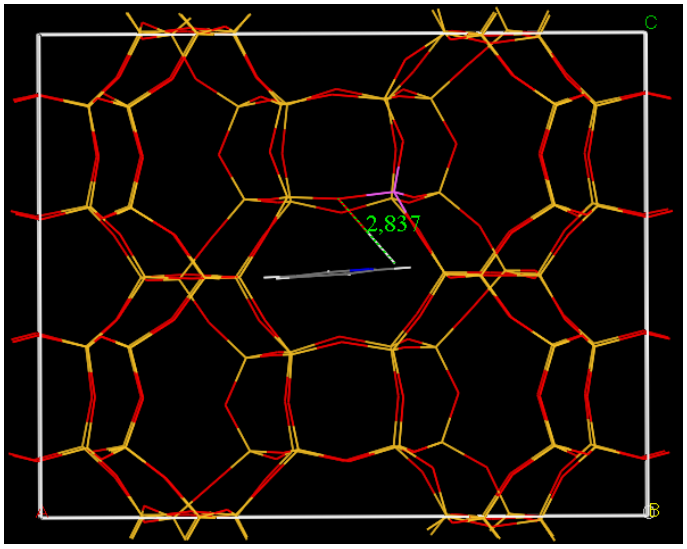

Figure C. 6: Illustration of H-SUZ-4 8-ring II case calculation result in Table 4. 8. H-SUZ-4 with a single acid site in the zeolite (two joint unit cells) interacting with a pyridine. Green number is a distance between O-H in hydroxyl group.

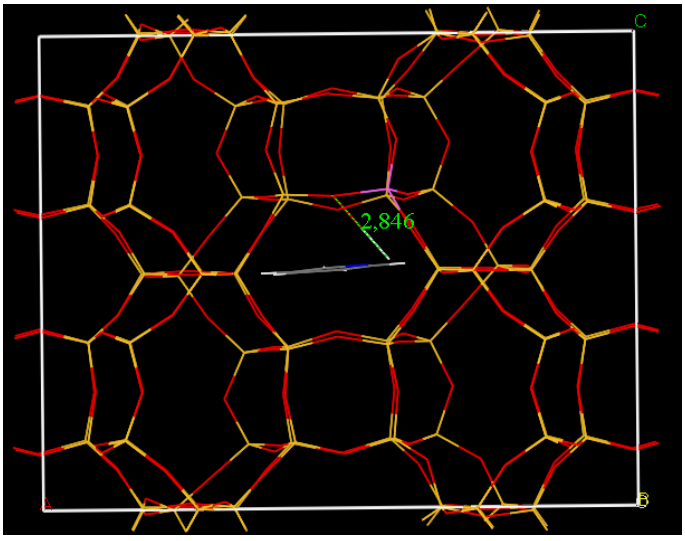

Figure C. 7: Illustration of H-SUZ-4 8-ring III case calculation result in Table 4. 8. H-SUZ-4 with a single acid site in the zeolite (two joint unit cells) interacting with a pyridine. Green number is a distance between O-H in hydroxyl group.

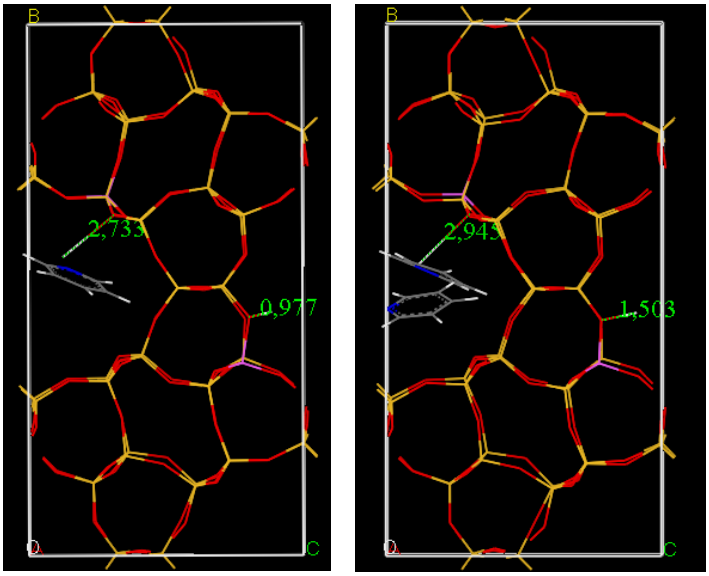

Figure C. 8: Illustration of H-ZSM-23 II case calculation result in Table 4. 9.(Left) One pyridine molecule in the zeolite (two joint unit cells) with two acid sites (Right) Two pyridine molecules in the zeolite (two joint unit cells) with two acid sites. Green number is a distance between O-H in hydroxyl group.

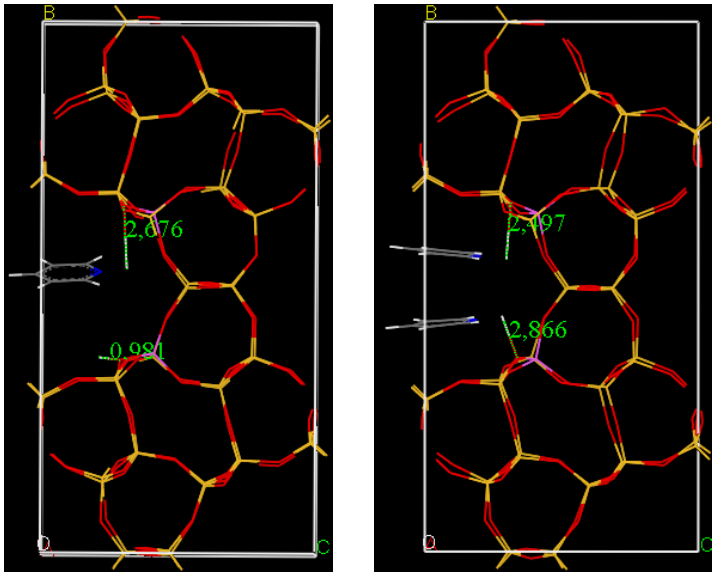

Figure C. 9: Illustration of H-ZSM-23 III case calculation result in Table 4. 9. (Left) One pyridine molecule in the zeolite (two joint unit cells) with two acid sites (Right) Two pyridine molecules in the zeolite (two joint unit cells) with two acid sites. Green number is a distance between O-H in hydroxyl group.

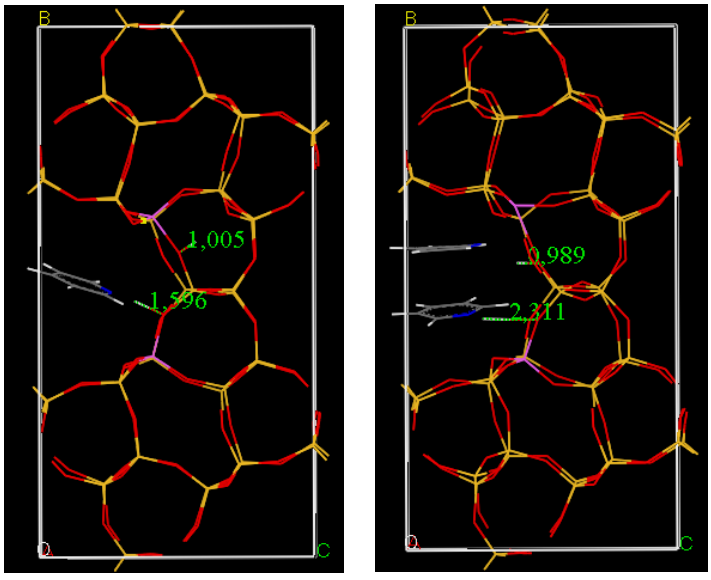

Figure C. 10: Illustration of H-ZSM-23 IV case calculation result in Table 4. 9. (Left) One pyridine molecule in the zeolite (two joint unit cells) with two acid sites (Right) Two pyridine molecules in the zeolite (two joint unit cells) with two acid sites. Green number is a distance between O-H in hydroxyl group.

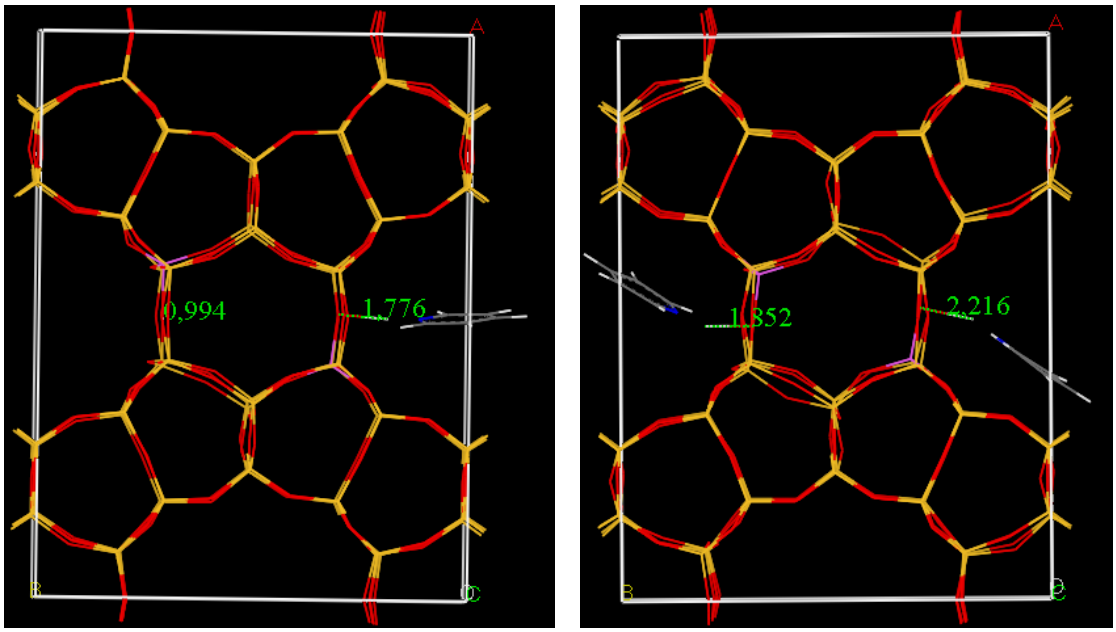

Figure C. 11: Illustration of H-SUZ-4 IV case calculation result in Table 4. 10. (Left) One pyridine molecule in the zeolite (two joint unit cells) with two acid sites (Right) Two pyridine molecules in the zeolite (two joint unit cells) with two acid sites. Green number is a distance between O-H in hydroxyl group.

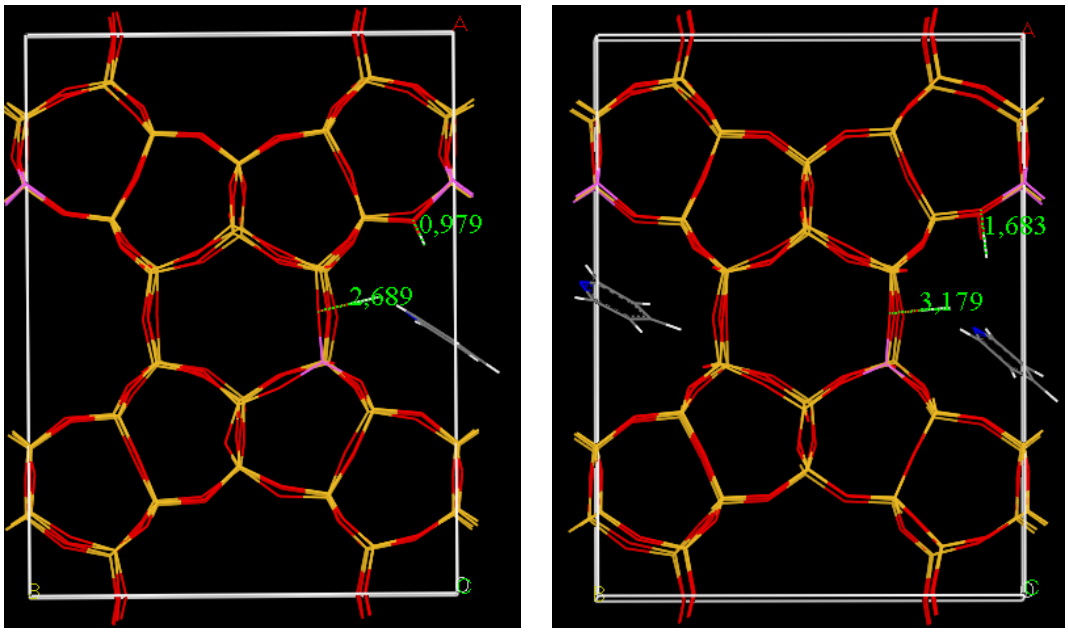

Figure C. 12: Illustration of H-SUZ-4 V case calculation result in Table 4. 10. (Left) One pyridine molecule in the zeolite (two joint unit cells) with two acid sites (Right) Two pyridine molecules in the zeolite (two joint unit cells) with two acid sites. Green number is a distance between O-H in hydroxyl group.

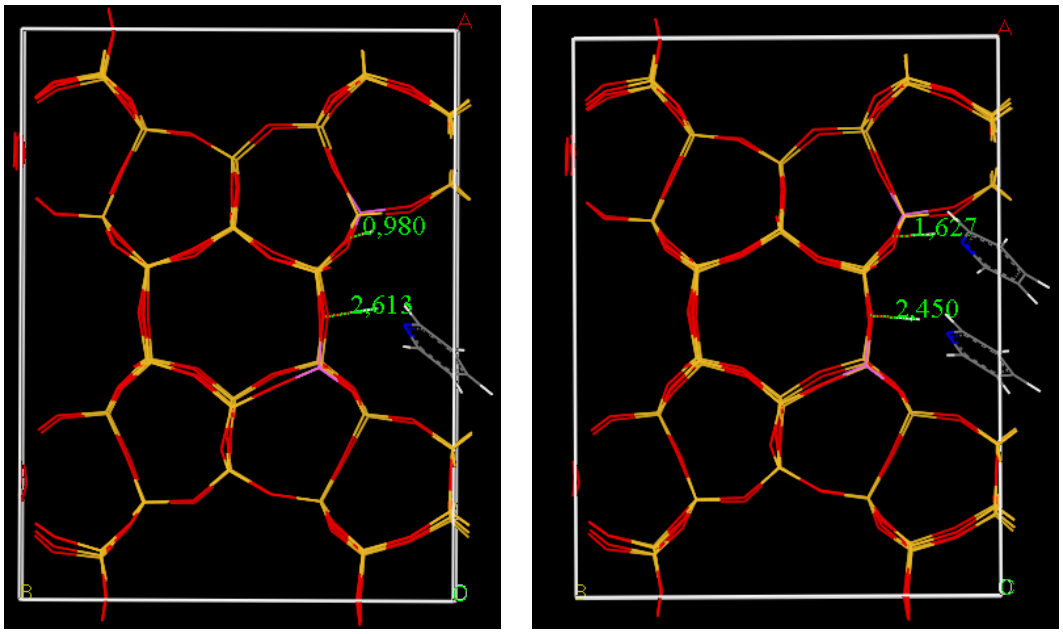

Figure C. 13: Illustration of H-SUZ-4 VI case calculation result in Table 4. 10. (Left) One pyridine molecule in the zeolite (two joint unit cells) with two acid sites (Right) Two pyridine molecules in the zeolite (two joint unit cells) with two acid sites. Green number is a distance between O-H in hydroxyl group.

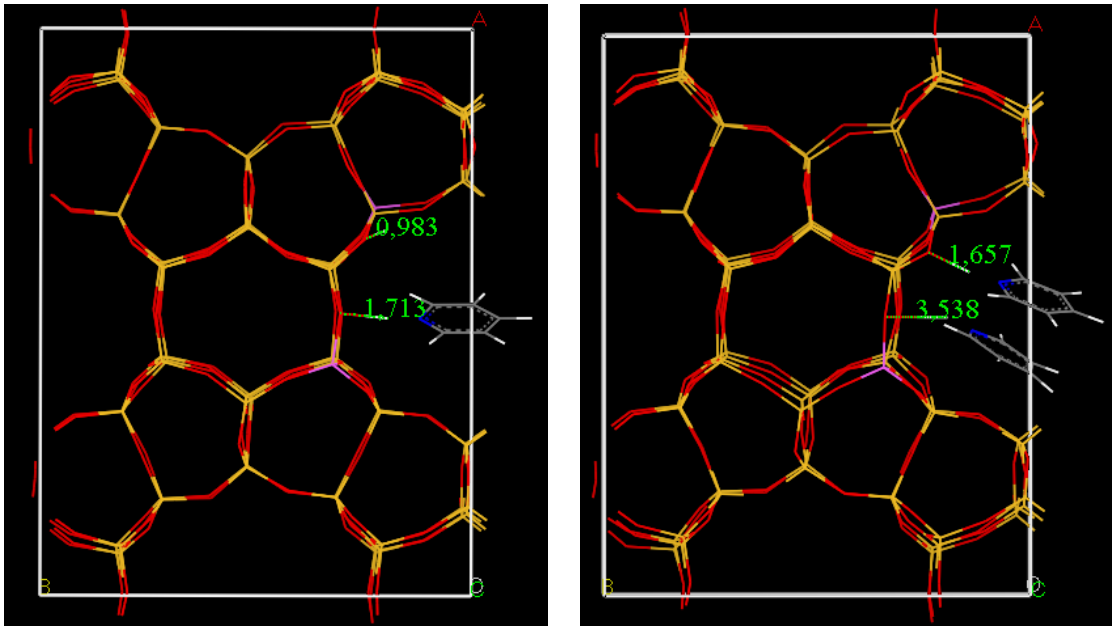

Figure C. 14: Illustration of H-SUZ-4 VII case calculation result in Table 4. 10. (Left) One pyridine molecule in the zeolite (two joint unit cells) with two acid sites (Right) Two pyridine molecules in the zeolite (two joint unit cells) with two acid sites. Green number is a distance between O-H in hydroxyl group.

Reference

1. U. Olsbye, S. Svelle, M. Bjørgen, P. Beato, T.V.W. Janssens, F. Joensen, S. Bordiga, K.P. Lillerud, Angew. Chem. Int. Ed., 51 (2012) 5810.

2. S. Etemadi, Master's degree thsis, Dept. of Chemistry, University of Oslo, 2014.

3. R. Chang, J. Overby, General Chemistry, The Essential Concepts. 6th ed. McGraw-Hill, New York, 2011.

4. S. Svelle, KJM3800-Petrochemistry, Lecture note, University of Oslo, 2013.

5. J.A. Moulijn, M. Makkee, A. van Diepen, Chemical Process Technology, John Wiley & Sons Ltd., Ireland, 2008.

6. I. Chorkendorff, J.W. Niemantsverdriet, Concepts of modern catalysis and kinetics, Wiley-vCH Verlag GmbH & Co. KGaA., Weinheim, 2003.

7. R.M. Barrer, New Scientist, 18 (1963) 497.

8. B. Rogers, J. Adams., S. Pennathur, Nanotechnology: The Whole Story, CRC Press, 2013.

9. P. Payra, P.K. Dutta, in: S.M. Auerbach, K.A. Carrado, P.K. Dutta (Eds) Handbook of Zeolite Science and Technology, CRC Press, 2003.

10. S. Svelle, M. Bjørgen, in: A. Zecchina, S. Bordiga, E. Groppo (Eds.) Selective Nanocatalysts and Nanoscience: Concepts for Heterogeneous and Homogeneous Catalysis, Wiley-VCH Verlag GmbH & Co. KGaA. 2011.

11. A. Dyer, An Introduction to Zeolite Molecular Sieves. John Wiley & Sons Ltd., Chichester, 1988.

12. S. Teketel, Master's degree Thesis, Dept. of Chemistry, University of Oslo, 2009.

13. B. Smit, T.L.M. Maesen, Nature, 451 (2008) 671.

14. Ch. Baerlocher, L.B. mcCusker, D.H. Olson, Atlas of Zeolite Framework Types, 6th revised ed., Elsevier, 2007.

15. S. Teketel, PhD Thesis, Dept. of Chemistry, University of Oslo, 2012.

16. L.B. McCusker, C. Baerlocher, in: J. Čejka, H. van Bekkum (Eds.) Zeolites and ordered mesoporous materials: progress and prospects, Elsevier, Amsterdam, 2005.

17. W. Song, D. Marcus, H. Fu, J.O. Ehresmann, J.F. Haw, J. Am. Chem. Soc., 124 (2002) 3844.

18. I.M. Dahl, S. Kolboe, J. Catal., 149 (1994) 458.

19. M.W. Erichsen, PhD Thesis, Dept. of Chemistry, University of Oslo, 2014.

20. D. Lesthaeghe, A. Horre, M. Waroquier, G.B. Marin, V. van Speybroeck, Chem. Eur. J. 15 (2009) 10803.

21. S. Svelle, F. Joensen, J. Nerlov, U. Olsbye, K.P. Lillerud, S. Kolboe, M. Bjørgen, J. Am. Chem. Soc., 128 (2006) 14770.

22. M. Bjørgen, S. Svelle, F. Joensen, J. Nerlov, S. Kolboe, F. Bonino, L. Palumbo, S. Bordiga, U. Olsbye, J. Catal., 249 (2007) 195.

23. M. Bjørgen, F. Joensen, K.P. Lillerud, U. Olsbye, S. Svelle, Catal. Today, 142 (2009) 90.

24. S.T. Forsido, PhD Thesis, Dept. of Chemistry, University of Oslo, 2013.

25. J.W. Niemantsverdriet, Spectroscopy in Catalysis: An Introduction. 3rd completely revised and enlarged ed., Wiley-VCH Verlag GmbH & Co. KGaA., 2007.

26. F. Krumeich, Generation of X-rays, http://www.microscopy.ethz.ch/xray.htm (Accessed 19/11/2014).

27. S.J. Park, M.K. Seo, Interface Science and Technology, 1st ed., Elsevier, Great Britain, 2011.

28. S. Brunauer, P.H. Emmet, E. Tell, J. Am. Chem. Soc., 60 (1938) 309.

29. I.M.K. Ismail, Carbon, 28 (1990) 423.

30. P. Larkin, Infrared and Raman Spectroscopy; Principles and Spectral Interpretation, Elsevier, USA, 2011.

31. D.N. Sathyanarayana, Vibrational Spectroscopy: Theory And Applications, New New Age International, Delhi, 2005.

32. B.C. Smith, Infrared Spectral Interpretation: A Systematic Approach, CRC Press, USA, 1999.

33. P. Atkins, R. Friedman, Molecular Quantum Mechanics, 5th ed., Oxford University Press Inc. USA, 2011.

34. C.E. Housecroft, E.C.Constable, Chemistry: An Introduction to Organic, Inorganic and Physical Chemistry, 4th ed., Pearson Education Ltd., Rotolito Lombarda, 2010.

35. D.L. Pavia, G.M. Lampman, G.S. Kriz, J.R. Vyvyan, Introduction to Spectroscopy. 4th ed., Brooks/Cole, California, 2009.

36. S.N. Singh, R.K. Agarwal, M. Katyal, Molecular Structure A Spectroscopic Approach, Discovery Publishing House, New Delhi, 1990.

37. J. A. Lercher, A. Jentys, in: J. Čejka, H. van Bekkum, A. Corma, F. Schueth (Eds.) Introduction to Zeolite Science and Practice, Elsevier, Hungary, 2007.

38. C. A. Emeis, J. Catal., 141 (1993) 347.

39. M. Guisnet, P. Ayrault, J. Datka, Pol. J. Chem., 71 (1997) 1455-1461.

40. E. Selli, L. Forni, Microporous Mesoporous Mater., 31 (1999) 129.

41. T. R. Hughes, H.M. White, J. Phys. Chem., 71 (1967) 2192.

42. J. Take, T. Yamaguchi, K. Miyamoto, H. Ohyama, M. Misono, in: Y. Murakami, A. Iijima, J.W. Ward (Eds.) New Developments in Zeolite Science and Technology, Proceedings of the 7th International Zeolite Conference, Elsevier, Tokyo, 1986.

43. S. Khabtou, T. Chevreau, J. C. Lavalley, Microporous Mater., 3 (1994) 133.

44. M.A. Makarova, K. Karim, J. Dwyer, Microporous Mater., 4 (1995) 243.

45. J. Datka, B.Gil, A. Kubacka, Zeolites, 17 (1996) 428.

46. B. Sulikowski, J. Datka., B. Gil, J. Ptaszynski, J. Klinowski, J. Phys. Chem. B, 101 (1997) 6929.

47. N. Echoufi, P. Gelin, Catal. Lett., 40 (1996) 249.

48. M. Guisnet, P. Ayrault, C. Coutanceau, M. Fernanda Alvarez, J. Datka, J. Chem. Soc., Faraday Trans., 93 (1997) 1661.

49. J. Datka, A.M. Turek., J.M. Jehng, I.E. Wachs, J. Catal., 135 (1992) 186.

50. A. Zecchina, S. Bordiga, G. Spoto, D. Scarano, J. Chem. Soc., Faraday Trans., 88 (1992) 2959.

51. H. Knözinger, S. Huber, J. Chem. Soc., Faraday Trans., 94 (1998) 2049.

52. C. Lamberti, A. Zecchina, E. Groppob, S. Bordiga, Chem. Soc. Rev., 39 (2010) 4963.

53. K.M. Neyman, P. Strodel, S.Ph. Ruzankin, N. Schlensog, H. Knözinger, N. Rösch, Catalysis Letters, 31 (1995) 273.

54. G.O. Spessard, G.L. Miessler, Organometallic Chemistry, 2nd ed., Oxford University Press, New York, 2010.

55. G. Frenking, C. Loschen, A. Krapp, S. Fau, S. H. Strauss, J Comput Chem, 28 (2006) 117.

56. M.J. Hazelrigg, Jr., P. Politzer J. Phys. Chem., 73 (1969) 1009.

57. A.S. Goldman, K. Krogh-Jespersen, J. Am. Chem. Soc., 118 (1996) 12159.

58. T. Bucko, J. Hafner, L. Benco, J. Phys. Chem. B, 109 (2005) 7345.

59. R. Buzzoni, S. Bordiga, G. Ricchiardi, C. Lamberti, A. Zecchina, Langmuir, 12 (1996) 930.

60. E.B. Wilson, J.C. Decius. P.C. Cross, Molecular Vibrations, McGraw-Hill, New York, 1955.

61. J.A. Boscoboinik, X. Yu, E. Emmez, B. Yang, S. Shaikhutdinov, F. D. Fischer, J. Sauer, H. Freund, J. Phys. Chem. C, 117 (2013) 13552.

62. G. Busca, in: S.D. Jackson, J.S.J. Hargreaves (Eds.) Metal Oxide Catalysis, John Wiley & Sons, 2008.

63. N. Schildknecht-Zanier, in: J. Lynch (Ed.) Physico-chemical Analysis of Industrial Catalysts: A Practical Guide to Characterisation, Technip, France, 2003.

64. J. Weitkamp, Solid State Ionics, 131 (2000) 175.

65. S. Forselv, Master's Thesis, Dept. of Chemistry, Norwegian University of Science and Technology, 2011.

66. Saepurahman, M. Visur, U. Olsbye, M. Bjørgen, S. Svelle, Top. Catal., 54 (2011) 1293.

67. F. Bauer, H.G. Karge, Mol. Sieves, 5 (2007) 249.

68. J.W. Park, G. Seo, Appl. Catal. A, 356 (2009) 180.

69. H.G. Karge, W. Nieβen, H. Bludau, Appl. Catal. A 146 (1996) 339.

70. L. Palumbo, F. Bonino, P. Beato, M. Bjørgen, A. Zecchina, S. Bordiga, J. Phys. Chem. C, 112 (2008) 9710.

71. M. Bjørgen, F. Bonino, S. Kolboe, K.P. Lillerud, A. Zecchina, S. Bordiga, J. Am. Chem. Soc., 125 (2003) 15863.

72. H.S. Cerqueira, P. Ayrault, J. Datka, P. Magnoux, M. Guisnet, J. Catalysis, 196 (2000) 149.

73. M. Rozwadowski, M. Lezanska, J. Wloch, K. Erdmann, R. Golembiewski, J. Kornatowski, Chem. Mater., 13 (2001) 1609.

74. P.E. Eberly, Jr., C.N. Kimberlin, Jr., W.H. Miller, H.V. Drushel, Ind. Eng. Chem. Process Des. Dev., 5 (1966) 193.

75. D. Wragg, Personal Communication, 2014.

76. C. Baerlocher, L.B. McCusker, Database of Zeolite Structures, http://www.iza-structure.org/databases (Accessed 17/10/2014).

77. S.H. Morejudo, Personal Communication, 2014.

78. N. Kasian, Personal Communication, 2014.

79. K.S.W. Sing, Pure & Appl. Chem., 54 (1982) 2201.

80. M. Thommes, in: J. Čejka, H. van Bekkum, A. Corma, F. Schueth (Eds.) Introduction to zeolite science and practice, Elsevier, Hungary, 2007.

81. B. Coasne, A. Grossman, C. Ortega, M. Simon, Phys. Rev. Lett. Physical Review Letters, 88 (2002) 256102.

82. W. Skistad, PhD Thesis, Dept. of chemistry, University of Oslo, 2014.

83. Y. Shu, D. Ma, L. Xu, Y. Xu, X. Bao, Catal. Lett., 70 (2000) 67.

84. J. Aguadoa, D.P. Serrano, J.M. Escola, A. Peral, J. Anal. Appl. Pyrol, 85 (2009) 352.

85. M. Bjørgen, S. Kolboe, Appl. Catal. A, 225 (2002) 285.

86. S. Teketel, W. Skistad, S. Benard, U. Olsbye, K.P. Lillerud, P. Beato, S. Svelle, ACS Catal., 2 (2012) 26.

87. K. Chakarova, K.Hadjiivanov, Chem. Commun., 47 (2011) 1878.

88. S. Bordiga, C. Lamberti, F. Geobaldo, A. Zecchina, Langmuir, 11 (1995) 527.

89. L.M. Kustov, V.B. Kazansky, J. Phys. Chem., 91 (1987) 5247.

90. M.S. Holm, S. Svelle, F. Joensen, P. Beato, C.H. Christensen, S. Bordiga, M. Bjørgen, Appl. Catal. A, 356 (2009) 23.

91. C. Morterra, V. Bolis, G. Magnacca, Langmuir, 10 (1994) 1812.

92. V.L. Zholobenko, M.A. Makarova, J. Dwyer, J. Phys. Chem., 97 (1993) 5962.

93. F. Wakabayashi, J. Kondo, A. Wada, K. Domen, C. Hirose, J. Phys. Chem., 97 (1993) 10761.

94. P. A. Jacobs, W.J. Mortier, Zeolites, 2 (1982) 226.

95. S.A. Bradley, R.W. Broach, T.M. Mezza, S. Prabhakar, W. Sinkler, in: S. Kulprathipanja (Ed.) Industrial Separation and Catalysis, Wiley-VCH Verlag GmbH & Co. KGaA, Great Britain, 2010.

96. V.L. Zholobenko, D.B. Lukyanov, J. Dwyer, J. Phys. Chem., 102 (1998) 2715.

97. T. Barzetti, E. Selli, D. Moscotti, L. Forni, J.Chem. Soc., Faraday Trans., 92 (1996) 1401.

98. F. Benaliouche, Y. Boucheffa, P. Ayrault, S. Mignard, P. Magnoux, Microporous Mesoporous Mater., 111 (2008) 80.

99. S.M. Campbell, X. Jiang, R.F. Howe, Microporous Mesoporous Mater., 29 (1999) 91.

100. T.R. Forester, R.F. Howe, J. Am. Chem. Soc., 109 (1986) 5076.

101. D.S. Bystrov, Zeolites, 12 (1992) 328.

102. S. Jolly, J. Saussey, J.C. Lavalley, Catal. Lett., 24 (1994) 141.

103. M. Bjørgen, F. Bonino, B. Arstad, S. Kolboe, K.P. Lillerud, A, Zecchina, S. Bordiga, ChemPhysChem, 6 (2005) 232.

104. J. Li, Y. Wei, Y. Qi, P. Tian, B. Li, Y. He, F. Chang, X. Sun, Z. Liu, Catal. Today, 164 (2011) 288.

105. L. Costa, F.R. Ribeiro, in: J.L. Figueiredo, M.M. Pereira, J. Faria (Eds.) Catalysis from theory to application, Imprensa da Univ. de Coimbra, 2008.

106. E.G. Derouane, in: B. Imelik, C. Naccache, G. Coudurier, Y. Ben Taarit, J.C. Vedrine (Eds.) Catalysis by Acids and Bases, Elsevier, Amsterdam, 1985.

107. M. Stöcker, Microporous Mesoporous Mater., 29 (1999) 3.

108. A.J. Marchi, G.F. Froment, Appl. Catal. A, 94 (1993) 91.

109. J. Coates, in: R.A. Meyers (Ed.) Encyclopedia of Analytical Chemistry, John Wiley & Sons Ltd., Chichester, 2000.

110. R.G. Jones, J. Kahovec, R. Stepto, E.S. Wilks, M. Hess, T. Kitayama, W.V. Metanomski (Eds.) Compendium of Polymer Terminology and Nomenclature: IUPAC Recommendations, Royal Society of Chemistry, Cambridge, 2008.

111. M. Bjørgen, S. Akyalcin, U. Olsbye, S. Benard, S. Kolboe, S. Svelle, J. Catal., 275 (2010) 170.

112. A. Lacarrierea, F. Luckb, D. Swierczynski, F. Fajulaa, V. Huleaa, Appl. Catal. A, 402 (2011) 208.

113. W. Skistad, S. Teketel, F.L. Bleken, P. Beato, S. Bordiga, M.H. Nilsen, U. Olsbye, S. Svelle, K.P. Lillerud, Top. Catal., 57 (2014) 143.

114. X. Zhu, S.Liu, Y. Song, L. Xu, Appl. Catal. A, 288 (2005) 134.

115. S. Svelle, F.Joensen, J. Nerlov, U. Olsbye, K.P. Lillerud, S. Kolboe, M. Bjørgen, J. Am. Chem. Soc., 128 (2006) 14770.

116. F. Bleken, W. Skistad, K. Barbera, M. Kustova, S. Bordiga, P. Beato, K. P. Lillerud, S. Svelle, U. Olsbye, Phys. Chem. Chem. Phys., 13 (2011) 2539.

117. M. Guisnet, L. Costa, F.R. Ribeiroa, J. Mol. Catal. A, 305 (2009) 69.

118. B.P.C. Hereijgers, F. Bleken, M.H. Nilsen, S. Svelle, K.P. Lillerud, M. Bjørgen, B.M. Weckhuysen, U. Olsbye, J. Catal., 264 (2009) 77.

119. E. Stavitski, in: J.A. Rodriguez, J.C. Hanson, P.J. Chupas (Eds.) In-situ Characterization of Heterogeneous Catalysts, John Wiley & Sons Inc., New Jersey, 2013.